3-D/2-D Registration of Left Atria Surface Models to Fluoroscopic Images for Cardiac Ablation Procedures

3D/2D-Registrierung von Oberflächenmodellen des linken Atriums zu Fluoroskopiebildern für Herzablationsprozeduren

Der Technischen Fakultät der
Friedrich-Alexander-Universität
Erlangen-Nürnberg

zur

Erlangung des Doktorgrades Dr.-Ing.

vorgelegt von

Matthias Weidler
aus Nürnberg

Als Dissertation genehmigt
von der Technischen Fakultät
der Friedrich-Alexander-Universität Erlangen-Nürnberg

Tag der mündlichen Prüfung:	
Vorsitzender des Promotionsorgans:	Prof. Dr.-Ing. Reinhard Lerch
Gutachter:	Prof. Dr.-Ing. J. Hornegger
	PD Dr.-Ing Markus Kowarschik

Abstract

Atrial fibrillation is one of the most common cardiac arrhythmias. It can be treated minimally invasive by catheter ablation. For guidance during the intervention, augmented fluoroscopy systems gain more and more popularity. These systems allow to fuse data which was pre-operatively acquired, e.g., using computed tomography, and intra-operative patient data. This facilitates navigation during the procedure by overlaying a 3-D model of the patient's left atrium to the fluoroscopic images. Moreover, if X-ray images are acquired from two views, 2-D image annotations can be displayed with respect to the 3-D patient model. Image fusion and annotation requires an accurate registration of pre-operative and intra-operative data which is mostly performed manually. This thesis is primarily concerned with methods for automatizing both the registration process and also steps which are required for registration. Thus, we propose also methods for reconstructing the 3-D shape of catheters from 2-D X-ray images as this is needed later for registration.

In the first part of this thesis, we present methods for fast 3-D annotation of catheters. The first method is able to annotate whole line-shaped catheters in 2-D X-ray images based on a single seed point. To this end, catheter-like image regions are transformed into a graph like structure which serves as reduced search space for the catheter detection method. Resulting annotations in two X-ray images from different views can then be used to compute a 3-D reconstruction of the catheters. Our proposed method establishes point correspondences based on epipolar geometry. We define an optimality criterion that makes this approach robust with respect to spurious and missing point correspondences. Both methods are then used to establish a method for automatic cryoballoon catheter reconstruction.

The second part investigates registration methods based on devices placed at certain anatomical structures. We present two different methods, one for thermal ablation and one for cryoablation. The first method relies on line-shaped devices placed outside the left atrium in the oesophagus and the coronary sinus. Their 3-D shape can be reconstructed using the algorithms presented in the first part and can then be aligned to their corresponding 3-D structures segmented from the preoperative data. The second method uses the pulmonary vein ostium which is a structure inside the left atrium in which cryoballoons are placed. A registration is established by relating the ostium position to a reconstruction of the cryoballoon computed using the approach presented in the first part. We use a skeletonization of the 3-D left atrium model to extract potential ostia from the model.

In the last part we consider an automatic registration method based on injected contrast agent. In this context we present a method for classification of contrasted frames. Moreover, we present a novel similarity measure for 3-D/2-D registration that takes into account how plausible a registration is. Plausibility is determined with respect to a reconstructed contrast agent distribution within the 3-D left atrium and the contrast agent in the 2-D images. We show that a combination of this similarity measure and a measure that relates edge information from the contrast agent in 2-D images to edges of the 3-D model increases accuracy substantially. As a final step, the frame-wise registration results are postprocessed by means of a Markov chain model of the cardiac motion. This method of temporal filtering reduces outliers and improves registration quality significantly.

Kurzfassung

Vorhofflimmern ist die am weitesten verbreitete Herzrythmusstörung Sie kann durch Katheterablation, einem minimalinvasiven Eingriff, behandelt werden. Damit der Arzt die Katheter an die richtige Stelle führen kann, wird der Patient mit Röntgenstrahlung durchleuchtet. Systeme, die erweiterte Durchleuchtung unterstützen können zudem 3D-Daten wie z.B. ein Herzmodell des Patienten das vor der Operation aufgenommen wurde oder Planungsdaten mit dem 2D Bild fusionieren. Wenn Röntgenbilder aus zwei Blickrichtungen aufgenommen werden, können 2D-Markierungen aus den Röntgenbildern auf das 3D-Modell des Patienten übertragen werden. Bildfusion und -annotation benötigen eine genaue Registrierung der 2D- zu den 3D-Koordinatensystemen. Die Registrierung wird meist manuell durchgeführt. Diese Arbeit befasst sich hauptsächlich mit der Automatisierung von Registrierung und weiteren Aufgaben, die im Kontext der Registrierung anfallen. Daher stellen wir ebenfalls Verfahren zur Rekonstruktion der 3D-Form von Kathetern anhand von 2D-Röntgenbildern vor, da dies später zur Registrierung benötigt wird.

Im ersten Teil der Arbeit präsentieren wir Algorithmen zur schnellen Markierung von Kathetern. Die erste Methode kann linienförmige Katheter vollständig auf Basis eines Startpunktes markieren. Die so generierten Annotationen von Kathetern in zwei Bildern aus unterschiedlichen Blickrichtungen können dann zur 3D-Rekonstruktion der Katheter verwendet werden. Die von uns vorgeschlagene Methode erzeugt Punktkorrespondenzen mit Hilfe der Epipolargeometrie. Wir definieren ein Optimalitätskriterium das unseren Ansatz robust gegenüber fehlerhaften und fehlenden Punktkorrespondenzen macht. Beide Verfahren werden dann verwendet um eine Methode zur automatischen Rekonstruktion von Cryoballonkathetern zu realisieren.

Der zweite Teil untersucht Registrierungsmethoden welche Katheter nutzen die an bestimmten anatomischen Bereichen platziert werden. Das erste Verfahren ist für thermische Ablationsverfahren entwickelt und nutzt Katheter in der Speiseröhre und dem Koronarsinus. Deren 3D-Form wird mit Hilfe der Algorithmen aus dem ersten Teil der Arbeit rekonstruiert. Die entsprechenden Strukturen aus dem präoperativen 3D-Datensatz werden anschließend an den rekonstruierten Kathetern ausgerichtet. Die zweite Methode nutzt den Cryoballonkatheter, der bei Ablation durch Kälte gegen das Pulmonalvenenostium gedrückt wird. Eine Registrierung wird erzeugt indem die Position des Ostiums zu der rekonstruierten Position des Cryoballons in Beziehung gesetzt wird.

Im letzten Teil der Arbeit betrachten wir automatische Registrierung anhand von injiziertem Kontrastmittel. Dazu stellen wir eine Methode zur Klassifizierung von kontrastmittelhaltigen Einzelbildern einer Bildsequenz vor und präsentieren ein neuartiges Ähnlichkeitsmaß für die 3D/2D-Registrierung. Dieses Ähnlichkeitsmaß erstellt auf Basis einer Registrierung eine 3D-Verteilung des Kontrastmittels im Vorhof und misst wie plausibel diese Verteilung im Hinblick auf das in den Röntgenbildern sichtbaren Kontrastmittel ist. Mit diesem Maß, in Verbindung mit einem Maß das Kanten des 3D-Modells und des Kontrastmittels im Röntgenbild aufeinander abstimmt, werden gute Registrierungen erreicht. Als letzten Schritt verwenden wir ein Markowketten-Modell der Herzbewegung um die Registrierungsergebnisse der Einzelbilder in Bezug zu setzen. Dadurch kann eine zeitliche Filterung der Registrierungen durchgeführt werden welche die Registrierungsgenauigkeit signifikant steigert.

Acknowledgments

First of all, I gratefully thank Prof. Dr.-Ing Joachim Hornegger for the opportunity to work at the Pattern Recognition Lab. I enjoyed very much the inspiring research environment and possibility to collaborate closely with partners from industry and hospitals which made this thesis possible at all. Especially I would like to thank him for his encouragement, the freedom to choose my research directions, and his valuable feedback. I thank Prof. Dr.-Ing. Andreas Maier who always took the time to discuss my ideas and approaches. Especially I would like to thank him for the support during preparation of publications and this thesis.

I really appreciate the intense collaboration with Prof. Dr. Norbert Strobel, my industrial partner at Siemens Healthineers AG. He has been with me for all these years and has shared his extensive experience in all aspects of augmented fluoroscopy, from technical details to possible clinical applications. He discussed my ideas and approaches and assessed my experimental results again and again. I got always critical feedback from him, not only when writing my publications.

I would especially like to thank Dr. med. Klaus Kurzidim and his team at the "Krankenhaus Barmherzige Brüder" in Regensburg. Without the clinical data he kindly provided, most of the experiments could not have been conducted. He also took the time to give me feedback on my approaches in terms of clinical applicability and impact on clinical workflow. At this point I would also like to thank Christopher Kowalewski and Dr. med. Felix Bourier, who helped me to understand the medical background and supported me in my work by labeling the clinical data.

I acknowledge support by the German Federal Ministry of Education and Research (BMBF) in the context of the initiative Spitzencluster Medical Valley-Europäische Metropolregion Nürnberg, Project Grants nos. 13X1012A and 13EX1012E, respectively.

I would like to thank my colleagues at the pattern recognition lab: Dr. Alexander Brost, who brought me to the topic and my room mate Martin Koch who helped me both with everyday things at the lab and with the scientific work, be it by reviewing the papers, discussing the ideas or common code. My thanks also go to the Medical Image Registration Group and to my colleagues who reviewed this thesis: Dr. Martin Berger, Dr. Florian Hönig, Dr. Thomas Köhler, Dr. Oliver Taubmann and Dr. Mathias Unberath.

A big *Thank You* goes to the students who I supervised: Alexandra Höfer, Andreas Kleinöder, Simone Müller, Sabrina Reiml und Xia Zhong. Their excellent work contributed to several publications.

Last but not least I would like to thank my family for their support during the last years.

Erlangen, 22.04.2018 Matthias Weidler

Contents

CHAPTER 1

Introduction

Within the last decades, minimally invasive procedures have become an established alternative to traditional open surgery for treatment of several diseases [Dezi 93, Irib 11, Attw 92, Jaco 91]. Especially in the field of electrophysiology (EP), catheter ablation has become the standard way of treatment that is in most cases preferred over open heart surgery [Fust 06]. For guidance during minimally invasive procedures, several imaging modalities can be used. Each of them has its own advantages, like real-time capability with high spatial resolution for fluoroscopy or 3-D imaging without harmful ionizing radiation for magnetic resonance imaging (MRI).

One drawback of fluoroscopy is its poor soft-tissue contrast such that the heart anatomy cannot be seen in X-ray images. This can be compensated by combining fluoroscopic images and 3-D data from a computed tomography (CT) or an MRI scan of the patient which was acquired prior to the procedure. From the 3-D volume, the heart surface is segmented and overlaid to the fluoroscopic images [De B 05], see Figure 1.1. This fusion of both modalities requires a registration of the data sets which maps the location of a point on the 3-D surface model to the corresponding location in the fluoroscopic image. Once the registration has been established, annotations on the 3-D model created during planning of the procedure can be displayed in the fused view. This is called augmented fluoroscopy. Moreover, 3-D information generated from 2-D interventional X-ray data can be visualized together with the 3-D surface model.

The way minimally invasive procedures are performed in clinical practice is subject to several factors of influence. In this chapter, we describe some of them as they form the motivation for this thesis. Afterwards, we present our contributions to the field of 3-D/2-D registration for electro-physiological procedures and give an overview of the structure of this thesis.

1.1 Motivation

The cost for the health care system is increasing rapidly. In Germany, the cost aside from basic medical service has doubled in the last 20 years [Stat 16]. For computer assisted interventions, trained medical staff is required to operate the computers or

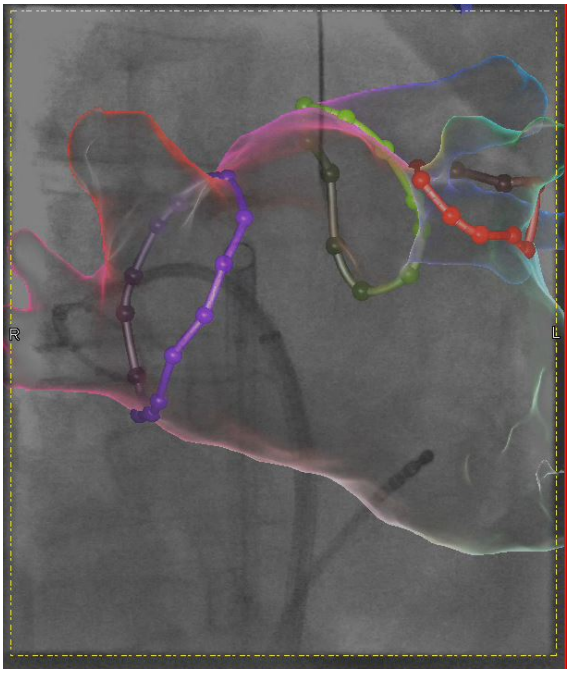

Figure 1.1: Due to the low soft tissue contrast of X-ray images, the heart anatomy is not visible in fluoroscopy images. To overcome this limitation, a 3-D model (coloured shape) of the patient's heart can be overlaid to the image. Moreover, annotations relevant to the procedure (lines with dots) can be displayed as well.

this is done by the physician resulting in prolonged interventions. This thesis aims at automatizing selected tasks of a catheter ablation procedure for the treatment of atrial fibrillation (AFib) which is one of the most common heart arrhythmia. As many processes within interventions in the field of EP are similar, the results can also be applied to other procedures.

For an augmented fluoroscopy system, time demanding tasks are registration, 2-D catheter annotation and 3-D catheter reconstruction. Although the focus of this thesis is on registration, we do not limit the automation to the registration process itself, but also consider the catheter reconstruction and catheter annotation. Both of them are important for registration if the registration utilizes catheters or devices and the corresponding anatomy in which they are placed. However, catheter annotation is also required for documentation which is an important part of the intervention. Reducing the user interaction for these tasks will also take some load off the medical staff.

We want to leave as much control as possible to the physician. This means that the physician or medical staff should have the possibility to inspect meaningful intermediate results of the automatic registration process and should be able to correct them. By doing so, small errors in early steps, e.g., the catheter detection can be corrected quickly to still get a meaningful registration result. Moreover, the registration process does not appear as a large "black box", as its intermediate results, i.e., the results of each module can be visualized. So, the functioning of the system becomes more transparent to the physician.

In this work, we focus on data acquired by a biplane C-arm X-ray system. These systems can acquire X-ray images simultaneously from two views. Although these systems are less common than monoplane systems, they support 3-D reconstruction of, e.g., devices visible in X-ray systems. This is more difficult for monoplane systems as the C-arm needs to be rotated leading to a deferred second acquisition which introduces motion artefacts.

1.2 Contributions

In this thesis, we present a framework for automatic registration of 3-D atrium models to fluoroscopic images. The parts of the framework and their relations are depicted in Figure 1.2. This framework consists of three main parts: The first part is the detection and reconstruction of different catheters and devices used in EP. Based on the resulting 3-D shapes of the catheters, device-based registration can be performed which is the second part of the framework. The third part are methods for automatic registration based on contrast agent that is injected into the left atrium. A detailed description of the contributions to each part is given below.

Contributions to the Field of Catheter Detection and Reconstruction

The contributions to the field of catheter detection are as follows:

- We propose a novel **detection method for curvilinear catheters** which adapts to the shape of different catheters in a training step. As an input, it requires a point marked at the catheter tip. This method is capable of detection not only the catheter tip but the **whole catheter including its shaft**. The method and the results have been presented at a conference [Hoff12b] and published as a journal article [Hoff16b].
- We developed a **reconstruction method** for curvilinear catheters which are visible in a X-ray image pair acquired with a biplane C-arm system. The reconstruction method is **robust to inaccurate calibration or cardiac and respiratory motion**. Parts of this method and evaluation have been presented in [Hoff12b, Hoff16b], a detailed description of the reconstruction method has been presented at a conference [Hoff13b].
- The previously catheter detection and reconstruction methods have been combined to a **fully automatic cryoballoon reconstruction** method. This method allows a robust 3-D location of the cryoballoon which is a part of a catheter and is hardly visible in X-ray images.

Contributions to the Field of Catheter-Based Registration

In this area, we distinguish between registration methods that make use of medical devices that are located outside the left atrium and methods that are based on catheters inside the left atrium.

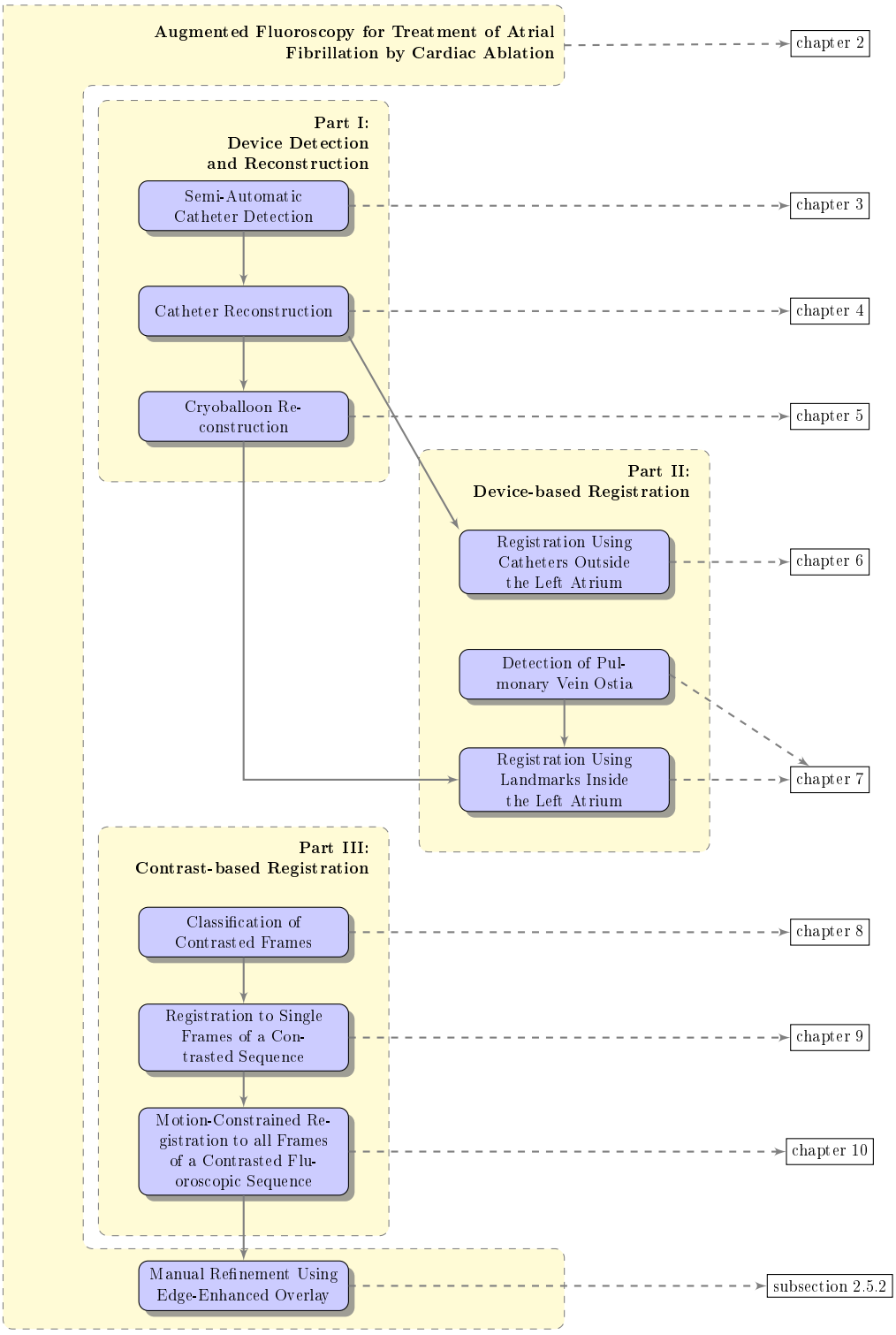

Figure 1.2: Structure of this thesis. The thesis consists of three parts. Part I contains methods for catheter detection and reconstruction. Some of these methods are used by the algorithms for device-based registration which are described in part II. Part III describes methods used in the context of contrast-based registration. Solid arrows describe dependencies between the methods. chapter 2 provides the medical and technical context for all parts.

- For registration using devices outside the left atrium, we propose an extension of the method in [Bros 11b]. This method registers anatomical structures to catheters located inside them. Instead of using only a single catheter we extend this method to a **combination of two medial devices** to achieve a higher robustness of this method. This method has been presented at a conference [Hoff 16g].

- For re-registration, i.e., correction of an already established registration within the procedure we propose a novel method that is based on the position of the cryoballoon inside the left atrium (LA) anatomy. This method relies on a skeleton representation of the LA and uses a learning based approach to detect pulmonary vein (PV) ostia in this skeleton representation. By selecting the PV ostium corresponding to the current location of the cryoballoon, a registration is performed.The PV ostium detection has been published at a conference [Hoff 16c].

Contributions to the Field of Contrast-Based Registration

For contrast-based registration we have developed a completely automatic registration pipeline. Its modules are described as follows:

- The first element of the pipeline is a detection method for contrasted frames in a sequence. This method is **learning based** and more robust than previous approaches [Zhao 13, Cond 04]. Due to the learning-based approach, the method can **adapt to the exposure control** specific to the angiography acquisition program. This method has been published at a conference [Hoff 15].

- For registration, we propose a similarity measure that combines edge information and a **new consistency measure** that measures how plausible a registration is with respect to its 3-D contrast agent distribution. This similarity measure was specifically designed for registration on biplane systems where the target volume is only partially visible. The method, together with a method for finding the **best reference frame for subtraction angiography**, has been published in a journal article [Hoff 16d].

- To combine registration results for each frame of a sequence, we modelled the **LA motion using a Markov chain**. This model was used to infer a **filtered registration with respect to motion constraints** which outperformed regularization-based motion constraints. It has been published in the journal article [Hoff 16d] and presented at a conference [Hoff 16a].

- To support a faster manual registration, we propose an overlay that focusses on **edges of the LA**. To relate corresponding parts in both views of a biplane system, the overlay is **color-coded according to its position in 3-D**. The overlay has been presented at at conference [Hoff 13a].

Further contributions to the field of catheter detection which are not described in this thesis are a semi-automatic combined detection and reconstruction of a basket catheter [Zhon 15, Zhon 16] and the detection of stent graft markers [Reim 15].

1.3 Organization of this Thesis

In chapter 2, we first describe atrial fibrillation and its treatment by catheter ablation as this is the procedure on which this thesis focusses on. Next, navigation techniques for this minimally invasive procedure are presented. As the methods in this thesis aim at enhancing augmented fluoroscopy systems, we describe briefly the camera geometry of a C-arm X-ray system which is used to acquire these fluoroscopic images. Finally, we describe state-of-the-art manual registration techniques and present a novel overlay that supports a better manual contrast-based registration.

The main body of the thesis is divided into three parts: The first part describes methods for catheter detection and reconstruction which are later required in the second part that presents methods for automatic device-based registration. The third part is independent from the other two parts and describes methods for contrast-based registration. These parts and their structure are also illustrated in Figure 1.2.

The first part starts in chapter 3 with a description of our catheter detection method that detects the catheter shaft based on a seed point at the catheter tip. In chapter 4, we present a method for the reconstruction of a catheter shaft based on annotations in two X-ray views. Then, we describe in chapter 5 a fully automatic method for cryoballoon reconstruction.

The second part consists of two methods for registration using catheters and devices: The first method described in chapter 6 uses catheters outside the LA to perform a registration. In chapter 7 we present a method that uses catheters attached to landmarks inside the LA to perform a re-registration.

The third part describes a pipeline for contrast-based registration It starts with a description of a method for the detection of contrasted frames in chapter 8. chapter 9 describes the actual contrast-based registration including a method to select, given a contrasted frame, a proper uncontrasted frame for subtraction angiography. This chapter also introduces the novel similarity measure based on a contrast distribution estimate. chapter 10 describes two methods for the integration of motion constraints into the registration process.

This thesis finishes with an outlook in chapter 11 and a summary in chapter 12.

CHAPTER 2

Augmented Fluoroscopy for Treatment of Atrial Fibrillation by Cardiac Ablation

Our registration methods are designed to be used in an electrophysiology-lab during minimally invasive procedures which are performed to treat cardiac arrhythmias. Atrial fibrillation (AFib) is a very common heart arrhythmia on which we focus in this thesis. This chapter presents the medical background on AFib and its treatment. Then, we describe currently used methods for navigation with a focus on augmented fluoroscopy systems. Subsequent to a short section about the mathematics associated with a (biplane) C-arm X-ray system, we give an overview of current methods for manual registration used in the context of today's augmented fluoroscopy systems.

2.1 Atrial Fibrillation

AFib is one of the most common cardiac arrhythmia. Its prevalence depends on the age and ranges from 2.3 % for people older than 40 years to 5.9 % for people older than 65 years [Fein 95]. AFib is characterized by a electrico-mechanical activation of the left atrium (LA). The LA is one of four heart chambers, see Figure 2.1. AFib has its origin in the electrical conduction system of the heart which is shown in Figure 2.2. The diagnosis and treatment of AFib and other cardiac arrhythmias belongs to the field of electrophysiology (EP).

Usually, electrical impulses are generated periodically by the sinus node and are propagated along the LA heart walls to the atrioventricular (AV) node from which the impulses continue to the ventricle walls. With AFib, these signals are disturbed in the LA by additional electrical currents. The most supported hypothesis for the formation of these additional currents postulates the existence of *focal triggers* and an arrhythmogenic *substrate* [Calk 07]. Focal triggers are spots which emit electrical

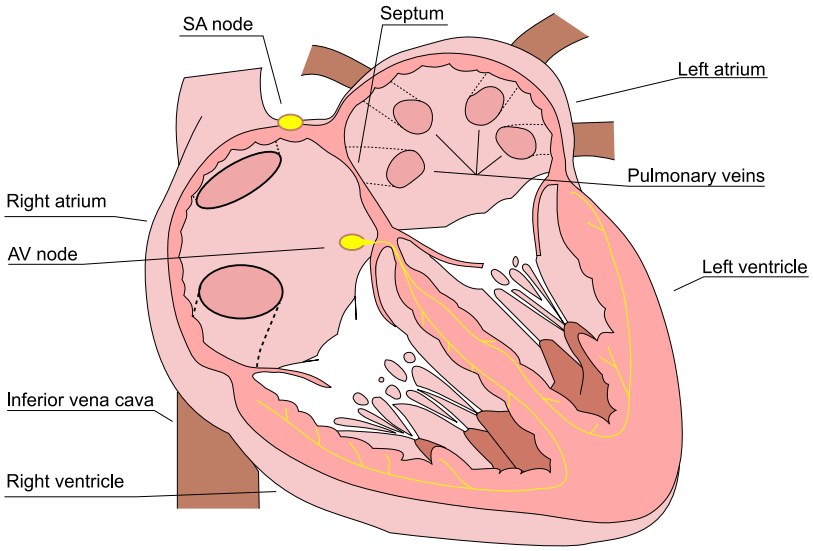

Figure 2.1: Anatomy of the human heart. From the pulmonary veins, blood enriched with oxygen comes from the lung and is ejected into the left ventricle. From here, the blood is distributed into the whole body. The blood flows back into the right atrium and from there over the right ventricle to the lungs. Image derived from [goog], CC-BY-SA 3.0

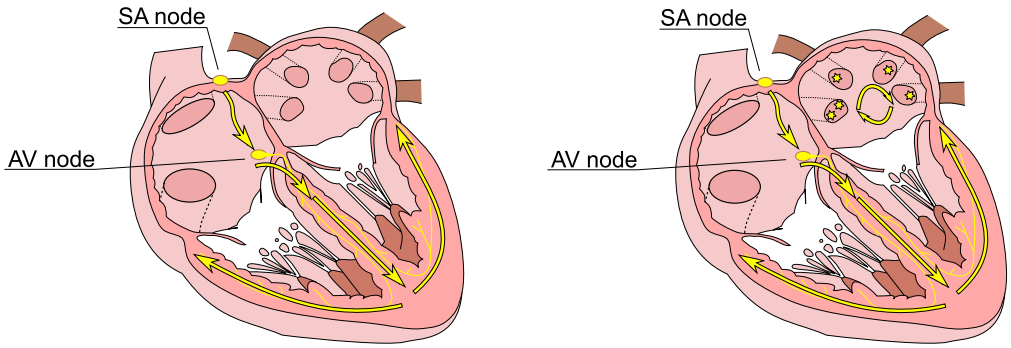

Figure 2.2: (a) Normal electrical pathways: The signals triggered by the sinus node run to the AV-node and then propagate along the ventricle wall. They lead to an synchronized contraction of atria and ventricles. (b) The normal electrical conduction system is disturbed by electrical signals originating from the pulmonary veins. As a result of these disorganized electrical impulses, the left atrium fibrillates. Images derived from [goog], CC-BY-SA 3.0

impulses. Most often, they are located in the pulmonary veins but they may also exist at other locations inside the LA. The impulses are maintained by an arrhythmogenic substrate, i.e. a certain electrophysiological structure in which the impulses are promoted circularly. These high-frequent rotors emit waves that let the LA fibrillate.

AFib can be divided into paroxysmal and persistent AFib [Calk 07]. Paroxysmal AFib denotes AFib that occoured more than two times but terminates spontaneously within seven days. Persistent AFib is defined as AFib lasting for more than seven days or requires cardioversion. One implication of AFib is an almost five-fold increased risk

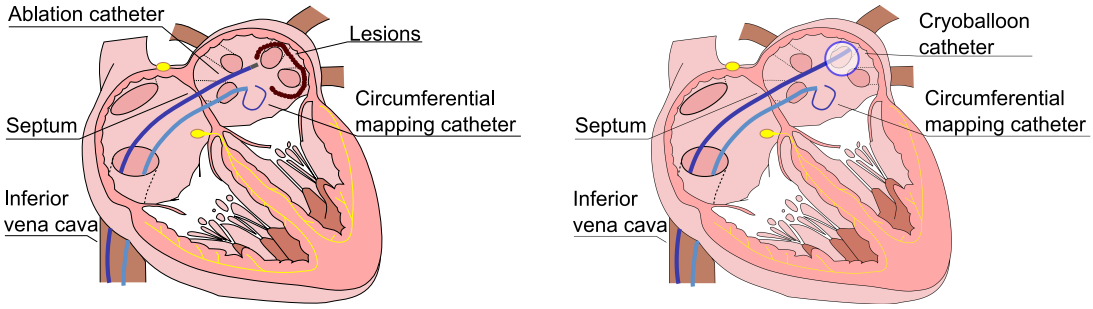

Figure 2.3: (a) An radio frequency (RF) catheter is inserted via the inferior vena cava and a transseptal puncture into the LA. To electrically isolate the PV, a contiguous line of point-shaped lesions is created by heating the tissue. (b) Alternatively, a cryoballoon catheter can be used. Its balloon is pushed against the PV ostium and cooled down using liquid nitrogen. As a result, tissue circularly around the PV ostium is freezed leading to electrically isolating scars. Images derived from [goog], CC-BY-SA 3.0

of suffering stroke compared to healthy patients [Wolf 91]. Due to AFib, the perfusion of the LA is low. Especially one part of the LA, the left atrial appendage (LAA) is only little perfused. This leads to the formation of blood clot which can result in an ischemic stroke [Siev 02]. Other symptoms of AFib are fatigue, palpitations or effort intolerance [Calk 07, Sing 06].

To avoid the formation of blood clots, anticoagulants can be prescribed [Pete 89] or the left atrial appendage can be closed mechanically [Siev 02]. However, AFib and other symptoms such as effort intolerance persist. To improve quality of life [Sing 06], the cause of AFib can be eliminated using a catheter ablation.

2.2 Cardiac Ablation

Cardiac ablation is a minimally invasive procedure with the goal of creating lesions at distinct positions in the LA. A common ablation strategy is *pulmonary vein antrum isolation* which aims at creating a continuous lesion around both pulmonary veins (PVs) on the left side of the LA and on the right side of the LA, respectively [Calk 07]. Along these lesions, scar tissue develops which is not conductive and blocks electrical impulses coming from a PV. It is important that the lesions form a closed ring around the PVs without gaps. Moreover, for a successful ablation, the created lesions need to be transmural, i.e. they reach to the outside heart wall [Calk 07].

Lesions can be created by either heating up the tissue or by freezing tissue. For destroying tissue by heat, an radio frequency (RF) catheter can be used. The tip of an RF catheter induces a high-frequently alternating current into the cardiac tissue which acts as a resistor and heats up. The size of these lesions is typically about 6 mm [Dick 06]. Using an RF catheter, a point-by-point ablation is performed, i.e., several single lesions are placed close to each other until they form a closed line, see Figure 2.3(a).

Freezing tissue for creating lesions can be performed using a cryoballoon catheter. This catheter has an inflatable balloon at its tip which is filled with liquid nitrogen to freeze tissue that touches the balloon. During the procedure, the inflated balloon is pushed into the PV ostium and cooled down, see Figure 2.3(b) This way, the PV is electrically isolated from the LA [Knec 13]. There are two different diameters on the market to account for different anatomies of the PV ostia [Furn 11, Chie 12, Furn 14]. Cryoballoon catheters are referred as single-shot devices as they are able to create a contiguous lesion with a single application. This way, it is possible to reduce procedure time compared to a point-by-point ablation approach of, e.g., RF catheters [Bour 13, Kojo 10]. In practice, gaps may still remain when using a cryoballoon. They can be closed by creating a few small lesions, e.g., using an RF catheter or a focal cryo catheter [Kojo 10]. A recent study showed that cryoballoon ablation has a similar long-term success compared to an RF point-by-point ablation [Vogt 13].

Compared to point-by-point RF ablation, cryo-ablation has a reduced risk of certain complications. During RF-based ablation, an esophageal fistula, i.e. a connection between the LA and the esophagus can be created if power delivery and wall contact force is too high. This complication can lead to severe infections and can even result into death of the patient [Calk 07]. Another complication is pulmonary vein stenosis, which means that the diameter of the PV is decreased due to the ablation. Ablation using a cryoballon appears to have no risk of esophageal fistula [Kojo 10] and occouring PV stenoses are not that severe compared to RF ablation [Andr 11].

Besides ablation catheters, other catheters such as the coronary sinus (CS) catheter or the circular mapping (CM) catheters are often involved. The CS is a coronary vein that is located between the left ventricle and the LA and drains into the right atrium (RA). During ablation a multi-electrode CS catheter is placed into this vein for diagnostic reasons and for pacing the patient within a procedure.

The CM catheter is also a multi-electrode catheter. This catheter has a circularly shaped tip on which the electrodes are located. It is used inside the LA to determine whether a PV is a potential source of abnormal electrical impulses and needs to be electrically isolated. It is also used after ablation to verify the success of the isolation and the absence of gaps in the created lesions.

A focal impulse and rotor mapping (FIRM)-based ablation strategy involves the use of a basket catheter. The end of this catheter is a sphere made up of eight semicircular wires, so-called splines. This catheter is placed in the RA and afterwards in the LA so that its splines touch the atrium wall. Each spline has got eight electrodes which are used to measure the electrical signals at the LA wall over a certain period of time. Using the Topera RhythmView software (Topera Inc., Palo Alto, CA, USA), positions of rotors can be derived from the signal recordings. The respective tissue in the LA can then be ablated. A recent study [Nara 12] stated that this ablation strategy may lead to a better long-term outcome, especially for persistent AFib.

A typical place to insert catheters into the patient's body is the groin, where catheters are led via the femoral vein into the RA. For ablation catheters and the CM catheter, a sheath, i.e. a thin plastic tube, is placed into the LA. To guide the sheath from the RA to the LA, the septum separating LA and RA needs to be punctated. Afterwards, the success of the transseptal puncture needs to be verified, e.g. by injecting contrast agent (CA) through the sheath into the LA. Then, a catheter

can be guided through the sheath into the LA. The sheaths are necessary to allow a bloodless and fast exchange of catheters and to steer the catheters.

Another device used in conjunction with catheter ablation is a esophageal temperature probe. This temperature probe is inserted into the esophagus and is used to monitor the temperature of the esophagus. This is typically done if tissue close to the esophagus is ablated to address the risk of an esophageal perforation [Calk 07].

2.3 Navigation During Caridac Ablation

As part of the procedure, the physician has to navigate the ablation catheter and the CM catheter to different regions of the LA. Especially when placing the ablation catheter, e.g., for creating point-wise ablations with the RF catheter, the physician needs to know where the catheters are with respect to the LA anatomy. Navigation and orientation during the procedure is usually facilitated using either an electro-anatomical mapping system (EAMS), fluoroscopy, or a combination of both. Additionally, intercardiac echography (ICE) and/or 3-D imaging can be used. In the remainder of this section, navigation using fluoroscopy or EAMS is explained in more detail. Moreover we describe augmented fluoroscopy which combines X-ray images with 3-D data, obtained by computed tomography (CT), magnetic resonance imaging (MRI) or C-arm CT.

2.3.1 Guidance by Fluoroscopic Images

Fluoroscopy is a continuous X-ray imaging of the patient. This allows the physician to see the catheter movement in real-time at high accuracy. To avoid unnecessary radiation exposure, both for the patient and the physician, imaging is performed with a very low dose and a low frame rate, e.g. 5 fps [Estn 15]. For documentation, e.g. of an angiography, images with a higher dose and, if necessary, a higher frame rate can be generated.

Modern EP-labs are usually equipped with a C-arm X-ray device. This allows the physician to acquire images from different views. Often, these C-arm systems can also acquire 3-D volumes of the patient (C-arm CT). Biplane C-arm systems involve a second C-arm which allows them to acquire images from two different views simultaneously. A picture of such a biplane system is given in Figure 2.4. The image planes of a biplane system are denoted as plane A for the floor stand and plane B for the top stand.

A major drawback of fluoroscopy is that both patient and physician are exposed to radiation. Moreover, soft tissue such as vessels or the LA are only visible if CA is injected and depth information is lacking.

2.3.2 Guidance by Electro-Anatomical Mapping Systems

Electro-anatomical mapping systems are able to determine the position of catheters in 3-D. In most cases, either CARTO (Biosense Webster, Diamond Bar, CA, USA) or the EnSite NavX system (St. Jude Medical, Inc., St. Paul, MN, USA) is used.

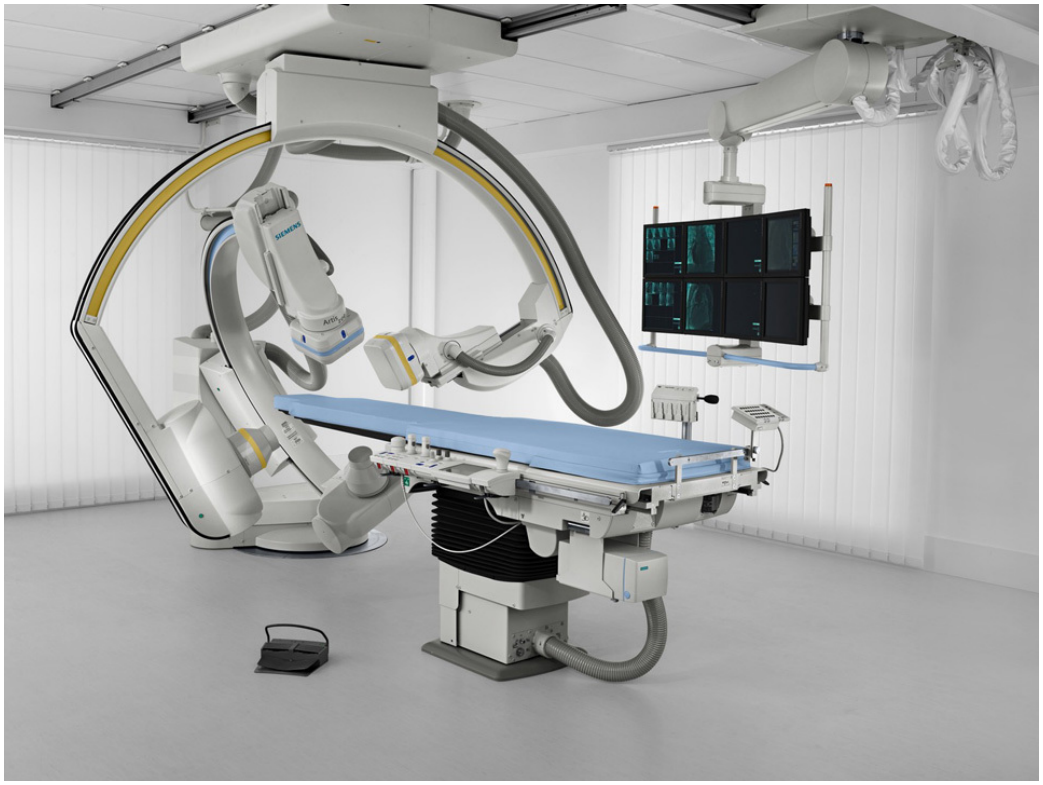

Figure 2.4: Biplane C-arm system. The image plane of the floor stand is denoted as plane A, the image plane of the top stand is referred as plane B. Image courtesy of Siemens Healthcare GmbH

The CARTO system uses static magnetic fields of different strength which are generated by three calibrated coils mounted below the patient table. Navigation using CARTO requires special catheters that comprise three magnetic sensors at the catheter tip. With these sensors, the CARTO system measures the strength of all three magnetic fields. This way, the position and orientation of the catheter tip can be measured [Geps 97].

EnSite NavX uses an electrical field generated by three patches which are attached orthogonally to the patient skin. The voltage and the impedance of the field is measured at each catheter electrode. As they are proportional to the distance of the electrode to the patches, the position of the catheter can be determined [Estn 06].

Both products allow tracing of the LA anatomy by moving, e.g., the CM catheter along the LA wall. This way, catheters can be displayed in 3-D with respect to the LA. Additionally, catheters may be used to generate activation maps which display how electrical impulses propagate through the atrium.

However, an EAMS require specialized catheters. As currently no cryoballoon catheter on the market is compatible to either EAMS, cryoablation procedures need to be performed under fluoroscopy. Moreover, the specialized catheters are more expansive than common EP catheters [Spor 04]. Depending on the reimbursement policy of the respective country, this may play an important role. In practice, EAMS do not replace C-arm systems as they are often required at certain phases of the

procedure, e.g., to verify the success of the transseptal puncture or serve as fallback imaging device in case of complications.

Another drawback may be that accuracy of the EnSite system can be influenced locally by changes in impedance of the tissue [Bour 14].

2.3.3 Augmented Fluoroscopic Image Guidance

To overcome two main drawbacks of fluoroscopy, namely lack of 3-D information and poor soft tissue contrast, augmented fluoroscopy has been proposed [De B 05, Ecto 08]. Here, 3-D objects are overlaid on fluoroscopic images. For example, a patient specific 3-D model of the LA is overlaid to the images to visualize the patient's anatomy during the procedure when no CA is injected, see Figure 2.5. The use of such an overlay was found to reduce procedure time and fluoroscopy time significantly [Sra 07].

Such 3-D models can, e.g., be segmented from preoperative CT or MRI angiography (MRA) acquisitions [Ecab 08, Kari 09a, Kari 09b, Zhen 12] that are routinely performed to obtain prior knowledge about a patient's anatomy of the LA. This is helpful to rule out an unusual configuration of the pulmonary veins or the existence of an accessory pulmonary vein. Segmentation results can be stored efficiently as a triangle mesh $M = (V_M, E_M)$ with vertices $V_M \subset \mathbb{R}^3$ and edges $E_M \subset V_M \times V_M$.

In addition, preprocedural 3-D planning data can be overlaid on the fluoroscopic images. Moreover, intraprocedural information from the 2-D images, e.g., anatomical landmarks, ablation positions, or catheter positions can be annotated and overlaid to fluoroscopic images. If the respective positions are available from two views, e.g., from images taken by a biplane C-arm system, their corresponding 3-D position can be triangulated. These information can be displayed in a freely-rotatable 3-D view together with the 3-D heart model, as shown in Figure 2.5 (c).

2.4 C-Arm Geometry

The 3-D world coordinate system is defined such that its origin coincides with the C-arm isocentre of the A-plane, i.e., the point around which the C-arm rotates. The x-axis corresponds to the transverse axis of the patient (left-right), the y-axis corresponds to the frontal axis (front-back, anterior-posterior) and the z-axis corresponds to the vertical body axis (head-foot). A C-arm can rotate about two axis. The rotation about the patients vertical axis is usually referred as primary rotation, the rotated views are denoted as left anterior oblique (LAO) views and right anterior oblique (RAO) views. The other possible rotation is a rotation towards the head or the feet of the patient, i.e. in cranial or caudal direction. The coordinate system and rotation axes are visualized in Figure 2.6.

The 3-D information and the 2-D fluoroscopic images are connected by a projection matrix $\boldsymbol{P} \in \mathbb{R}^{3\times4}$ for each view. For a biplane system, the projection matrix for plane A is denoted by $\boldsymbol{P}_\mathrm{A}$, the projection matrix for plane B is denoted by $\boldsymbol{P}_\mathrm{B}$. If the projection matrix is known, the projected 2-D position $\boldsymbol{p}^{2\mathrm{D}} \in \mathbb{R}^2$ of a 3-D point $\boldsymbol{w} \in \mathbb{R}^3$ can be obtained by

$$\lambda \hat{\boldsymbol{p}}^{2\mathrm{D}} = \boldsymbol{P}\hat{\boldsymbol{w}} \tag{2.1}$$

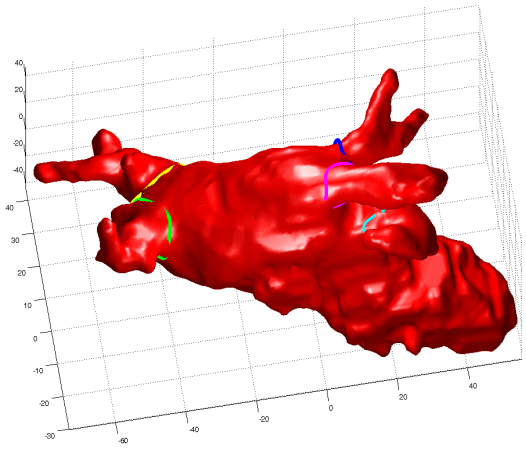

(a)

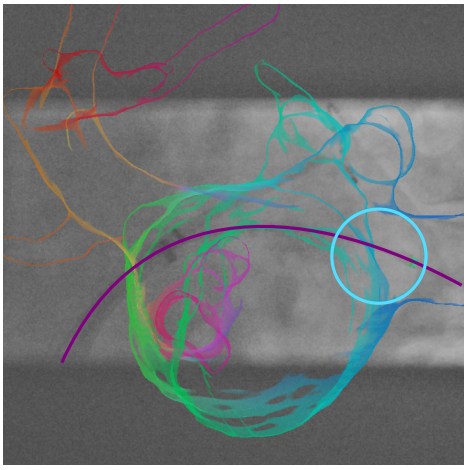

(b)

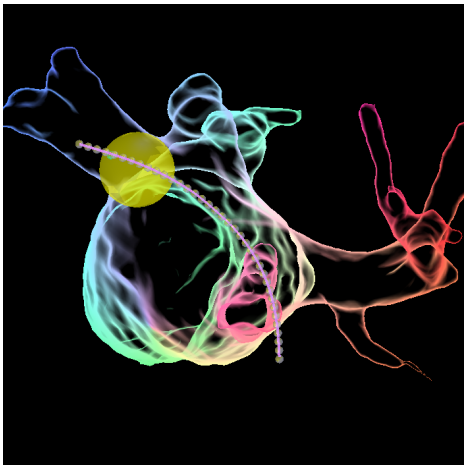

(c)

Figure 2.5: (a) LA segmented from MRI data with annotated pulmonary vein ostia and left atrial appendage. (b) 3-D LA model overlaid to fluoroscopic image with annotated cryo balloon (blue circle) and cryo cathter shaft (purple line). (c) 3-D view of LA model with triangulated 3-D cryo balloon catheter

where $\hat{\boldsymbol{p}}$ denotes the homogeneous representation of a point $\boldsymbol{p}$ [Hart 03]. A point $\boldsymbol{p}$ can be transferred into homogeneous coordinates using

$$\hat{\boldsymbol{p}} = \begin{pmatrix} \boldsymbol{p} \\ 1 \end{pmatrix}. \tag{2.2}$$

Given a point $\hat{\boldsymbol{p}} = \begin{pmatrix} \boldsymbol{p}' \\ h \end{pmatrix}$ in homogeneous coordinates, the point coordinates $\boldsymbol{p}$ can be obtained by

$$\boldsymbol{p} = \frac{1}{h}\boldsymbol{p}'. \tag{2.3}$$

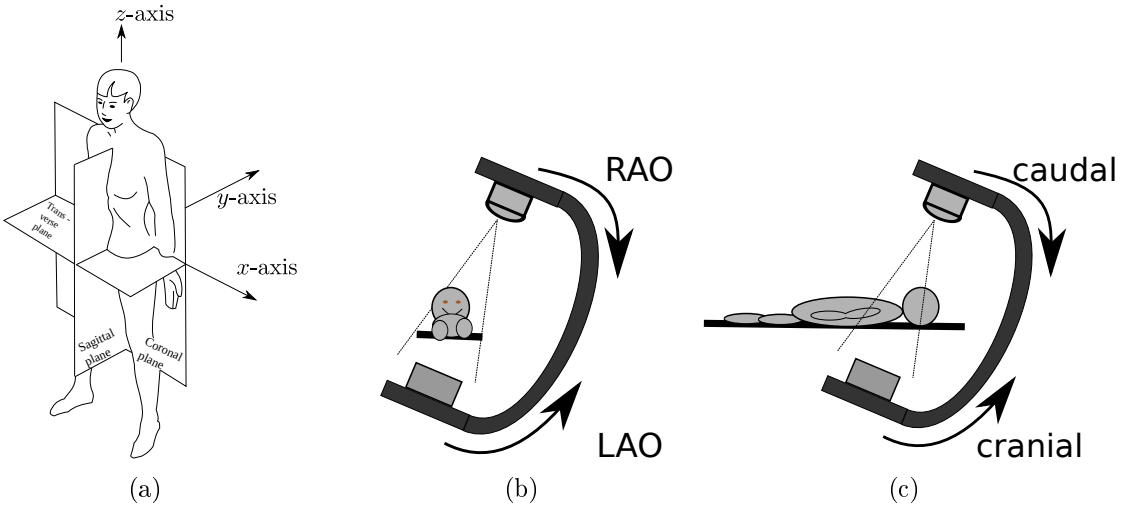

Figure 2.6: (a) Patient coordinate system. Image CC-0 from [Ozha] (b) The primary rotation of a C-arm denotes rotations about the patient's head-foot-axis. (c) Secondary rotations denote rotations of the detector towards the patient's head (cranial) or feet (caudal)

The entries of a projection matrix can be obtained either by a calibration procedure [Hart 03, Misc 00, Roug 93] or they can be approximated using the known geometric properties of the C-arm such as primary and secondary roatation angle, pixel spacing and source-to-image distance [Bros 09c].

The relationship between plane A and plane B of a fluoroscopic system is described by means of epipolar geometry [Hart 03]. A 2-D point $\boldsymbol{p}^{\mathrm{A}} \in \mathbb{R}^2$ in image plane A can be mapped to the epipolar line $\boldsymbol{l}_{\mathrm{B}} \in \mathbb{R}^3$ using the fundamental matrix $\boldsymbol{F} \in \mathbb{R}^{3\times3}$. The epipolar line describes a line in plane B, which runs through the point in plane B that corresponds to $\boldsymbol{p}^{\mathrm{A}}$, see Figure 2.7. With known projection matrices $\boldsymbol{P}_{\mathrm{A}}$ and $\boldsymbol{P}_{\mathrm{B}}$, the fundamental matrix can be computed by

$$\boldsymbol{F} = [\boldsymbol{P}_{\mathrm{B}}\hat{\boldsymbol{o}}_A]_\times \boldsymbol{P}_{\mathrm{B}}\boldsymbol{P}_{\mathrm{A}}{}^{\dagger} \tag{2.4}$$

where $\boldsymbol{o}^{\mathrm{A}} \in \mathbb{R}^3$ denotes the optical centre of plane A which can be computed as the null-space of $\boldsymbol{P}_{\mathrm{A}}$. The epipolar line $\boldsymbol{l}_{\mathrm{B}}$ is then calculated as

$$\boldsymbol{l}_{\mathrm{B}} = \boldsymbol{F}\hat{\boldsymbol{p}}^{\mathrm{A}}. \tag{2.5}$$

2.5 Manual Registration of 3-D Heart Models

If the 3-D model is acquired during the intervention using C-arm CT, the 3-D information resides in the same coordinate system as the C-arm. The position of the overlay can then be computed straight forward if the projection matrix is known. For preoperatively acquired 3-D heart models, the coordinate system of the C-arm system needs to be registered to the coordinate system of the 3-D model.

Registration can be distinguished based on the transformation T that is used to transform points from one coordinate system into another system: Non-rigid registration is the most unconstraint type of transformation. The object which is transferred

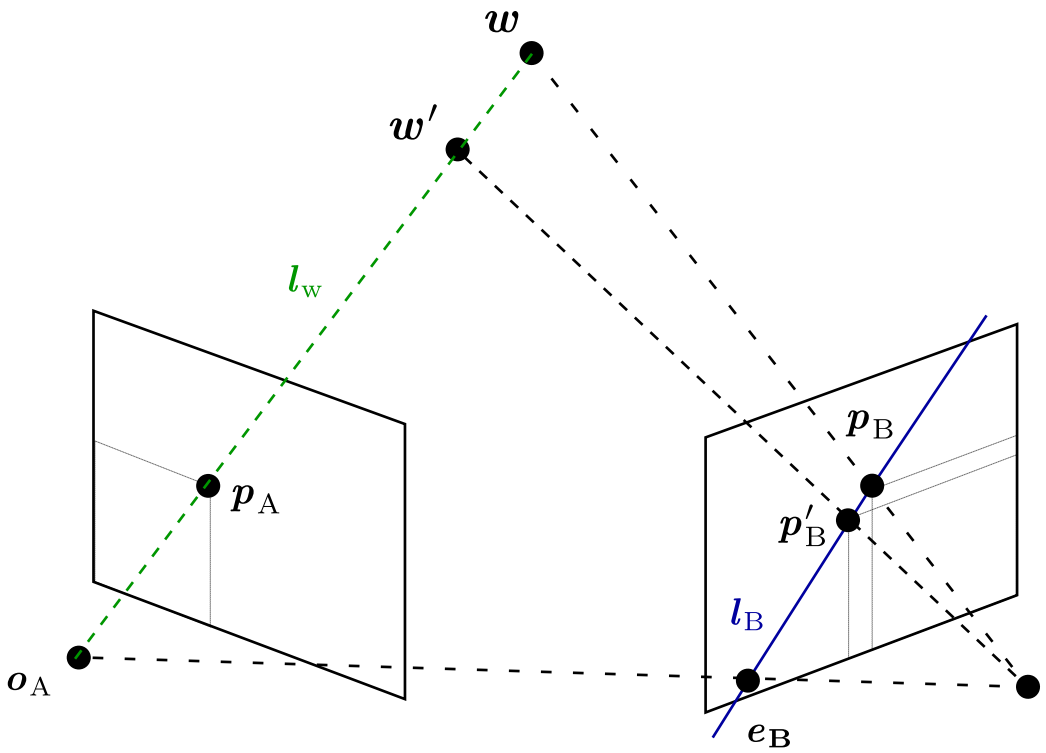

Figure 2.7: Computation of the epipolar line. The green line $\boldsymbol{l}_{\mathrm{w}}$ denotes the projection ray of the worldpoint $\boldsymbol{w}$ into the left image plane. It is given by $\boldsymbol{o}_{\mathrm{A}}$ and $\boldsymbol{p}^{\mathrm{A}}$. The blue epipolar line $\boldsymbol{l}_{\mathrm{B}}$ in the right image is the projection of $\boldsymbol{l}_{\mathrm{w}}$. The projection of $\boldsymbol{w}$ lies on this epipolar line.

from one coordinate system to the other may be deformed arbitrarily, however, in most cases the deformation is constraint, e.g., by describing the transformation field as thin plate splines [Davi 97, Mull 13]. Non-rigid registration is usually required when an object deforms or is flexible like the heart, lung or soft tissue in general.

Affine registration describes a transformation that may involve shearing, scaling, rotation and translation. Scaling is, e.g., needed to compensate different measurement units. Rigid registration constraints affine registration to rotation and translation.

Although the LA deforms due to cardiac motion, for 3-D/2-D registration of the LA to fluoroscopic images, usually a transformation is used that involves only translation $\boldsymbol{t}$ [Bour 10, Stev 10, Bour 13]. This is seen as valid as the patient is both during preoperative 3-D imaging and during intervention in a supine position and the table coordinate system is defined equally. Due to a slightly different positioning of the patient, a rotation around the frontal axis may occour. Rotation about the transverse axis may happen if the arms of the patient are positioned beneath the head as it is usually done for breast CT scans. In both cases, the rotation comprises only a few degrees. The data available in an augmented fluoroscopy environment is usually not suited to identify such low rotations.

2.5.1 Strategies for Manual Registration

Registration can be performed manually using an angiography of the LA [Knec 08, Stev 10, Van 12, Bour 13]. A good moment to get contrast enhanced X-ray images for initial registration is after the transseptal puncture, in particular if physicians use contrast injections to verify puncture success. Here, the projected 3-D LA model is shifted manually until its projected shadow covers the shape appearing in the X-ray images due to the CA injection. For this approach, registration times of 9.5±3.5 s and an average projected landmark to surface error of 1.1±1.4 mm to 1.8±2.3 mm was reported [Bour 13].

For a registration without contrast agent, e.g., prior to the transseptal puncture different methods were investigated. Bourier *et al.* [Bour 10] suggested to extract the CS from the 3-D data set and to register it manually to the CS catheter in a biplane X-ray image pair. Registration time was in most cases below one minute. The registration result was compared to a registration based on a subsequent CA injection and they differed on average by 10.6 mm.

Alternative registration strategies were presented by Li *et al.* [Li 09] and Knecht *et al.* [Knec 08]. Li *et al.* [Li 09] proposed manual registration based on the spine or the carina of trachea or a combination of both which are visible in both the 3-D CT data set and the 2-D X-ray images. As a third option, the registration of landmarks inside the LA to catheters placed at these landmarks has been proposed. The time needed for registration was 8±4 minutes for catheter-based registration and less than one minute for a combination of spine and carina. The accuracy was measured by placing catheters at anatomical landmarks and calculating the distance, probably in 2-D. The resulting registration error was not broken down by the registration strategy and was for all strategies between 0.9±0.5 mm and 1.6±1.4 mm.

Knecht *et al.* [Knec 08] also evaluated two manual registration methods. The first method involved a registration to catheters in the CS and the LA, the second method comprises a registration of a segmentation of the whole heart to the cardiac contour which is visible on an anterior-posterior 2-D fluoroscopic view. The registration process took 7±2 minutes. Also registration using a combination of the CS, the heart shadow and the spine was shown to be accurate and fast [Bour 16]. The 2-D contour offset error in this case was less than 1.7 mm, the 3-D registration error was 4.9±2.7 mm and the registration time was 18±8 seconds.

As a drawback of registration methods using anatomical landmarks, the respective anatomical structure needs to be visible both in the 3-D data set and the X-ray images. This is often the case for CT voxel data but not necessarily for 3-D data obtained by MRA. Especially soft tissue structures such as the carina or the CS are difficult to segment.

2.5.2 Edge-enhanced overlay for precise manual registration

Overlays used for augmented fluoroscopy are usually generated by rendering the surface of the 3-D model [Ecto 08, Knec 08, Bour 13]. Especially for registration of the 3-D model to LA angiographies, important structures in the 2-D images might be occluded by the overlay. To overcome this issue, the opacity of the rendered overlay

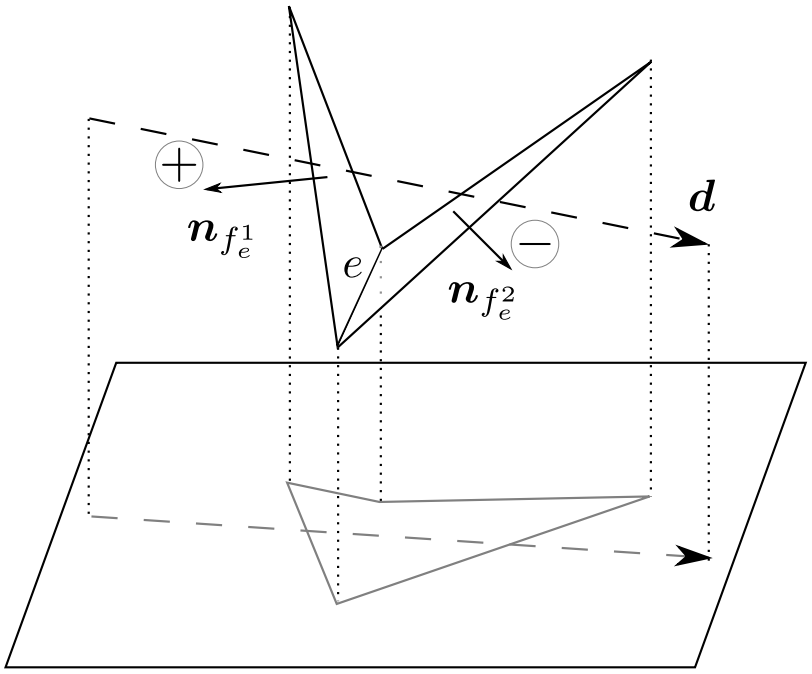

Figure 2.8: Edges of a 3-D model appear visible if their adjacent faces are seen from different directions. Mathematically, the scalar products of the viewing direction $\boldsymbol{d}$ and the respective face normal vectors $\boldsymbol{n}_{f_e^1}$ and $\boldsymbol{n}_{f_e^2}$ have different signs.

can be reduced. By doing so, however, relevant anatomical structures may not be visible well.

In [Hoff 13a], we proposed to use an overlay for registration that is different than a rendering of the 3-D model surface. Instead, an overlay can be used that highlights the edges of the 3-D model that are apparent from the viewing direction of the C-arm during angiography. Furthermore, a colouring of these edges according to their 3-D position was introduced to allow for better orientation in a biplane environment.

Edge Selection

Given the 3-D model as triangle mesh $M = (V_M, E_M), V_M \subset \mathbb{R}^3, E_M \subset V_M \times V_M$. Edges appear visible in a 2-D projection if their gradient in the aligned 3-D model is perpendicular to the viewing direction of the C-arm. To determine apparent edges given a projection matrix $\boldsymbol{P}$, the optical centre $\boldsymbol{o} \in \mathbb{R}^3$ needs to be computed first as the null space of the projection matrix.

An edge $e = (\boldsymbol{v}_1, \boldsymbol{v}_2) \in E_M$ of the mesh M, defined by two vertices $\boldsymbol{v}_1, \boldsymbol{v}_2 \in V_M$ appears as an edge from the current view if the adjacent faces f_e^1, f_e^2 are visible from different sides. A face is an area of the graph defined by its surrounding edges. This is the case if the scalar product of the viewing direction $\boldsymbol{o} - \boldsymbol{v}_1$ and the normal $\boldsymbol{n}_{f_e^1} \in \mathbb{R}^3$ of the first face has a different sign than the respective scalar product of the second face [Toma 05], see Figure 2.8. The set E of visible edges is hence given by

$$E_{M\,\text{visible}}(\boldsymbol{o}) = \left\{ e \in E_M \mid \operatorname{sgn}((\boldsymbol{o} - \boldsymbol{v}_1)^\intercal \boldsymbol{n}_{f_e^1}) \neq \operatorname{sgn}((\boldsymbol{o} - \boldsymbol{v}_1)^\intercal \boldsymbol{n}_{f_e^2}) \right\} \tag{2.6}$$

Instead of performing a binary decision on the visibility of an edge, a continuous value that defines how prominent this edge is, can be computed. For this purpose, the dot product $(\boldsymbol{o} - \boldsymbol{v}_1)^\intercal \boldsymbol{n}_{v_1}$ is suited well [Toma 05]. This way of rendering visible edges has the advantage that the rendering depends solely on the vertex position and its normal, and an assignment of vertices to edges or faces is not necessary.

Edge Colouring

One drawback of fluoroscopy is the lack of depth information. With a rendered overlay, depth can be visualized, e.g., by allowing to cut open the mesh [Knec 08, Van 12, Klei 12] or by colouring parts brighter the closer they are to the spectator. For a biplane system, closeness is different for each view and therefore, we proposed a global colouring scheme which allows the physician to recognize corresponding parts more quickly.

Due to the imaging setup in clinical practice, the 3-D z-coordinate corresponds usually to the vertical 2-D v-axis and to match structures based on their vertical position. Matching becomes more involved when two structures have a similar position on the z-axis but a different position within the xy-plane. To facilitate matching, we colour the visible edges according to their position in the xy-plane, i.e., to perform a mapping from cartesian coordinates to the RGB colour space. In this colour scheme, the green channel corresponds to the position of the edge on the x-axis and the blue channel is mapped to the coordinates on the y-axis. The red channel is set to a fixed medium intensity. This way, colours with a low saturation appear mainly at the LA centre but the PVs have saturated colours which allows a better identification of corresponding PVs in both views.

One drawback of this colouring is that some edges assume a colour with a low saturation, i.e., they become grey and are difficult to perceive on the greyscale fluoroscopy images. This issue can be solved by mapping the edge coordinates to the HSV colour space [Gonz 08] and assuring a non-zero saturation. The HSV colour space is cylindrical shaped, the circular slices correspond to different darkness values. The angle of the circle corresponds to the colour hue and the distance to the centre defines the saturation. As the mesh contours should be well visible, the cartesian x- and y-coordinates are mapped to the brightest slice. To this end, they are transformed to polar coordinates (r, ϕ) with the mesh centre of gravity as coordinate system origin. The angle ϕ corresponds to the hue, and r is mapped to a range of, e.g., 30 % to 100 % saturation to avoid unsaturated edges.

Evaluation and Results

We compared the overlay with binary visible edges and the RGB-colouring of the edges to an overlay showing just the outline of the LA. Five people familiar with images from EP procedures were asked to perform a registration on six different angiographies from two patients using first the outline overlay and then the edge-enhanced overlay. They performed first a registration using an overlay showing just the outline of the LA and then a registration using the proposed overlay. A registration provided by a physician served as ground truth. The registration error was

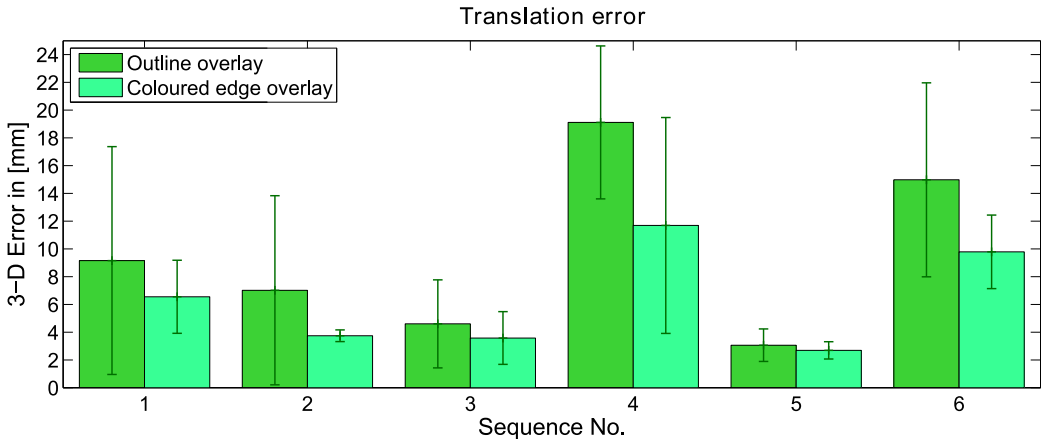

Figure 2.9: 3-D Translation errors for each angiographic sequence. The error was reduced significantly ($p < 0.05$) when using the coloured edge-overlay.

calculated as the 3-D translation error, i.e., the distance between the centre of gravity of the mesh registered by the user to the ground truth centre of gravity.

The mean registration error when using the outline overlay was 9.7 ± 7.9 mm and decreased to 5.8 ± 4.7 mm when the edge enhancing overlay was used. The improvement was found to be significant ($p < 0.05$) using a Wilcoxon signed rank test [Wilc 45]. Registration errors for every angiographic sequence are given in Figure 2.9.

Discussion

The evaluation showed that an overlay showing edges of the 3-D model can lead to significant better registration results, especially for people that have only little experience. The improvement due to the new overlay was only small if the LA was well delineated by the contrast agent or if CA was injected against, e.g., the LA roof which is also visible in the outline. High improvements were observed if the CA was injected into a PV or the LAA for two reasons: The edges of the PV that appear in the angiography are often not part of the LA outline. Moreover, due to the colouring, the user could identify the structure into which CA was injected and could verify the plausibility of the registration. So, it was, e.g., possible to see in the angiography shown in Figure 2.10 that the CA cannot be located inside the left superior pulmonary vein (LSPV) but rather in the LAA.

As a conclusion, the internal anatomical structure of the LA model is important for registration. If the overlay is simplified to allow a view on the contrast agent, the simplified overlay should still contain all edges. Moreover it is important to facilitate the identification of corresponding anatomical structures. This is important to assess the plausibility of the registration with respect to the contrast agent distribution within the LA. In chapter 9, we will explained how these conclusions are transferred to an automatic registration approach.

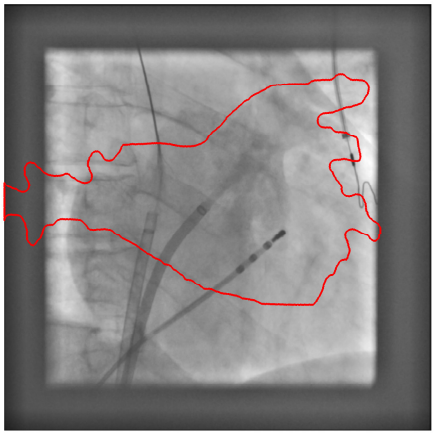

(a) Plane A with overlay showing the outline.

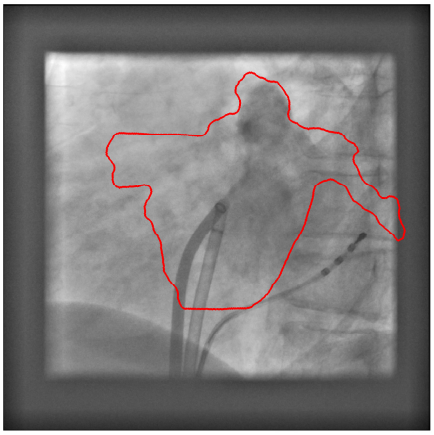

(b) Plane B with overlay showing the outline.

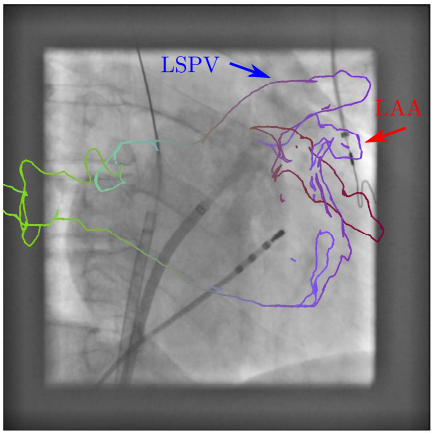

(c) Plane A with new overlay.

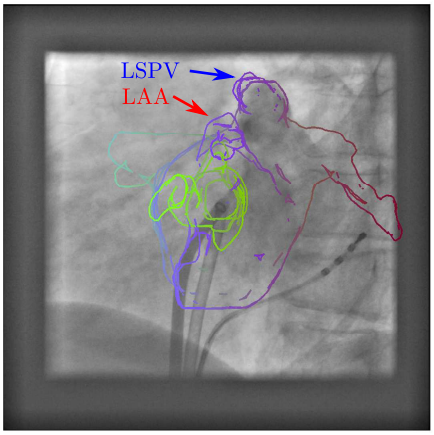

(d) Plane B with new overlay.

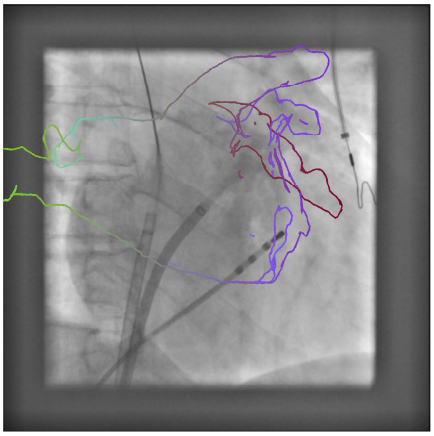

(e) Plane A with correctly registered overlay.

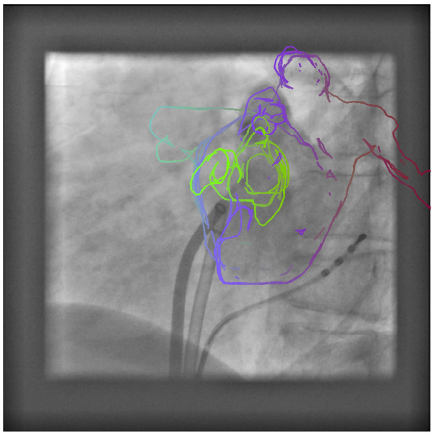

(f) Plane B with correctly registered overlay.

Figure 2.10: Using the overlay showing only the outline, the registration results given in 2.10(a) and 2.10(b) seem to be correct. When using the structure enhancing overlay, one can see that the left superior pulmonary vein (LSPV) in 2.10(c) is uncontrasted while it is filled with contrast agent in 2.10(d). Instead, the left atrial appendage (LAA) is the contrasted structure. By aligning the overlays such that the LAA is filled with contrast agent in both images, a correct registration, 2.10(e) and 2.10(f), is achieved.

22 Augmented Fluoroscopy for Treatment of Atrial Fibrillation by Cardiac Ablation

Part I

Device Detection and Reconstruction

CHAPTER 3

Linear Catheter Detection

We present in this chapter a method for semi-automatic annotation of catheters in X-ray images. The user marks a single point on the catheter. The shaft of the catheter is then automatically detected. The method presented in this chapter is based on [Hoff 12a] and was already published at the MICCAI conference [Hoff 12b] and at IEEE TMI [Hoff 16b].

3.1 Motivation

The main goal of 2-D linear catheter detection is to provide a simple annotation tool to generate input data for the reconstruction approach presented in chapter 4 or similar approaches [Cane 00, Baer 03]. Such reconstruction algorithms require a 2-D annotation of the catheter in two different views. As manual point-by-point annotation is time-consuming, semi-automatic catheter annotation algorithms are important tools. Together with automatic X-ray marker detection methods [Kurz 13] or catheter tip detection algorithms [Schm 05, Kapp 13, Ma 13, Wu 13] a fully automatic detection of the whole catheter can be achieved.

Catheter segmentation in fluoroscopic X-ray images is not only beneficial for reconstruction algorithms. The position and shape of a catheter is also needed for catheter tracking in 2-D fluoroscopic images which requires an initial pose of the catheter or guidewire [Wang 09, Wu 11]. In a registration context, 2-D tracking can be used to compensate for registration errors due to respiratory or cardiac motion [Kapp 12, Ma 10]. Also for device-based registration, the segmentation of catheters in 2-D can be required [Sra 05].

3.2 Related Work

A detection method for the whole catheter has recently been proposed by Wang *et al.* [Wang 10]. This method first detects curve segments using a classifier and

organizes the detected segments in a graph structure. The cost of an edge in this graph is determined by the probability of a segment given by the classifier. Based on this graph a hypergraph is generated. The edge costs of the hypergraph represent the likelihood of two segments belonging to a cathteter incorporating geometric properties such as smoothness. Finally, the user marks two or more points on this graph and a shortest path between these points is calculated.

Another approach that is capable of detecting the whole catheter was presented by Franken *et al.* [Fran 06]. It also uses segment grouping to combine segments that probably belong to a catheter. First, catheter tips are detected based on a blobness image and known geometric properties of catheter tips, e.g., electrode spacing. Then, possible shafts are detected and the most likely path shaft is selected. In this context, the likelihood of a certain path to be the correct shaft is determined based on its curvature and curvature change. However, the focus of this method was on automatic electrode detection and the performance of the whole catheter detection was low. Given the catheter tip was detected, a detection of the entire catheter was only possible for 44 % of the catheters.

Yatziv *et al.* [Yatz 12] presented a method for the detection of multiple tips in fluoroscopic sequences using a single click. They first compute a background image by temporal averaging to obtain a catheter image by means of subtraction. Starting from the manually annotated sheath end, they calculate geodesics using a fast marching method and classified catheter tips based on geodesic properties and template matching. Although this is a tip detection method, it is related to the detection of the whole catheter due to the geodesic computation from the sheath.

There is more work focusing on catheter tips or catheter electrodes [Ma 13, Caza 13, Mill 13, Mill 14]. However, these methods cannot be used if the shape of the complete catheter is required, e.g., for device-based registration or if the catheter has no electrodes such as the cryoballoon catheter.

Methods for guidewire detection [Barb 07, Bism 12, Spie 09, Wang 09] cannot be transferred directly to catheter detection. This is because guidewires appear as homogeneous objects under X-ray whereas catheters vary in thickness and constrast, especially in the region around catheter electrodes.

Tracking of catheters [Wu 13, Bros 09a] or guidewires [Baer 03] is also related to detection. However, tracking usually requires a manual initialization of the guidewire or the catheter.

3.3 Catheter Detection

The catheter detection algorithm comprises three steps:

1. The user places a seed point on the catheter and an image filter is applied to enhance catheter-like structures (Figure 3.1(b)). Additionally, the search space is reduced such that it only contains catheter-like structures close to the seed point (Figure 3.1(d)).

2. The algorithm identifies candidates for catheter segments and organizes them in a graph structure (Figure 3.1(e)).

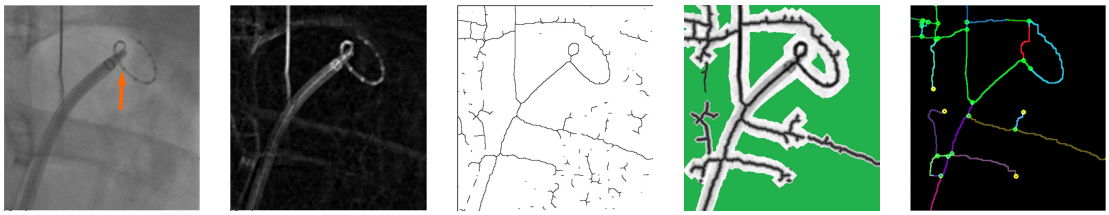

(a) (b) (c) (d) (e)

Figure 3.1: Catheter detection pipeline: First, the user places a seed point (marked by an arrow) in the the original image (a) and the image is medialness filtered to highlight catheter-like structures (b). It is then binarized using a variable threshold and thinned (c). Subsequently, we define a cost for each pixel based on the medialness filtered image and the skeleton. The search space Ω_r is then reduced to pixels close to the seedpoint with respect to this cost. A slightly modified cost definition (d) is used to compute a shortest path tree from the seedpoint to each pixel. Green pixel have an infinite cost as they are outside the search space Ω_r. Then, we select the shortest paths from, amongst others, skeleton endpoints to transform the skeleton into a graph (e). Each shortest path to the seedpoint was drawn in a different color. Finally, paths starting from the seedpoint are evaluated to find a path which best fitting properties such as curvature and length.

3. Catheter properties, e.g., curvature and length, are calculated for different combinations of catheter segments. An evolutionary algorithm selects the combination with the best fitting properties.

These steps are explained in detail below.

3.3.1 Search Space Reduction

To start catheter detection, the user specifies the catheter type to be detected and marks the catheter in the X-ray image by placing a seed point $\boldsymbol{s} \in \Omega, \Omega = \{1, ..., m\} \times \{1, ..., n\}$ in the image. For linear catheters, such as the CS and the RF catheter, the seed point needs to be placed on the catheter tip. If the user wants to annotate a CM catheter, he places the seed point shortly after the transition of the shaft to the tip. The seedpoint should lie on the ellipse formed by the tip.

While placing the seed point, the first preprocessing steps are applied as they are independent on the user input. At first, a medialness filter is applied to the image, see Figure 3.1(b). The medialness filter was originally designed for 3-D volumes [Guls 08] and adapted to work with 2-D images [Poly 12]. Our version omits contrast normalization to benefit from the high contrast changes at catheters. This filter enhances line-like structures in the image, e.g., catheters, guide wires, and rip borders, while suppressing homogeneous regions. The resulting image $\boldsymbol{I}_\mathrm{f} \in \mathbb{R}^{m \times n}$ is normalized to values between 0 and $\boldsymbol{I}_\mathrm{f}^\mathrm{max}$. As the intensities are real-valued, the choice of $\boldsymbol{I}_\mathrm{f}^\mathrm{max}$ has no impact on the quantization and is, thus, arbitrary. In our case, $\boldsymbol{I}_\mathrm{f}^\mathrm{max} = 255$. Other filters that enhance tubular structures such as the vesselness filter [Fran 98] could, in principle, also be employed. For the task presented here, however, medialness filtering yielded the best results, especially around catheter electrodes.

A binarization of $\boldsymbol{I}_\mathrm{f}$ is generated by means of *adaptive thresholding* [Gonz 08]. Thus we compensate for the contrast normalization omitted in the medialness filtering. As the binarization is noisy, a morphological opening and closing is performed. Based on this binary image $\boldsymbol{I}_\mathrm{b}$, a skeleton image $\boldsymbol{I}_\mathrm{s}$is computed [Cych 94], see Figure 3.1(c) and the seed point $\boldsymbol{s}$ in moved to the closest skeleton pixel.

In the next step, the search space is reduced to catheter-like structures close to the seed point. Closeness is not only defined spatially but also incorporates the likelihood of a pixel belonging to the catheter. The reduced search space is denoted by $\Omega_\mathrm{r} \subset \Omega$. As the binarized image $\boldsymbol{I}_\mathrm{b}$ and, thus, the skeleton may contain gaps, it is not sufficient to reduce the searchspace to skeleton pixels connected to the seed point. Instead, to overcome gaps in the skeleton, a fixed number $|\Omega_\mathrm{r}|$ of pixels which are closest to the seedpoint are included in Ω_r. Closeness is defined by a cost imposed on each pixel $\boldsymbol{p}$ such that skeleton pixels are favoured. The size $|\Omega_\mathrm{r}|$ of the reduced search space is chosen in advance based on the expected number of pixels belonging to catheters and the gaps in the segmentation.

To compute the set of closest pixels, the image is considered as graph $G_{\boldsymbol{I}} = (\Omega, E_{\boldsymbol{I}})$. The set Ω of vertices contains all pixels $\boldsymbol{p}$, and connections between pixels $\boldsymbol{p}_1$, $\boldsymbol{p}_2$ in a 4-neighbourhood are represented by directed edges $(\boldsymbol{p}_1 \to \boldsymbol{p}_2), (\boldsymbol{p}_2 \to \boldsymbol{p}_1) \in E_{\boldsymbol{I}}$. The cost $c_\mathrm{r}(\boldsymbol{p}_1 \to \boldsymbol{p}_2)$ of an edge depends solely on the target pixel $\boldsymbol{p}_2$ and is defined as

$$c_\mathrm{r}(\boldsymbol{p}_1 \to \boldsymbol{p}_2) = \begin{cases} c_\epsilon & \text{if } \boldsymbol{I}_\mathrm{s}(\boldsymbol{p}_2) = 1 \\ \min\left(\boldsymbol{I}_\mathrm{f}^\mathrm{max} - \boldsymbol{I}_\mathrm{f}(\boldsymbol{p}_2), \lambda \|\boldsymbol{p}_2 - \boldsymbol{s}\|_2\right) & \text{if } \boldsymbol{I}_\mathrm{b}(\boldsymbol{p}_2) = 1 \\ \boldsymbol{I}_\mathrm{f}^\mathrm{max} - \boldsymbol{I}_\mathrm{f}(\boldsymbol{p}_2) & \text{otherwise} \end{cases}. \tag{3.1}$$

This cost function assigns a fixed low cost c_ϵ to pixels on the skeleton as those pixels are most likely to represent catheter centrelines. For non-skeleton pixels, the cost is defined by the medialness value such that c_r assigns low costs to pixels with high medialness values.

Low cost is also assigned to pixels close to $\boldsymbol{s}$ and segmented in $\boldsymbol{I}_\mathrm{b}$ as catheter. Allowing for small discontinuities is beneficial because the segmentation of the circular CM catheter tip often contains several small gaps, especially around the electrodes. Electrodes may lead to small blobs in $\boldsymbol{I}_\mathrm{b}$ that may shrink to a single point during skeletonization, which results in having large distances to the next skeleton pixels. By assigning a low cost to pixels in $\boldsymbol{I}_\mathrm{b}$ close to $\boldsymbol{s}$ a low cost, they, and thus the circular tip, will be included in Ω_r. The impact of this special rule is determined by a weighting factor λ setting the size of the circular tip in relation to the difference of a pixel to $\boldsymbol{I}_\mathrm{f}^\mathrm{max}$.

The $|\Omega_\mathrm{r}|$ closest pixels are determined using Dijkstras' algorithm [Corm 90] which is terminated after $|\Omega_\mathrm{r}|$ iterations.

3.3.2 Search Graph Generation

Prominent structures of the skeleton within Ω_r represent potential catheter segments. In the next step, these structures are transformed in a graph as illustrated in Figure 3.1(e). The potential segments are represented by graph edges, nodes of the graph denote pixels where one segment joins another one.

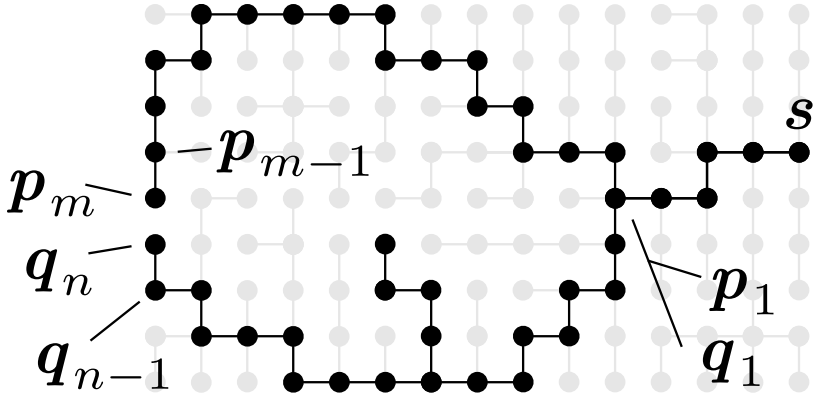

Figure 3.2: Sketch of the shortest path tree with the seed point $\boldsymbol{s}$ as root. A circle on the skeleton (black) can be detected by searching for neighbouring pixels of the skeleton which belong to different paths. Here, the pixel $\boldsymbol{p}_m$ has a neighbouring pixel $\boldsymbol{q}_n$ which belongs to a different shortest path to $\boldsymbol{s}$. The paths $\boldsymbol{p}_1 \to \ldots \to \boldsymbol{p}_m$ and $\boldsymbol{q}_n \to \ldots \to \boldsymbol{q}_1 = \boldsymbol{p}_1$ will be merged to a circle after the complete subtree is computed.

To construct this graph, we compute a shortest path tree on $G_{\boldsymbol{I}}$ for all pixels in Ω_r using $\boldsymbol{s}$ as root. By using a similar cost function as in Equation 3.1, we make sure that the branches of the tree follow mainly the skeleton. From this tree, we select a subtree such that main structures of the skeleton are retained. Finally, circles are introduced leading to the graph for catheter search.

Tree Generation

The tree branches should follow the catheter smoothly, however, the skeleton is not smooth and the cost function in Equation 3.1 puts too much weight on the skeleton. To introduce smoothness, we weigh the cost of a pixel according to its distance to the skeleton. To this end, we compute a distance transform [Felz 04] $\boldsymbol{I}_\mathrm{DT}$ of the skeleton such that $\boldsymbol{I}_\mathrm{DT}(\boldsymbol{p})$ yields the Euclidean distance to the next skeleton pixel. The cost $c_\mathrm{t}(\boldsymbol{p}_1 \to \boldsymbol{p}_2)$ for a target pixel $\boldsymbol{p}_2$ is defined by

$$c_\mathrm{t}(\boldsymbol{p}_1 \to \boldsymbol{p}_2) = \begin{cases} \infty & \boldsymbol{p}_2 \notin \Omega_\mathrm{r} \\ (\boldsymbol{I}_\mathrm{f}^\mathrm{max} - \boldsymbol{I}_\mathrm{f}(\boldsymbol{p}_2)) \cdot \min\left(\frac{\boldsymbol{I}_\mathrm{DT}(\boldsymbol{p}_2)+1}{\varrho}, 1\right) & \text{otherwise.} \end{cases} \tag{3.2}$$

The smoothness of the branches is steered by ϱ. Within a range of ϱ pixels around the skeleton, the actual cost $\boldsymbol{I}_\mathrm{f}^\mathrm{max} - \boldsymbol{I}_\mathrm{f}(\boldsymbol{p}_2)$ is reduced linearly towards the skeleton. Thus, the shortest path may not follow the skeleton, but some nearby pixels that have also a low cost. In Figure 3.1(d), an example of this cost function is given.

Subtree Selection

From the shortest path tree, a subtree is extracted that contains tree branches that follow the skeleton. At first, we select branches that form circles in the skeleton. To this end, we iterate over all skeleton pixels and examine their neighbouring skeleton pixels. We consider a pixel $\boldsymbol{p}_m$ and its neighbour $\boldsymbol{q}_n$. If $\boldsymbol{p}_m$ is a successor of $\boldsymbol{q}_n$ on

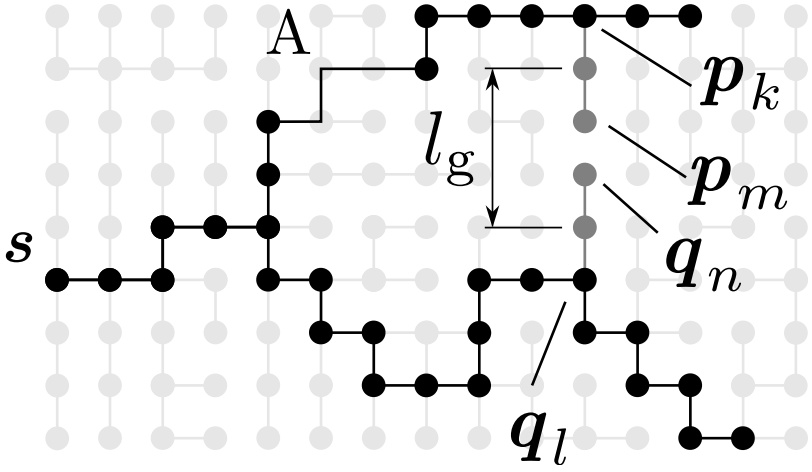

Figure 3.3: The skeleton (black dots) may contain gaps. The subtree extraction is robust w.r.t. gaps in the skeleton (A) between seedpoint and skeleton endpoints. They are bridged as the complete shortest path from the endpoint is included. This is also the case for gaps in circles unless the endpoints, $\boldsymbol{p}_m$ and $\boldsymbol{q}_n$, of both circle paths are within the gap. In this case, a bridge between both paths of length l_g is determined to close this gap.

the shortest path tree or vice versa, they belong to the same path. If this is not the case, they belong to partially different paths

$$(\boldsymbol{p}_m \to \boldsymbol{p}_{m-1} \to \ldots \to \boldsymbol{p}_1 \to \ldots \to \boldsymbol{s}) \text{ and}$$
$$(\boldsymbol{q}_n \to \boldsymbol{q}_{n-1} \to \ldots \to \boldsymbol{q}_1 \to \ldots \to \boldsymbol{s}) \text{ with } \boldsymbol{p}_1 = \boldsymbol{q}_1.$$

Thus, the shortest paths from both pixels form a circle

$$(\boldsymbol{p}_1 \to \ldots \to \boldsymbol{p}_m \to \boldsymbol{q}_n \to \ldots \to \boldsymbol{q}_1 = \boldsymbol{p}_1)$$

in the image, see Figure 3.2. This circle has a length $l_c = (m+n-1)$. To be included in the subtree, l_c needs to exceed a certain threshold.

The next set of branches to be included in the subtree are shortest paths from skeleton endpoints. Sometimes, circles in the skeleton have a gap at the place where the points $\boldsymbol{p}_m$ and $\boldsymbol{q}_n$ would be located. Instead of including them in the first step and recognizing them as a circle, only two subpaths from endpoints $\boldsymbol{p}_k$ and $\boldsymbol{q}_l, k < m, l < n$ are included, see Figure 3.3. In the next step, these remaining gaps are closed in a way that is similar to the detection of circles.

Instead of considering only skeleton pixels, all pixels in Ω_r and their neighbours are considered. We consider each pair of pixels consisting of $\boldsymbol{p}_m$ and one of its neighbours $\boldsymbol{q}_n$. If neither of them is a successor of the other one, the shortest paths from them to the seed point will be evaluated. The first pixels on the path which are already included in the subtree are denoted as $\boldsymbol{p}_k$ and $\boldsymbol{q}_l$. The length l_g of the gap is $l_g = m - k + n - l$, the length l_c is computed as above. For each pair of pixels $\boldsymbol{p}_m$ and $\boldsymbol{q}_n$ which result in different shortest paths, the fraction l_c/l_g is computed. If this fraction exceeds a certain threshold, the respective paths will be included in the subtree. If more than one pair connects the same edges of the subtree, only the paths having the highest value of l_c/l_g will be added.

Finally, all edges are replaced by undirected edges. Then, all pairs $\boldsymbol{p}_m$ and $\boldsymbol{q}_n$ which are endpoints of paths added during circle detection or gap closing are considered. As we are still dealing with a subtree, an edge $(\boldsymbol{p}_m, \boldsymbol{q}_n)$ is added to the set of edges to transform the subtree into the final catheter search graph. For all paths, the number of edges from the endpoint to the first bifurcation is counted. If the number of edges is below a certain threshold this short path is removed.

3.3.3 Catheter Search

Based on the seedpoint $\boldsymbol{s}$ given by the user and the graph, the search for the catheter is performed. Depending on the catheter type indicated by the user, a different detection scheme is used. For linear catheters, such as the CS and the RF catheter, only a shaft search is required. For the CM catheter, the shaft search is followed by a dedicated search for its elliptical upper part which we denote as 'tip' or 'tip section', respectively.

Shaft Search

Due to the standard view directions of the C-arm used in electrophysiology procedures, prior knowledge of the image orientation can be taken into account. In our case, we can assume that the catheters enter the image at the bottom border as they are led through the inferior vena cava. Therefore, we consider all shortest paths from graph leaf nodes in the lower 60 % of the image to the seedpoint as shaft candidates. The shortest paths do not need to be calculated again as they were already computed during graph generation.

Depending on the image content, the number of paths varies. For images where many tools or devices such as ECG-leads cross the catheter, we may reach, e.g., 20 partially overlapping paths. This effect is particularly strong for noisy images. If no other device crosses the selected catheter and the image quality is good, we may end up with very few shortest paths. The catheter does not need to be identical with a complete shortest path from a leave node $\boldsymbol{p}_n$. Often, the paths are longer than the catheter as the paths may follow other structures at their end. However, evaluating all possible pixel sequences from the seed point to any point on the shortest path is not possible due to performance reasons. Therefore, we evaluate for each path $(\boldsymbol{s}-\boldsymbol{p}_1-\boldsymbol{p}_2-\ldots-\boldsymbol{p}_n)$ several subsequences $\{(\boldsymbol{s}-\ldots-\boldsymbol{p}_m)|m = 100+k\cdot 30, m \leq n\}$ of increasing length. So, the first subsequence comprises the first 100 pixel, the next subsequence the first 130 pixel and the third the first 160 pixel starting from the seed point. This turned out to be a good compromise between performance and accuracy.

On each subsequence $\mathcal{F}$, a set of features is evaluated by the optimization step:

- The length $|\mathcal{F}|$ of the subsequence, since as much as possible of the catheter should be detected.
- The mean squared value a_c of the curvature, which is given by

$$a_\mathrm{c}(\mathcal{F}) = \frac{1}{|\mathcal{F}|}\sum_{t=1}^{|\mathcal{F}|}\kappa_\mathcal{F}(t)^2. \tag{3.3}$$

$\kappa_{\mathcal{F}}(t)$ denotes the curvature of the sequence at pixel $\boldsymbol{p}_t$. We use the squared value to penalize a high curvature more strongly while favouring a low curvature which is common for linear catheters.

- The direction of the catheter is supposed to be downwards. Therefore, the integral a_d of the deviation to this direction,

$$a_{\mathrm{d}}(\mathcal{F}) = \sum_{t=1}^{|\mathcal{F}|} \left| \phi_{\mathcal{F}}(t) - \frac{-\pi}{2} \right|, \tag{3.4}$$

  is evaluated. The angle $\phi_{\mathcal{F}}(t)$ denotes the direction angle of the pixel sequence at pixel $\boldsymbol{p}_t$. This feature can be applied if catheters are inserted into the LA via a transseptual puncture. Here, the overall shaft direction should be around $-90°$. If devices are aligned differently, e.g., an esophagus probe, this feature must be adapted accordingly.

- The end angle feature a_{a} depending on the path angle at the proximal end is computed as

$$a_{\mathrm{a}}(\mathcal{F}) = \left| \phi_{\mathcal{F}}(|\mathcal{F}|) - \frac{-\pi}{2} \right| \tag{3.5}$$

  Similar to $a_{\mathrm{d}}(\mathcal{F})$, we know that the catheter leaves the image in an almost vertical direction, i.e., the direction of the shaft is close to $-90°$. Due to the length feature, the size of the catheter tends to increase. The curvature feature is not suitable to determine a proper end as a local high curavature has little impact due to the averaging over the whole pixel sequence. The intention of the end angle feature is to ensure a proper end of the detected sequence. It focusses, therefore, only at the last part of the pixel sequence. As a consequence, a path with an end direction of $-90°$ will be preferred over a slightly longer path with a higher deviation from $-90°$ at the end.

Depending on the catheter type, some features might be more important. Therefore, we weigh each feature with a corresponding factor α. The sub-sequence $\hat{\mathcal{F}}$ optimizing the objective function

$$\hat{\mathcal{F}} = \arg\min_{\mathcal{F}} (-\alpha_l \cdot |\mathcal{F}| + \alpha_c \cdot a_{\mathrm{c}}(\mathcal{F}) + \alpha_d \cdot a_{\mathrm{d}}(\mathcal{F}) + \alpha_a \cdot a_{\mathrm{a}}(\mathcal{F})) \tag{3.6}$$

is selected as the result of the catheter shaft detection. Since the length $|\mathcal{F}|$ is the only feature to be maximized, α_l has a negative sign.

Tip Section Search

For the shaft search problem, we incorporated prior knowledge in the shaft search as both a seed point and a favourable search direction were known. For the tip search, however, only the start is given by the seed point. Additionally, as the tip is approximately circular, its 2-D projection in the fluoroscopic images approximates an ellipse. This property of the catheter was already used for tracking [Bros 09b, Bros 10a, Bros 10b] and can also be efficiently exploited for the task described here.

We therefore need to evaluate all combinations $\mathcal{G} = [\boldsymbol{p}_1 \dots \boldsymbol{p}_{|\mathcal{G}|}]$ of paths that start from the seed point and were not used for the shaft. Similarly to the shaft search, the tip search is performed in several stages where we increase the length of the considered tip candidate in each step.

For assessing a tip candidate $\mathcal{G}$, an ellipse $\mathcal{E}(\mathcal{G})$ is fitted to its points and features are computed that reflect how elliptical the path combination is. Moreover, the medialness response $\boldsymbol{I}_\mathrm{f}$ is accumulated along the fitted ellipse. To reduce computation time of the ellipse fitting [Hali 98], only six points are used. They are equidistantly sampled from the point sequence $\mathcal{G}$ of the tip candidate. We denote the resulting ellipse as a set $\{\boldsymbol{e}_1 \dots \boldsymbol{e}_{|\mathcal{E}(\mathcal{G})|}\}$ of pixels $\boldsymbol{e}$ which lie on the ellipse. Based on the fitted ellipse $\mathcal{E}$, the following features are computed for the catheter tip section candidate $\mathcal{G}$:

- The average medialness filter value b_fe of pixels on the ellipse is calculated as

$$b_\mathrm{fe} = \frac{1}{|\mathcal{E}|} \sum_{i=1}^{|\mathcal{E}|} \boldsymbol{I}_\mathrm{f}(\boldsymbol{e}_i). \tag{3.7}$$

  If an ellipse represents the real catheter tip section, it should have high values in the medialness filtered image $\boldsymbol{I}_\mathrm{f}$. Therefore, the value of this feature needs to be maximized.

- The mean distance b_d of the points in $\mathcal{G}$ to $\mathcal{E}$:

$$b_\mathrm{d} = \frac{1}{|\mathcal{G}|} \sum_{i=1}^{|\mathcal{G}|} \min_j \|\boldsymbol{p}_i - \boldsymbol{e}_j\|_2. \tag{3.8}$$

  This feature measures how much the point sequence $\mathcal{G}$ deviates from an elliptical shape.

- The feature b_c states how much of the ellipse is covered by the points in $\mathcal{G}$. It is calculated by

$$b_\mathrm{c} = \frac{\#\{\boldsymbol{e}_i \mid \min_j \|\boldsymbol{p}_j - \boldsymbol{e}_i\|_2 < \varepsilon\}}{|\mathcal{E}|}. \tag{3.9}$$

  A pixel of the ellipse is considered as covered if the distance to the next pixel of $\mathcal{G}$ is within ε. The choice of ε depends on the image quality as the detected paths may be located next to the actual catheter tip due to noise and gaps in the segmentation.

- A feature regarding the circumference of the ellipse is given as

$$b_\mathrm{l} = \max(\Pi - |\mathcal{E}|, 0). \tag{3.10}$$

  The intention of this feature is to penalize ellipses with a circumference less than Π. Consequently, b_l should be low. It is unlikely that a small ellipse represents the catheter tip. However, small ellipses tend to have extraordinary good values of the coverage b_c and the filter value b_fe if they are located at small bright spots in the filtered image. Furthermore, if the length of the minor axis is close to ε, most of the ellipse points are considered as covered by the path. The choice of Π depends on ε.

- Difference angle b_a between tip candidate and shaft

$$b_\mathrm{a} = |\phi_\mathrm{s} - \phi_\mathrm{t} - 180°|. \tag{3.11}$$

  The transition between shaft and tip section should be smooth. Their start angle is given as ϕ_s for the shaft and ϕ_t for the tip section, respectively. As both angles represent the direction away from the seed point, the difference angle should be close to 180°. This feature is important if the tip section search yields the ellipse in clockwise and counter clockwise direction. In this case, both ellipses have similar values of the so far defined features and the difference angle is used to decide between both solutions.

To reject candidates with an ellipse that does not fit the known catheter shape, additional features are defined:

- The frist rejection criterion depends on the length b_M and b_m of the major axis and minor axis of $\mathcal{G}$, respectively. For currently available Lasso® catheters (Biosense Webster, Diamond Bar, CA, USA) the diameter is 25 mm. For the data we had, the resulting diameter of the CM catheter is less than 205 pixel[1]. So, catheter candidates can be rejected safely if $b_\mathrm{M} > 220$ pixels. We also reject candidates with $b_\mathrm{m} < 20$ pixels. A small minor axis corresponds to a line-like structure which if often the result of filter artefacts but may also originate from a CM catheter seen from a certain perspective. Consequently, this approach is limited to non-degenerated catheter shapes.

Similar to the shaft search, see Equation 3.6, the features for the tip search are weighted by factors β. This results in an objective function

$$b(\mathcal{G}, \mathcal{E}) = -\beta_\mathrm{fe} \cdot b_\mathrm{fe} - \beta_\mathrm{c} \cdot b_\mathrm{c} + \beta_\mathrm{d} \cdot b_\mathrm{d} + \beta_\mathrm{l} \cdot b_\mathrm{l} + \beta_\mathrm{a} \cdot b_\mathrm{a} \tag{3.12}$$

which depends on a catheter tip section path $\mathcal{G}$ and the ellipse $\mathcal{E}(\mathcal{G})$ fitted to it. This objective function needs to be minimized. Features that need to be maximized therefore have a negative sign.

The evaluation of all possible paths may be very time consuming if image quality is low. In this case, the complexity of the graph and thus the number of tip candidates increases. To still achieve a result within reasonable time, a population based method is used to find the best path [Back 97].

The optimization starts with an initial population of all paths that start from the seed point with a length of 100 pixels. After evaluating these paths, the child generation is created by prolonging the paths by 30 pixels. If for a path a bifurcation occurs within this 30 pixel segment, the path is split and each child path follows a different path. A tip section candidate may include only a limited number of pixels twice. This is required to enable self-crossings which are necessary if the shape of the catheter tip is similar to the letter φ.

Each tip candidate is evaulated with respect to Equation 3.12. To reduce computation time, only the 700 candidates of each generation with respective values closest

[1]The estimated radiographic magnification factor was less than 1.5 and the pixel spacing was 0.183 mm.

Table 3.1: Clinical data used for evaluation

Catheter	Number of biplane image pairs	Number of patients
RF	47	27
CS	61	47
CM	58	45
all	88	59

Table 3.2: Parameter values determined heuristically for detection

Description	Symbol	Value	Appears in
Reduced search space size	$\lvert\Omega_\mathrm{r}\rvert$	150,000	Sec. 3.3.1
Closeness gain weighting	λ	1.25	Eq. 3.1
Skeleton pixel cost	c_ϵ	1	Eq. 3.1
Cost reduction range width	ϱ	7 pixels	Eq. 3.2
Minimal circle length	l_c	75 pixels	Sec. 3.3.2
Circle-gap-ratio	$l_\mathrm{c}/l_\mathrm{g}$	10	Sec. 3.3.2
Ellipse coverage buffer	ε	10 pixels	Eq. 3.9
Small ellipse penalty	Π	200	Eq. 3.10

to the best value found so far are kept in the population. Optimization is terminated after the 10th generation as soon as no improvement was achieved three times in a row, but in any case after the 16th generation. In the 16th generation, a length of 600 pixels is reached which corresponds to the length of a 25-mm Lasso® catheter tip.

3.4 Experiments and Results

We evaluated the proposed catheter detection method on clinical data consisting of 88 biplane sequences (176 monoplane sequences) from 59 patients. We evaluated the method only on the first frame of each sequence as the image content was similar within each sequence.

The images used for evaluation differ between catheter types as some images were excluded from evaluation of a certain catheter. In Table 3.1 we list the number of remaining images and number of individual patients for each catheter type. A biplane pair was excluded if the respective catheter was not present, only visible at the lower border or very short. For the CM catheter evaluation, biplane pairs were excluded where the tip section was degenerated to a line. The biplane pair was also excluded if one of the aforementioned criteria applied to only one plane as this would inhibit the use of this data set for reconstruction in chapter 4.

The images were acquired using a C-arm biplane system (Artis zee biplane, Siemens AG, Healthcare Sector, Forchheim, Germany) during standard ablation procedures performed at three sites:

- Krankenhaus Barmherzige Brüder Regensburg, Germany (50 patients)
- Hôpitaux Universitaires de Genève, Switzerland (5 patients)

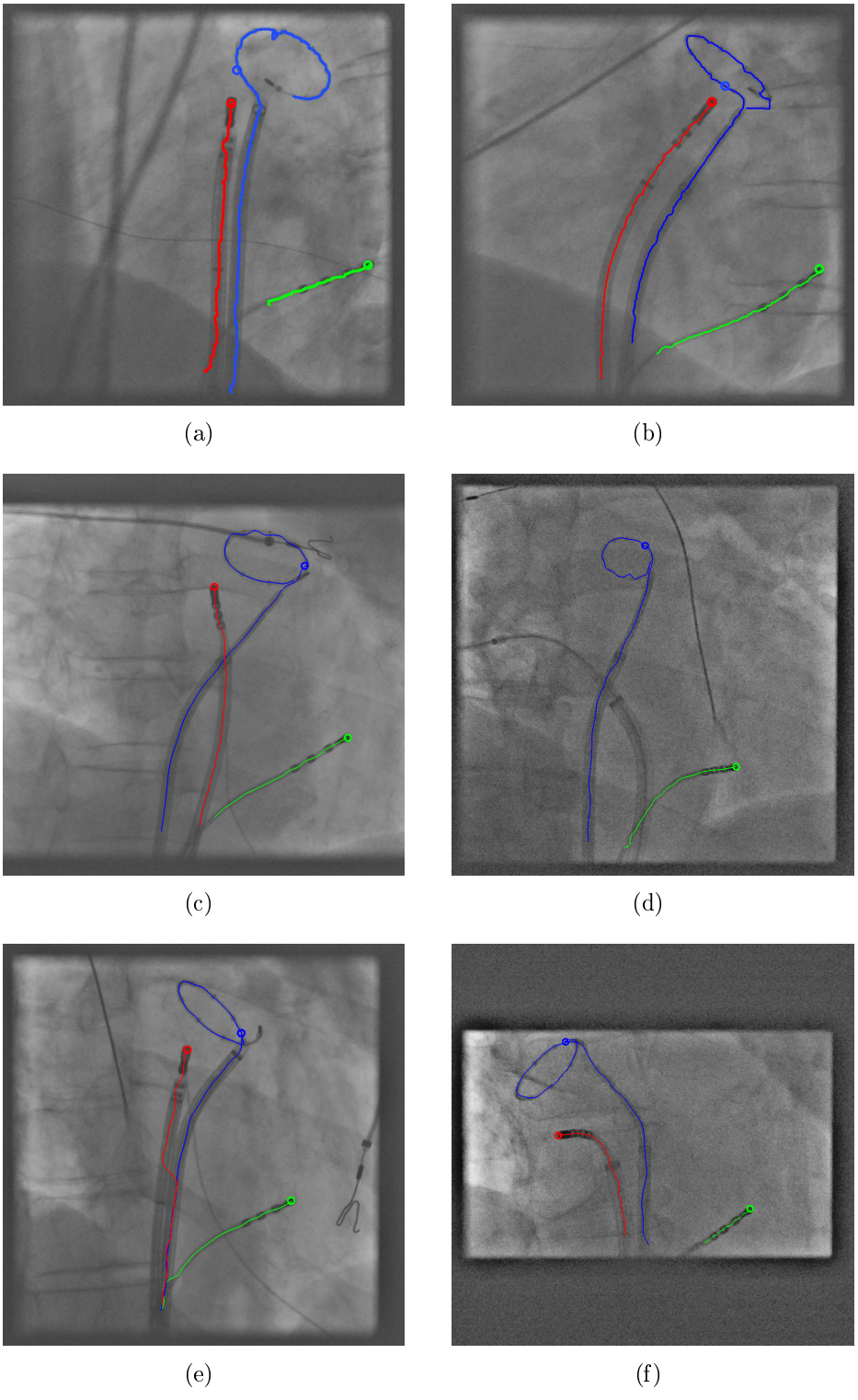

(a) (b) (c) (d) (e) (f)

Figure 3.4: Results of successful catheter detections. The detection of each catheter was performed independently of the other catheters but the results are shown in a common image. The seed point was placed at the transition from the shaft to the tip section for the CM catheters, for linear catheters, it was placed at the catheter tip. The seed points are marked by a circle in both images.

Table 3.3: Catheter detection results.

	All detections			
Catheter type	Mean dist. to reference ± std dev	Mean coupling distance ± std dev.	False negative / false positive	Success rate
RF	3.1 ± 5.5 mm	3.9 ± 7.0 mm	31.1 % / 27.5 %	84.0 %
CS	2.9 ± 7.5 mm	5.6 ± 12.1 mm	25.2 % / 16.4 %	82.8 %
CM	0.9 ± 1.3 mm	3.3 ± 3.0 mm	18.5 % / 7.8 %	83.6 %
all	2.3 ± 5.6 mm	4.3 ± 8.4 mm	24.5 % / 16.6 %	83.4 %
	Successful detections			
Catheter type	Mean dist. to reference ± std dev	Mean coupling distance ± std dev.	False negative / false positive	
RF	1.3 ± 1.1 mm	1.6 ± 1.2 mm	21.2 % / 17.7 %	
CS	0.7 ± 0.7 mm	1.2 ± 0.8 mm	13.7 % / 6.8 %	
CM	0.6 ± 0.5 mm	2.3 ± 1.3 mm	14.0 % / 4.3 %	
all	0.9 ± 0.8 mm	1.7 ± 1.2 mm	15.9 % / 9.0 %	

- Swedish Medical Center, Seattle, USA (4 patients)

Ground truth was established manually by annotation of catheter centrelines. All annotations were verified by an electrophysiologist.

The 2-D error was measured in two ways. First, the accuracy of the detection was assessed by determining the average and maximum error to the ground truth. To this end, we sampled points along the detected catheters and calculated their mean and maximum distance to the associated ground truth. This measure is a lower bound for the coupling error described below.

Additionally, we computed the coupling distance [Eite 94] normalized by the catheter length. This measure is symmetric and dedicated for curves. It establishes a mapping from points of the detected catheter to points of the ground truth annotation in which the points are ordered along the line. The normalized coupling error is defined as the distance between the points of a mapping normalized by the number of mappings. The measure is symmetric as it takes both wrongly detected catheter parts and undetected catheter parts into account.

The detections were performed on an Intel Core i7 2.6 Ghz CPU with 8 GB RAM and a Nvidia Quadro K1000M GPU. For generation of the medialness image and the skeleton image, the GPU was used.

Parameters of the detection method that depend on image size, quality, intensity quantification and spatial resolution were set heuristically, the resulting values are given in Table 3.2. The values of Π and l_g were adapted to a pixel spacing between 0.173 mm and 0.183 mm. For a different pixel spacing, these parameters need to be adapted accordingly.

The weights for the parameters of the objective functions for the shaft and the tip section, Equation 3.6 and Equation 3.12, were determined in a training step. Training of the parameters was performed in a leave-one-patient-out crossvalidation. As the parameters need to be determined up to a scaling, the value of α_l and β_{fe} were set to 1 without loss of generality. Training of the shaft parameters was performed separately for each catheter type. As the shaft parameters are mostly independent

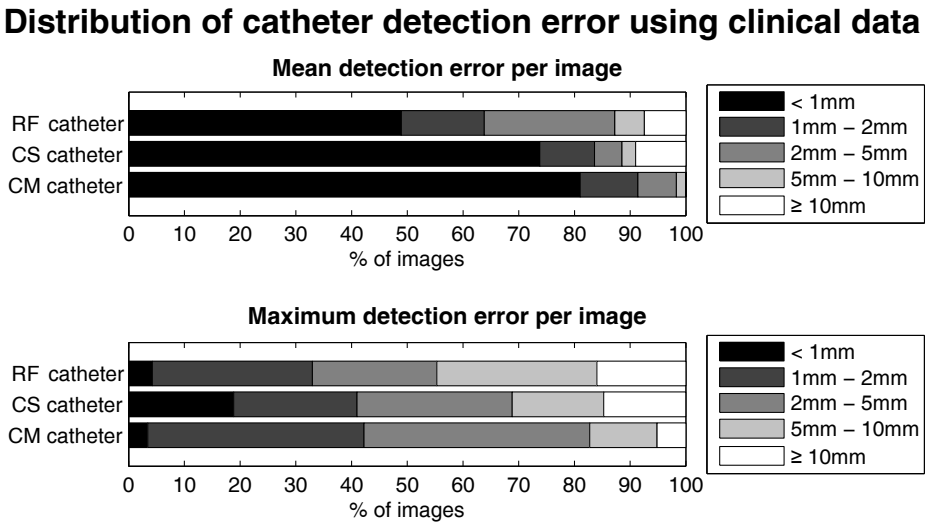

Figure 3.5: Distribution of mean and maximum error of the detected catheter to the ground truth.

of the tip parameters, the CM shaft parameters were trained using a heuristically determined set of tip section parameters. Based on the resulting shaft parameters, the tip parameters were trained. The seed point was set manually for each catheter. For linear catheters it was placed at the top of the tip, while for the CM catheter it was placed after the transition from shaft to the tip section as shown in Figure 3.4. The placement of the seed points was performed once, i.e. the position of the seed points did not change within the leave-one-patient-out crossvalidation.

Catheter detection was considered as failure if the mean error was larger than 5.0 mm. We considered pixels with a distance of more than 2.0 mm to the ground truth as false positives. Pixels of the ground truth with no detected pixel within a 2.0 mm radius were considered undetected, i.e. as a false negative. Successful detection results are shown in Figure 3.4. The mean and maximum distances of the detection to the ground truth are given in Figure 3.5. In Table 3.3, we present detailed results for all catheters.

Moreover, we evaluated how sensitive the method is to the seed point placement. To this end, we evaluated the inter-user and intra-user variability on a subset of 20 images for each catheter type. To allow for a general statement, this data set included images with low detection errors as well as images resulting in high detection errors. We assessed the intra-user variability by computing the detection error using three seed points from the same person. The variance in the coupling error was 0.1 mm or less for linear catheters and 0.5 mm for the CM catheter. Inter-user variability was assessed based on the detection errors when using seed points from three different persons. For linear catheters the variance was, again, 0.1 mm and the variance for the CM catheter was 0.6 mm.

For the CM catheter, the computation time for a single image was $2.8\,\mathrm{s} \pm 3.6\,\mathrm{s}$ for the RF and the CS catheter the runtime was $1.1\,\mathrm{s} \pm 0.2\,\mathrm{s}$ as no tip search was required.

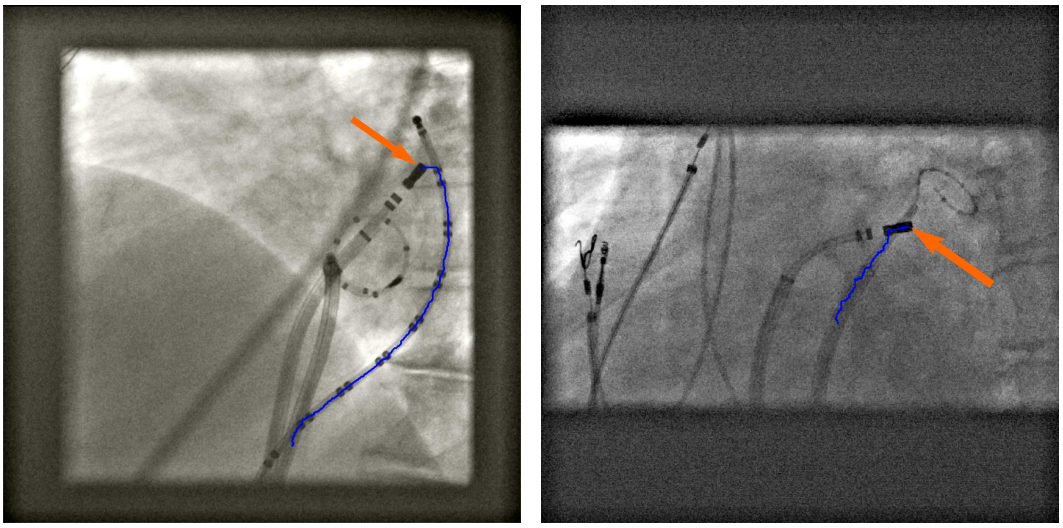

Figure 3.6: Examples for misdetections. In both cases, the seed point was set at the top of the RF catheter tip as indicated by the orange arrow. The part between the first and the second RF catheter electrode has low contrast. In (a), the algorithm decides for the CS catheter as the gap between the seed point and the CS catheter shaft is smaller than the gap between first and second RF catheter electrode. In (b), the seed point is too close to the CM catheter. As the skeleton is not smooth, the angle and curvature are computed by fitting a curve to a larger set of points to reduce the influence of small cusps. As a consequence, the kink at the beginning is not reflected in the curvature feature. So, the high curvature is not detected as it happens at the beginning of the catheter.

3.5 Discussion and Conclusions

In over 82 % of all cases the detection was successful with average errors below 2 mm. According to [Este 08, Bour 14, King 09], the results are within the clinically acceptable error range. Catheter detection failed mostly due to poor contrast of the catheter. This resulted in a low medialness filter value and, consequently, in gaps in the binary image that were too large. This was often the case for RF catheters which have a poor contrast between the first and the second electrode or for some CS catheter types. Sometimes, the gap between first and second electrode was larger than the gap of the seed point to the neighbouring catheter such that the wrong catheter was selected by the algorithm, see Figure 3.6(a). Here, incorporating results of an electrode detection algorithm [Caza 13, Ma 13, Kapp 13] could improve results. For low dose images, we observed poor contrast in the area of the diaphragm. In these cases, the catheter was sometimes only detected up to the beginning of the diaphragm.

Crossing of catheters with other catheters or guide wires was mostly handled correctly. However, if the angle between the crossing catheters is low, especially in conjunction with bad contrast, a wrong catheter might be selected, see Figure 3.6(b).

Our detection algorithm is able to adapt itself to different catheter types by estimating weights for the objective functions in a training step. The estimation of different weights per catheter type is important as we found that the weights for each catheter type differ. The CS catheter had, e.g., the highest weight for the length feature, but a low weight for the direction feature. This corresponds to the position-

ing of the CS catheter which is often horizontal due to the anatomy of the coronary sinus.

For the RF catheter and the CM catheter, the weights obtained from training for the direction feature and the curvature were higher. The other weights for these catheters, however, were similar as both are placed at the PV ostia in the LA and their shafts have a similar appearance. The feature for the end-angle which ensures a vertical end had, compared to the other features, a low weight. A probable explanation is that a non-vertical end angle or a sharp bend to a horizontal direction are readily addressed by the direction and the curvature feature.

We found a low intra- and inter-user variability for the linear catheters. The variance of the user input was very low as all users were told to place the seed point at the top of the catheter tip which is an unambiguous position. On the other hand, the seed point was moved to the closest skeleton point as part of the initialization. As a consequence, the effective seed point was in many cases identical. The position where the seed point for the CM catheter should be placed is not described as distinctively. However, the impact of a misplaced seed point is even higher as it may affect the direction of the catheter tip section which reflects in the coupling error.

A related method by Wang *et al.* [Wang 10] also performs also a graph search to find catheters. They reported a false positive rate of 17.8 % which is similar to our results, except for the RF catheter. Regarding the false negative rate, their approach performed better compared to our method. However, they required several, at least two seed points from the user such that the start *and* the end was clearly defined. Moreover, the value of comparison between the methods based on published numbers is limited as the evaluation was performed on a different data set and on guide wires instead of catheters.

CHAPTER 4

Linear Catheter Reconstruction

In this chapter, the reconstruction of a 3-D curve based on corresponding 2-D curves in two fluoroscopic images from different views is presented. Typically, these images are acquired using a biplane C-Arm system to minimize motion between the images to ensure proper reconstruction of the curve geometry. The original method has been proposed in [Hoff 12a]. Parts of this chapter have been published at the MICCAI conference [Hoff 12b], at the SPIE conference [Hoff 13b] and the evaluation has been published at IEEE TMI [Hoff 16b].

4.1 Motivation

In the context of registration, a 3-D reconstruction of catheters is required if anatomic structures such as the CS [Bour 10, Bros 11b] or the esophagus [Hoff 16g] are used as registration target. Without contrast agent, these structures are difficult to see in fluoroscopic images. However, if a catheter or another device is placed in these structures, the devices can be reconstructed and the counter part segmented from previously acquired 3-D data can be registered to the reconstructed devices. In some cases, for example endovascular aneurysm repair, the device deforms the anatomical structure. Here, a 3-D reconstruction of the device allows for a correction of the overlaid mesh representing the deformed anatomical structure [Toth 15].

Once a registration is established, it can, if required, be adapted continuously to account for cardiac or breathing motion. Motion compensation can involve a 3-D reconstruction of the elliptical CM catheter tip [Bros 09b, Bros 10b, Bros 12], or a CS catheter [Ma 10, Kapp 12]. These catheters are tracked over time [Sche 10] and serve as a surrogate for breathing motion. If tracking is not only performed on catheter electrodes but on the complete catheter, a 3-D initialization is required [Sche 10, Bros 09b, Bros 10b, Bros 12] which can be provided by this reconstruction algorithm.

If catheter ablation is performed using an augmented fluoroscopy system that supports a freely rotatable 3-D view, a 3-D reconstruction of the catheter can be displayed together with the 3-D LA model. The bending of the RF catheter allows the physician to estimate the force used to press the RF catheter against the heart wall. This force is a key figure which has an impact on the quality of the lesions created with the RF catheter [Redd 12]. Recently a method to compute the force value based on a 3-D reconstruction of an RF catheter has been proposed [Khos 13].

4.2 Related Work

A first reconstruction method for catheters has been proposed by Molina *et al.* [Moli 98] and has been later extended [Cane 00]. Based on a set of roughly corresponding points that are placed along the catheter or vessel to be reconstructed, an initial 3-D spline curve is computed. This curve is later refined to fit to the enhanced target structure in two 2-D images from orthogonal views while preserving curvature. The optimization is formulated as an energy minimization problem.

Bender *et al.* [Bend 99] detect and reconstruct a catheter simultaneously. The associated medical task was catheter placement verification in intensive care using X-ray images. However, some assumptions like low catheter curvature are not fulfilled in an EP environment. The CM catheter, for example, has a sharp 90° bending at the transition between shaft and tip section.

A reconstruction based on corresponding curves rather than corresponding points was presented by Baert *et al.* [Baer 03]. This method samples points from the one curve and searches for correspondences in the other curve by means of epipolar geometry. As we will discuss in this chapter, this method is not robust and small inaccuracies that lead to a missed intersection with the epipolar line cause a wrong reconstruction.

4.3 Catheter Reconstruction

The catheter is reconstructed in 3-D using two views from different directions, image plane A and B. The result of the catheter detection for both image planes is given as parametric 2-D curves, $S_\mathrm{A}(t_\mathrm{A})$ and $S_\mathrm{B}(t_\mathrm{B})$, $t_\mathrm{A}, t_\mathrm{B} \in [0,1]$, usually provided as cubic spline curves. It is assumed, that the splines run from the bottom to the top, i.e. $S_\mathrm{A}(0)$ denotes the lowest point at the shaft, $S_\mathrm{A}(1)$ is the last point at the tip of the catheter. Given the projection matrices for both views, an accurate reconstruction using triangulation can be performed if pairs of corresponding points are available [Bros 09c].

As both catheters are given as parametric curves, the correspondences can be expressed by a mapping $f_c(t_\mathrm{A}) : t_\mathrm{A} \rightarrow t_\mathrm{B}$ of the curve parameter. A pair of corresponding points is then given as $(S_\mathrm{A}(t_\mathrm{A}), S_\mathrm{B}(f_c(t_\mathrm{A})))$. We consider a point sequence that follows the catheter in A from the beginning to the tip given by the curve parameters $t_1 < t_2 < \ldots < t_n$. The corresponding points in B must also be a sequence following the course of the catheter, such that $f_c(t_1) \leq f_c(t_2) \leq \ldots \leq f_c(t_n)$. This means the mapping function $f_c(t_\mathrm{A})$ has to be monotonic. Once this mapping function

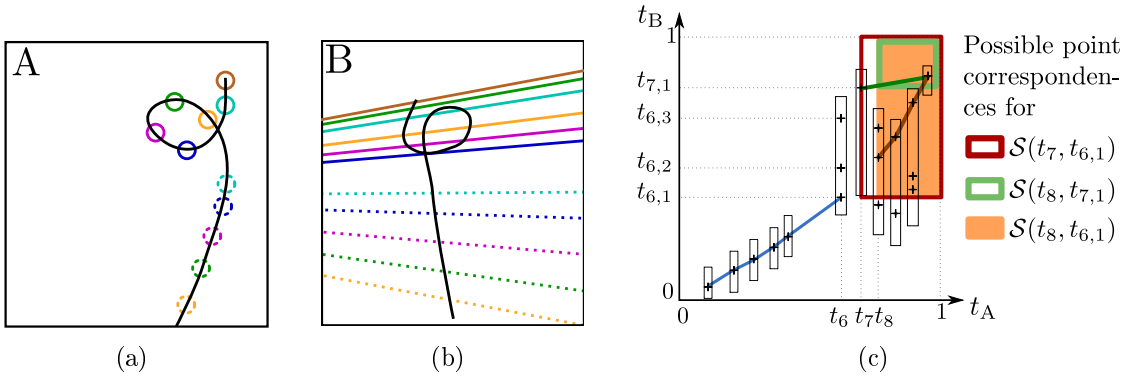

Figure 4.1: The spline in (a) is sampled and for each sampling point, possible point correspondences are computed by intersecting the epipolar line with the spline in (b). In some cases, the spline might not be intersected at the corresponding point as demonstrated by the solid green line. (c) For each possible point correspondence, the spline parameters are stored. A correspondence function that computes for each spline point $S_A(t_A)$ the corresponding spline point $S_B(t_B)$ has to be monotonic. This correspondence function for the first points is denoted by a blue line. For the computation of the remaining point correspondences given by $\mathcal{S}(t_7, t_{6,2})$ two options exist: First, to include the point correspondence $(t_7, t_{7,1})$ and return it together with the optimal set $\mathcal{S}$ of the green area. The corresponding mapping function is given by the green line and a greedy strategy would choose this option. Second, to discard the correspondences from t_7 and return the optimal set $\mathcal{S}$ that contains point correspondences from the orange area. In this case, the resulting mapping function is denoted by the brown line. As the second option returns the larger set $\mathcal{S}$, it will be chosen by the algorithm and the value for t_7 is computed by means of interpolation.

is defined, arbitrary point correspondences of the catheter can be generated and used for reconstruction. In practice this is done by interpolation between sample points of f_c.

To compute these sample points of the mapping function, we select n 2-D-points $\boldsymbol{a}_1 = S_A(t_1), \ldots, \boldsymbol{a}_n = S_A(t_n)$ equidistantly along S_A. For each resulting curve parameter t_i, the set of possible corresponding points is computed as the intersection points between S_B and the epipolar line [Hart 03] corresponding to the point $\boldsymbol{a}_i$. For objects with high curvature, a point in A might yield multiple intersections in B. Assuming m intersections of S_B and the epipolar line, they are denoted as $\boldsymbol{b}_{i,1} = S_B(t_{i,1}), \ldots, \boldsymbol{b}_{i,m} = S_B(t_{i,m})$. For choosing the right point of this set of possible corresponding points, a greedy and an optimal selection strategy exists.

The greedy strategy was proposed by Baert *et al.* [Baer 03]. Here, the correspondences are determined point-by-point, so the correspondence for the point $\boldsymbol{a}_i$ depends only on the corresponding point of the previous point $\boldsymbol{a}_{i-1}$ which is denoted as $\boldsymbol{b}_{i-1,j'} = S_B(t_{i-1,j'})$. From the points in B that possibly correspond to $\boldsymbol{a}_i$, the algorithm selects that point which follows the previous selected corresponding point on the catheter. This is the point with the smallest parameter $t_{i,j}$ s.t. $t_{i-1,j'} \leq t_{i,j}$. This procedure maintains the monotony constraint but is not optimal.

It assumes that for every point of S_A the actual corresponding point is within the intersection points of the epipolar line and S_B. If this assumption is violated due to inaccuracies in a practical setup, this method fails.

To illustrate this problem, consider a point $\boldsymbol{a}_i$ and its corresponding epipolar line. The spline in B, S_B, would ideally be intersected at two points $\boldsymbol{b}_{i,1}$ and $\boldsymbol{b}_{i,2}$. In this example, the intersection at $\boldsymbol{b}_{i,1}$ is the point that actually corresponds to $\boldsymbol{a}_i$. However, due to inaccuracies, the epipolar line does not intersect S_B at $\boldsymbol{b}_{i,1}$ and this corresponding point cannot be found. As a consequence, the only intersection point, $\boldsymbol{b}_{i,2}$, will be erroneously chosen as corresponding point. Now, we consider following points in A, that have their true corresponding point on S_B located before the wrongly chosen point $\boldsymbol{b}_{i,2}$. For these points, the actual corresponding point cannot be chosen due to the monotony constraint. Often, these points have to be omitted as there is no further corresponding point candidate that fulfils the monotony constraint. An illustration of this situation is given in Figure 4.1. In practice, this situation happens frequently if the catheter is curved and the epipolar line is rather a tangent to the spline than intersecting it. In such cases a small error is enough to inhibit an intersection.

To overcome this issue, we propose a different selection strategy that computes out of a given set of possible point correspondences $(t_i, t_{i,j})$ the largest subset that still fulfils the monotony constraint. This largest subset is called optimal subset $\mathcal{S}$. The selection strategy is robust with respect to missing intersections as it searches for the mapping function $f_c(t_\mathrm{A}) : t_\mathrm{A} \rightarrow t_\mathrm{B}$ globally. So, it might omit a few points $\boldsymbol{a}_i$ in order to allow for inclusion of points following afterwards with respect to the monotony constraint. The computation of this subset $\mathcal{S}$ can be seen as shortest path problem [Hoff 12b] or can be defined recursively [Hoff 13b]. For the recursive computation, we look at subcurves of S_A and S_B that run from $S_\mathrm{A}(t_i)$ and $S_\mathrm{B}(t_\mathrm{B})$, respectively, to the end. The optimal set for these subcurves is denoted as $\mathcal{S}(t_i, t_\mathrm{B})$ and uses a reduced set of possible point correspondences as illustrated in Figure 4.1 (c).

For the computation of set $\mathcal{S}(t_i, t_\mathrm{B})$, we take the intersections of S_B and the epipolar line corresponding to $\boldsymbol{a}_i$. The correspondence function is monotonic and we do not want to deprive us of including subsequent intersection points by proceeding too far along S_B. Therefore, we consider the correspondence pair $(t_i, t_i^+(t_\mathrm{B}))$ with

$$t_i^+(t_\mathrm{B}) = \min_{t \in \{\infty\} \cup \{t_{i,j} | t_{i,j} \geq t_\mathrm{B}\}} t. \tag{4.1}$$

$S_\mathrm{B}(t_i^+(t_\mathrm{B}))$ is the next intersection point of S_B and the epipolar line, directly after $S_\mathrm{B}(t_\mathrm{B})$. If there is no such intersection point, $t_i^+(t_\mathrm{B})$ is set to ∞, thereby ignoring the i-th sampled point. In this case, we set $\mathcal{S}(t_i, t_\mathrm{B}) = \mathcal{S}(t_{i+1}, t_\mathrm{B})$.

If there is an intersection point after $S(t_\mathrm{B})$, two options for the intersection $(t_i, t_i^+(t_\mathrm{B}))$ are possible: First, we could accept this point correspondence. Then, the set $\mathcal{S}(t_i, t_\mathrm{B})$ would include this correspondence as well as all correspondences in $\mathcal{S}(t_{i+1}, t_i^+(t_\mathrm{B}))$. $\mathcal{S}(t_{i+1}, t_i^+(t_\mathrm{B}))$ contains the optimal set of correspondences of the remaining curves that have to begin at $S_\mathrm{A}(t_{i+1})$ and $S_\mathrm{B}(t_i^+(t_\mathrm{B}))$ due to the inclusion of $(t_i, t_i^+(t_\mathrm{B}))$. The second option would be to discard this point correspondence. This option is needed for cases in which the actual corresponding point is located before $t_i^+(t_\mathrm{B})$ or is not found as illustrated by the solid green line in Figure 4.1. In this case, we would step to the next point $S_\mathrm{A}(t_{i+1})$ while leaving the parameter for B

unchanged. So, $\mathcal{S}(t_i, t_\mathrm{B})$ is identical to the optimal set $\mathcal{S}(t_{i+1}, t_\mathrm{B})$ of the remaining subcurve.

Whether to include the correspondence pair $(t_i, t_i^+(t_\mathrm{B}))$ into $\mathcal{S}$ or to omit can be decided based on the sizes of the optimal sets of the smaller subcurves. As we want to maximize the size of $\mathcal{S}$, we decide for the option that results into the larger set $\mathcal{S}(t_i, t_\mathrm{B})$:

$$\mathcal{S}(t_i, t_\mathrm{B}) = \begin{cases} (t_i, t_i^+(t_\mathrm{B})) \cup \mathcal{S}(t_{i+1}, t_i^+(t_\mathrm{B})) & \text{if } t_i^+(t_\mathrm{B}) \leq 1 \text{ and} \\ & \quad 1 + |\,\mathcal{S}(t_{i+1}, t_i^+(t_\mathrm{B}))\,| \;>\; |\,\mathcal{S}(t_{i+1}, t_\mathrm{B})\,| \\ \mathcal{S}(t_{i+1}, t_\mathrm{B}) & \text{else} \end{cases} \tag{4.2}$$

Given n sampled points, a base case of the recursion is defined for the n-th point as

$$\mathcal{S}(t_n, t_\mathrm{B}) = \begin{cases} \{\} & \text{if } t_n^+(t_\mathrm{B}) > 1 \\ (t_n, t_n^+(t_\mathrm{B})) & \text{else} \end{cases} \tag{4.3}$$

since there are no further correspondences after the end of the curve. $\mathcal{S}(t_1, 0)$ yields the optimal set for the whole curves and can be computed efficiently by dynamic programming [Corm 90].

Based on the correspondences in $\mathcal{S}$, the mapping function f_c can be defined. Then, for all points $S_\mathrm{A}(t_\mathrm{A})$, a corresponding point $S_\mathrm{B}(f_c(t_\mathrm{A}))$ can be determined and a 3-D point can be reconstructed using the known projection matrices for plane A and plane B [Hart 03, Bros 09d, Bros 09c].

4.4 Experiments and Results

For the evaluation of the proposed catheter reconstruction algorithm, we used both clinical data and data from phantom experiments. Although clinical data reflects reality better, we could not use it to assess 3-D accuracy due to the lack of associated 3-D ground truth. Instead, 2-D catheter centrelines in the images were extracted manually to obtain 2-D ground truth data. We carried out a phantom study involving tomographic reconstruction using C-arm CT to still provide insights into the 3-D reconstruction accuracy. The 3-D ground truth data was obtained by a manual segmentation of catheter centrelines in the C-arm CT volume. We generated two-dimensional ground truth the same way as described for clinical data.

We carried out two types of evaluation: First, we focused on inaccuracies related to our 3-D reconstruction method. As no 3-D ground truth was available for clinical data, we performed this error analysis on phantom experiment data. We used 2-D ground truth centrelines as input for 3-D reconstruction. Then, we compared the results to the 3-D ground truth to asses the reconstruction error independent of possible detection errors. Second, we combined our detection and 3-D reconstruction approach to estimate how detection inaccuracies affect the reconstruction result (combined approach). For clinical data, 3-D reference data was generated from 2-D ground truth centrelines using our reconstruction method. Note that this reference data is subject to the 3-D reconstruction inaccuracies studied in the phantom experiment. Finally, we applied the combined approach also to phantom data. Although the results have

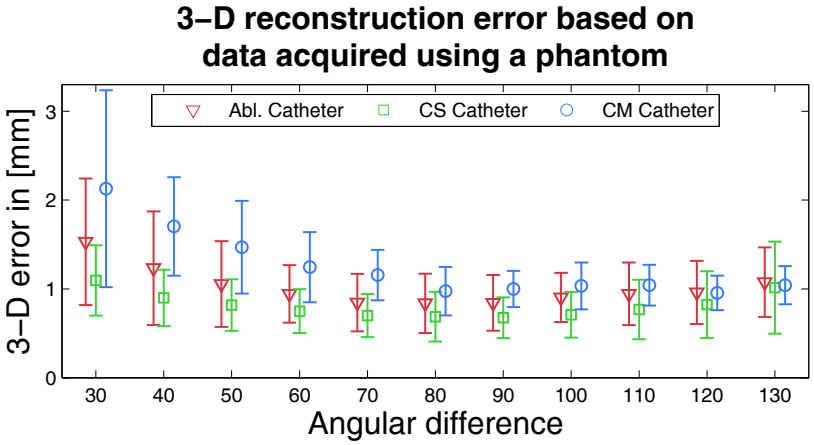

Figure 4.2: 3-D coupling distance of reconstruction results to ground-truth position from C-arm CT. For angulations with 90° angular difference, the mean error was 0.7 mm ± 0.2 mm for the CS catheter, 0.8 mm ± 0.3 mm for the RF catheter and 1.0 mm ± 0.2 mm for the CM catheter, respectively. The view angle difference of our biplane system was constrained between 30 and 130 degree due to mechanical limitations.

less clinical significance, they are still valuable since the 3-D ground truth was not affected by any detection and triangulation errors as it had been obtained from 3-D tomographic C-arm CT data.

4.4.1 Experimental Setup and Data

The phantom study was performed on a C-arm biplane system (Artis zee biplane, Siemens AG, Healthcare Sector, Forchheim, Germany). Our experimental setup comprised a CM catheter, a CS catheter and a RF ablation catheter all inserted into a thorax phantom. Images were taken from different primary angles (RAO/LAO) and a static secondary angle (Cran/Caud) of 0°. The primary angle ranged from -120° to -20° for plane A and from -30° to 70° for plane B. The step width was 10° resulting in 11 biplane pairs. The angular difference was always 90° as this is currently clinical practice [Koch 15]. However, it is possible to combine monoplane images to synthetic biplane pairs. With the angular difference increased by 10°, the number of combinations of A-plane and B-plane images resulting in this angle decreases by one. For a 30° angular difference, 17 image pairs could be created, for 130° angular difference, only 7 pairs were available. Angles less than 30° or above 130° were not considered as they are mechanically not possible with this system. All images show the CM, the CS and the RF catheter. For the catheters in these images, the 3-D ground truth position was extracted manually from a C-arm CT volume (*syngo* DynaCT, Siemens AG, Healthcare Sector, Forchheim, Germany).

The clinical data was the same as the data used for catheter detection evaluation, see section 3.4.

Table 4.1: Monoplane pairs comprising only successful detections

Catheter	30°	40°	50°	60°	70°	80°	90°	100°	110°	120°	130°
RF catheter	10	11	10	8	8	8	8	7	5	4	4
CS catheter	11	11	10	9	8	9	9	7	6	6	6
CM catheter	12	11	10	9	8	7	6	5	4	3	2

4.4.2 Catheter Reconstruction Performance

Three-dimensional reconstruction performance could only be evaluated for the phantom experiments. To this end, we used the ground truth catheter centrelines in the biplane sequences as input for 3-D reconstruction. The result was then compared to the 3-D ground truth catheter positions derived from the C-arm CT using the coupling distance [Eite 94]. For 90° angular difference, the mean coupling distance was 0.8 mm ± 0.3 mm for the RF ablation catheter, 0.7 mm ± 0.2 mm for the CS catheter and 1.0 mm ± 0.2 mm for the circular mapping catheter, respectively. The evaluation results for other difference angles are given in Figure 4.2.

Unfortunately, the same 3-D information of the catheters cannot be obtained in a clinical setup, since it is not possible to perform a C-arm CT for each biplane fluoroscopy scene. This is why an evaluation of the reconstruction accuracy on clinical data was not possible. The median runtime of the reconstruction was 32 ms.

4.4.3 Combined Detection and Reconstruction Performance

We also evaluated a combination of detection and reconstruction (combined approach). We performed first an automatic detection on the catheters first and fed the detection results then directly into the reconstruction algorithm. Since our goal was to investigate the overall accuracy when detection was successful, failed detections were not considered for evaluation of the combined approach. A detection was considered as failed if the mean distance to the ground truth was larger than 5.0 mm.

From the phantom study data, four monoplane images were not used for RF catheter evaluation, and three images were not used for CS catheter evaluation due to misdetection. Misdetections happened e.g. because the CS catheter tip section in certain angulations was so close to the RF catheter that the RF catheter was detected instead of the CS catheter. For the CM catheter, five images could not be used as the tip section appeared as a line rather than a loop. An overview over the remaining number of monoplane pairs per angle is given in Table 4.1.

For the angulations with 90 degrees difference, the resulting mean 3-D coupling distance was 1.8 mm ± 1.1 mm. Broken down by catheter type, we got an error of 1.7 mm ± 0.8 mm for the RF catheter, 1.0 mm ± 0.3 mm for the CS catheter and 3.1 mm ± 1.2 mm for the CM catheter, respectively. The errors for other angular differences are given in Figure 4.3.

With clinical data, a combined approach was performed as well. As no 3-D ground truth information was available, 3-D catheter reconstruction based on 2-D ground truth centrelines was used as reference. The computed differences can therefore only be considered as an estimation of the actual 3-D error. We found a mean coupling error of 2.2 mm ± 2.2 mm. In particular, the error was 1.7 mm ± 1.0 mm for the RF

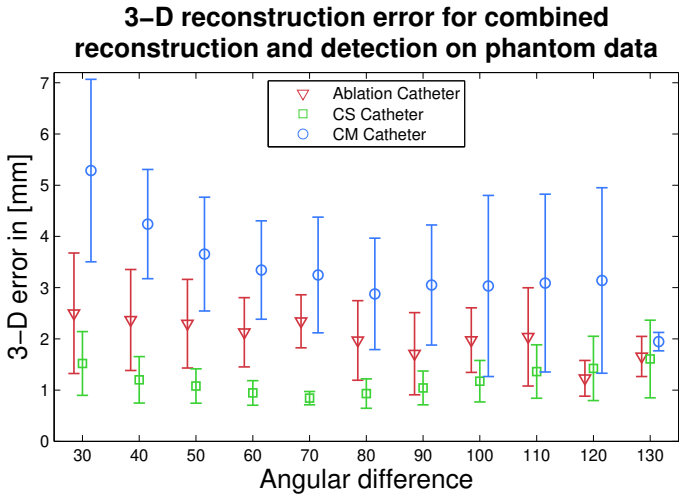

Figure 4.3: Coupling distance between results of the combined approach and ground-truth position on phantom study data. For 90° angular difference, the overall mean error for the ablation catheter was 1.7 mm ± 0.8 mm, for the CS catheter 1.0 mm ± 0.3 mm and 2.9 mm ± 1.5 mm for the mapping catheter. The maximum error for the RF catheter, CS catheter and CM catheter were 2.9 mm, 1.6 mm and 4.5 mm. Only successful detections were evaluated. The standard deviation of the CM catheter at 130 degree is low as only for two image pairs succesful detections were available.

catheter, 1.8 mm ± 3.2 mm for the CS catheter and 3.1 mm ± 1.1 smm for the CM catheter. The coupling error is largely influenced by undetected catheter parts. To evaluate the accuracy of the actually reconstructed parts, we also calculated their distance to the ground truth. The overall mean displacement was 1.4 mm ± 1.7 mm. The error was 1.5 mm ± 1.0 mm for the RF catheter, 1.4 mm ± 2.5 mm for the CS catheter and 1.5 mm ± 0.8 mm for the CM catheter. A distribution of the displacement is given in Figure 4.4.

4.5 Discussion and Conclusions

We found that our proposed reconstruction method dealt better with curved catheters than the previously suggested approach by Baert *et al.* [Baer 03]. An example for the different reconstruction results is presented in Figure 4.6. We conducted also a quantitative evaluation to comparing both approaches: For all possible pairs of 2-D images from the phantom study data, a reconstruction was computed using both approaches. The mean distance from the ground-truth data to the reconstruction results is given in Figure 4.7. It shows that the approach by Baert *et al.* can deal well with objects that have a small-curvature. But without the proposed search for point correspondences, a reconstruction of more strongly curved structures fails. However, some remaining limitations became apparent in the evaluation. They are discussed below.

The phantom study revealed a mean 3-D reconstruction error of up to 1.0 mm for a 90 degree angular difference between the two views. There are several possible

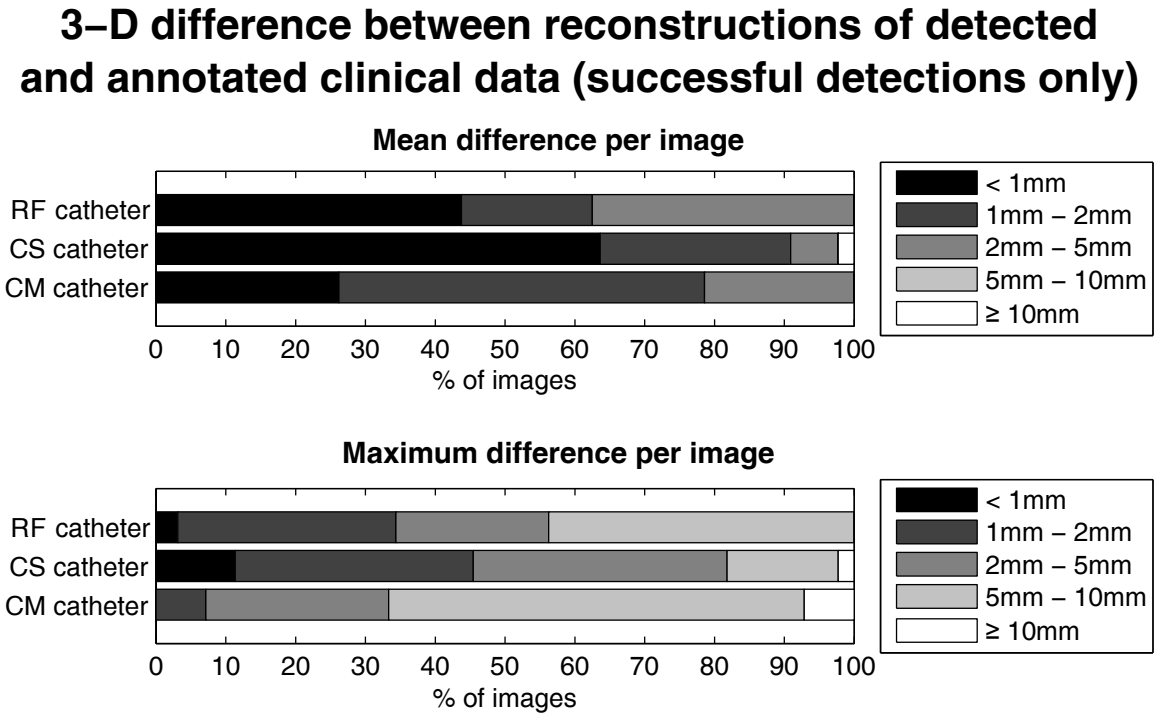

Figure 4.4: Mean and max distance of catheter parts reconstructed by the combined approach to a reconstruction result based on manual ground truth annotation of the clinical data. The overall mean displacement was $1.5\,\text{mm} \pm 1.0\,\text{mm}$ for the RF catheter, $1.4\,\text{mm} \pm 2.5\,\text{mm}$ for the CS catheter and $1.5\,\text{mm} \pm 0.8\,\text{mm}$ for the CM catheter.

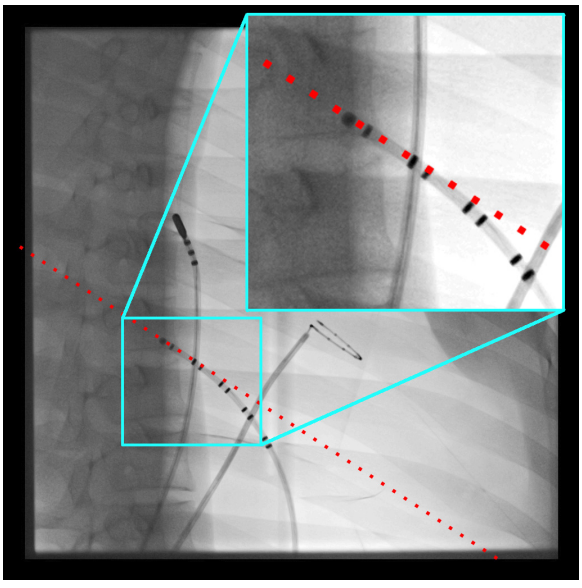

Figure 4.5: Epipolar line for the CS catheter tip. The epipolar line is nearly parallel to the end of the catheter. Computing intersections with the centreline of the catheter and the epipolar line is therefore numerically instable.

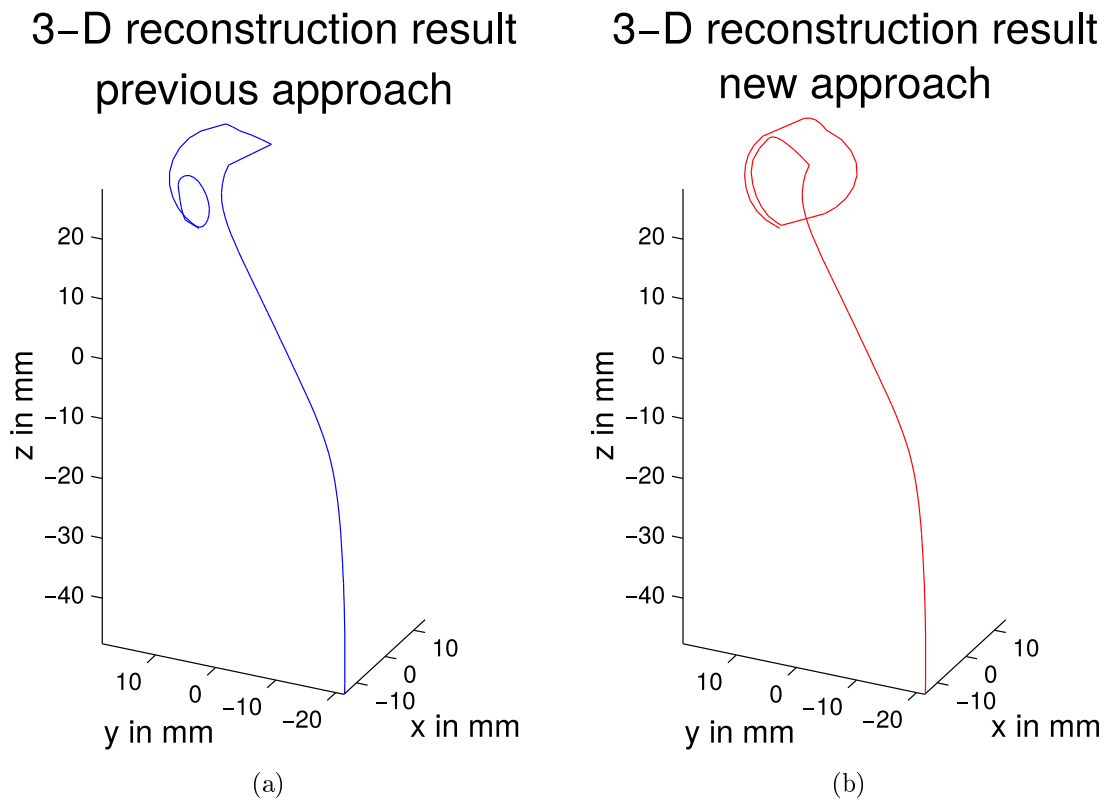

Figure 4.6: Reconstruction result using a re-implementation of the previously suggested approach by Baert *et al.* (a) and our proposed method (b). While both methods perform well for the catheter shaft, the previous approach fails for the curved catheter tip section.

sources for errors. First, the manually annotated ground truth centrelines of the catheters, both in the 2-D fluoroscopic images and in the 3-D C-arm CT volume, may contain small errors. We also noticed that the error for the CM catheter was highest. High errors appear if for some parts of the catheter no point correspondences can be found. This can be the case when the epipolar line does not precisely intersect the catheter, e.g., due to small inaccuracies when estimating the biplane projection geometry. This can occur especially at points where the catheter is tangent to the epipolar line, see Figure 4.5. The CM catheter is more prone to this kind of error as it has a circular part. In such a case, the missing points need to be interpolated. The difficulty to find the right point correspondences if the catheter is tangential to the epipolar line is the major limitation of the reconstruction algorithm. However, this is a general problem that also affects manual reconstruction by triangulation.

The overall reconstruction results showed similar 3-D reconstruction errors as observed when triangulating a single point [Bros 09d]. Also the dependency on the angle between the two viewing directions was found to be similar.

The combined approach using clinical data showed a correlation between detection quality and accuracy of the 3-D reconstruction. As no 3-D ground-truth was available, 3-D reconstruction based on 2-D ground-truth data was used as reference. We measured the error using the coupling distance between this reference and the

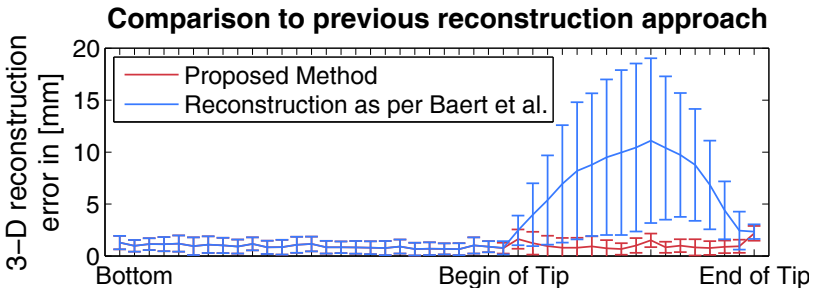

Figure 4.7: The CM catheter of the phantom was reconstructed from the manual annotations of all pairwise combinations of the acquired images. The distance of the reconstructions to each point of the ground-truth annotation is plotted for a re-implementation of the method of Baert *et al.* (blue) and our proposed method (red). For the catheter shaft, the new method is equal to the previous approach. For the curved catheter tip section, the method of Baert *et al.* fails while the new proposed method is able to deal with this curved structure.

result of a combined detection and reconstruction. As a consequence, both inaccurate as well as missing parts in the 3-D reconstruction result contributed to this error. If the detection succeeded, the 3-D error was found to be $1.7\,\text{mm} \pm 1.0$ mm for the RF catheter and $1.8\,\text{mm} \pm 3.2$ mm for the CS catheter. A 2.0 mm error is considered acceptable from a clinical point of view [Este 08]. For the CM catheter, the average coupling distance was $3.1\,\text{mm} \pm 1.1\,\text{mm}$. This is because the tip section of the CM catheter forms a circular structure which sometimes overlaps at the end. The ground-truth annotation included the overlapping part but it was often not detected and therefore missing in the 3-D reconstruction result, thus, leading to a higher coupling error. Considering only the actually reconstructed parts, the error reduced to $1.5\,\text{mm} \pm 0.8\,\text{mm}$.

The evaluation using data of our phantom study yielded notably lower 3-D errors for the RF catheter and the CS catheter. This is likely due to the detection step, as the phantom contained fewer additional structure such as ECG leads which can lead to small detection errors. However, for some images, the detection failed as the tip of one catheter was close to another catheter. For the CM catheter, the error was comparable to the clinical data as also here, the overlapping parts of the tip section were not always reconstructed.

The overall runtime of combined detection and reconstruction is about 2 s for the CS and the RF catheter. This facilitates computing a 3-D shape of the CS catheter for initial registration or as a registration reference throughout the case [Bros 11b, Hoff 16g]. Real-time performance is not needed at this step, as this registration is only performed a few times during the procedure (possibly only once). Due to the run-time requirements and the user interactions involved, our method as currently implemented is not yet suited for continuous 3-D modelling. For this use case, tracking methods should be used [Sche 10, Bros 09b]. However, our combined detection and reconstruction can be used to compute the initialization of the catheter required by these methods.

In combination with the semi-automatic detection, we have provided a tool for two-click catheter reconstruction suitable for clinical application. Due to the small user interaction needed and high accuracy achievable, our method can be used for augmented fluoroscopy applications or as input for motion compensation algorithms in the context of EP procedures [Bros 12]. In fact, if a mechanical model of the RF catheter was available, then our a 3-D model may even be used to estimate contact force [Khos 13]. As the largest error of this approach are introduced in the detection step, an optional correction step should be provided in clinical practice. A workflow using our approach could be comprise following steps: First, the assistant selects the type of catheter that should be reconstructed and sets the seed point on the catheter in each image. After reconstruction, the 3-D shape of the catheter is shown, and the 2-D detection results, e.g. represented as spline curve, are overlaid on the fluoroscopic images. If severe detection errors are present, they can be corrected manually by moving or adding control points to the 2-D detection result. As detection and reconstruction are decoupled, the manually corrected 2-D shape of the catheter can be directly used to perform a new 3-D catheter reconstruction.

CHAPTER 5

Cryoballoon Reconstruction

In this chapter, we present two fully automatic approaches to compute the balloon boundary and reconstruct the balloon in 3-D. Both rely on the detection of the X-ray marker [Kurz 13]. The first method extracts the balloon boundary from 2-D fluoroscopic images and uses it for balloon reconstruction. The second method is model-based and uses shaft detection and reconstruction presented in chapter 3 and chapter 4 to obtain the shape of the catheter shaft in 3-D. By applying a model of the cryoballoon catheter on the reconstructed shaft, the centre of the balloon is estimated.

5.1 Motivation

A cryoballoon catheter is an ablation catheter that can be used to destroy tissue around the PV ostium by freezing it. It consists of a shaft and a balloon, see Figure 5.1(a). The shaft has an inner lumen, i.e., it is hollow, as the cryoballoon catheter is an *over-the-wire* system. This means that a guidewire can be directed to the target and the catheter can be advanced along the wire. The catheter lumen can also be used to inject CA or to bring a diagnostic catheter behind the balloon [Chie 12].

For ablating tissue on the PV ostium, the balloon on the catheter is inflated and pushed against the ostium. To verify proper seal of the ostium, CA can be injected through the catheter lumen. If contrast agent flows into the LA, a proper seal was not achieved and the cryoballoon needs to be replaced. Once proper seal is reached, liquid nitrogen is shot into the balloon with high preassure. The nitrogen expands and cools down on the balloon wall and the tissue touching the balloon freezes.

In clinical practice, 3-D catheter localization is very often performed by an electro-anatomical mapping system (EAMS). However, catheter localization using a EAMS is limited to catheters which include electrodes or magnetic field sensors. Current cryobaloon catheters have neither of them and can therefore not be located by an EAMS directly [Bour 12]. As a workaround for this problem, a diagnostic catheter

may be placed behind the balloon, see Figure 5.1(a). The electrodes of this diagnostic catheter can then be located by an EAMS. However, this localizes the balloon only indirectly.

Fluoroscopic guidance, on the other hand, allows a direct localization of the balloon, see Figure 5.1. Under fluoroscopy, the shaft and a radio-opaque X-ray marker is visible. Once the balloon is inflated, it can be seen as well, depending on the X-ray dose, as the liquid is replaced by less dense gas. However, for low-dose images, the cryoballoon boundary is not well delineated. This renders viewing of the fluoroscopic images straining and verification of the seal difficult. If the balloon outline is known to the system, it could be highlighted on the monitors to make it better visible. In contrast to EAMSs, fluoroscopy does not provide direct 3-D information. Using a biplane C-Arm system, a 3-D reconstruction of the balloon can be obtained by a method of Kleinöder *et al.* [Klei 10, Klei 11], but this method requires the user to mark the balloon boundary. The 3-D information was found to be helpful for storing previous cryoballoon positions, e.g., for documentation or assessing the fit of a cryoballoon to the anatomy given by the 3-D patient model [Bour 12]. Moreover, once a cryoballoon was placed at the PV ostium, a re-registration of the patient's mesh could be performed.

Our proposed fully automatic balloon detection and reconstruction approaches rely both on the detection of the X-ray marker [Kurz 13]. The first method is appearance-based. It extracts the 2-D boundary from the fluoroscopic images and uses them to reconstruct the balloon using a method by Kleinöder *et al.* [Klei 10, Klei 11]. The second method is model-based and uses shaft detection and reconstruction presented in chapter 3 and chapter 4 to obtain a 3-D model of the catheter shaft. By applying the model on the reconstructed shaft, the centre of the balloon is estimated. So, this method allows to display a balloon boundary even if the balloon is not inflated yet.

5.2 Related Work

So far there has only been little research on detection and reconstruction of cryoballoons. Kurzendorfer *et al.* [Kurz 12] presented a work on tracking of the cryoballoon catheter. For this approach, the user clicks on the X-ray marker and the region around the marker is extracted as template. In the following frames, template matching based on sum of squared differences (SSD) as similarity measure is used to track the catheter. Yet, this approach does not detect the boundary. So the boundary or the balloon centre still needs to be marked by the user. Moreover, this approach comprises only translation of the balloon, a re-initialization is necessary if the catheter is moved to another PV.

Another approach by Kurzendorfer *et al.* [Kurz 13] detects dark spots based on a Hessian matrix. In a first step, strong dark spot are considered as marker candidates. Based on the fact that electrodes of other catheters are occur often in a group, distances to neighbouring electrodes are used to reject electrodes belonging to other catheters. An improved approach by Kurzendorfer *et al.* [Kurz 16] computes a specialized feature to detect the marker using an Support Vector Machine (SVM).

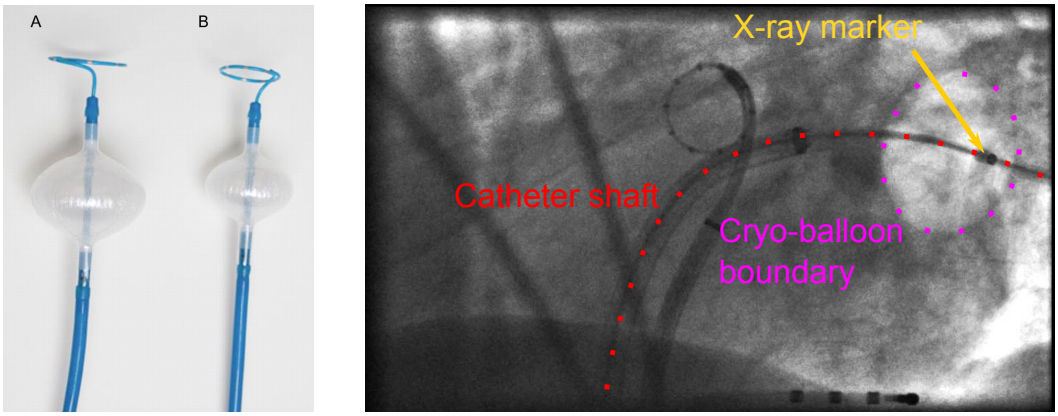

(a) (b)

Figure 5.1: (a) Cryoballoon catheters of different sizes with an Achieve mapping catheter (Medtronic, Minneapolis, USA). Image courtesy by [Chie 12], Oxford university press. (b) A cryoballoon catheter as seen under X-ray. A previous approach for cryoballoon reconstruction [Klei 11] involves manual annotation of the balloon boundary (dotted, magenta). We propose two new methods for automatic reconstruction: in the appearance based approach, the X-ray marker (yellow arrow) is found first followed by a detection of the balloon boundary. The automatically detected balloon boundary replaces the manual annotation of the previous reconstruction approach. The second, model-based approach uses the automatically detected X-ray marker for detection of the catheter shaft (dashed, red). After 3-D reconstruction of both the X-ray marker and the catheter shaft, the 3-D centre of the balloon is found using prior knowledge regarding the catheter model used during the procedure.

For balloon reconstruction, Kleinöder *et al.* [Klei 11] proposed a reconstruction approach based on the intersection of cones. The user marks the boundary in each view of a biplane image pair. An ellipse is fitted to the marked points which serves as base of the cone. The tip of the cone is set as the camera centre of the C-arm. This approach then follows the method by Wijewickrema *et al.* for reconstruction of spheres from two cameras [Wije 06].

An approach for detection of elliptical boundaries using snakes with special parametrization has been proposed by Delgado *et al.* [Delg 12]. This approach has been used to find boundaries of cells in microscopic images and to delineate heart chambers in MRI slices after manual initialization. However, this approach requires the area within the boundary to be homogeneous which is not the case for cryoballoon X-ray images as the balloon contains a guidewire and may be overlapped by other catheters, too.

5.3 Cryoballoon Reconstruction Methods

Our cryoballoon reconstruction methods require two 2-D X-ray images acquired simultaneously from two different views, e.g., using a biplane C-arm angiography system. In addition, we need to know for both approaches the cryoballoon catheter model used during the intervention. The two different X-ray views are denoted as image plane A and image plane B. Both cryoballoon reconstruction methods require the presence of

an X-ray marker on the shaft of the cryoballoon catheter, see Figure 5.1. This X-ray marker is built into all cryoballoon catheters currently available on the market.

After the detection of the X-ray marker, the first, appearance-based approach detects points along the balloon boundary to replace the manual boundary annotation used by the approach by Kleinöder et al. [Klei 11]. The second, model-based approach uses the detected X-ray marker to identify and reconstruct the catheter shafts in both images. From the known 3-D distance along the shaft between X-ray marker and cryoballoon centre, the 3-D position of the cryoballoon centre is then determined. Based on the obtained 3-D balloon centre, a sphere representing the cryoballoon can be drawn in the augmented fluoroscopy view.

5.3.1 Appearance-Based Cryoballoon Reconstruction

The first, appearance-based, reconstruction method detects the balloon boundary in the image. Based on the X-ray marker, which serves as reference point inside the balloon, gradients pointing inside the balloon are extracted from the image. They are used to determine a preliminary balloon centre which is then used to extract a refined set of gradients. Using the refined set of gradients, a first estimate of the balloon boundary is computed which serves as an initialization of a snake algorithm. The snake adapts then to the boundary in the image. As we know the balloon to be an ellipsoid, we fit an ellipse to the points resulting from the snake algorithm. An overview of the method is given in Figure 5.2, the steps are detailed below.

Preprocessing and Gradient Extraction

First, the image regions covered by shutters are cropped. As the contrast between the areas within the balloon and outside the balloon is low, see Figure 5.3 (a), a histogram equalization is performed to enhance the contrast [Prat 91], see Figure 5.3 (b). The resulting image is denoted as $\boldsymbol{I}_{\text{eq}}$.

As the gas inside the inflated balloon has a lower density than the surrounding blood, the balloon appears as brighter elliptical area. As we are interested in the balloon boundary, the image $\boldsymbol{I}_{\text{eq}}$ is convolved with the first derivative of Gaussian [Prat 91] to smooth the noisy image and extract gradients simultaneously. Given a 2-D Gaussian

$$\boldsymbol{K}_{\sigma}(x,y) = \frac{1}{2\pi\sigma^2} \exp\left(-\frac{x^2+y^2}{2\sigma^2}\right) \tag{5.1}$$

with a standard deviation σ, the gradient in x-direction is obtained by convolution of $\boldsymbol{I}_{\text{eq}}$ and the derivative of the Gaussian in x direction. Using the convolution operator $\star$, $\boldsymbol{I}_{\text{x}}(x,y)$ is given by

$$\boldsymbol{I}_{\text{x}}(x,y) = \frac{\partial \boldsymbol{K}_{\sigma}}{\partial x} \star \boldsymbol{I}_{\text{eq}}. \tag{5.2}$$

Together with the image gradient in y-direction,

$$\boldsymbol{I}_{\text{y}}(x,y) = \frac{\partial \boldsymbol{K}_{\sigma}}{\partial y} \star \boldsymbol{I}_{\text{eq}}, \tag{5.3}$$

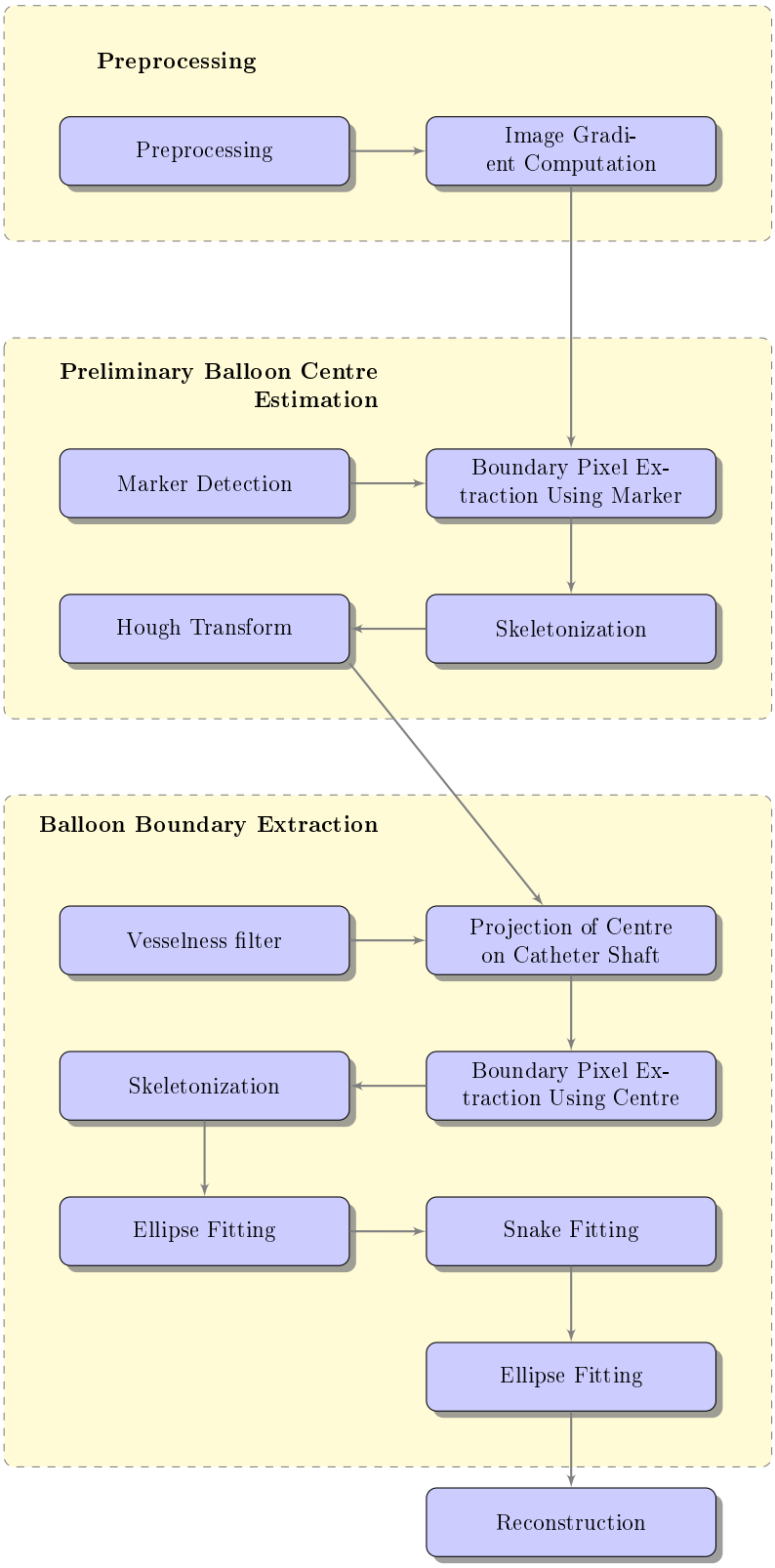

Figure 5.2: Appearance-based cryoballoon reconstruction overview

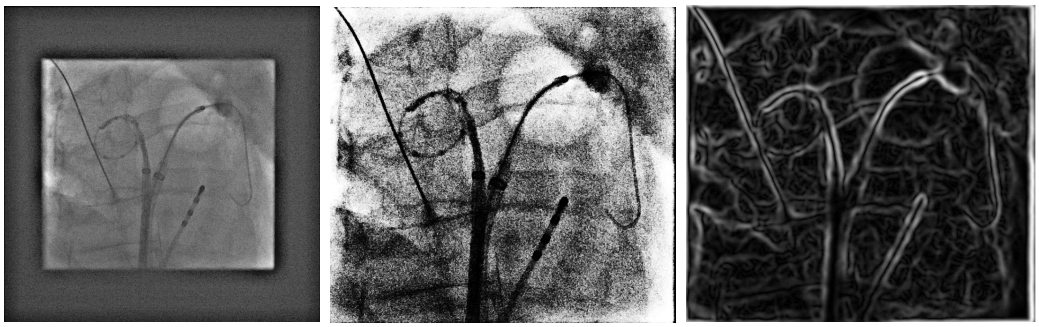

(a) (b) (c)

Figure 5.3: Original X-ray image showing the cryoballoon (a), image after removing the area under the shutters and histogram equalization (b), gradient magnitude image obtained by applying the first derivative of a Gaussian (c).

the image gradient vector is defined as

$$\nabla \boldsymbol{I}_{\text{eq}}(x,y) = \begin{pmatrix} \boldsymbol{I}_{\text{x}}(x,y) \\ \boldsymbol{I}_{\text{y}}(x,y) \end{pmatrix}. \tag{5.4}$$

An example of the gradient magnitude image is given in Figure 5.3 (c).

To select only strong edges, we apply a threshold θ_∇ to the gradient magnitude image $||\nabla \boldsymbol{I}_{\text{eq}}||_2$ to select pixels representing strong edges. These pixels are denoted as set $\mathcal{B}$ with

$$\mathcal{B} = \{\boldsymbol{p} |\ \|\nabla \boldsymbol{I}_{\text{eq}}(\boldsymbol{p})\|_2 > \theta_\nabla\} \tag{5.5}$$

Preliminary Balloon Centre Estimation

If the balloon centre was known, all boundary edges which have a gradient pointing to the centre and which have a distance to the centre similar to the balloon radius could be selected as boundary pixels. However, as the centre is unknown we use as first estimate the X-ray marker position $\boldsymbol{m} \in \mathbb{R}^2$. Based on the angle

$$\measuredangle(\nabla \boldsymbol{I}_{\text{eq}}(\boldsymbol{p}), \boldsymbol{m} - \boldsymbol{p}) = \arccos\left(\frac{\nabla \boldsymbol{I}_{\text{eq}}(\boldsymbol{p})^T(\boldsymbol{m} - \boldsymbol{p})}{\|\boldsymbol{I}_{\text{eq}}(\boldsymbol{p})\|_2 \cdot \|\boldsymbol{m} - \boldsymbol{p}\|_2}\right) \tag{5.6}$$

between the image gradient of a pixel $\boldsymbol{p}$ and the vector pointing from $\boldsymbol{p}$ to the X-ray marker $\boldsymbol{m}$ and the distance $\|\boldsymbol{m} - \boldsymbol{p}\|_2$, a first estimate $\mathcal{B}_{\boldsymbol{m}}$ of boundary pixels is determined.

The distance of the marker to the centre is approximately half the balloon radius r. Therefore, the maximum distance from an edge pixel to the marker is $1.5 \cdot r\frac{w}{s}$ pixel where w denotes the radiographic magnification factor and s denotes the pixel spacing. Given the distance between marker and balloon centre, the maximum angular difference $\alpha_{\max}$ between the direction from a balloon boundary pixel to the balloon centre and the direction to the X-ray marker can be computed. With a distance of $\frac{1}{2}r$, we get $\alpha_{\max} = 30°$. As the gradient computation is sensitive to noise, we use at

(a) (b)

Figure 5.4: (a) Pixels in $\mathcal{B}_{\boldsymbol{m}}$. These pixels are close to the X-ray marker and point to the X-ray marker. (b) The and associated skeleton.

first a threshold of $2\alpha_{\max}$ to filter out gradients that do not point inside the balloon. So, we define the first estimate

$$\mathcal{B}_{\boldsymbol{m}} = \{\boldsymbol{p} \in \mathcal{B} | \ \measuredangle(\nabla \boldsymbol{I}_{\text{eq}}(\boldsymbol{p}), \boldsymbol{m} - \boldsymbol{p}) \leq 2\alpha_{\max} \ \wedge \ \|\boldsymbol{m} - \boldsymbol{p}\|_2 \leq 1.5 \cdot r\frac{w}{s}\}, \tag{5.7}$$

see Figure 5.4 (a) for an example.

Due to the filtering with the derivative of the gaussian, the edges are blurred and therefore, the pixels in $\mathcal{B}_{\boldsymbol{m}}$ form rather thick lines. They are reduced to lines using a skeletonization method [Cych 94]. Moreover, a border of 30 pixels around the image boundary defined by the shutters is set to zero as this area might still contain edges caused by the shutters. As the balloon is rarely placed that close at the image boundary, see Figure 5.4, this step does not affect the boundary estimation.

A first estimate $\boldsymbol{c}' \in \mathbb{R}^2$ of the balloon centre is obtained using a Hough transform for circles [Prat 91, Duda 72] on the skeleton image. As the radius of the cryoballoon is known, we use $r \cdot \frac{w}{s}$ as fixed radius for the Hough transform.

We also know that the shaft of the cryoballoon catheter runs through the balloon centre, which is enforced as additional constraint. Therefore, we apply a vesselness filter [Fran 98, Buda 13] to the input image, see Figure 5.5 (a). If the centre estimate $\boldsymbol{c}'$ is not located on the catheter shaft, it is replaced by the closest pixel on the catheter or the guidewire running inside the shaft, respectively. An example result of the first centre estimate is given in Figure 5.5 (b).

Ballon Boundary Extraction

Since a first centre estimate is now available, we can use this estimate for the constraints of Equation 5.7. As the constraints refer no longer to the marker but to the centre, the threshold θ_α for the angle and the tolerance θ_r for the distance to the centre can be chosen smaller than in Equation 5.7. The refined set of boundary pixels is then defined as

$$\mathcal{B}_{\boldsymbol{c}} = \{\boldsymbol{p} \in \mathcal{B} | \ \measuredangle(\nabla \boldsymbol{I}_{\text{eq}}(\boldsymbol{p}), \boldsymbol{c} - \boldsymbol{p}) \leq \theta_\alpha \ \wedge \ | \ \|\boldsymbol{c} - \boldsymbol{p}\|_2 - r| \leq \theta_r\}. \tag{5.8}$$

The cryoballoon is actually not a regular sphere but onion-shaped with the pointed end at the distal part of the balloon. For the final boundary extraction we thus

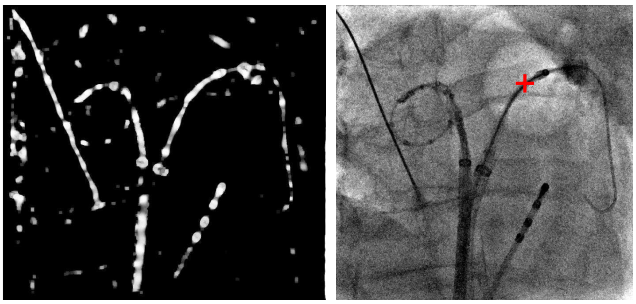

(a) (b)

Figure 5.5: (a) Catheter shafts highlighted by a vesselness filter. (b) The estimated cryoballoon centre after projection onto the guidewire inside the catheter.

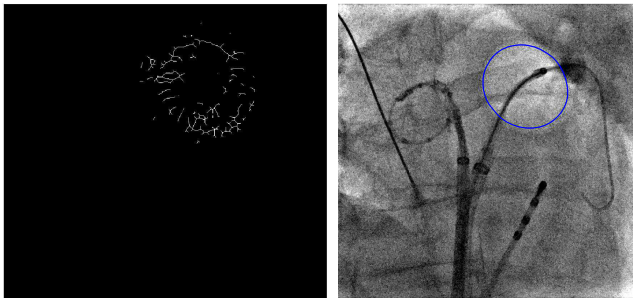

(a) (b)

Figure 5.6: (a) Refined set of boundary pixels using the first centre estimate $\boldsymbol{c}'$. (b) Ellipse fitted based on the boundary points shown in (a).

drop the assumption of a circle which we made for the hough transform. Instead, we generalize this assumption to an ellipse. This is reasonable as the pointed end is hardly perceivable in X-ray images and therefore, the boundary appears as an ellipse. Moreover, an ellipse representation of the balloon boundary is required for the reconstruction of the cryoballoon as a sphere which is performed after the detection.

On the refined set $\mathcal{B}_{\boldsymbol{c}}$, a skeletonization is performed, see Figure 5.6 (a) and the resulting set $\mathcal{B}_{\mathrm{S}}$ of pixels is used for ellipse fitting, see Figure 5.6 (b). The ellipse fitting is a least square approach [Hali 98] and thus, the result is influenced by outliers. Moreover, the result of the skeletonization is not always a single line as in the top region of Figure 5.6 (a) but may consist of several lines as in the bottom region of Figure 5.6 (a). These regions will have a higher influence to the least square fitting. The result of the ellipse fitting may not follow the boundary as it is, e.g., too small as shown in Figure 5.6 (b).

To align the detected boundary to the boundary pixels, a snake algorithm is performed [Kass 88, Prat 91]. This is an energy-minimization approach to align a smooth curve to certain image features. Given snake points $\boldsymbol{p}_1, \ldots, \boldsymbol{p}_n$, the snake energy is defined as

$$E_{\text{snake}} = \sum_{i=1}^{n} E_{\text{int}}(\boldsymbol{p}_i) + E_{\text{image}}(\boldsymbol{p}_i) \tag{5.9}$$

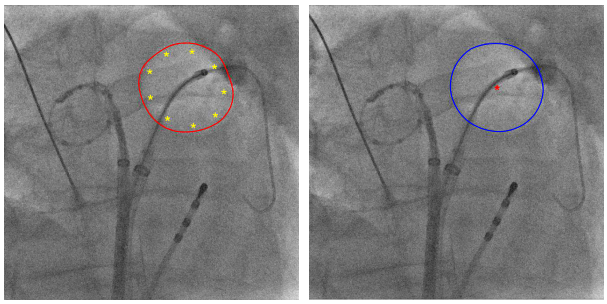

(a) (b)

Figure 5.7: (a) Initialization of the snake (yellow points) and resulting contour (red) after the snake step, (b) the resulting ellipse (blue) fitted to the snake contour and associated centre (red point)

where E_{int} defines smoothness constraints as described in [Kass 88] and E_{image} describes the energy that attracts the snake to certain image features. In our case, we use

$$E_{\text{image}}(\boldsymbol{p}) = \min_{\boldsymbol{p}_s \in \mathcal{B}_{\text{S}}} \|\boldsymbol{p} - \boldsymbol{p}_s\|_2 \tag{5.10}$$

which is the distance transform [Felz 04] of the skeleton. This way, the snake gets attracted to the skeleton. As initialization of the snake points $\boldsymbol{p}_1, \ldots, \boldsymbol{p}_n$, the points of the fitted ellipse are used. The boundary after applying the snake algorithm is shown in Figure 5.7 (a).

Most of the detected boundary now follows the actual balloon boundary. However, in some images, contrast agent from the PVs will appear inside the balloon area, either due to the X-ray projection or because the balloon does not seal the ostium completely and the contrast agent flows past the balloon. In this case, the snake will adapt to the resulting spurious edges. As a result, the snake may no longer resemble an ellipse. To enforce an elliptical shape, the ellipse which is most alike the result of the snake algorithm is computed using the ellipse fitting with the snake points as input. The resulting boundary is shown in Figure 5.7 (b).

Based on the detected 2-D balloon boundaries, one in each X-ray image, the 3-D balloon is then computed using the reconstruction approach by Kleinöder *et al.* [Klei 11]. This method requires an ellipse annotation in each image plane as input which is provided by the detected 2-D balloon boundary.

5.3.2 Model-Based Cryoballoon Reconstruction

The model-based reconstruction applies a cryoballoon catheter model to a reconstructed 3-D catheter shaft which includes the 3-D position $\boldsymbol{m}_{\text{3-D}}$ of the X-ray marker. This model involves two parameters: The first parameter is the distance d between balloon centre and X-ray marker along the catheter shaft. The second parameter is the balloon radius r. Based on this information, the 3-D catheter shaft is traversed backwards from $\boldsymbol{m}_{\text{3-D}}$ for a distance d. The resulting point is considered as 3-D centre $\boldsymbol{c}_{\text{3-D}}$ and a sphere of radius r is placed around this point.

The model-based reconstruction involves four steps: First, the 2-D cryoballoon marker $\boldsymbol{m}$ in each image of a biplane image pair is detected. For detection, the method by Kurzendorfer *et al.* [Kurz 13] is used.

As a second step, based on the detected marker position, the catheter shaft is detected by the catheter detection method described in chapter 3. Alternatively, a second point can be placed at the position where the catheter enters the image to increase the robustness of the catheter shaft detection. In this case a shortest path from $\boldsymbol{m}$ to the second point is computed based on the catheter cost function described in Equation 3.2.

In the third step, the detected catheter shafts are used as input for the catheter reconstruction method described in chapter 4. The resulting 3-D shaft is denoted as $S_{3\text{-D}}$.

As last step, the cryoballoon model is applied to the 3-D shaft reconstruction. From the two 2-D X-ray marker positions, $\boldsymbol{m}_{\text{A}}$ and $\boldsymbol{m}_{\text{B}}$, the 3-D X-ray marker position $\boldsymbol{m}_{3\text{-D}}$ is computed. The resulting point $\boldsymbol{m}_{3\text{-D}}$ may not be located on the 3-D curve $S_{3\text{-D}}$. This can be due to inaccuracies in the calibration, due to inaccuracies in the shaft reconstruction or due to motion between the acquisitions of the image in plane A and the acquisition in plane B. Therefore, the projection $\boldsymbol{m}'_{3\text{-D}}$ of the reconstructed X-ray marker onto $S_{3\text{-D}}$ is used instead. As the 2-D catheter shafts used for reconstruction end at the X-ray marker, the reconstructed shaft usually ends at or, in case of reconstruction errors, before $\boldsymbol{m}_{3\text{-D}}$. If this is the case and the projection of $\boldsymbol{m}_{3\text{-D}}$ onto $S_{3\text{-D}}$ results in the endpoint of the 3-D shaft curve, i.e. $\boldsymbol{m}'_{3\text{-D}} = S_{3\text{-D}}(1)$, $S_{3\text{-D}}$ is extended to $\boldsymbol{m}_{3\text{-D}}$ and we set $\boldsymbol{m}'_{3\text{-D}} = \boldsymbol{m}_{3\text{-D}}$, see Figure 5.8.

From $\boldsymbol{m}'_{3\text{-D}}$, the shaft $S_{3\text{-D}}$ is traversed backwards until a point $\boldsymbol{c}_{3\text{-D}} \in \mathbb{R}^3$ is reached such that

$$\delta_{S_{3\text{-D}}}(\boldsymbol{m}'_{3\text{-D}}, \boldsymbol{c}_{3\text{-D}}) = d \tag{5.11}$$

where $\delta_{S_{3\text{-D}}}$ denotes the geodesic distance with respect to the 3-D catheter shaft curve $S_{3\text{-D}}$. The point $\boldsymbol{c}_{3\text{-D}}$ is considered as cryoballoon centre and a sphere around this point with radius r is considered as reconstruction of the cryoballoon. As the 3-D direction of the shaft is known, it would also be possible to place a predefined onion-like shape at the centre. However, we decided for a sphere as this was previously proposed as 3-D representation of a cryoballoon [Klei 11, Klei 12, Bros 11a] and allows a comparison of this reconstruction method and the appearance-based reconstruction.

5.4 Experiments and Results

For evaluation, we used 62 clinical biplane image pairs (124 monoplane images) from 27 patients acquired during several cryoballoon ablation procedures. The catheters used in these images were ArcticFront, Medtronic, Minneapolis, MN, USA with a diameter of 23 mm and 28 mm, respectively. On each 2-D X-ray image, ground-truth annotation of the X-ray marker, the catheter shaft and the balloon boundary was available. Since there is no routine 3-D imaging during cryoballoon procedures, no 3-D ground truth data was available for the clinical images. This is why we generated 3-D data from the 2-D ground truth data using the cryoballoon reconstruction approach by Kleinoeder et al. [Klei 11]. So ground-truth data was obtained indirectly. Still, the

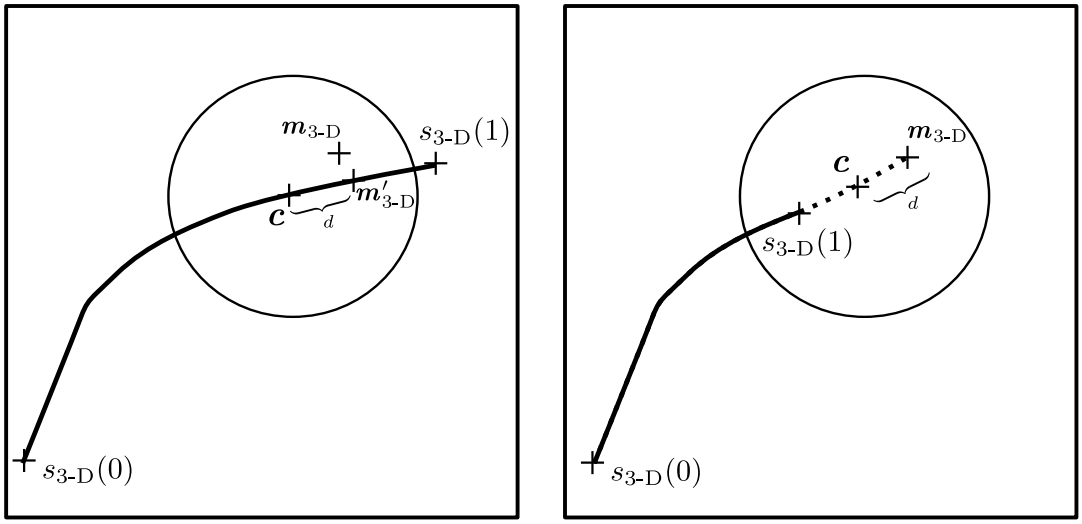

(a) (b)

Figure 5.8: (a) The reconstructed X-ray marker $\boldsymbol{m}_{3\text{-D}}$ is projected onto the shaft $S_{3\text{-D}}$. (b) If $\boldsymbol{m}_{3\text{-D}}$ is projected onto the end of the reconstructed shaft, denoted by $S_{3\text{-D}}(1)$, the spline will be extended to $\boldsymbol{m}_{3\text{-D}}$, instead. The shaft $S_{3\text{-D}}$ is then traversed back towards $S_{3\text{-D}}(0)$ until a maximum distance d is reached.

Table 5.1: Parameter values used during evaluation

Description	Symbol	Value	Appears in
Threshold for edge detection	θ_∇	$5\% \cdot \max_{\boldsymbol{p}} \boldsymbol{I}_{\text{eq}}$	Eq. 5.5
Angle threshold for boundary extraction	θ_α	25°	Eq. 5.7
Radius tolerance for boundary extraction	θ_r	50 pixels	Eq. 5.7
Size of the border around the shutters	e	30 pixels	Sect. 5.3.1
Balloon radius, 23 mm catheter Balloon radius, 28 mm catheter	r	11.5 mm 14 mm	Eq. 5.7
Distance to balloon centre, 23 mm catheter Distance to balloon centre, 28 mm catheter	d	11.5 mm 14 mm	Eq. 5.11

resulting ground truth data can be used for evaluation as the input was annotated carefully, the reconstruction method was found to be very accurate [Klei 11] and the correctness of the resulting 3-D reconstruction was approved by a medical expert.

To obtain the model parameters, a 3-D reconstruction of the catheters was established from the ground-truth data using triangulation. Then, the distance between X-ray marker and cryoballoon centre on the reconstructed catheter was measured. As model parameter d, the average distance from the data set of the respective balloon type was used. The other parameters used for this method were determined heuristically. All parameter values are lister in Table 5.1.

We evaluated different variants of our methods with different levels of user interaction to estimate the impact of various error sources. An overview is given in Table 5.2. In the remainder of the evaluation, we use two different data collections:

Table 5.2: Algorithm variants with different user interaction levels

Appearance-Based Reconstruction

Variant	Marker Detection	Boundary Detection
automatic	automatic using [Kurz 13]	automatic
2-click	manual	automatic
ground truth	n.a.	manual

Model-Based Reconstruction

Variant	Marker Detection	Catheter Detection
automatic	automatic using [Kurz 13]	automatic
2-click	manual	automatic
4-click	manual	semi-automatic
manual annotation	manual	manual

The first set contains only images on which X-ray marker detection was successful, the second data set contains all cases. Fully automatic 3-D cryoballoon reconstruction can only be performed on the first data set, but we also investigated semi-automatic approaches with manually annotated X-ray markers. The semi-automatic approaches were evaluated on both data sets. This way, we obtained a larger test dataset and were also able to compare results to those of the fully-automatic approaches.

5.4.1 X-Ray Marker Detection

In 89.5 % of all 124 monoplane images, the X-ray marker detection was successful. For the other images, no marker was found or, for one image, a marker at a different catheter was found. For these successful cases, we computed the 2-D error in mm using the pixel spacing of the detector and the radiographic magnification factor estimated by the X-ray system. The resulting spatial accuracy was 0.9 ± 1.5 mm. Considering biplane-pairs, we ended up with 51 biplane pairs (82.3 %) which had a successful X-ray marker detection in both images

5.4.2 Results for Appearance-Based Reconstruction

First, we present the 2-D results of the balloon boundary detection. To this end, we compared the ellipse parameters, i.e., the centre coordinates and the length of the two semi-axes to the associated ellipse parameters established during ground-truth annotation. For images on which the X-ray marker detection was successful, the average 2-D error of the detected ellipse centre point to the centre point of the ground-truth ellipse was 3.2 ± 5.9 mm. To assess the impact of the automatic X-ray marker detection on the boundary detection, we also evaluated a 2-click-method of the boundary detection using a manually annotated X-ray marker in each image. In this case, the error reduced to 3.0 ± 2.8 mm on the same set of cases. When including

Table 5.3: 2-D errors of detected balloon boundary ellipse im mm

	Centre	Major axis	Minor axis
Automatic X-ray marker detection (Cases with succesful marker detection)	3.2 ± 5.9	2.6 ± 2.2	2.4 ± 1.8
Manual X-ray marker annotation (Cases with succesful marker detection)	3.0 ± 2.8	2.5 ± 2.0	2.2 ± 1.7
Manual X-ray marker annotation (all cases)	3.0 ± 2.8	2.5 ± 2.0	2.3 ± 1.7

those cases on which the automatic X-ray marker detection had failed, the error was, again, 3.0 ± 2.8 mm. A complete overview of the errors is given in Table 5.3.

We also evaluated the accuracy of 3-D balloon reconstruction using the detected ellipse boundaries. The resulting 3-D error of the reconstructed balloon centre was 3.6 ± 4.8 mm if the detected X-ray marker positions were used. To investigate the impact of the X-ray marker detection, we evaluated a variant of the reconstruction (2-click-method) where the X-ray marker was annotated manually in the image. For data with a successful X-ray marker detection, the error reduced to 3.5±2.6. Using all cases and manually annotated X-ray markers, an error of 3.6 ± 3.0 mm was obtained. The distributions of the errors are shown in Figure 5.9(a) and Figure 5.9(b).

5.4.3 Results for Model-Based Reconstruction

To assess the impact of the automatic X-ray marker detection on the 3-D reconstruction error, we evaluated a 2-click method for model-based reconstruction as well. In this case, the X-ray marker was manually annotated in both image planes, A and B. To evaluate errors related to shaft detection, two further approaches were investigated: First, the shaft detection method using two manually annotated points per plane (4-click method) was used to assess the impact of direction confusions, i.e. the distal part of the guide wire starting from the X-ray marker is detected as catheter shaft. Second, the shaft detection was replaced by manual annotation of the complete shaft. To check for significance ($p < 0.05$) or high significance ($p < 0.01$), Student's t-test was performed.

If marker detection was successful, the fully automatic method yielded a 3-D error of 2.5 ± 1.7 mm for the remaining 51 cases. Compared to the fully automatic detection, a significant improvement was found when semi-automatic methods were used: The 3-D error of the 2-click method was 2.1 ± 1.6 mm and the 3-D error for the 4-click method was 2.1 ± 1.2 mm. The 3-D error using the manual shaft annotation was 2.1 ± 1.2 mm as well. The differences between the alternatives using manual interaction were found to be not significant.

Considering all 62 cases, the 3-D error of the 2-click method was 2.1 ± 1.5 mm and the 3-D error for the 4-click method was 2.0 ± 1.1 mm. The 3-D error using the manual shaft annotation was 2.1 ± 1.9 mm. The distributions of the errors are shown in Figure 5.9(a) and Figure 5.9(b), qualitative results are shown in Figure 5.10. Again, these differences were found to be not significant.

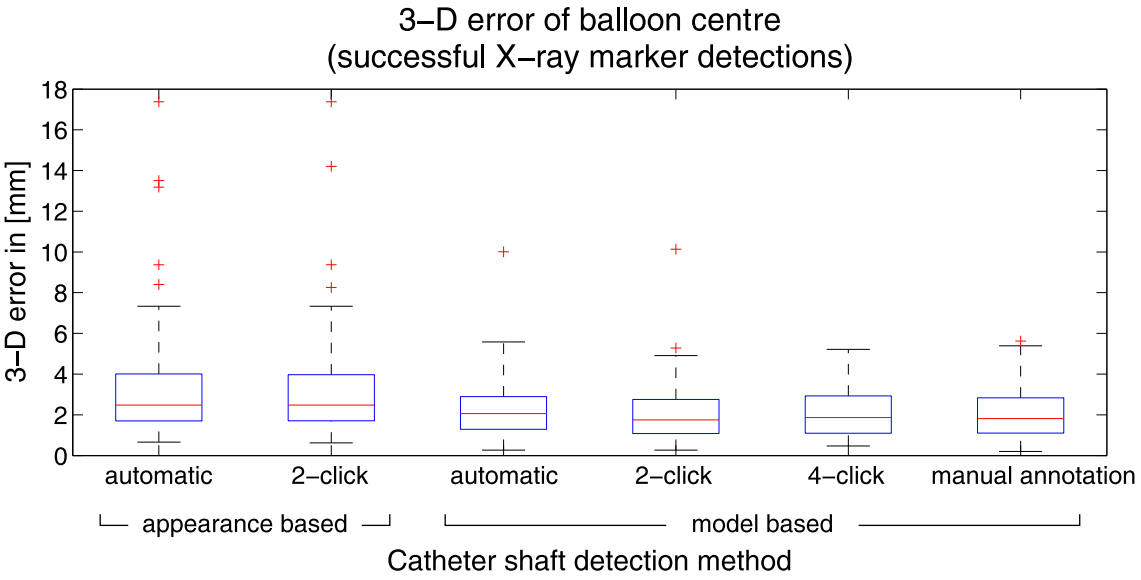

(a) Distribution of the 3-D error of the cryoballoon centre for 51 biplane image pairs in which automatic X-ray marker detection was successful

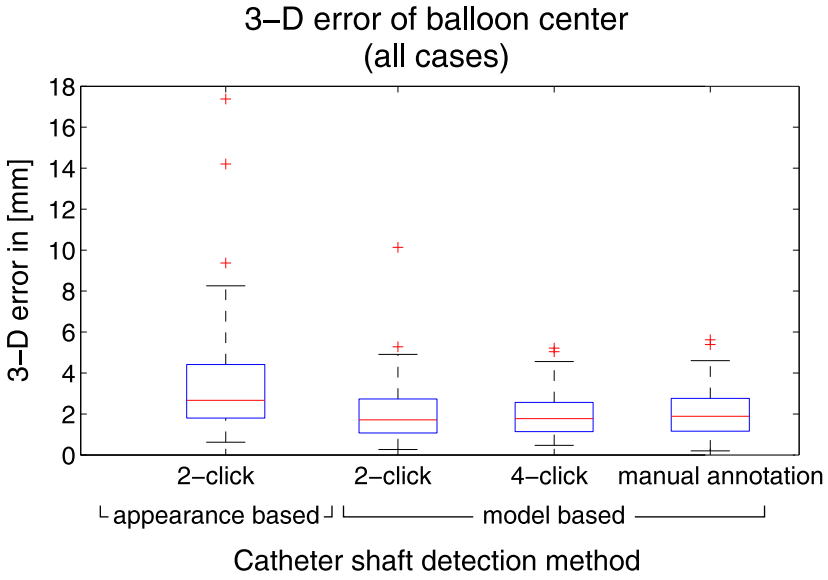

(b) Distribution of the 3-D error of the cryoballoon centre for all 62 biplane image pairs

Figure 5.9: Quantitative comparison of the reconstruction methods. The improvement of the model-based reconstruction compared to the appearance-based reconstruction was highly significant ($p<0.01$).

When comparing the appearance-based reconstruction to the respective model-based reconstruction methods, the improvement of model-based methods, both for the automatic and the 2-click method, was highly significant.

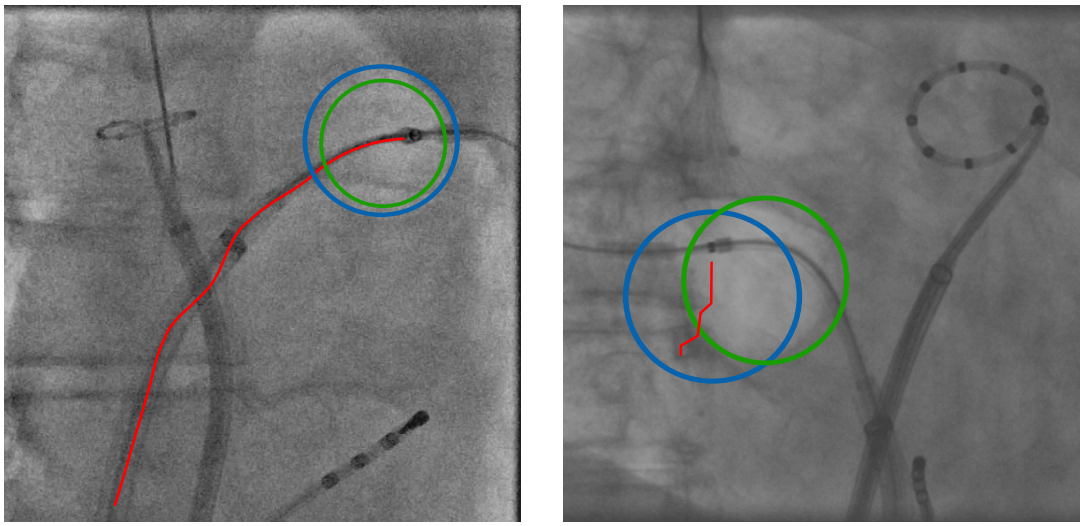

(a) successful reconstruction (b) failed reconstruction

Figure 5.10: Example reconstruction results. The forward projected boundary of the 3-D ground-truth cryoballoon obtained using [Klei 11] is shown in green, the result of the 0-click model based reconstruction is shown in blue. The reconstructed shaft is shown in red. In (a), the reconstruction of the cryoballoon was successful. Although the reconstruction of the shaft is slightly inaccurate, the balloon reconstruction is unaffected as the shaft part close to the balloon is reconstructed correctly. Note that the diameter of the green balloon reconstruction is smaller than the diameter specified by the manufacturer. The cryoballoon boundary's visibility depends on a change in X-ray density. For this density difference to become apparent, the X-ray path through the different material needs to be sufficiently long. At the sphere borders, the path length through the balloon is short. As a consequence, the balloon may appear smaller in X-ray projections than its actual size. Therefore, the method of Kleinoeder et al. [Klei 11] tends to underestimate the size of the cryoballoon. In (b) a failed reconstruction is displayed. Here, the the shaft (red) was not detected correctly.

5.5 Discussion and Conclusions

Our evaluation showed that the X-ray marker detection was successful in 82 % of all cases. The biplane images in which no X-ray marker was found often contained contrast agent around the area of the X-ray marker. This issue should be considered when integrating an automatic cryoballoon reconstruction method into the clinical workflow.

5.5.1 Discussion of the Appearance-Based Reconstruction

For the appearance-based detection and reconstruction, errors appeared mainly for images in which other catheters overlapped with the cryoballoon shadow or were close to it and introduced spurious edges this way. This also happened if contrast agent was flowing around the distal part of the balloon when verifying cryoballoon seal at the PV-ostia. In this case, contrast agent covered the distal part of the cryoballoon shadow in the fluoroscopic images.

We also tried a variant of the Hough transform where the radius was not fixed but part of the parameter space. The radius was then to be determined by the Hough transform in a range of ±2 mm around the nominal radius. However, the performance was not that good for the variable radius. As a conclusion, the available prior knowledge of the radius should be used.

Although it was obvious to combine the snake fitting and the enforcement of the elliptical shape in a joint optimization problem it turned out that a separation into two consecutive steps was required. It was tried to use a higher weight on the internal energy which favours elliptical shapes as well as a hard incorporation of the ellipse constraint in the parametrization of the snake [Delg 12]. With the images at hand, these approaches were not robust enough to deal with false positive boundary pixels which came from either ribs in front of the balloon or contrast agent. As a result, the snake optimization was stuck in a local minimum where the boundary was attached to, e.g., the border of a rib.

The runtime of the current implementation which is not optimized for speed is 1.8 s. A large part of the computation time is spent for active contour fitting. This runtime is sufficient for a single cathteter reconstruction, e.g., for documentation. If, however, a continuos reconstruction of the cryoballoon is required, dedicated tracking methods need to be developed which could use the appearance based reconstruction as initalization.

5.5.2 Discussion of the Model-Based Reconstruction

For model-based reconstruction, the X-ray marker is the central anchor of our method. Errors in the detection are propagated directly to the final reconstruction result. The errors introduced by the catheter detection are in most cases low as a comparison to the manual annotation shows. Even if the shaft detection has some errors, the impact on the cryoballoon reconstruction is in most cases small as they occur far away from the small part around the X-ray marker. Marking two points in the image helped only little to reduce outliers.

The source of the remaining error cannot be determined definitely. However, there are some explanations:

1. Model inaccuracy: The distance from the X-ray marker to the cryoballoon centre was measured with a standard deviation of 0.9 mm. This can be partly explained by annotation errors, i.e. the annotation was not always set exactly at the centre of the marker. On the other hand, there is also some variability of the distance due to the manufacturing process.

2. Deformation: In one case, the catheter was strongly bent in the cryoballoon region. The assumption that the balloon centre is on the catheter shaft was not valid in this case leading to an error of over 5 mm for all methods.

3. Reconstruction errors: The reconstruction method depends on the intersection of the catheter with the epipolar line to identify corresponding points in both images. If the catheter is parallel to the epipolar line, the intersection computation becomes numerically ill-conditioned. If small inaccuracies are present in

this case, the epipolar line intersects the catheter at a different position leading to wrong correspondences. In some cases even no intersection might be found. These small inaccuracies can be a result of the catheter detection process. As the biplane images are acquired sequentially with a small temporal delay, inter-frame cardiac motion may contribute to these inaccuracies as well.

To conclude, our model-based approach led to significantly ($p < 0.01$) better results compared to the appearance-based approach. Using the model-based approach, fully automatic cryoballoon reconstruction has shown to be possible with a 3-D accuracy of 2.5 $\pm$ 1.7 mm. If a higher accuracy is required, the user could mark the X-ray marker of the cryoballoon in each image plane. However, more user interaction does not necessarily lead to significantly better results. The mean 3-D error of 2.1 $\pm$ 1.5 mm for the two-click reconstruction is below a clinically relevant threshold of 3 mm [Bour 14]. So, this method may be considered for clinical use. Compared to a previous method [Klei 11], this method does not require the balloon boundary to be well visible. This is especially important for low-dose fluoroscopic images where the balloon may be more difficult to see. Our model-based approach offers another interesting option: thanks to the known balloon model, it is possible to simulate the cryoballoon position both in 3-D and in 2-D without actually inflating it.

Part II

Device-based Registration of the Left Atrium

CHAPTER 6

Registration Using Catheters Outside the Left Atrium

In this chapter, we present a method to register the 3-D LA model to fluoroscopic images based on devices placed in the vicinity of the LA. The devices are placed in the CS and the esophagus which can be segmented from the same volume as the LA. As the devices are also visible in the X-ray images, they can be used for registration. Parts of this chapter have been published at the BVM conference [Hoff 16g].

6.1 Motivation

At the beginning of a catheter ablation procedure, the CS catheter is placed in the coronary sinus. It serves as diagnostic catheter but is also used to stimulate the LA if required. The coronary sinus is a coronary artery that is located between the LA and the left ventricle. Although attached to the LA, there is relative motion between the CS and the PVs caused by respiration [Klem 07]. Moreover, the cardiac motion of the CS depends not only on the cardiac motion of the LA but also on the ventricular motion. The different motion of CS and LA influences a registration of the LA based on the CS. To this end, we want to investigate if the integration of second device can make the registration more robust.

The esophageal temperature probe is another device that may be placed in the esophagus. The esophagus runs along the back wall of the LA and ablating in this region with RF can result in an atrioesophageal fistula, i.e. a hole connecting the esophagus and the atrium [Good 05]. This is a severe complication which can lead to death [Calk 07]. To avoid the creation of esophageal fistula, physicians can place a temperature probe into the esophagus to monitor the temperature at the esophagus wall. If they see an increase in temperature, they can stop the ablation at the current spot.

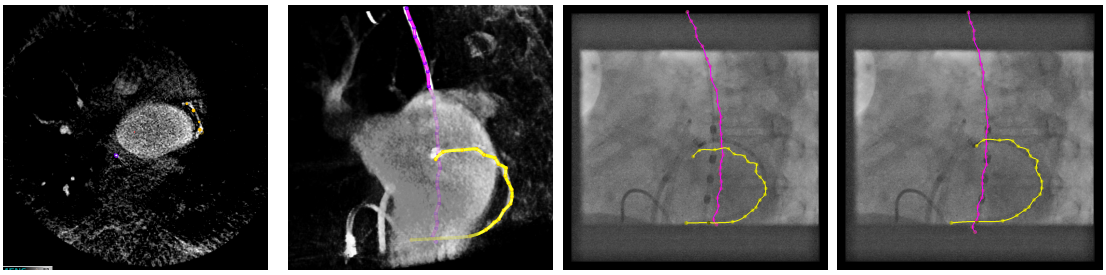

(a) (b) (c) (d)

Figure 6.1: (a) The coronary sinus (yellow) and the esophagus (purple) are annotated in a slice-view of the volume. (b) Annotated devices rendered together with the volume. (c) Devices segmented from volume overlaid to fluoroscopic images before registration and (d) after registration.

Compared to contrast-based registration presented in Part III, a registration based on these devices can be performed before the transseptal puncture such that the registered overlay can be used for guidance of the puncture. This can be helpful, especially for physicians with less experience [Bour 10, Bour 16]. Some physicians do not routinely inject contrast agent after the transseptal puncture. In this case, a contrast-based registration would imply a contrast injection just for the sake of registration. When using a device-based registration, the additional contrast injection can be avoided.

6.2 Related Work

Manual registration involving the CS has been evaluated by Bourier *et al.* using the CS only [Bour 10] or using a combination of spine, heart shadow and the CS [Bour 16]. Another approach for manual registration using the CS and catheters inside the LA was proposed by Knecht *et al.* [Knec 08]. It is referred to subsection 2.5.1 for more details on these manual methods.

A first automatic approach to registration of 3-D catheters to a single fluoroscopic image was proposed by Meyer and Wolf [Meye 99]. They used special catheters with transducers that enabled 3-D localization of catheters by means of sonomicrometry. The method required an accurate annotation of the 2-D position of each transducer in the image. The registration minimized the distance of projected 3-D transducers to their corresponding image locations.

Automatic registration using the CS was first proposed by Sra *et al.* [Sra 05]. An algorithmic description of an automatic registration method was given by Brost *et al.* [Bros 11b]. They used a rigid registration based on the iterative closest point algorithm (ICP) to align a CS catheter reconstructed manually from fluoroscopic images to a CS model segmented from an MRI volume.

6.3 Registration to Esophagus and Coronary Sinus

Our proposed method registers the centreline of the CS and the esophagus, extracted from a 3-D volume, to the respective centrelines computed from the X-ray images. The resulting transformation is also valid for the LA which is segmented from the same volume as the esophagus and the CS.

6.3.1 Acquisition of 3-D Catheter Shape

At first, the 3-D centreline of the esophagus $\mathcal{A}_{\mathrm{V}}^{3\text{-D}}$ and the CS $\mathcal{C}_{\mathrm{V}}^{3\text{-D}}$ needs to be segmented from a volume data set of the heart, either obtained with CT, MRI, or C-arm CT. To this end, the coronary sinus and the esophagus are marked manually in the slice images of the volume. The result can be verified visually in a volume rendering, see Figure 6.1.

Depending on the acquisition modality, the effort of segmenting the esophagus and the CS varies. A segmentation of the CS and the esophagus is straightforward for 3-D image data that was acquired intra-operatively using C-arm CT, with devices positioned both in the CS and the esophagus. This is because, the devices are well visible, e.g., in the axial slices, see Figure 6.1(a) and, as only the centreline of the anatomical structure is required, it is sufficient to locate the catheter itself.

If CT is used, the esophagus can be segmented automatically [Fies 08]. For manual segmentation, the esophagus may not be as clearly visible compared to C-arm CT since there is no temperature probe, yet. It still can be located as the neighbouring spine and aorta descendens provide means of orientation. Once the LA has been segmented from the volume, also the CS, which runs next to it, can be annotated.

Segmentation of the CS, however, becomes difficult if MRI is used as acquisition technique. Here, the visibility of the CS is often poor in commonly used acquisition protocols and it may only be possible to identify the first part of the CS. A description for manual segmentation of the CS in MRI images is given in [Bour 10].

As a second step, the 3-D shapes of the esophagus and the CS have to be computed within the C-arm coordinate system. To this end, two fluoroscopic images of the patient from two views, Plane A and Plane B, are acquired. Then, the user marks the tip of the CS catheter and of the esophageal temperature probe. Using the methods described in chapter 3 and chapter 4 the 3-D centreline $\mathcal{A}_{\mathrm{F}}^{3\text{-D}}$ of temperature probe and the 3-D centreline $\mathcal{C}_{\mathrm{F}}^{3\text{-D}}$ of the CS catheter is obtained.

As the catheter detection method expects the catheter to enter the image at the bottom border of the image, the method described in subsubsection 3.3.3 needs to be adapted slightly for the temperature probe detection. Instead of computing the shortest paths to all points in the lower 60% of the image, the paths from the marked tip to points in the upper 60% of the image need to be computed. Moreover, equation 3.4 needs to be changed to

$$a_{\mathrm{d}}(\mathcal{F}) = \sum_{t=1}^{|\mathcal{F}|} \left| \phi_{\mathcal{F}}(t) - \frac{+\pi}{2} \right| \quad , \tag{6.1}$$

to favour paths going upwards.

If neccessary, the resulting 2-D centreline can be corrected manually before automatic 3-D reconstruction.

6.3.2 Registration Using Iterative Closest Point Algorithm (ICP)

The 3-D curves of the volume, $\mathcal{A}_{\mathrm{V}}^{3\text{-D}}$ and $\mathcal{C}_{\mathrm{V}}^{3\text{-D}}$, are registered to the 3-D curves $\mathcal{A}_{\mathrm{F}}^{3\text{-D}}$ and $\mathcal{C}_{\mathrm{F}}^{3\text{-D}}$ computed from the fluoroscopic images using the ICP method [Besl92]. As the ICP is point-based, 10 to 60 3-D points were sampled from each curve, depending on their length.

For each point of the curves $\mathcal{A}_{\mathrm{V}}^{3\text{-D}}$ and $\mathcal{C}_{\mathrm{V}}^{3\text{-D}}$, a matching needs to be performed, i.e. the closest point sampled from the curves $\mathcal{A}_{\mathrm{F}}^{3\text{-D}}$ and $\mathcal{C}_{\mathrm{F}}^{3\text{-D}}$ is found. As each curve is labelled, either as esophagus or as CS, points from $\mathcal{A}_{\mathrm{V}}^{3\text{-D}}$ were matched only to points $\mathcal{A}_{\mathrm{F}}^{3\text{-D}}$ and points from $\mathcal{C}_{\mathrm{V}}^{3\text{-D}}$ only to points from $\mathcal{C}_{\mathrm{F}}^{3\text{-D}}$. As the number of points was small, exhaustive search could be applied.

The CS segmentation in the volume and the CS reconstructed from the fluoroscopic images may describe different, yet, overlapping parts of the CS. To compensate for this, matchings having a large distance between their points are rejected. The number of matchings omitted is defined by the rejection rate o. The value of o should correspond to the fraction of the reconstructed 3-D model that has no counterpart in the 3-D device segmented from voxel data.

Finally, the translation and rotation that minimizes the distance between both 3-D point sets is computed using SVD as described in [Besl92] and a next iteration is performed. The iteration number was set to 10, where a higher number of iterations could not substantially improve the registration results.

6.4 Experiments and Results

For evaluation, we used data from six different patients. Each patient data set comprised a C-arm CT volume (256× 256× 256 voxels, 0.92 mm/voxel) and a biplane image sequence (512 × 512 pixels, 0.43 mm/pixel) acquired directly after the C-arm CT. All data (3-D and 2-D) was recorded on an AXIOM Artis biplane C-arm system (Siemens Healthcare GmbH, Forchheim, Germany) under breath-hold and rapid pacing. The left atrium was acquired in five data sets, whereas the sixth data set included a right atrium.

A reference registration was performed for the first frame of the biplane sequence with respect to the contrast agent that was injected into the atrium. The 3-D shape of the anatomy in the volume was extracted by manually segmenting the catheters visible in the C-arm CT volume.

In clinical practice, the relative rotation between 2-D projection data and forward projected 3-D data of atria is very small and not perceivable in the fluoroscopic images and therefore typically ignored. In the experiments, we considered therefore only the 3-D translation error as in [Bros11b]. So, the error is calculated as the distance from the centre of gravity of the reference registration to the centre of gravity of the computed registration. Nevertheless, we tested robustness against rotation

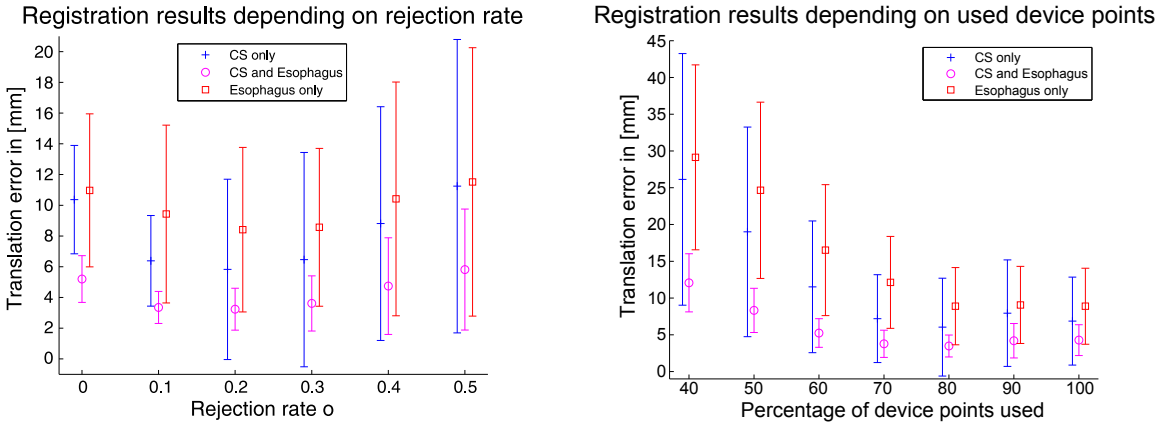

(a) (b)

Figure 6.2: 3-D registration translation error. (a) Regardless of the choice of o, the combination of CS and esophagus outperforms a registration based on only a single anatomical structure. For this figure, $k = 20\,\%$ of the reconstruction of the 2-D devices were neglegted. Note that results are best for $o = 20\,\%$ which corresponds to the value of k. (b) Results when using only a certain percentage of the catheter reconstructed from two 2-D images.

by using 30 different random initializations. The initialization involved a normally distributed translation and rotation with zero mean and standard deviations of 10 mm and 5 degree, respectively applied on x, y and z-axis.

Depending on the anatomy and the physician's preference, the CS catheter may or may not be introduced far into the CS. As a result, it may happen that only a shorter piece of the catheter is visible in the 2-D images. To evaluate the registration performance for devices introduced less far, we removed points from the device tip to reduce their lengths by a certain percentage k. Additionally, we investigated the impact of the parameter o on the registration performance.

The evaluation results for different values of the rejection rate o are shown in Figure 6.2(a), for a fixed length reduction $k = 20\,\%$ of the reconstructed catheters. Registration using both the CS and the esophagus outperformed registration using only one anatomical structure considerably. The best results were obtained for $o = 20\,\%$. In this case, the 3-D translational registration error was 3.2 ± 1.4 mm when relying on both CS and esophagus and 5.8 ± 5.9 mm when only the CS was used. These results when using CS and esophagus for registration were found to be significantly better compared to a registration based on the CS only according to Student's t-test. Evaluation results of the registration performance when using only parts of the catheters reconstructed from 2-D are shown in Figure 6.2(b). While the registration using the esophagus depends heavily on this percentage, the registration using the CS is less affected. Still, a combination of CS and esophagus is superior.

6.5 Discussion and Conclusions

Our experiments showed that a registration using the CS is possible for our C-arm CT data. For EP applications, an error of below 5 mm is required [King 09]. Our

results show that in this case the esophagus needs to be integrated into the registration as well. Although the esophagus alone is not well suited for finding a unique registration solution in head-foot-direction due to its line-like shape, see Fig. 6.2(b), it helps constraining the result in the transverse plane. This could be also achieved by including the spine into the registration procedure [Li 09, Bour 16]. Note, however, that the spine may only be partially visible depending on the detector size and C-arm angulation.

The accuracy depends on the fraction of the CS and the esophagus that was annotated and on the choice of the rejection rate o. The results generated from annotations shortened by k percent showed that o should be chosen such that it corresponds to the relative length of the parts which the 3-D segmentation and the 2-D annotation do not have in common.

In our data, only linear temperature probes were used. For spiral-shaped temperature probes, a spatial averaging with respect to the transverse plane might be required after 3-D reconstruction to obtain the esophagus centreline.

The way the data was acquired was well suited for device-based registration: The patients were fully anesthetized and intubated and both the C-arm CT and the following X-ray biplane images, were acquired under breath-hold and rapid pacing. Thus, there was almost no cardiac and respiratory motion between the volume and the X-ray images. A registration using image acquisition without rapid pacing would be more difficult as the position of the CS depends highly on the cardiac phase, i.e. the contraction of both the ventricle and the atrium. For patients suffering from AFib, this motion might be irregular.

The esophagus moves slowly, even within a procedure [Good 05]. As the fluoroscopic images were acquired directly after the volume, this motion could be neglected. If the volume would have been acquired, e.g., a day before, the error might have been larger.

As a conclusion, integrating the esophagus into device based registration improves results for data acquired using a C-arm CT setup. Having an esophagus model available could also be helpful, e.g., for re-registration which may be required during intervention. The improvement holds also for a less ideal fit which we generated by cutting parts of the catheter away, see Fig. 6.2(b). In future work, a study should be conducted to assess the accuracy of a registration based on multiple devices. In particular, the study should focus on the variety of clinical workflows including unpaced heart rhythm and free breathing.

CHAPTER 7

Registration Using Landmarks Inside the Left Atrium

In this chapter, we present a method for registration based on the cryoballoon position and the PV ostium annotation. Moreover, a method for the localization of ostia annotation is proposed. Parts of this chapter have been presented at the BVM conference [Hoff 16c] and a patent has been granted for this method [Hoff 16f].

7.1 Motivation

For the documentation of ablation procedures it is important to mark the locations where tissue was ablated. To this end, the position of the ablation catheter needs to be determined. Localization can be achieved by means of reconstruction as shown in Part I, ideally in combination with tracking [Wu 11], if applicable. Moreover, an accurate registration of the LA is required to relate the catheter position to the LA.

Having a good initial registration, e. g. using catheters outside the LA (chapter 6) or using a CA injection (Part III), is not sufficient as the LA is subject to external motion.

For RF based ablations, the dominant motion of the LA is caused by breathing and can be compensated by tracking the CM catheter [Bros 10b, Bros 12] or the CS catheter [Kapp 12]. The LA motion for cryoballoon based ablation is, however, different. The dominant motion is caused by the cryoballoon beeing pushed into the PV ostium. Moreover, the motion is no longer rigid as the LA is deformed, too.

This necessitates a re-registration of the LA. A registration based on anatomical landmarks as presented in chapter 6 is likely to fail due to the deformation of the anatomy in the region of the LA which invalidates the relations between anatomical

structures outside the LA and the position of the LA. Therefore, we propose a method that registers the cryoballoon to the PV ostium.

Parts of the computations required for this cryoballoon-based registration can also be used for an assisted annotation of the PV ostia. The PV ostia are important anatomic landmarks whose annotation is not only required for the registration approach presented in this chapter: For cryoballoon-based ablation, the cryoballoon model needs to be selected depending on the PV ostium diameter. This selection can be performed either by measuring the diameter of the ostium in the 3-D model or by using a tool which shows how well the PV ostium is covered by a cryoballoon [Klei 12]. Given an annotation of the PV ostia, the selection of the appropriate cryoballoon model could be automated. Moreover, other important numbers such as the ovality index [Schm 13] can be computed.

Currently, the ostia are often annotated manually in the model. This is a time-consuming task as it involves manual rotation and translation of the LA in the 3-D view to place the annotation points. A simplification of this step is also a prerequisite for the smooth integration of a method for automatic planning of ablation lines [Koch 14] into the current clinical workflow. A method for the selection of well suited C-arm viewing angles [Koch 15] requires annotations of the pulmonary vein ostia as well.

7.2 Related Work

Currently, to the best of our knowledge, there is no literature available that assesses the accuracy of a registration based on the cryoballoon and the PV ostium. However, the ostium is often used to verify the accuracy of registration, mostly by comparing the caudal drop of a catheter pulled back from the PVs to the anatomy outlined by the overlay [Tang 09, Knec 08].

For ostium localization, several approaches have been published so far: Recent segmentation approaches were designed such that the pulmonary veins are treated separately from the atrial body [Kari 09a, Zhen 11, Zhen 12]. Karim et al. [Kari 09a] proposed a three-step approach in which first, the complete LA is segmented using a manually placed seed point and an interactive bounding box. Then, within the LA, the atrial body is segmented and finally, based on a vesselness score, pulmonary vein centrelines are extracted and tracked to, e. g., measure the diameter interactively. Zheng et al. [Zhen 11, Zhen 12] use a model-based approach to segment the left atrial body, four PVs and the left atrial appendage (LAA). These parts are later merged together. However, the main focus of both approaches is on the overall segmentation accuracy of atrium and PV trunks but not on the precise location of the PV ostia. Rettmann et al. [Rett 09] presented a semi-automatic approach for PV ostium localization on a segmented volume. This method requires the user to manually click on each of the four pulmonary veins to compute a centreline. For each centreline point, the cross-section area of the PV is calculated and the first point where the cross-section area increases significantly is considered as ostium.

7.3 Registration to Pulmonary Vein Ostia

The key idea of this method is that the user indicates the PV to which the cryoballoon is currently attached. We assume that the cryoballoon is pushed as far as possible into the PV and that an annotation of the ostium is available. Our method finds a position at the corresponding PV ostium such that the diameter of the mesh at this position corresponds to the diameter of the cryoballoon. Our method comprises the following steps: (i) Skeleton generation, (ii) Cryoballoon reconstruction and (iii) Cryoballoon registration.

We continue by describing the methods for skeletonization and registration. For cryoballoon reconstruction, we use the procedure described in chapter 5.

7.3.1 Mesh Skeletonization

We compute the skeleton for the complete left atrium and not for individual pulmonary veins indicated by the user as in [Rett 09]. This has the advantage that the centrelines can be computed prior to the procedure, after the pre-operative 3-D scan. Moreover, having a complete skeleton later facilitates the detection of PV ostia. We decided for the skeletonization method by Telea *et al.* [Tele 12]. This method comprises two steps that are described below very briefly.

First, the original 3-D LA mesh $M = (V_M, E_M), V_M \subset \mathbb{R}^3, E_M \subset V_M \times V_M$ is transformed into a so-called surface skeleton. This is a 2-D manifold consisting of all points which are centre of spheres inscribed by the mesh: Along the normal of a surface vertex, spheres of decreasing size that are touching the surface vertex are generated. The size of the sphere is decreased iteratively until only two points are touching the surface: The surface vertex and a second contact point. The resulting sphere centres form a 3-D point cloud. Based on the corresponding surface vertices and their associated second contact points, the topology of the point cloud is inferred from the structure of the original 3-D mesh, resulting in a 2-D manifold. An example of such a surface skeleton is given in Figure 7.1(b)

In a second step, the 2-D manifold is iteratively shrunk until a 1-D manifold, the curve skeleton $M_C = (V_C, E_C)$ is reached. The shrinking direction is defined for each point by an implicit gradient field on the surface skeleton. This gradient field is computed based on the geodesic distance on the mesh from each surface vertex to the second contact point associated with the corresponding inscribing sphere, see [Tele 12] for details. The gradient field has singularities at the positions of the curve skeleton, hence, the points of the 2-D manifold converge to the curve skeleton.

As the LA mesh is not as smooth as the examples used in [Tele 12], our implementation differs at some points to the algorithm described in [Tele 12]. First, Laplacian smoothing is performed after each shrinking step to maintain a smooth surface. Moreover, the maximum number of iterations of the shrinking step was set to 50 which is more than suggested in [Tele 12]. Still, the result of the shrinking step is not a clear 1-D manifold but reveals 2-D structures, see Figure 7.1(c). When using a higher iteration number, these structures would collapse, too. As a drawback, the shape of the remaining curve skeleton would become also smoother and would no longer represent the LA structure well.

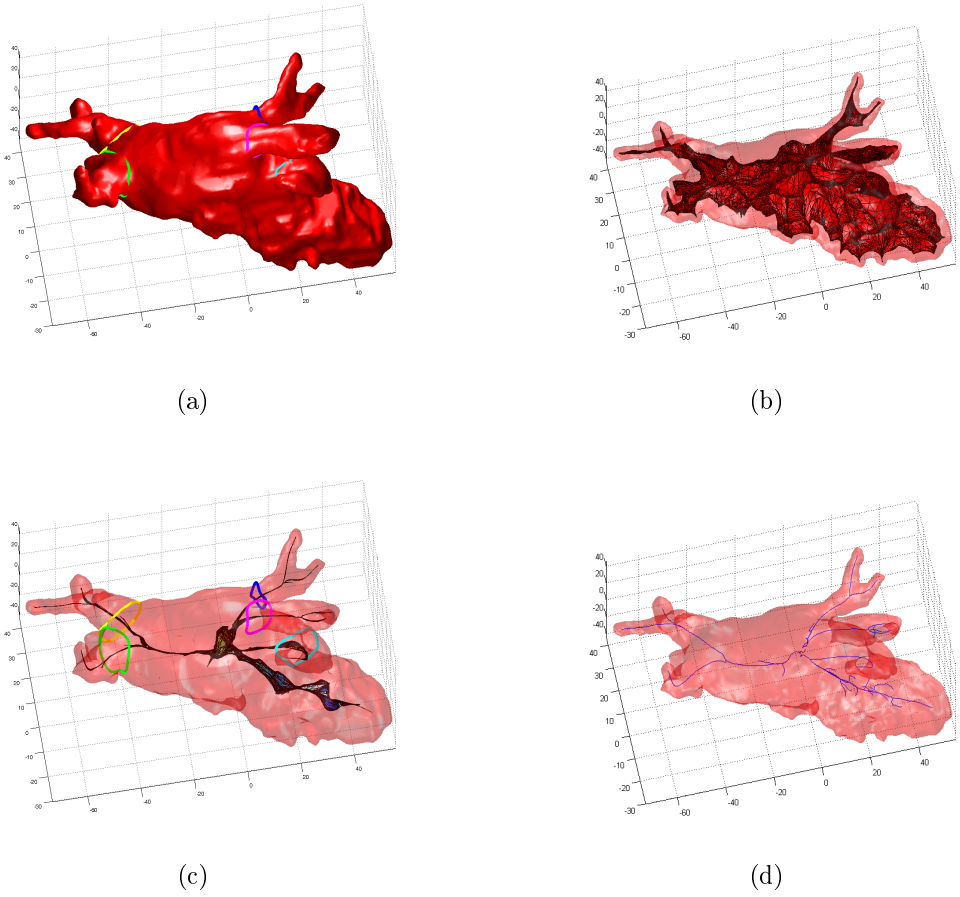

(a) (b)

(c) (d)

Figure 7.1: (a) LA with annotated ostia and left atrial appendage (cyan). (b) Surface skeleton of the LA. (c) Curve skeleton obtained by iteratively moving points of the surface skeleton along an implicitly defined vector field. (d) Splines representing the main structure of the curve skeleton

Our goal is to model the curve skeleton explicitly by a small number of cubic splines. We therefore seek a subset of points and edges of this curve-skeleton mesh defining an abstract graph structure which allows to extract the main lines along this mesh. To this end, a shortest path tree $\mathcal{T}'$ on M_C is computed. The root of $\mathcal{T}'$ is defined to be the 3-D point $\boldsymbol{r} \in V_C$ that is closest to the centre of gravity of the points V_M of the original mesh M, i. e.

$$\boldsymbol{r} = \arg\min_{\boldsymbol{r}' \in V_C} \left\| \boldsymbol{r}' - \frac{1}{|V_M|} \sum_{\boldsymbol{w}' \in V_M} \boldsymbol{w}' \right\|_2 . \tag{7.1}$$

We then select from $\mathcal{T}'$ the main branches. This is done in an iterative way by creating a new tree $\mathcal{T}$ to which new branches are added successively. In each iteration, the longest branch of $\mathcal{T}'$ is selected and added to $\mathcal{T}$ as a first step. Then, all branches in $\mathcal{T}'$ with a leaf node closer than 3 mm to the selected branch are removed to get rid of duplicate branches that provide no additional information. The value of 3 mm corresponds to the usual pulmonary vein diameter at the distal end of the LA mesh. This is repeated until $\mathcal{T}'$ is empty.

After removing very short branches, each path from a leaf in $\mathcal{T}$ to the root $\boldsymbol{r}$ is transformed into a cubic spline curve. The curve is defined as $\mathcal{V}(t) \rightarrow \boldsymbol{w} \in \mathbb{R}^3$ where t is the distance along the spline to the centre $\boldsymbol{r}$ of the LA and $\boldsymbol{w}$ denotes the 3-D coordinate in a coordinate system centred at the LA centre of gravity. An example of resulting skeleton splines is given in Figure 7.1(d).

7.3.2 Cryoballoon Registration

Once the spline representation of the skeleton is computed, the physician needs to indicate the ostium in which he has pushed the cryoballoon. In the next step, a spline curve corresponding to the associated ostium annotation is determined. As the shape of the ostia is simple, a point-in-polygon algorithm [Berg 08] is not required. Instead, the centre of gravity of the ostium annotation is computed. The spline closest to this centre of gravity is determined as corresponding spline $\hat{\mathcal{V}}$.

From the spline $\hat{\mathcal{V}}$ we sample points $\hat{\mathcal{V}}(t)$ equidistantly and compute the radius $r_{\mathrm{PV}}(\hat{\mathcal{V}}(t))$ of the PV: As the PV cross-section may be rather elliptical than circular [Witt 03, Haus 08], we first compute the cross-section plane defined by the point $\hat{\mathcal{V}}(t)$ and its normal vector $\nabla\hat{\mathcal{V}}(t)$. Then we compute the intersection of the mesh with this plane. In most cases, the plane will intersect the mesh not only at the PV of interest but also at other structures. To suppress the other structures, a set of circular sectors around $\hat{\mathcal{V}}(t)$ is established in the intersection plane. The point closest to $\hat{\mathcal{V}}(t)$ in each sector is considered as a point corresponding to the PV of interest.

Based on the distances to these points, we select the median distance as the PV radius $r_{\mathrm{PV}}(\hat{\mathcal{V}}(t))$. Afterwards, a spatial median filtering is applied to the radii along the PV. Given the radius r of the cryoballoon, the position of the cryoballoon in the LA coordinate system is determined as

$$\hat{\mathcal{V}}(\hat{t}), \quad \hat{t} = \max t' \quad \text{such that} \quad r_{\mathrm{PV}}(\hat{\mathcal{V}}(t')) < r. \tag{7.2}$$

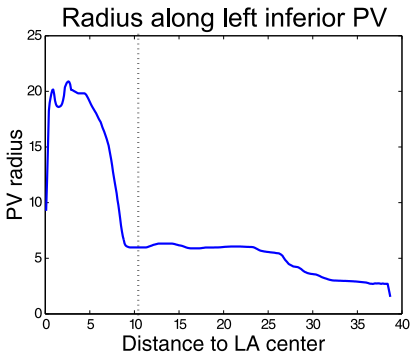

Figure 7.2: Radius of the pulmonary vein with respect to the distance to the LA centre. The dotted line indicates the position of the PV ostium.

Table 7.1: Features used for ostium classification

Feature for point ($\mathcal{V}(t)$)	Description
$r_{\mathrm{PV}}(\mathcal{V}(t')), t' \in \{t-7, t-6, \ldots t+1\}$	Radius at position $\mathcal{V}(t)$ and its vicinity
$\frac{\mathrm{d}r_{\mathrm{PV}}(\mathcal{V}(t'))}{\mathrm{d}t'}, t' \in \{t-7, t-6 \ldots t+1\}$	Radius increase at position $\mathcal{V}(t)$ and its vicinity
$\max_{t'>t} r_{\mathrm{PV}}(\mathcal{V}(t'))$	Maximum radius in distal direction
$\min_{t'<t} r_{\mathrm{PV}}(\mathcal{V}(t'))$	Minimum radius in proximal direction
$\mathcal{V}(t)$	3-D position
$\nabla\mathcal{V}(')$	Direction of PV
t	Distance to the LA centre

Given the cryoballoon centre $\boldsymbol{c}$ in the world coordinate system, the registration transformation vector $\boldsymbol{t}$ is then defined by

$$\boldsymbol{t} = \boldsymbol{c} - \hat{\mathcal{V}}(\hat{t}). \tag{7.3}$$

7.4 Localization of Pulmonary Vein Ostia

In this context, we also investigated how reliably PV ostia can be localized on a mesh representation of the LA. Our approach is a learning based method that relies on features derived from the PV splines $\mathcal{V}$.

The most important feature that we use is the radius $r_{\mathrm{PV}}(\mathcal{V}(t))$ of the PV at the 3-D position $\mathcal{V}(t)$. The PV ostium is characterized by an increase of the diameter towards the LA centre, see Figure 7.2. Therefore, we use not only the radius at t as a feature to classify whether an ostium is located at position $\mathcal{V}(t)$, but also the radii

$$r_{\mathrm{PV}}(\mathcal{V}(t')), \quad t' \in \{t-7, t-6, \ldots t+1\} \tag{7.4}$$

in the neighbourhood. To capture the increase of the diameter, also the derivatives of the radius in the vicinity of $\mathcal{V}(t)$ are used as features.

To make sure that the large increase at position $r_{\mathrm{PV}}(\mathcal{V}(t))$ is not due to a local minimum of the PV diameter, we add the maximum radius in distal direction as feature. To distinguish the PV ostium from a local widening, e.g., caused by merging of two smaller veins, the minimum radius in proximal direction is also considered as feature. Additional features are described in Tab. 7.1.

For each point along the splines representing the branches of the curve skeleton, the set of features is computed. A decision tree is used to classify the set $\mathcal{M}$ of points

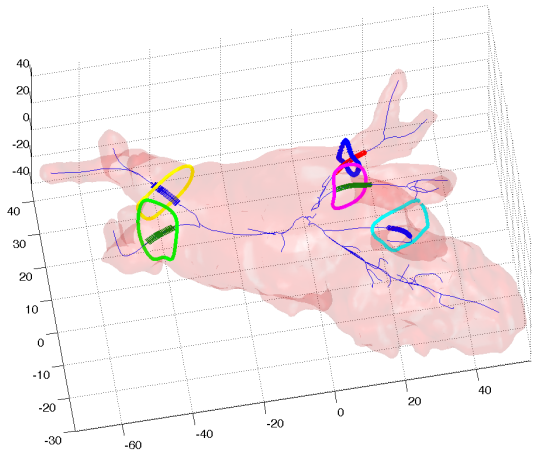

Figure 7.3: LA skeleton (blue lines) with positions classified as belonging to a PV ostium. These positions are coloured according to the clustering result. Additionally, the ground truth annotations of LAA (cyan circle) and PV ostia (other circles) are shown.

that belong to an ostium. In a second stage, this group is split up to points $\mathcal{M}_{\text{left}}$ belonging to a left PV ostium and points $\mathcal{M}_{\text{right}}$ of right PV ostia using, again, a trained classifier. Clustering of the points is performed based on a connected components approach considering all points with a distance below a threshold as connected. An example of this clustering is shown in Figure 7.3. Then, the largest cluster on the right side is considered as first right PV. All points in $\mathcal{M}_{\text{right}}$ that are distal, i.e., behind this cluster are removed from $\mathcal{M}_{\text{right}}$. Then the largest remaining cluster is considered as the other right PV ostium. This procedure is similarly performed for the left side. However, three clusters are extracted here to also find the place where the left atrial appendage (LAA) joins the atrium.

7.5 Experiments and Results

We evaluated our proposed method for cryoballoon-based registration qualitatively by comparing the results visually to a registration based on initial contrast injection. To this end, a LA mesh of a patient was segmented from MRI volumes using InspaceEP (Siemens Healthcare GmbH, Forchheim, Germany). The four PVs were annotated manually and a manual contrast-based registration was performed. We overlaid the LA onto the X-ray images showing the cryoballoon in the respective PV using the registration obtained by our method and the contrast-based registration. The resulting images for a cryoballoon placed in the left inferior PV are shown in Figure 7.4 to Figure 7.7.

A quantitative evaluation of the cryoballon registration requires a ground truth registration. As the cryoballoon pushes the LA from its natural position, a manual reference registration based on surrounding anatomical structures is not possible. For a contrast-based registration, the CA injected behind the cryoballoon to detect leakage is not sufficient. Therefore, an additional CA injection just for establishing a reference registration would have been required. As CA is harmful for the patient, this was not an option for ethical reasons.

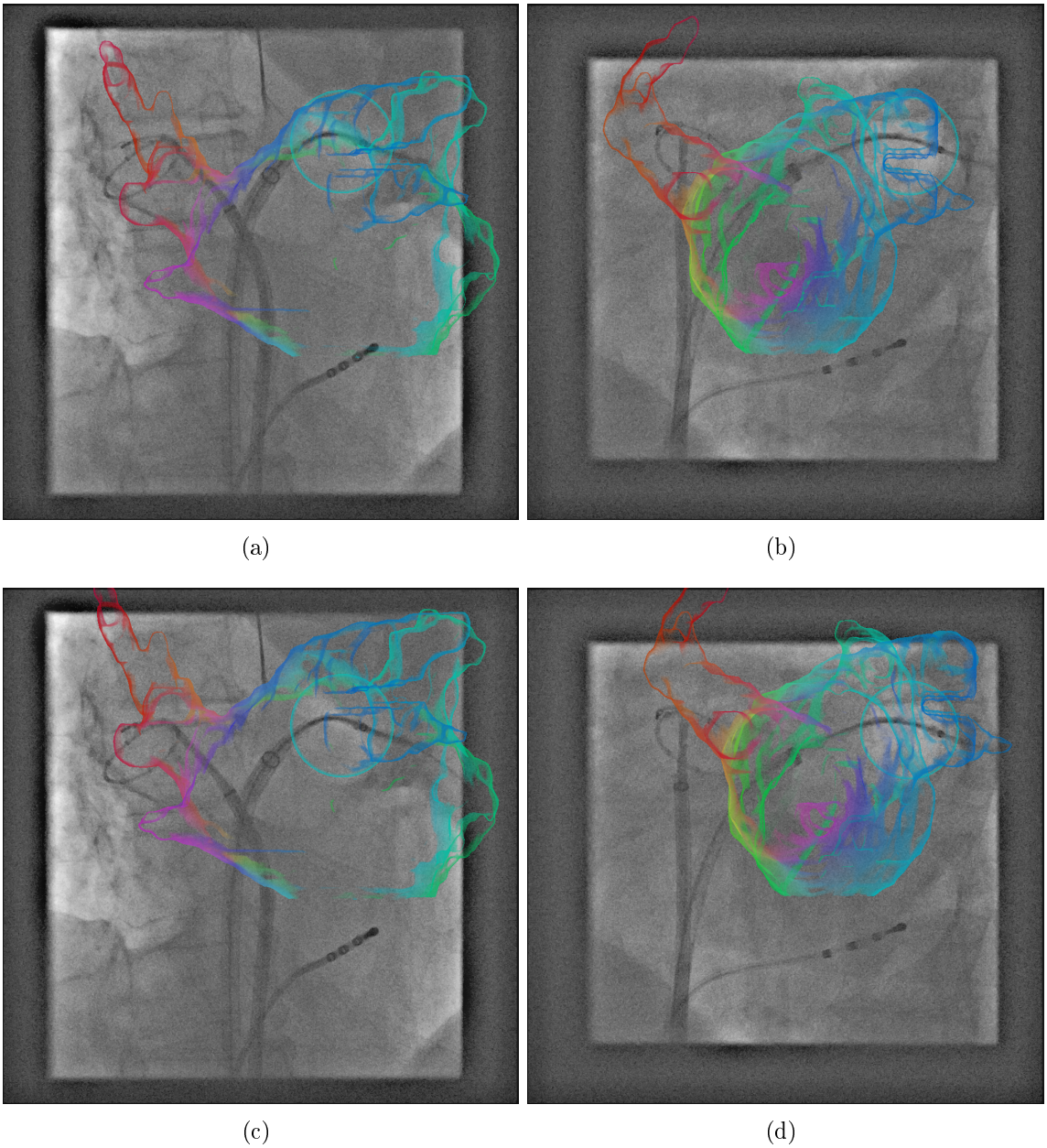

(a) (b)

(c) (d)

Figure 7.4: Registration results with a cryoballoon in the left inferior PV. The top row shows the registration result based on the initial contrast injection, the bottom row shows the corresponding registration result using the cryoballoon. The left and right columns show view A and view B, respectively.

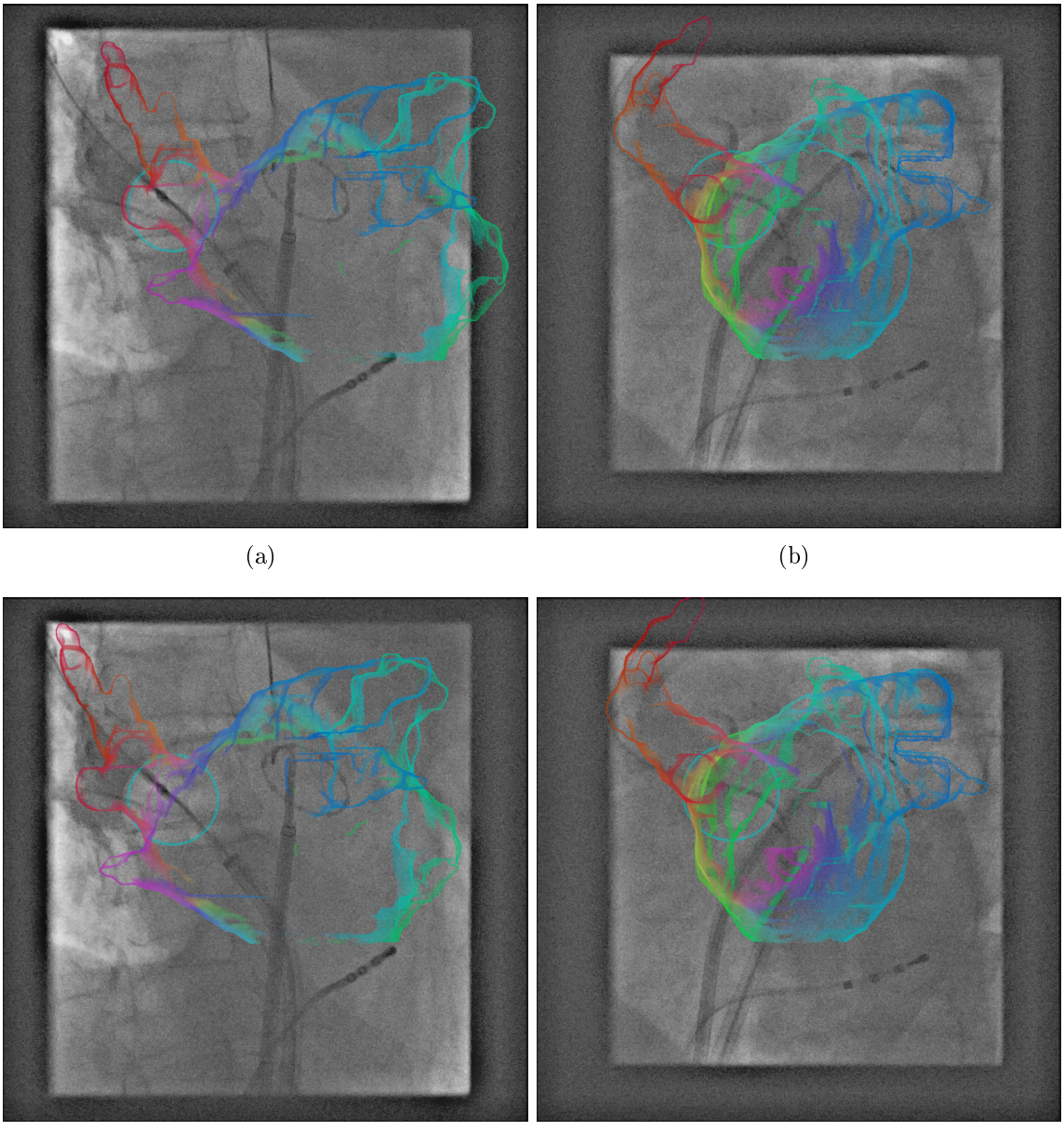

(a) (b)

(c) (d)

Figure 7.5: Qualitative results of cryoballoon based registration for the right superior PV

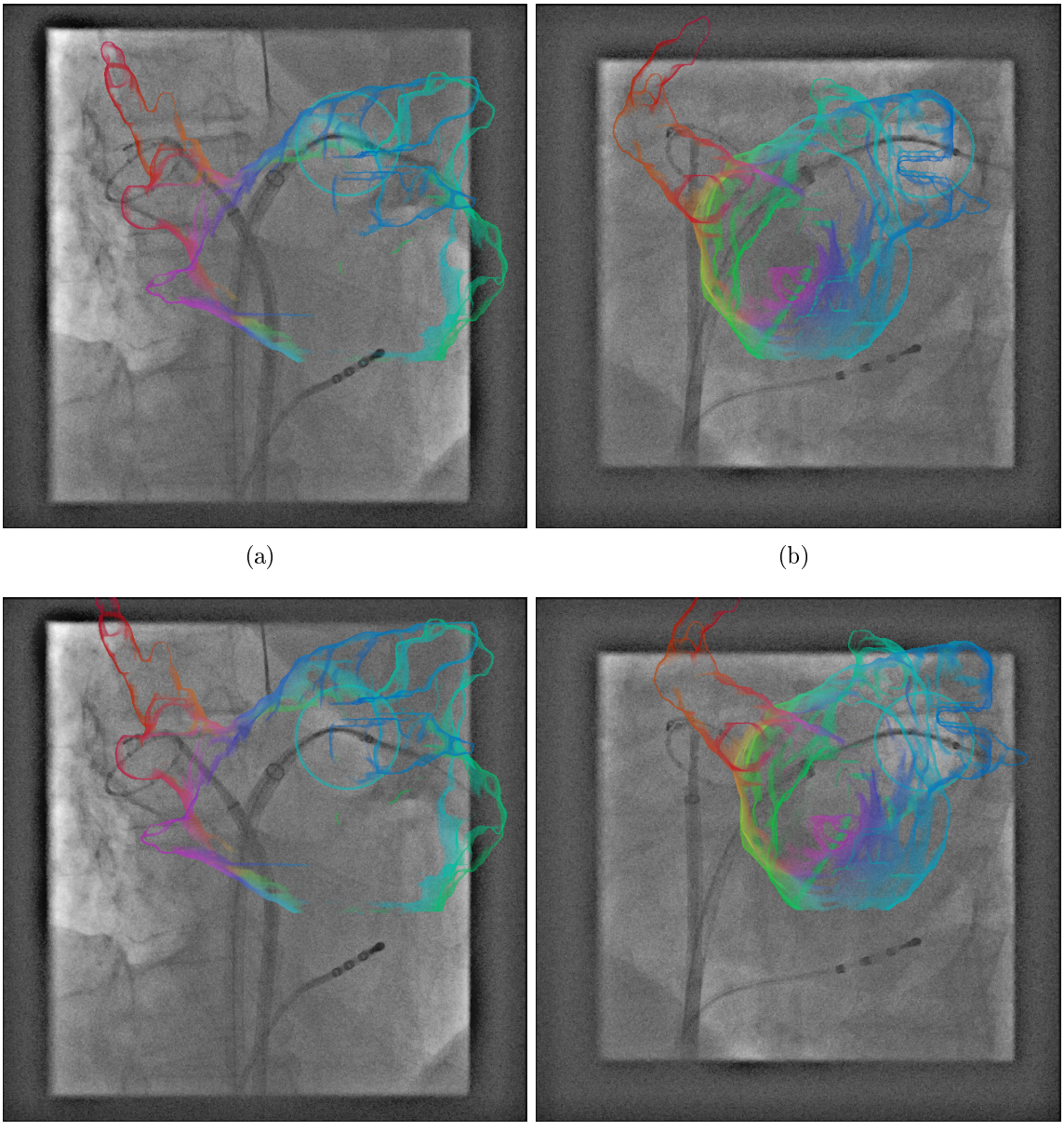

(a) (b)

(c) (d)

Figure 7.6: Qualitative results of cryoballoon based registration for the left inferior PV

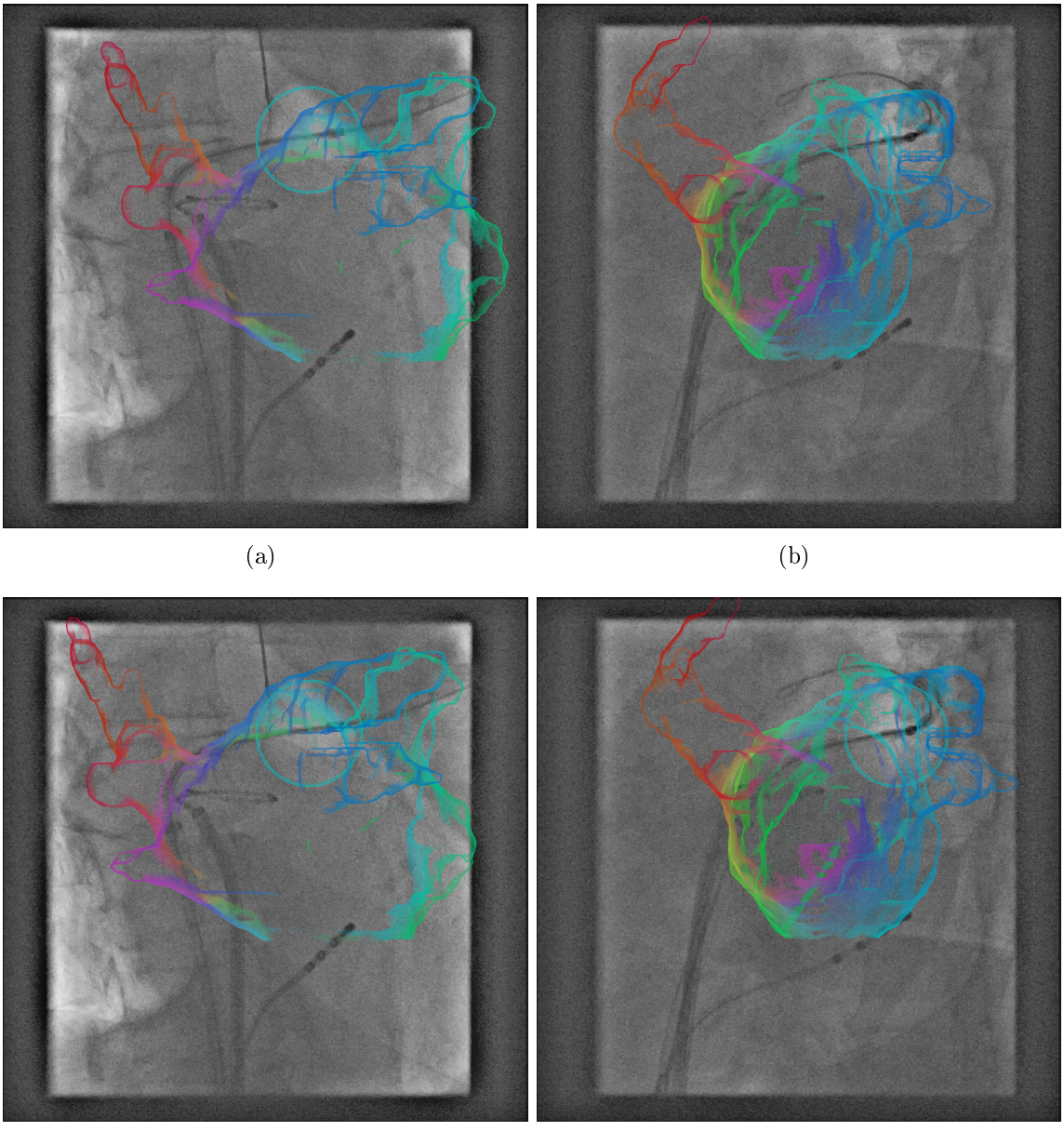

(a) (b)

(c) (d)

Figure 7.7: Qualitative results of cryoballoon based registration for the left superior PV

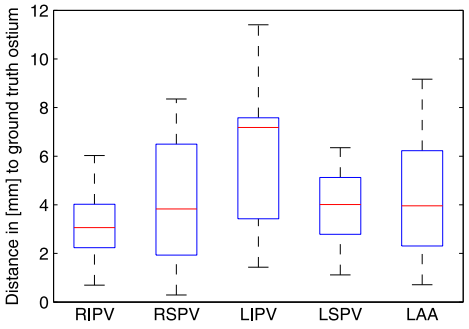

Figure 7.8: Detection results grouped for right inferior and superior vein (RIPV and RSPV, respectively), left inferior and superior vein (LIPV and LSPV, respectively), and the left atrial appendage (LAA).

We evaluated the extraction of PV ostia based on nine left atrium meshes from different patients. These meshes were all segmented from MRI volumes using InspaceEP (Siemens Healthcare GmbH, Forchheim, Germany). The PV ostia were annotated by a physician; if a LAA was present in the 3-D mesh, it was annotated by an expert. The data comprised in total 36 PV ostia and 8 LAA annotations. Training of the classifier and evaluation was performed as a leave-one-out cross-validation. We used the MATLAB implementation of the decision tree for the classifier. As a position error measure, we used the distance of the detected ostium centre to the regression plane defined by the ground truth ostium annotation. A detection of a single ostium is counted as unsuccessful if for a PV no cluster was left or if the selected cluster is not located on a PV or the LAA. In our evaluation, we achieved a success rate of 86%. The mean error was 4.3 ± 2.6 mm. The errors for each PV are shown in Figure 7.8.

7.6 Discussion and Conclusions

7.6.1 Cryoballoon-based Registration

The LA overlay images resulting from the cryoballoon registration reflect a cryoballoon position that appears plausible with respect to the cardiac anatomy and the clinical workflow. Although the actual position of the cryoballoon is not known, it can be stated that the results of the cryoballoon-based registration are better than the results of the contrast-based registration. This is illustrated in Figure 7.4. Here, the cryoballoon is placed in the left inferior PV. The contrast-based registration in Figure 7.4 (a) and (b) results in an overlay where the balloon appears to be in the left superior vein. For the cryoballoon-based registration, however, the balloon is shown at the ostium of the left inferior vein.

When comparing Figure 7.4 (b) and (d) it is apparent that the motion comprises not only is not only in superior-inferior direction, as the LA is shifted not only upwards but also to the right. Hence, approaches that compensate breathing motion based on the diaphragm [Cao 12] can only compensate parts of the motion.

The deformation induced by pushing the cryoballoon into the PV ostium is very strong. Therefore, the assumption of rigid motion is no longer valid which can be seen in Figure 7.4 (d): The LA is pushed so strongly towards the right image border that, based on a rigid transformation, the CM catheter is no longer inside the LA.

The distance between CS catheter and the LA in the overlay does not resemble the patient's anatomy either.

As a consequence, methods based on the CM catheter [Bros 10b, Bros 12] or the CS catheter as the method proposed in chapter 6 or in [Kapp 12, Ma 10, Ma 13, Bros 11b] cannot be used as an alternative since they focus on the anatomy at the position of the respective catheter. This also raises the question whether our approach based on a rigid transformation is applicable in clinical practice. We believe that the results based on a rigid registration are useful as the region of interest at this point of the procedure is the respective PV ostium such that deformation errors at other parts of the LA are negligible. Deformation errors that might have an impact on the registration at the ostium may, however, arise as the PV is flexible and the balloon may be pushed farther into the PV, i. e. beyond the point where the PV diameter matches the balloon diameter. The flexibility of the PV at this point needs to be examined in a clinical study. In this context it could also be determined how large the registration error is and if this error can be compensated by selecting a point on the PV with a slightly smaller diameter as the registration target.

7.6.2 Extraction of the Pulmonary Vein Ostia

A comparison with the segmentation methods [Kari 09a, Zhen 12] is difficult. They report how well the PV was segmented but not the accuracy of the PV ostium localization. Rettman *et al.* [Rett 09] reported a mean error of 1.5 mm to 5.0 mm, depending on the PV. These results are slightly better than ours, however, they require user input whereas our method was designed to be fully automatic. Misdetections happened mostly because the LAA was not detected correctly. In one case, the right PVs merge so early that this patient could be considered to have a common ostium. In this case, only one of the two right PVs was detected.

The average accuracy is below the 5 mm threshold which is considered relevant for LA registration [King 09]. When considering the found error, it is important to know that there is no exact definition of the PV ostium position [Haus 08]. So, the required accuracy for ostium and LAA annotation could be determined by studying the inter-user-variability of physicians. In any case, the result can serve as initialization that can be refined manually, if necessary.

Part III

Contrast-based Registration of the Left Atrium

CHAPTER 8

Classification of Contrasted Frames in a Fluoroscopic Sequence

In this chapter, we present a method for detecting contrast agent in LA angiographies and compare it to two other methods for contrast agent detection. Our method is a learning based method and generalizes better for unseen data than previous approaches based on a single threshold. Parts of this chapter were also published at the BVM conference [Hoff 15].

8.1 Motivation

When angiographies are acquired, is injected into the vasculature while X-ray images are acquired. If only vessels are about to be imaged, the background can be removed by subtracting from an uncontrasted mask image $\boldsymbol{I}_\mathrm{u}$ an image $\boldsymbol{I}_\mathrm{c}$ filled with contrast agent. This procedure is called digital subtraction angiography (DSA) [Brod 82] and the corresponding DSA image is denoted by

$$\boldsymbol{I}_\mathrm{DSA} = \boldsymbol{I}_\mathrm{u} - \boldsymbol{I}_\mathrm{c}{}^{1}. \tag{8.1}$$

Subtraction based on a single acquisition can be obtained by either estimating the background using inpainting methods [Unbe 16] for small structures, e.g., coronary arteries or using energy decomposition [Mull 16]. Modern C-arm systems have a dedicated DSA imaging mode where first the mask image $\boldsymbol{I}_\mathrm{u}$ is acquired followed by an acquisition of the contrasted image. In this mode, the imaging parameters are

[1] Using this notation, contrast agent appears bright in the subtraction images. It is, however, also possible to subtract the uncontrasted image from the contrasted one, i.e., $\boldsymbol{I}_\mathrm{DSA} = \boldsymbol{I}_\mathrm{c} - \boldsymbol{I}_\mathrm{u}$.

kept the same for both acquisitions such that the background cancels out as a result of the subtraction. Moreover, the subtraction is performed on the logarithm of the raw images to conform with the X-ray attenuation physics.

In our case, however, the manual contrast-based registration is performed based on angiographic sequences which were not acquired using the DSA acquisition mode. Our automatic contrast-based registration described in chapter 9 requires that the contrast agent is extracted by means of DSA. Subtraction images can be generated from an angiographic sequence if the sequence contains both contrasted and uncontrasted frames, i.e., if the acquisition is started before contrast is injected. We denote the angiographic sequence as sequence $\boldsymbol{I}_k$, $k = 1, \ldots, n$, of n fluoroscopic images. Given a frame $\boldsymbol{I}_\mathrm{u} = \boldsymbol{I}_j, j < n$ known to be acquired prior to the contrast injection, the DSA image for a following frame $l, l > j$ is then given by $\boldsymbol{I}_{\mathrm{DSA},l} = \boldsymbol{I}_\mathrm{u} - \boldsymbol{I}_l$.

As the goal of this thesis is to automatize registration as much as possible, an automatic detection of contrasted frames in a sequence is desired.

8.2 Related Work

An automatic detection of the first contrasted frame in an LA angiography has been proposed by Zhao *et al.* [Zhao 13]. In this work, a Difference Digital Subtraction Angiography (DDSA) $\boldsymbol{I}_{\mathrm{DDSA},k}$ is calculated by subtracting two neighboring fluoroscopic frames to estimate how the amount of contrast agent changes.

$$\boldsymbol{I}_{\mathrm{DDSA},k} = \boldsymbol{I}_{\mathrm{DSA},k} - \boldsymbol{I}_{\mathrm{DSA},k-1} = -\boldsymbol{I}_k + \boldsymbol{I}_{k-1}.^{2} \tag{8.2}$$

A threshold T_Z, determined e.g. by a training step, is applied to $\boldsymbol{I}_{\mathrm{DDSA},k}$ to detect the region with newly contrasted pixels. The number of pixels $\boldsymbol{p}$, with $\boldsymbol{I}_{\mathrm{DDSA},k}(\boldsymbol{p}) > T_\mathrm{Z}$ is denoted by n_k. Given a second threshold value N_pixel, the first frame with $n_k > N_\mathrm{pixel}$ is taken as the first contrasted frame. The value of N_pixel was empirically set to 1000 in a 256×256 image, i.e. 1.53% of the image size.

Another approach was proposed by Condurache et al. [Cond 04] for detection of contrast agent injections in coronary artery angiographies. Here, vessel-like structures in the image are highlighted using a tophat-filter [Doug 92]. Then, the 98-percentile value $p_{98}(\boldsymbol{I}_k)$ of the pixel intensities is computed for each frame k and a temporal averaging is performed on these values. The distribution of $p_{98}(\boldsymbol{I}_k)$ in uncontrasted images in this sequence is modeled as a Gaussian $\mathcal{N}_0(\mu_0, \sigma_0^2)$. The values of μ_0 and σ_0 are estimated using frames which are known to be uncontrasted. Based on the concept of a significance test, the authors compute a threshold $T_\mathrm{C} = \mu_0 + l \cdot \sigma_0$. A frame k is considered to be contrasted if $p_{98}(\boldsymbol{I}_k) > T_\mathrm{C}$.

Liao *et al.* [Liao 13] proposed a different approach for angiographies of the aortic root. In this approach, DSA images are computed for each frame of the sequence. $\boldsymbol{I}_\mathrm{u}$ is set to the average of the first frames which are assumed to be uncontrasted. To reduce global intensity changes caused by the automatic exposure control of the X-ray system, a histogram matching is performed. First, the frames presumably containing maximum contrast agent are identified based on the difference between

[2] In [Zhao 13], the notation $\boldsymbol{I}_\mathrm{DSA} = \boldsymbol{I}_\mathrm{c} - \boldsymbol{I}_\mathrm{u}$ was used. The following equations where therefore adapted accordingly.

the percentiles p_5 and p_{75} of the DSA images. An aortic root model is then registered to these frames and the histogram within the region covered by the aortic root model is analysed over time by comparing the histogram of a frame k to reference histograms of presumably contrasted and known uncontrasted frames. If the similarity curve contains no distinct peak, the sequence is considered as uncontrasted, otherwise the sequence is classified as showing a contrast injection. This method is very complex but distinguishes only between contrasted and uncontrasted sequences and classifies not on a per-frame level.

8.3 Feature-based Contrast Classification

Our goal was to find a simple method for per-frame classification that does not rely on heuristically found thresholds. To this end, we combined several features which are partially derived from the methods by Zhao and Condurache using a linear Support Vector Machine (SVM) [Vapn 13].

After removing the parts of the image which are covered by shutters, the first set of features is computed. It is based on pixel intensity percentiles as proposed by Condurache *et al.* [Cond 04]. As the tophat filter used in [Cond 04] is not suited to enhance the contrasted area of the LA, the contrasted parts are extracted using subtraction images $\boldsymbol{I}_{\mathrm{DSA},k}$ with $\boldsymbol{I}_0$ as reference frame. The underlying assumption is that the acquisition always starts before the contrast injection such that the first frame is uncontrasted. Moreover, we rely not only on the 98-percentile p_{98}, but used a set of 15 percentiles $p_i, i \in \{0, 2, 5, 10, 20, \ldots, 80, 90, 95, 98, 100\}$ of DSA images. As the percentile values vary strongly at the borders, the range at the bottom and at the top is sampled more densely. These features for frame k are denoted by f_1^k to f_{15}^k. Values of the percentiles for a sample sequence are given in Figure 8.1.

We added also features proposed by Zhao et al. [Zhao 13] based on the computation of DDSA-images, see Equation 8.2. Instead of using only the number of pixels below a single threshold, we used several thresholds. They are selected heuristically for the data at hand such that the complete cumulative histogram is covered. In our case, the number of pixels with an intensity below a threshold value of $T_i, i \in \{-200, -150, \ldots, 150, 200\}$ are considered as features f_{16}^k to f_{24}^k, respectively.

We added also features related to the intensity of the fluoroscopic images itself. To this end, we measured the average intensity in a quadratic window located at the centre of the image and at a horizontal stripe at the top of the image area not covered by shutters. The box width and height corresponded to 20% of the image width and height, the height of the horizontal stripe was 10% of the image height. While at the beginning, both should have a similar intensity, the intensity will change as contrast agent will appear in the centre window. The upper region of the image will not, or, hardly be affected by the contrast agent. These features are denoted as f_{25}^k for the centre region and f_{26}^k for the top region.

To set these values in relation to the intensities of frames known to be uncontrasted, each feature vector contains also a feature f_{25}^1 which is set to the intensity within the centre region averaged over the first two frames. This is also done for the top region resulting in the feature f_{26}^1. These features are identical for all frames of a sequence.

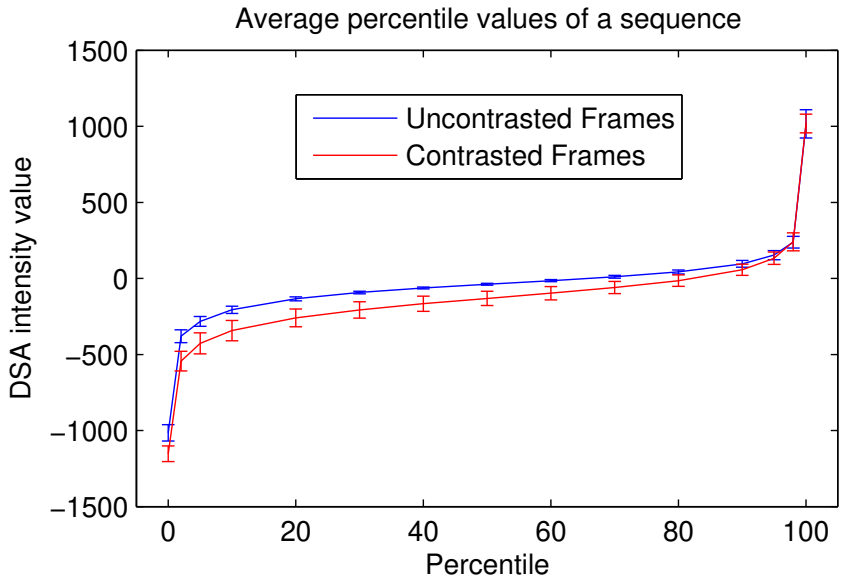

(a)

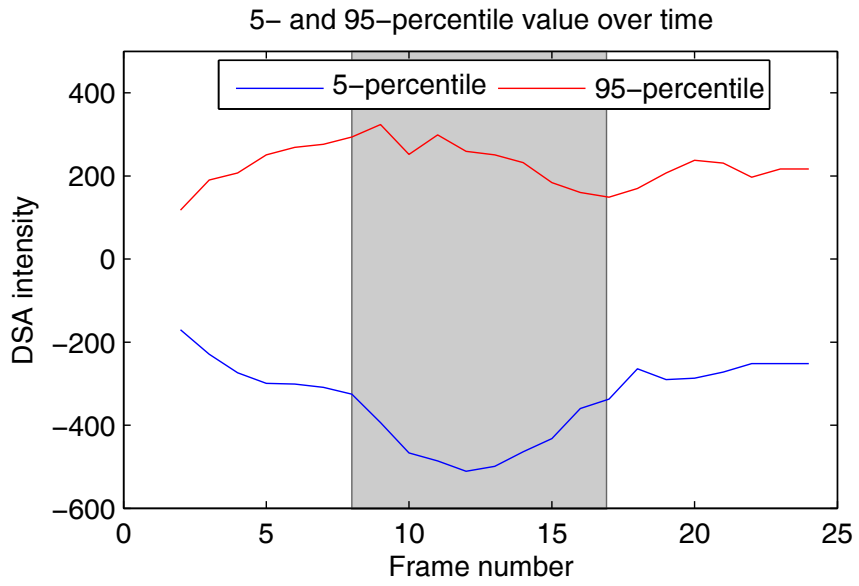

(b)

Figure 8.1: (a) Mean value and standard deviation of the percentiles for contrasted and uncontrasted frames. (b) Value of the 5- and 95-percentile. It becomes clear that the 5-percentile is better suited to distinguish contrasted frames (grey area) from uncontrasted frames.

Algorithm 1 ComputeFeaturesForSequence(
Image sequence of plane A $\boldsymbol{I}_k^{\mathrm{A}}$, $k = 1, \ldots, n$,
Image sequence of plane B $\boldsymbol{I}_k^{\mathrm{B}}$, $k = 1, \ldots, n$):

for every plane $\Phi \in \{\mathrm{A}, \mathrm{B}\}$ **do**
  for $k = 2$ to $k = n - 1$ **do**
    $\boldsymbol{I}_{\mathrm{DDSA},k}^{\Phi} \leftarrow -\boldsymbol{I}_k^{\Phi} + \boldsymbol{I}_{k-1}^{\Phi}$
    $\boldsymbol{I}_{\mathrm{DSA},k}^{\Phi} \leftarrow \boldsymbol{I}_0^{\Phi} - \boldsymbol{I}_k^{\Phi}$

    for $i \in \{0, 2, 5, 10, 20, \ldots, 80, 90, 95, 98, 100\}$ **do**
      $p_i \leftarrow$ value of i-th intensity percentile in $\boldsymbol{I}_{\mathrm{DSA},k}^{\Phi}$
    end for
    $f_1^{k,\Phi}$ to $f_{15}^{k,\Phi} \leftarrow p_i, i \in \{0, 2, 5, 10, 20, \ldots, 80, 90, 95, 98, 100\}$

    for $i \in \{-200, -150, \ldots, 150, 200\}$ **do**
      $T_i \leftarrow$ number of pixels below an intensity of T_i in $\boldsymbol{I}_{\mathrm{DSA},k}^{\Phi}$
    end for
    $f_{16}^{k,\Phi}$ to $f_{24}^{k,\Phi} \leftarrow T_i, i \in \{-200, -150, \ldots, 150, 200\}$
    $f_{25}^{k,\Phi} \leftarrow$ mean intensity of center region in $\boldsymbol{I}_k^{\Phi}$
    $f_{26}^{k,\Phi} \leftarrow$ mean intensity of top region in $\boldsymbol{I}_k^{\Phi}$
  end for
  $f_{26}^{1,\Phi} \leftarrow$ mean intensity of centre region in $\boldsymbol{I}_0^{\Phi}$ and $\boldsymbol{I}_0^{\Phi}$
  $f_{26}^{1,\Phi} \leftarrow$ mean intensity of top region in $\boldsymbol{I}_0^{\Phi}$ and $\boldsymbol{I}_0^{\Phi}$
end for

for $k = 3$ to $k = n - 2$ **do**
  $\boldsymbol{f}^{k,\mathrm{A}} = (f_1^{k-1,\mathrm{A}}, \ldots, f_{26}^{k-1,\mathrm{A}}, f_1^{k,\mathrm{A}}, \ldots, f_{26}^{k,\mathrm{A}}, f_1^{k+1,\mathrm{A}}, \ldots, f_{26}^{k+1,\mathrm{A}}, f_{25}^{1,\mathrm{A}}, f_{26}^{1,\mathrm{A}})^T$
  $\boldsymbol{f}^{k,\mathrm{B}} = (f_1^{k-1,\mathrm{B}}, \ldots, f_{26}^{k-1,\mathrm{B}}, f_1^{k,\mathrm{B}}, \ldots, f_{26}^{k,\mathrm{B}}, f_1^{k+1,\mathrm{B}}, \ldots, f_{26}^{k+1,\mathrm{B}}, f_{25}^{1,\mathrm{B}}, f_{26}^{1,\mathrm{B}})^T$
end for

return $(\boldsymbol{f}^{k,\mathrm{A}T}, \boldsymbol{f}^{k,\mathrm{B}T})^T$ for all $3 \leq k \geq n - 2$

Whether a frame is contrasted or uncontrasted depends also on its neighbouring frames. If the previous and the next frame are found to contain contrast agent (CA), the current frame will very likely also contain CA. To include this dependency into the classification process, the features f_1^{k-1} to f_{26}^{k-1} of the previous frame and the features f_1^{k+1} to f_{26}^{k+1} of the following frame are included into the feature vector of each frame.

As the features identical for all frames of the sequence need to be contained only once in the feature vector, we end up with a 80-dimensional feature vector for frame k: $\boldsymbol{f}^k = (f_1^{k-1}, \ldots, f_{26}^{k-1}, f_1^k, \ldots, f_{26}^k, f_1^{k+1}, \ldots, f_{26}^{k+1}, f_{25}^1, f_{26}^1)^T$. In our case, biplane image pairs are used and for each time point, the information from two images is available. The feature vectors from both planes can then be combined and we end up with 160 features per frame. Algorithm 1 sums up the feature computation.

These features were used to train an SVM. The training comprised a feature selection based on the wrapper approach performed as three-fold crossvalidation nested

Algorithm 2 SELECTFEATURESANDTRAINSVM(Set $\mathcal{I}$ of biplane image sequence, class annotations for which frames contain CA):

$\mathcal{K} \leftarrow$ All features
$\mathcal{H} \leftarrow \varnothing$ *//Selected features*
for 1 to 8 **do**
  Select most distinctive feature f using wrapper approach in a three-fold cross-validation
  $\mathcal{H} = \mathcal{H} \cup \{\hat{f}\}$
end for

for each feature f in $\mathcal{H}$ **do**
  Select least distinctive feature f using wrapper approach in a three-fold cross-validation
  $\mathcal{H} = \mathcal{H} \cup \{f\}$
end for
$\mathcal{H} = \mathcal{H} \setminus \{\hat{f}\}$

for each feature f in $\mathcal{K} \setminus \mathcal{H}$ **do**
  Select most distinctive feature f using wrapper approach in a three-fold cross-validation
  $\mathcal{H} = \mathcal{H} \cup \{\hat{f}\}$
end for
$\mathcal{H} = \mathcal{H} \cup \{\hat{f}\}$
svm $\leftarrow$ train SVM using features in $\mathcal{H}$ and contrast / no-contrast label of frames

return *svm*

into the leave-one-out crossvalidation. The feature selection was performed to get an insight into the importance of the different features. Eight features[3] were selected using a greedy selection strategy: Successively the most distinctive feature was added to the feature set. In the final round, the least significant feature was removed from the selection and the most distinctive feature from the whole feature set was added. The training procedure is summarized in Algorithm 2.

8.4 Experiments and Results

An evaluation of the previous methods by Condurace *et al.* [Cond 04] and Zhao *et al.* [Zhao 13] as well as our SVM-based approach was performed on 34 biplane angiographic sequences. The sequences were acquired during clinical procedures from 15 different patients. The image series had a resolution of 1024×1024 pixels, 7 fps and different frame counts from 8 up to 57.

[3] For the sake of simplicity, the selection was based on the single features f_i, i.e., selecting feature f_i included the feature triplet $f_i^{k-1}, f_i^k, f_i^{k+1}$ for both planes into the feature set.

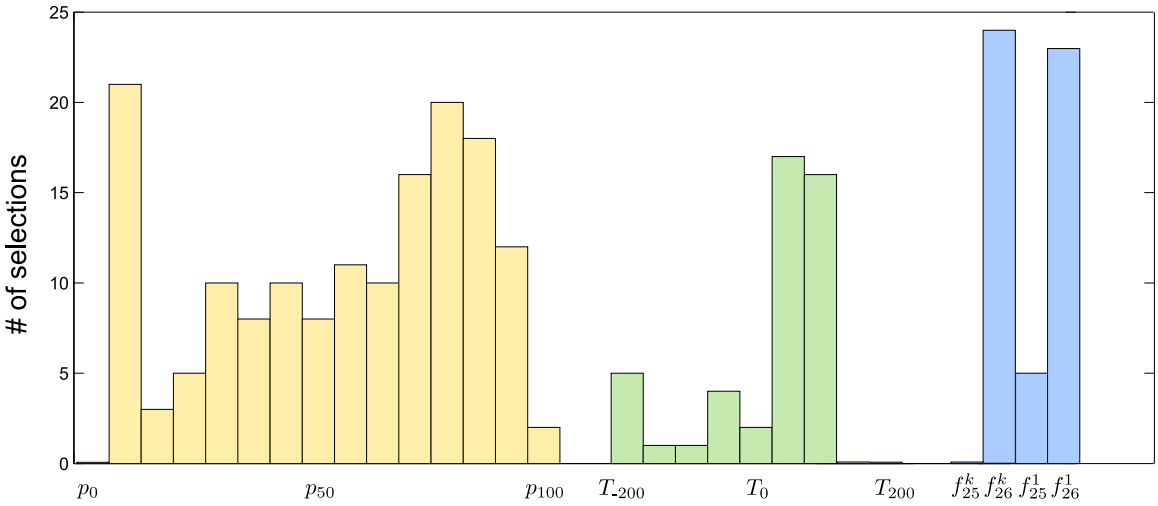

Figure 8.2: Histogram of features selected during the feature selection step. The yellow group denotes the features based on the percentiles of the DSA image histogram, the green group denotes features based on the cumulative histogram of the DDSA images and the blue groups denote the features based on the mean value of the centre region (f_{25}) and the top region (f_{26}).

As the method by Condurache *et al.* was designed for coronary arteries, the authors used a tophat filter to extract the thin vessels highlighted by contrast agent. While the tophat filter is suited to extract thin structures, it fails for larger structures such as the contrasted area of a LA angiography. Therefore, we replaced the tophat filter by a DSA. The values of μ_0 and σ_0 were estimated based on the first three frames which were in all sequences uncontrasted. The value of l was determined in a leave-one-out manner. The parameter T_{Z} for the approach from Zhao *et al.* was determined the same way.

We used the MATLAB implementation of the SVM. The value of the parameter C of the SVM was set to $\frac{n_{\text{c}}+n_{\text{u}}}{2n_{\text{c}}}$ and $\frac{n_{\text{c}}+n_{\text{u}}}{2n_{\text{u}}}$ for the training samples of n_{c} constrasted and n_{u} uncontrasted frames, respectively. This is the default setting for this implementation. The first frame was used as uncontrasted reference frame and was excluded from training and evaluation. As the feature vector for the second frame contains features from the first frame, too, the second frame was also excluded from training and evaluation. Frames with contrast agent flowing out from the LA to the ventricle are also not used for training as it is hard to determine whether there is still contrast present. Thus, they are prone to labelling errors. However, these ambiguous frames were used for evaluation but marked separately.

The evaluation data contained 350 contrasted and 241 uncontrasted frames. When considering unambiguous frames, 167 contrasted and 116 uncontrasted frames were available. Training and evaluation of the SVM was performed in a leave-one-out crossvalidation. A histogram of the selected features is given in Figure 8.2. We performed two types of evaluations: First, we evaluated how accurately the beginning of contrast agent injection can be detected. This is important for automatic contrast based registration [Thiv 12, Zhao 13], see also section 9.3. To this end, we computed the difference between the frame number of the first contrasted frame and number of

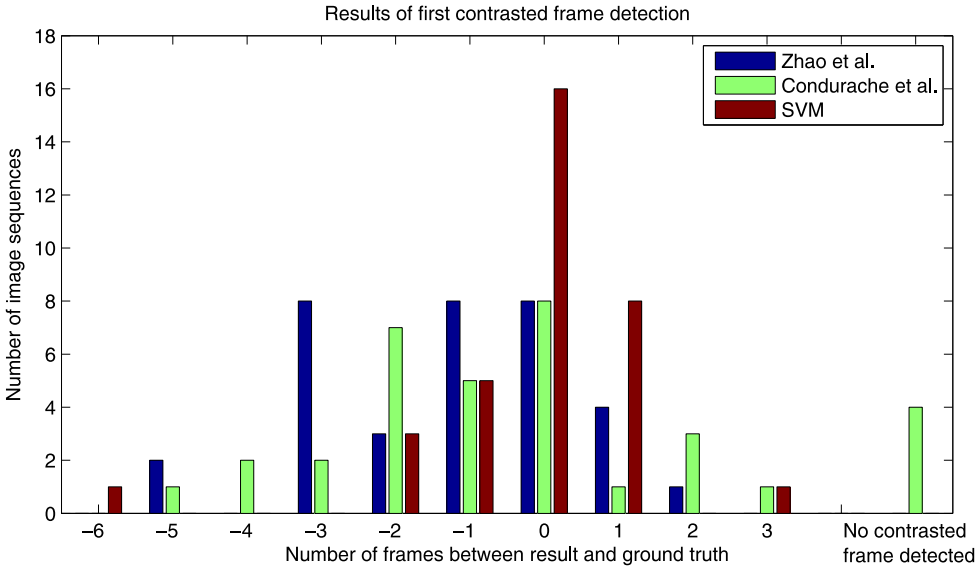

Figure 8.3: Difference between the position of the first contrasted frame and the position of first frame classified as contrasted. Negative differences denote that the contrast injection was detected too early.

Table 8.1: Confusion matrices for classification of all frames

		classification result			
		Condurache		SVM-based	
		contr.	uncontr.	contr.	uncontr.
class	contrasted	240	90	296	34
	uncontrasted	110	131	73	168

the first frame classified as contrasted. Sequences where the position of the detected first contrasted frame was off by one or less were considered as detected correctly.

Second, we measured the classification rate. This evaluation was performed on the approach by Condurache *et al.* [Cond 04] and the SVM-based approach. The method by Zhao *et al.* [Zhao 13] detects only the first contrasted frame and thus cannot detect uncontrasted frames at the end of the sequence.

Results for the detection of the first contrasted frame are provided in Figure 8.3. The SVM-based approach had a success rate of 85.3%, the success rate for the approach by Zhao *et al.* was 58.8% and 41.2% for the adapted method by Condurache *et al.*

The evaluation of the classification for all frames showed a classification rate of 81.2% for the SVM-based approach and 65.0% for the adaption of Condurache's method. If ambiguous frames were excluded from the evaluation such that only clearly contrasted and clearly uncontrasted frames remained, the classification rate improved to 88.0% for the SVM-based approach and 78.4% for the approach according to Condurache *et al.* The respective confusion matrices are given in Table 8.1 and Table 8.2.

Table 8.2: Confusion matrices for classification of unambiguous frames

		classification result			
		Condurache		SVM-based	
		contr.	uncontr.	contr.	uncontr.
class	contrasted	142	25	149	18
	uncontrasted	36	80	13	103

8.5 Discussion and Conclusions

The features selected most often during feature selection, see Figure 8.2, were:

- the mean intensity of the top image region for the respective frame and the first frame,
- the 2-, 90- and 95-percentile values,
- the number of pixels in the DDSA images with an intensity of over 50 and 100, respectively

It turns out that the 95-percentile of the intensities is much less distinctive than the 5-percentile, see Figure 8.1. On first sight this appears to be counterintuitive as for DSA images, contrast agent appears bright in the images and, thus, should reflect in the high percentile values. Here, the reason is in the automatic exposure control (AEC) used to acquire these image sequences. The AEC is designed in a way that the radiation arriving at the detector centre is kept more or less constant. If contrast agent absorbs energy, the current is increased. Therefore, the whole image gets brighter at regions where no contrast agent is present. This explains also why the features regarding the top image region are selected most often as they measure the energy increase caused by the AEC when energy in the image centre is reduced by contrast agent.

The approach by Condurache *et al.* gives less accurate results. It turns out that a single percentile value is not sufficient to discriminate between uncontrasted and contrasted frames. Also the approach by Zhao *et al.* yields unsatisfying results as it compares each frame only to its previous frame and relies on a strong diffusion of contrast agent from one to the next frame. This introduces a dependency on the frame rate. Thus, the threshold needs to be adapted, e.g. if higher frame rates were used where the difference in the contrasted regions from one frame to the next is less. Alternatively, the frame after the next frame could be selected for DDSA computation to increase the time interval between the subtracted frames.

The SVM-based approach, on the other hand, can take much more information into account to distinguish contrasted from uncontrasted frames compared to a single threshold. Due to its feature-based nature, it allows the integration of additional information, e.g. from previous frames or from a second image plane. In future work, X-ray parameters like the used current or voltage could be added to the feature vector to provide information regarding the AEC explicitly.

CHAPTER 9

Registration to Single Frames of a Contrasted Fluoroscopic Sequence

The shape of the LA cannot be seen in X-ray images unless contrast agent (CA) is injected. A CA injection highlights the shape of the LA and projections of the LA volume can be aligned to the contrast-enhanced LA shape in the X-ray images. Example images of such CA injections performed after the transeptal puncture are shown in Figure 9.1 to illustrate the images available. To automatize the registration process, we propose a method that automatically selects a suitable mask frame for contrast extraction by means of DSA. Based on the observation that an automatic registration based on the projected shadow may not provide unique solutions we propose to use a combination of two similarity measures instead.

The first similarity measure described in subsection 9.3.2 focusses on edges that can be perceived in the contrast enhanced images. Although this similarity measure has been used for registration before, we are to our knowledge the first using it in the context of contrast-based registration. The second contribution described in subsection 9.3.3 is the introduction of a novel similarity measure for biplane X-ray that is tailored to cases in which only parts of an object are visible. Based on a 3-D model of the LA, our second method estimates the CA distribution inside the 3-D object from a simultaneously acquired pair of fluoroscopic images taken under two different view angles. Then we evaluate how consistent the Contrast agent distribution estimate (CADE) is with the acquired fluoroscopic images. As the CADE depends on the transformation used for registration, the transformation leading to the most plausible CADE is used as final position estimate.

A brief description of both methods was previously published on ArXiv [Hoff 16e]. This extended description is a part of the publication in the International Journal of Biomedical Imaging [Hoff 16d].

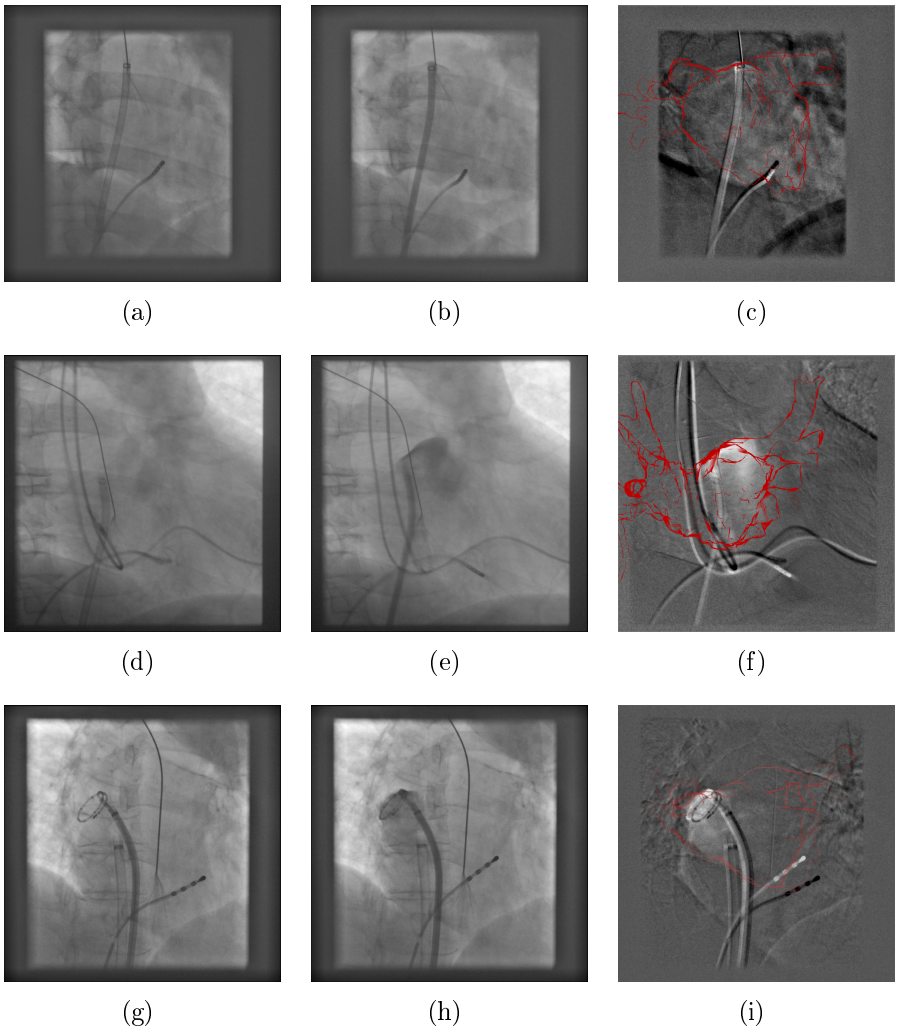

Figure 9.1: Three different CA injections. The left column shows an uncontrasted frame, the middle column a contrasted frame of the sequence and the rightmost column shows a subtraction of both images. The manually established ground-truth position of the left atrium is overlayed with red. The LA in image (c) appears only faintly contrasted and the CA just flows into the ventricle. On the other hand, image (f) shows disturbing motion artefacts caused by leads and wires associated with an implanted device. In image (i), the CA is injected into a pulmonary vein and catheter motion artefacts are visible. While the spine in the centre of this image vanishes, soft tissue motion artefacts related to the lungs are visible at the left and right border, respectively.

9.1 Motivation

A registration based on external anatomical structures as presented in chapter 6 is advantageous as, for example, a registration can be performed prior to the transeptal puncture [Bour 16]. On first sight a registration based on CA appears to be more complicated as a CA injection is required which may not be part of the clinical

workflow yet. On the other hand, a registration based on CA has some advantages compared to contrast-free registration methods:

Universality. Contrast-free registration methods require segmentations of further landmarks from the same volumetric data set as the LA model is segmented from. Anatomical structures used so far for manual or automatic registration are the carina [Li 09], the coronary sinus (CS) [Sra 05, Bros 11b], the spine [Knec 08] or a combination of spine and heart anatomy [Bour 16]. A segmentation of these structures is usually possible if the 3-D heart model was acquired using CT. For 3-D volumes acquired by MRI, e.g., MRI angiographies (MRAs) [Haus 08], however, a segmentation of the CS or the carina can be very challenging, or has not yet been adopted for routine clinical procedures. So, contrast-free registration methods are primarily suited for 3-D data from CT acquisitions. Fluoro overlay images derived from MRA data sets are, however, relevant, because MRI can provide not only anatomical information but also convey physiological information such as fibrotic tissue and scar regions. If used properly, this kind of information may improve the success rates of EP ablation procedures [Burs 08].

On the other hand, a registration based on CA is universal. It requires no other data than a segmentation of the LA which is always present as it is the object to be registered. So, it depends neither on the 3-D acquisition modality nor on the acquisition protocol.

Speed. Even if an easy segmentation of additional structures is possible, as for CT data, the segmentation of further structures takes time and introduces an additional step into the clinical workflow.

For 3-D MRI data, considerably more time is required, either for the segmentation or for data acquisition. Bourier *et al.* [Bour 10] and Brost *et al.* [Bros 11b] have worked on 3-D MRA data as a proof-of-concept for CS-based registration. As they used MRA data acquired with a standard MRI acquisition protocol [Haus 08], the segmentation process was rather time consuming. A switch to a more involved cardiac MRI protocol or an additional MR acquisition would be needed to acquire data in which the CS can be seen better. This protocol will likely require a gating as the CS catheter is subject to strong cardiac motion. Thus, such an acquisition protocol has probably a higher acquisition time.

Contrast based registration facilitates a fast workflow. In our particular case, the segmentation of the LA requires a single click and about 10 seconds using *syngo* InSpace EP (Siemens Healthcare GmbH, Forchheim, Germany). Manual registration can then be achieved in about 10 seconds on average [Bour 13]. If a contrast injection is not yet part of the workflow, e.g., to verify puncture success [Feld 07], the additional procedure time needed to perform a hand injection would be below one minute.

Accuracy. As presented in section 6.1, the accuracy of catheter-based registration varies between 10.6 mm [Bour 10] and 4.9 mm [Bour 16] if the 3-D error is considered. If cardiac motion and breathing motion is ruled out, the error can even reduce to 3.2 mm as demonstrated in section 6.4. The 2-D error is less and is reported to be between 1.3 mm at the roof and 1.7 mm at the PVs [Bour 16].

Registration based on contrast injection has been shown to be an accurate alternative with an average 2-D error of 1.1 mm at the LA roof and 1.3 mm at the PVs [Bour 13]. It serves therefore as reference for the evaluation of other registration methods [Bour 10, Bros 11b, Knec 08].

9.2 Related Work

There is a significant body of research on registration of 3-D objects to 2-D fluoroscopic images, e.g., for bones [Guez 98, Hama 98, Livy 03], implants, joints [Kapt 03] or vessels [Bens 13]. An overview is given by Markelj *et al.* [Mark 12]. Compared to implants, a registration of the LA is more complicated for at least two reasons: First, for implants and bones, all parts of the object are visible. During a contrast injection, however, only a part of the left atrium may appear under X-ray.

Second, depending on the amount of CA injected, the overall LA visibility may be poor. For example, in our case EP physicians use contrast at the beginning of the procedure to verify the success of the transseptal puncture. It may also be used later to enhance the anatomy, e.g., to make sure that a catheter, e.g., a circumferential mapping catheter or a cryoballoon catheter, was placed correctly. This is different to vessel angiography. In this case, higher amounts of contrast are injected to derive diagnostic information, e.g., about a stenosis. For ablation procedures in the LA, the CA density and so the visibility of the LA under X-ray may be poorer as the small amount of contrast is injected into the high blood volume of the LA. As a consequence, further effort is needed to develop robust registration methods that can also be applied if CA is used sparingly.

Currently, very few publications deal with registration based on CA: In a first approach towards automatic LA registration, Thivierge-Gaulin *et al.* [Thiv 12] tried to find a 3-D pose of a model such that its projected shadow matches the contrasted area in a selected image, enhanced by digital subtraction angiography (DSA), best. However, if only a small amount of CA is injected into a somewhat large chamber such as the left atrium, this approach will not lead to an distinct optimum, because the anatomy may not be fully opacified.

Based on CT images, a second approach by Zhao *et al.* [Zhao 13] relied on digitally rendered radiographies (DRRs) of the segmented left atrium. The rendered image was compared to a DSA image using normalized gradient correlation. This approach uses a weighting scheme that puts the focus on the roof of the LA. It is still unclear how well this method performs for injections into other areas of the LA.

Besides contrast-based registration, 3-D data and 2-D data can also be aligned using devices. A feature-based method by Sra *et al.* [Sra 05] uses a segmentation of the coronary sinus (CS) in a CT volume to register a 3-D LA model to a single 2-D fluoroscopic image. A further approach by Brost *et al.* [Bros 11b] uses a segmentation of the CS in an MRI volume and a 3-D reconstruction of the CS catheter from two fluoroscopic images. Unfortunately, it depends very much on the MRI scan protocol how well the CS can be extracted from a 3-D MRI data set. Furthermore, due to the strong motion of the CS, it is difficult to relate the position of the CS catheter to the position of the LA, especially for patients having no sinus rhythm but a heart arrhythmia [Klem 07, Kapp 12].

9.3 Contrast-based Registration Framework

For registration, two X-ray sequences showing a CA injection are used. These sequences are acquired simultaneously from two different angles using a biplane system. For each plane, the projection matrix that describes the X-ray camera setup is known. We denote the associated projection operator by P_{A} and P_{B} for the A-plane and the B-plane of the system, respectively. We also assume that a 3-D model of the patient's LA is available, either as a triangle mesh or a binary volume, as they can be converted into each other. The description of the method is not restricted to a certain type of transformation, hence, the transformation is denoted by T.

9.3.1 Contrast Agent Extraction

The contrasted area is found based on a difference image (DSA) $\boldsymbol{I}_{\mathrm{DSA}} = \boldsymbol{I}_{\mathrm{u}} - \boldsymbol{I}_{\mathrm{c}}$, $\boldsymbol{I} \in \mathbb{R}^{k \times l}$ involving a frame $\boldsymbol{I}_{\mathrm{c}}$ that contains CA and an uncontrasted frame $\boldsymbol{I}_{\mathrm{u}}$. To distinguish between contrasted and uncontrasted frames, either manual annotation or a learning based method can be used e.g. the method described in chapter 8. Depending on the chosen contrasted frame $\boldsymbol{I}_{\mathrm{c}}$, $\boldsymbol{I}_{\mathrm{DSA}}$ may contain artefacts, e.g., due to motion of the diaphragm or from catheters, if they are at different positions in $\boldsymbol{I}_{\mathrm{u}}$ and $\boldsymbol{I}_{\mathrm{c}}$. Such motion artefacts depend, unlike the information about CA, to a large degree on the choice of $\boldsymbol{I}_{\mathrm{u}}$. For example, if the catheters in $\boldsymbol{I}_{\mathrm{u}}$ are at the same position as in $\boldsymbol{I}_{\mathrm{c}}$, their intensities cancel out. Otherwise, $\boldsymbol{I}_{\mathrm{DSA}}$ has high positive values at the position of the catheter in $\boldsymbol{I}_{\mathrm{c}}$ and high negative values at the position of the catheter in $\boldsymbol{I}_{\mathrm{u}}$. To keep motion artefacts to a minimum, we propose a best reference selection, which chooses an appropriate reference frame $\hat{\boldsymbol{I}}_{\mathrm{u}}$ that matches the chosen contrasted frame $\boldsymbol{I}_{\mathrm{c}}$ as much as possible. Out of all uncontrasted frames, that frame $\hat{\boldsymbol{I}}_{\mathrm{u}}$ is selected which minimizes the L_1-norm of the resulting DSA image

$$\hat{\boldsymbol{I}}_{\mathrm{u}} = \arg\min_{\boldsymbol{I}_{\mathrm{u}}} \sum_{x=0}^{k-1} \sum_{y=0}^{l-1} |\boldsymbol{I}_{\mathrm{u}}(x,y) - \boldsymbol{I}_{\mathrm{c}}(x,y)|. \tag{9.1}$$

By following Equation 9.1, we get frames for which the catheters and the diaphragm cancel out as much as possible. See Figure 9.3(b) for an example. In $\boldsymbol{I}_{\mathrm{DSA}}$, only pixels with positive values contain CA. To extract them, we set the intensity of pixels with negative value to 0. Afterwards, we compute a filtered image $\boldsymbol{I}_{\mathrm{m}}$ by applying a median filter with a large kernel size. The size should be small enough such that all relevant parts of the LA are retained. On the other hand, it should be large enough such that smaller structures, e.g., caused by motion artefacts that remained despite the optimized choice of $\boldsymbol{I}_{\mathrm{u}}$, do not pass this filter, and the noise in the contrasted area is reduced as well. For our images of size 1024×1024, a kernel size of 30 pixels was determined heuristically. Finally, a binary image $\boldsymbol{I}_{\mathrm{thr}}$ of the filtered image $\boldsymbol{I}_{\mathrm{m}}$ is computed using a threshold at $\mu_{\mathrm{m}} + \sigma_{\mathrm{m}}$ where μ_{m} and σ_{m} denote the mean and standard deviation of $\boldsymbol{I}_{\mathrm{m}}$, respectively. Thus, a contrasted pixel $\boldsymbol{p} \in \mathbb{R}^2$ is indicated by $\boldsymbol{I}_{\mathrm{thr}}(\boldsymbol{p}) = 1$.

A previous approach [Thiv 12] tried to find a transformation T of the 3-D model such that the projected shadows $\boldsymbol{S}_T^{\mathrm{A}}$, $\boldsymbol{S}_T^{\mathrm{B}}$ of the model into the A-plane and the B-plane

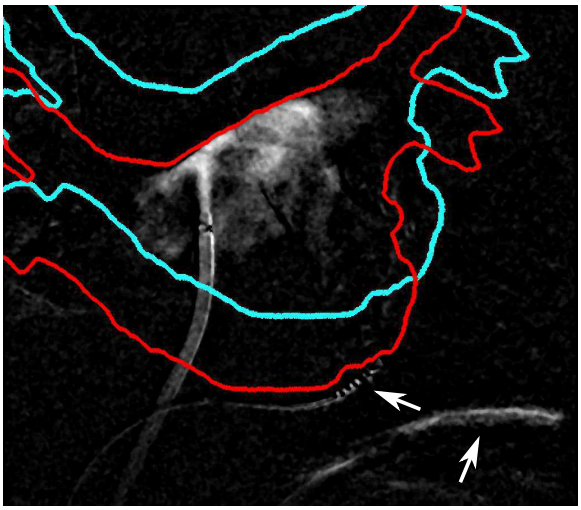

Figure 9.2: A correct (red) and wrong (cyan) registration result. In both cases, the contrasted area is fully inside the projection shadow represented by the coloured outlines. Both registration results lead to a similar NCC value when using an area-based feature for automatic registration. Note that motion artefacts could be kept to a minimum thanks to the best reference frame selection. Only some residual artefacts remained in the vicinity of the moving coronary sinus (CS) catheter and the diaphragm, see white arrows.

of a biplane C-arm system fit best to the contrasted region. Using the normalized cross correlation (NCC), denoted as ρ, of two images $\boldsymbol{I}_1, \boldsymbol{I}_2$ with corresponding mean values μ_1, μ_2 and standard deviations σ_1, σ_2

$$\rho(\boldsymbol{I}_1, \boldsymbol{I}_2) = \sum_{x=0}^{k} \sum_{y=0}^{l} \frac{(\boldsymbol{I}_1(x,y) - \mu_1) \cdot (\boldsymbol{I}_2(x,y) - \mu_2)}{\sigma_1 \cdot \sigma_2}, \tag{9.2}$$

the similarity of the projected shadow and $\boldsymbol{I}_{\mathrm{DSA}}$ can be measured. Instead of $\boldsymbol{I}_{\mathrm{DSA}}$, one can also use the binary version of it, i.e., $\boldsymbol{I}_{\mathrm{thr}}$. Then a registration transformation can be estimated by maximizing either one of the two functions

$$\rho^{\mathrm{DSA}}_{\mathrm{shad}}(\boldsymbol{I}^{\mathrm{A}}_{\mathrm{DSA}}, \boldsymbol{I}^{\mathrm{B}}_{\mathrm{DSA}}, T) = \rho(\boldsymbol{I}^{\mathrm{A}}_{\mathrm{DSA}}, \boldsymbol{S}^{\mathrm{A}}_{T}) \cdot \rho(\boldsymbol{I}^{\mathrm{B}}_{\mathrm{DSA}}, \boldsymbol{S}^{\mathrm{B}}_{T}), \tag{9.3}$$

$$\rho^{\mathrm{thr}}_{\mathrm{shad}}(\boldsymbol{I}^{\mathrm{A}}_{\mathrm{thr}}, \boldsymbol{I}^{\mathrm{B}}_{\mathrm{thr}}, T) = \rho(\boldsymbol{I}^{\mathrm{A}}_{\mathrm{thr}}, \boldsymbol{S}^{\mathrm{A}}_{T}) \cdot \rho(\boldsymbol{I}^{\mathrm{B}}_{\mathrm{thr}}, \boldsymbol{S}^{\mathrm{B}}_{T}). \tag{9.4}$$

9.3.2 Edge Feature

Unfortunately, a registration approach only based on contrasted area has multiple solutions if the amount of CA is so little that it does not completely fill the LA, see Figure 9.2. Fortunately, CA is often injected against the roof or into the pulmonary veins. This results in perceivable edges of the contrasted area which can then be used as registration features. Edge-based registration can be carried out using only the silhouette boundary of the projected object [Kapt 03], see Figure 9.2 or all apparent edges [Guez 98, Hama 98], see Figure 9.3(f).

We decided to consider all apparent edges to improve robustness against injections of small amounts of CA, as the silhouette-based approach requires that the LA is contrasted in its entirety. For a partially contrasted left atrium, internal contours may, however, also appear in the fluoroscopic images. This was already found to be beneficial for manual LA registration [Hoff 13a]. Instead of considering edges implicitly by comparing the DSA image to a DRR using gradient correlation [Zhao 13], we computed them explicitly. To extract edges in the fluoroscopic images, we used the filtered image $\boldsymbol{I}_{\mathrm{m}}$. After applying a median filter, edge-like variations *inside* the contrasted areas may remain. They, however, correspond rarely to anatomical

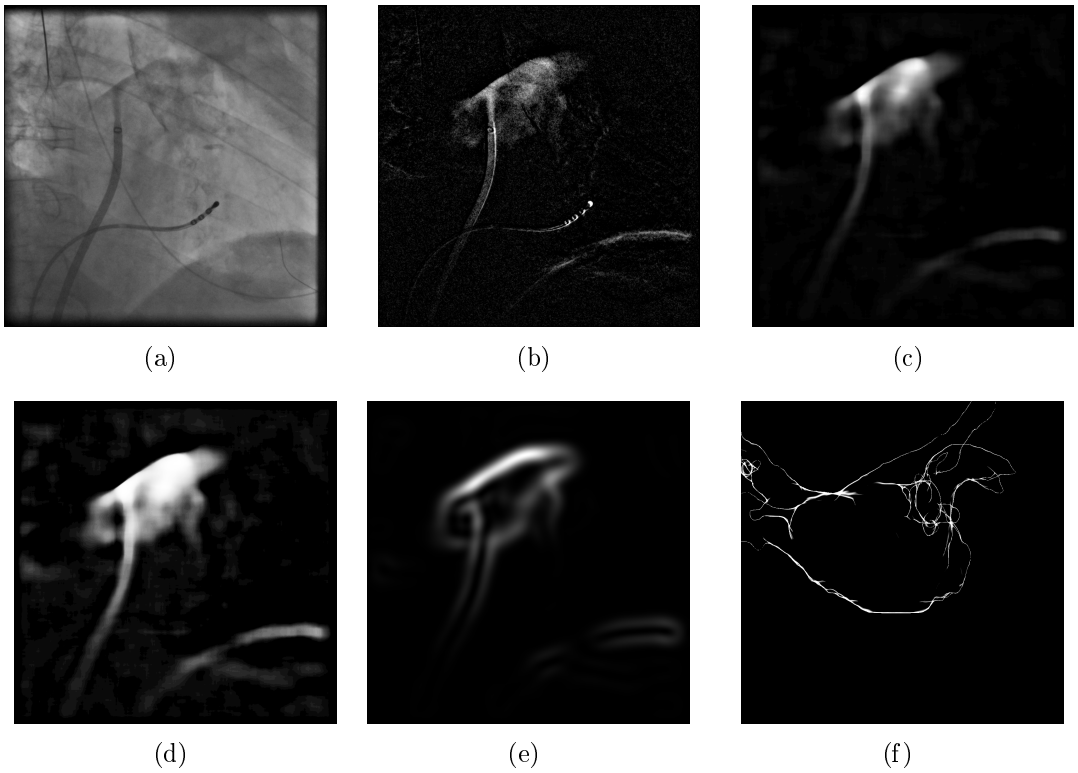

Figure 9.3: Using the original image (a), a DSA image (b) is computed. After median filtering (c), the remaining motion artefacts from the catheter have vanished. Only the boundary at the diaphragm remained. Afterwards, all pixels are weighted by a sigmoid function (d) to get a more homogeneous value distribution inside the contrasted area. Edges are extracted using derivatives of Gaussian with a large kernel size (e). Finally, the similarity to the rendered edges (f) is evaluated.

structures and would trigger a response, if an edge filter was applied. To obtain an edge response only at the boundaries of the contrasted area, the image needs to be homogenized before applying an edge filter. Using a simple threshold method would result in a loss of the intensity drop-off at the boundary which provides important information about the edge intensity. Therefore, we weigh all image pixels by a sigmoid function

$$\boldsymbol{I}_{\text{sig}}(x,y) = \frac{1}{1+\mathrm{e}^{-(\boldsymbol{I}_{\text{m}}(x,y)+t)\cdot s}}. \tag{9.5}$$

The value of t is set with respect to the mean intensity μ_{m} and corresponding standard deviation σ_{m} of $\boldsymbol{I}_{\text{m}}$ to $\mu_{\text{m}} - \sigma_{\text{m}}$. The parameter s depends on the pixel intensity range of the input image and is determined heuristically. An example of $\boldsymbol{I}_{\text{sig}}$ is given in Figure 9.3(d). Finally, $\boldsymbol{I}_{\text{sig}}$ is filtered using a derivative of Gaussian (DOG) filter to obtain the edge image $\boldsymbol{I}_{\text{DOG}}$. The kernel size of the DOG-filter is set to a large value to get a smooth similarity measure, see Figure 9.3(e).

The projection of the 3-D triangle mesh edges into 2-D is done differently than in [Guez 98, Hoff 13a] but use the method described in [Toma 05]: We rendered the whole surface mesh and, depending on the viewing direction $\boldsymbol{d}$ and the surface normal

$\boldsymbol{n}$ at a point, we set the opacity o of projected triangles to $o = 1 - |(\boldsymbol{d}^\intercal \boldsymbol{n})|$, see Figure 9.3(f) for an example. By doing so, areas that are parallel to the imaging plane are rendered transparent while areas with a normal vector orthogonal to the viewing direction are rendered opaque. The similarity between edges extracted from the fluoroscopic images and the edge images $\boldsymbol{E}_T^{\mathrm{A}}, \boldsymbol{E}_T^{\mathrm{B}}$ rendered from the 3-D model transformed by T is measured by

$$\rho_{\mathrm{edge}}(\boldsymbol{I}_{\mathrm{DOG}}^{\mathrm{A}}, \boldsymbol{I}_{\mathrm{DOG}}^{\mathrm{B}}, T) = \rho(\boldsymbol{I}_{\mathrm{DOG}}^{\mathrm{A}}, \boldsymbol{E}_T^{\mathrm{A}}) \cdot \rho(\boldsymbol{I}_{\mathrm{DOG}}^{\mathrm{B}}, \boldsymbol{E}_T^{\mathrm{B}}). \tag{9.6}$$

9.3.3 Contrast Agent Distribution Estimation (CADE)

Previous approaches [Thiv 12, Zhao 13] for LA registration searched for a rigid transformation of the LA such that either its projected shadow or its DRR fit to the contrasted area in both fluoroscopic images. 3-D information was taken into account insofar as the resulting projections came from the same 3-D position of the model. However, such an approach does not necessarily guarantee that corresponding objects in both fluoroscopic images are matched to the same 3-D structure of the LA. More precisely, the registration result could be such that in plane A, the CA is located in a left pulmonary vein (PV) whereas in plane B, the contrasted area corresponds to a right PV. This is possible as for a given 2-D registration in one plane, the 2-D registration in the other plane has one degree of freedom, which corresponds to an out-of-plane motion in the first plane. An illustration of this problem can be found in Figure 9.4.

To solve this problem, we compute for a given transformation T a CADE inside the LA using binary reconstruction. Then, T is optimized such that the CADE is most consistent with the projection images. More precisely, a voxel $\boldsymbol{v}$ is estimated as contrasted if it satisfies all of the following conditions: The voxel $\boldsymbol{v}$ transformed by T is (a) projected on a contrasted pixel in plane A, (b) projected on a contrasted pixel in plane B, and (c) $\boldsymbol{v}$ is part of the left atrium (as contrast agent can only be found inside the LA). To compute the CADE, we define the indicator function

$$\chi(\boldsymbol{v}) = 1 \Leftrightarrow \boldsymbol{v} \in \mathbb{R}^3 \text{ is inside the left atrium.} \tag{9.7}$$

Given the binary images $\boldsymbol{I}_{\mathrm{thr}}^{\mathrm{A}}$ and $\boldsymbol{I}_{\mathrm{thr}}^{\mathrm{B}}$ with corresponding projection operators $P_{\mathrm{A}}, P_{\mathrm{B}}$ and the indicator function $\chi(\boldsymbol{v})$, the CADE $C_T^{\text{3-D}}$ for a transformed voxel, $T(\boldsymbol{v})$ can be computed as

$$C_{T(\boldsymbol{v})}^{\text{3-D}} = \boldsymbol{I}_{\mathrm{thr}}^{\mathrm{A}}\left(P_{\mathrm{A}}\left(T(\boldsymbol{v})\right)\right) \cdot \boldsymbol{I}_{\mathrm{thr}}^{\mathrm{B}}(P_{\mathrm{B}}(T(\boldsymbol{v}))) \cdot \chi(\boldsymbol{v}) \tag{9.8}$$

for a given rigid transformation T. This product is the mathematical equivalent of the three conditions introduced above.

If T is chosen suboptimally, the resulting 3-D CADE will be inconsistent with the CA observed in the 2-D images. That is, a pixel in the 2-D image is constrasted but no corresponding voxel along its projection ray is estimated as contrasted. This can be due to following reasons as shown in Figure 9.5: (a) the projection ray from a contrasted pixel does not intersect the left atrium as the LA has not been placed at the proper position yet; (b) the projection ray hits the LA, but all voxels intersected by this ray cannot contain CA because their corresponding pixels in the other

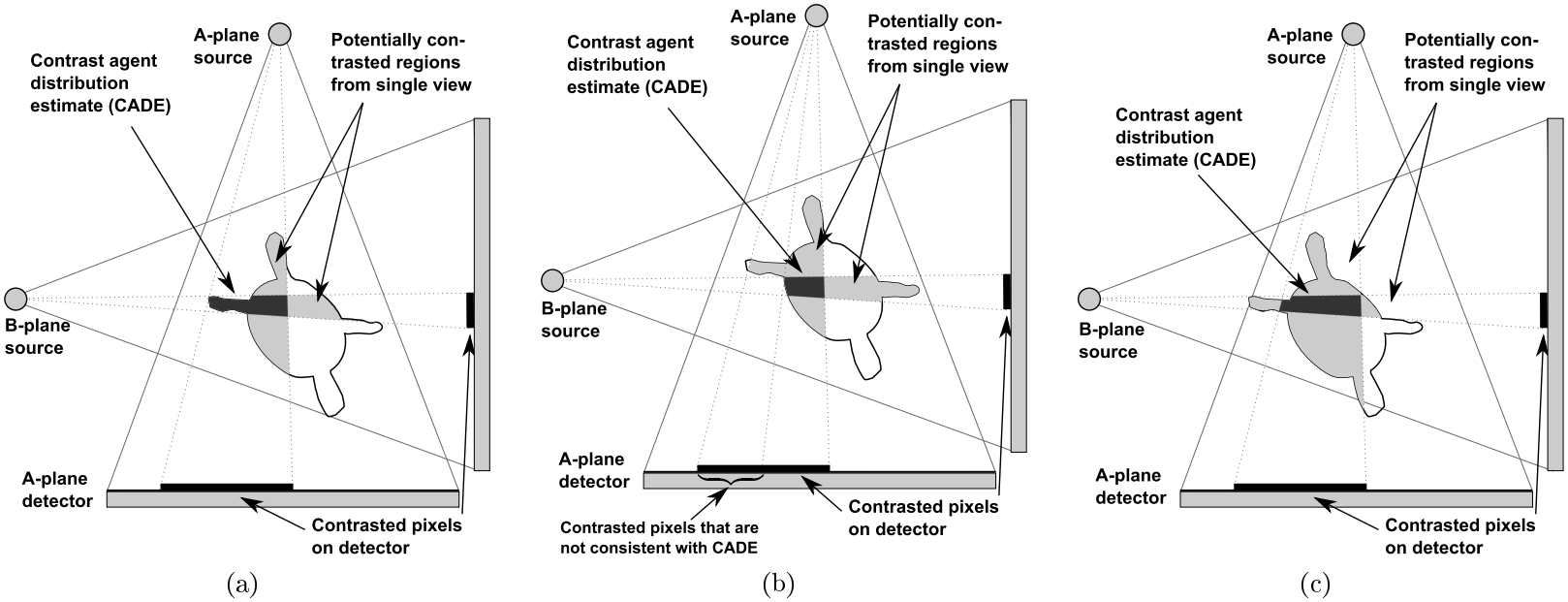

Figure 9.4: Top-down view on a left atrium and associated contrast-enhanced projections showing a correct registration (a) and two misregistrations (b) and (c). When looking at the contrasted pixels on each detector independently, all LA positions seem to be feasible. Considering the LA position in (b), the area, which can contain CA according to the combination of both detectors is, partially outside the LA. For the CADE, however, only CA inside the LA is considered. So, the registration in (b) gives rise to contrasted pixels on the A-plane detector that cannot be explained by the CADE. This will result in a low CADE value and indicate misregistration. There exist, however, also misregistrations that can lead to a consistent CADE as shown in (c). This is why a combination of CADE and edge-based methods yields improved results.

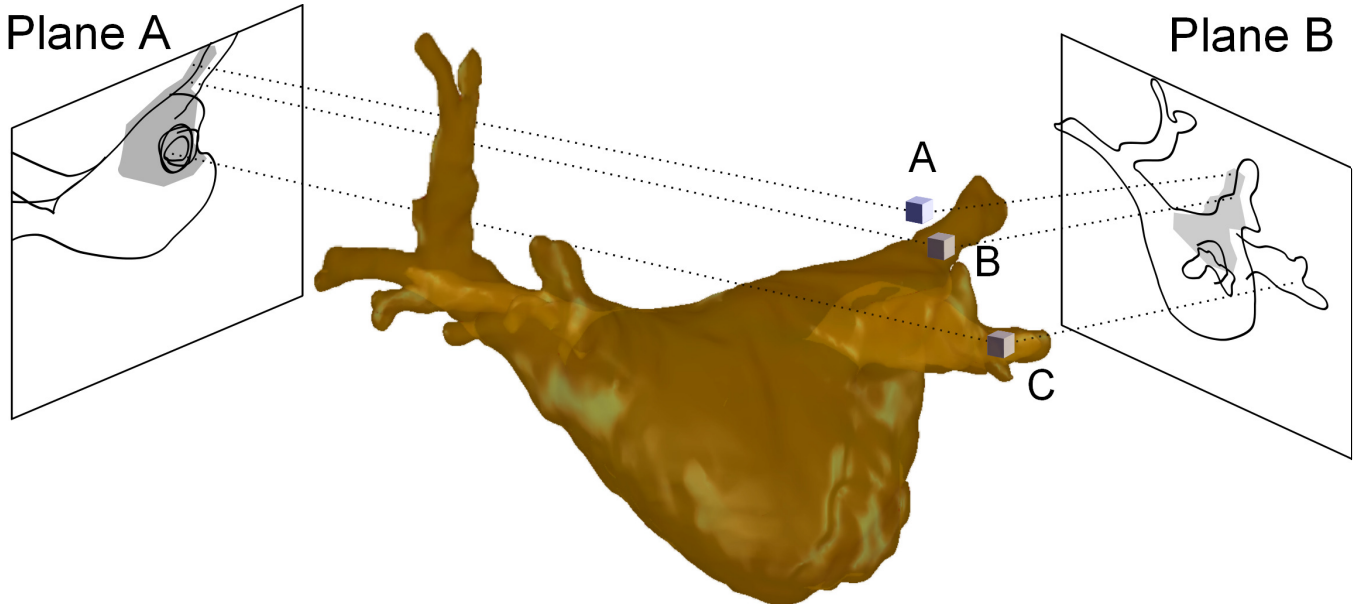

Figure 9.5: For the transformation shown, only voxel B is estimated as containing CA as it is inside the LA and contrasted in both planes. Voxel C is only contrasted in Plane A but not in Plane B. Voxel A is filled with contrast in both planes, but it is outside of the LA and therefore considered as uncontrasted. If the LA is moved such that its projections in A and B cover the contrasted area, this voxel will also be considered as contrasted, hence, increasing the consistency with the CADE.

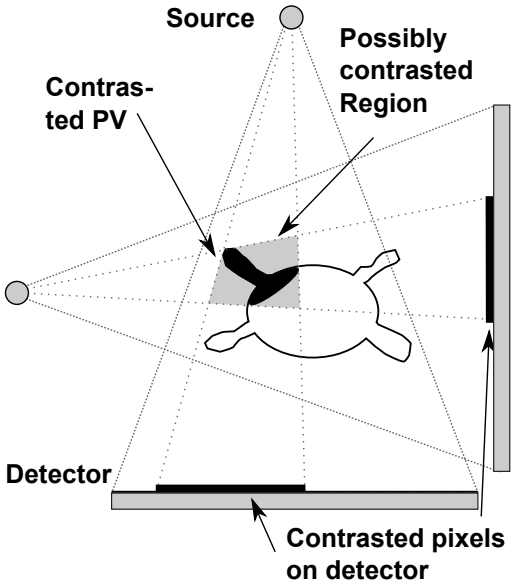

Figure 9.6: Top-down view on a left atrium with a contrasted pulmonary vein. The gray region denotes the area which may contain CA based on the CA observed in the 2-D images. If the number of contrasted voxels in the volume was to be optimized, the optimization process would find a transformation such that as much of the potentially contrasted region was included within the LA as possible causing a registration bias towards larger LA regions.

plane are uncontrasted. Additional inconsistencies are introduced by pixels which are erroneously labeled as contrasted e.g. due to motion artefacts. To verify the validity of the CADE, we compute binary 2-D images $\boldsymbol{C}_T^{\mathrm{A}}$, $\boldsymbol{C}_T^{\mathrm{B}}$ by forward projecting all contrasted voxels in $C_T^{\text{3-D}}$ using $P_{\mathrm{A}}, P_{\mathrm{B}}$. We assess the consistency of the CADE for the given transformation T by computing the similarity between the fluoroscopic images and the projected CADE by

$$\rho_{\mathrm{CADE}}(\boldsymbol{I}_{\mathrm{thr}}^{\mathrm{A}}, \boldsymbol{I}_{\mathrm{thr}}^{\mathrm{B}}, T) = \rho(\boldsymbol{I}_{\mathrm{thr}}^{\mathrm{A}}, \boldsymbol{C}_T^{\mathrm{A}}) \cdot \rho(\boldsymbol{I}_{\mathrm{thr}}^{\mathrm{B}}, \boldsymbol{C}_T^{\mathrm{B}}). \tag{9.9}$$

Alternatively, the number of contrasted voxels inside the volume could be maximized. The set of potentially contrasted voxels is defined by the intersection of the projection ray bundles of all contrasted pixels from view A and B, respectively. Maximizing the number of contrasted voxels would lead to a transformation such that as much as possible of this set is contained inside the LA. If, for example, a pulmonary vein was filled with CA, the transformation would be chosen such that the set of possible contrasted pixels was located in the main body of the LA which provides most space to include most possibly contrasted voxels, see Figure 9.6. To avoid this registration bias towards large structures inside the LA, we decided to optimize the consistency to the 2-D images.

The above mentioned similarity measures can be combined by computing a weighted sum, see Algorithm 3. Due to the shape of the similarity measure function, the capture range of the optimal transfrom for gradient-based methods is very small and the initialization may be beyond this capture range. Therefore we apply an octree-like coarse-to-fine scheme where we evaluate several positions at a coarse resolution. On transformations that yield a good similarity value, we perform subsequent evaluations at an increasingly finer resolution to find the transform $\hat{T}$ that maximizes the similarity. The registration method for a single frame is summarized in Algorithm 4.

Algorithm 3 ComputeSimilarityMeasure(
Preprocessed images $\boldsymbol{I}^{\mathrm{A}}_{\mathrm{DSA}}, \boldsymbol{I}^{\mathrm{A}}_{\mathrm{thr}}$ and $\boldsymbol{I}^{\mathrm{A}}_{\mathrm{DOG}}$,
Preprocessed images $\boldsymbol{I}^{\mathrm{B}}_{\mathrm{DSA}}, \boldsymbol{I}^{\mathrm{B}}_{\mathrm{thr}}$ and $\boldsymbol{I}^{\mathrm{B}}_{\mathrm{DOG}}$,
Mesh M, Transformation T, Projection Operators P_{A} and P_{B}):

$M_T \leftarrow$ Apply transformation T to M

$\boldsymbol{S}^{\mathrm{A}}_T \leftarrow$ Render shadow of M_T with projection given by P_{A}
$\boldsymbol{S}^{\mathrm{B}}_T \leftarrow$ Render shadow of M_T with projection given by P_{B}
$\boldsymbol{E}^{\mathrm{A}}_T \leftarrow$ Render edges of M_T with projection given by P_{A}
$\boldsymbol{E}^{\mathrm{B}}_T \leftarrow$ Render edges of M_T with projection given by P_{B}

for all voxels $\boldsymbol{v}$ in 3-D space **do**
  Compute if transformed voxel $T(\boldsymbol{v})$ contains contrast agent according to Equation 9.8 using $\boldsymbol{I}^{\mathrm{A}}_{\mathrm{thr}}, \boldsymbol{I}^{\mathrm{B}}_{\mathrm{thr}} M_T, P_{\mathrm{A}}$ and P_{B}
end for
$\boldsymbol{C}^{\mathrm{A}}_T \leftarrow$ Render all transformed voxels $T(\boldsymbol{v})$ containing contrast agent using P_{A}
$\boldsymbol{C}^{\mathrm{B}}_T \leftarrow$ Render all transformed voxels $T(\boldsymbol{v})$ containing contrast agent using P_{B}

if use $\rho^{\mathrm{DSA}}_{\mathrm{shad}}$ **then**
  $similarity \leftarrow \rho(\boldsymbol{I}^{\mathrm{A}}_{\mathrm{DSA}}, \boldsymbol{S}^{\mathrm{A}}_T) \cdot \rho(\boldsymbol{I}^{\mathrm{B}}_{\mathrm{DSA}}, \boldsymbol{S}^{\mathrm{B}}_T)$
else if use $\rho^{\mathrm{thr}}_{\mathrm{shad}}$ **then**
  $similarity \leftarrow \rho(\boldsymbol{I}^{\mathrm{A}}_{\mathrm{thr}}, \boldsymbol{S}^{\mathrm{A}}_T) \cdot \rho(\boldsymbol{I}^{\mathrm{B}}_{\mathrm{thr}}, \boldsymbol{S}^{\mathrm{B}}_T)$
else if use ρ_{CADE} **then**
  $similarity \leftarrow \rho(\boldsymbol{I}^{\mathrm{A}}_{\mathrm{thr}}, \boldsymbol{S}^{\mathrm{A}}_T) \cdot \rho(\boldsymbol{I}^{\mathrm{B}}_{\mathrm{thr}}, \boldsymbol{S}^{\mathrm{B}}_T)$
else
  $similarity \leftarrow 0$
end if
if use ρ_{edge} **then**
  $similarity \leftarrow similarity + \alpha \cdot \rho(\boldsymbol{I}^{\mathrm{A}}_{\mathrm{DOG}}, \boldsymbol{E}^{\mathrm{A}}_T) \cdot \rho(\boldsymbol{I}^{\mathrm{B}}_{\mathrm{DOG}}, \boldsymbol{E}^{\mathrm{B}}_T)$
end if

return *similarity*

Algorithm 4 RegisterSingleFrame(
Frames $\boldsymbol{I}^{\mathrm{A}}_{\mathrm{u}}$ of plane A without contrast agent,
Single frame $\boldsymbol{I}^{\mathrm{A}}_{\mathrm{c}}$ of plane A with contrast agent,
Frames $\boldsymbol{I}^{\mathrm{B}}_{\mathrm{u}}$ of plane B without contrast agent,
Single frame $\boldsymbol{I}^{\mathrm{B}}_{\mathrm{c}}$ of plane B with contrast agent,
3-D triangle mesh of patient's LA $M = (V_M, E_M)$,
Projection Operators P_{A} and P_{B})):

$\boldsymbol{I}^{\mathrm{A}}_{\mathrm{DSA}}, \boldsymbol{I}^{\mathrm{A}}_{\mathrm{thr}}, \boldsymbol{I}^{\mathrm{A}}_{\mathrm{DOG}} \leftarrow$ Preprocess$(\boldsymbol{I}^{\mathrm{A}}_{\mathrm{u}}, \boldsymbol{I}^{\mathrm{A}}_{\mathrm{c}})$
$\boldsymbol{I}^{\mathrm{B}}_{\mathrm{DSA}}, \boldsymbol{I}^{\mathrm{B}}_{\mathrm{thr}}, \boldsymbol{I}^{\mathrm{B}}_{\mathrm{DOG}} \leftarrow$ Preprocess$(\boldsymbol{I}^{\mathrm{B}}_{\mathrm{u}}, \boldsymbol{I}^{\mathrm{B}}_{\mathrm{c}})$
$\hat{T} \leftarrow \arg\max_T$ ComputeSimilarityMeasure$(\boldsymbol{I}^{\mathrm{A}}_{\mathrm{DSA}}, \boldsymbol{I}^{\mathrm{A}}_{\mathrm{thr}}, \boldsymbol{I}^{\mathrm{A}}_{\mathrm{DOG}}, \boldsymbol{I}^{\mathrm{B}}_{\mathrm{DSA}}, \boldsymbol{I}^{\mathrm{B}}_{\mathrm{thr}}, \boldsymbol{I}^{\mathrm{B}}_{\mathrm{DOG}}, M, T, P_{\mathrm{A}}, P_{\mathrm{B}})$

return $\hat{T}$

9.4 Experiments and Results

We retrospectively evaluated our method on 21 clinical biplane X-ray sequences from 10 different patients. All of the patients provided their informed consent for the analysis of their clinical data. For all patients, a segmentation of their left atrium from a preoperatively acquired MRI scan was available as a triangle-mesh. When using the CADE measure, this mesh was converted into a binary volume. The data set comprised 11 sequences showing an initial CA injection where 15 ml CA was injected into the LA centre through a sheath to verify the success of the transseptal puncture. Besides the sheath, only a coronary sinus catheter was present. There were 10 more sequences showing subsequent injections to verify catheter placement. In these cases, about 10 ml CA was injected and additional catheters were present. All X-ray angiography sequences were acquired during normal breathing using a standard acquisition protocol. This resulted in a total number of 133 contrasted frames. For our experiments, the first contrasted frame was determined manually. For 129 frames, reference registrations performed by three clinical experts were available, for the remaining four frames registrations performed by two clinical experts were available. Reference 3-D registrations were established by manually shifting the mesh rigidly in each of two orthogonal views. The resulting 3-D translation $\boldsymbol{t}$ was refined this way until a good match to the associated contrast distributions as seen in the two 2-D X-ray projections had been found. These reference registrations covered only 3-D translation for following reasons: First, patients were positioned head first, supine, both during pre-operative and intra-operative imaging. This patient positioning rules out large degrees of rotation a priori. Furthermore, given the small amounts of contrast injected in our cases, the remaining small rotations were very difficult to detect. This made it practically impossible for our clinical experts to reliably correct them. This is why we decided to evaluate our approach without rotation.

As initialization for optimization, the 3-D model was placed at that 3-D position which corresponded to the centres of both 2-D images. The 3-D translation $\hat{\boldsymbol{t}} = \arg\max_{\boldsymbol{t}} \rho(\boldsymbol{t})$ found by the optimization process of the respective objective function ρ was compared to the mean translation vector $\boldsymbol{t}^*$ of the three manual registration results. The distance $||\hat{\boldsymbol{t}} - \boldsymbol{t}^*||_2$ was used as error measure. The significance of the results was measured using a Wilcoxon signed-rank test [Wilc 45] and a significance level of $p = 0.05$.

All sequences contained 12-bit images of size 1024×1024 pixels, all image processing, including rendering from the 3-D model, was performed on the full image size. The kernel size for median filter was 30 pixels, the value s of Equation 9.5 was 0.1. The standard deviation of the DOG filter was 24 pixels.

In the evaluation, we compared the similarity measures $\rho^{\text{thr}}_{\text{shad}}$, $\rho^{\text{DSA}}_{\text{shad}}$, ρ_{CADE} and ρ_{edge} and the combined similarity measures $\rho^{\text{thr}}_{\text{shad}} + \alpha\rho_{\text{edge}}$, $\rho^{\text{DSA}}_{\text{shad}} + \alpha\rho_{\text{edge}}$ and $\rho_{\text{CADE}} + \alpha\rho_{\text{edge}}$. We investigated different weightings. Giving both terms equal weights, i.e. setting $\alpha = 1$, turned out to be a good choice. We did two types of evaluation: an evaluation on all frames and an evaluation using only a single frame of each sequence namely the one which provides the best similarity measure.

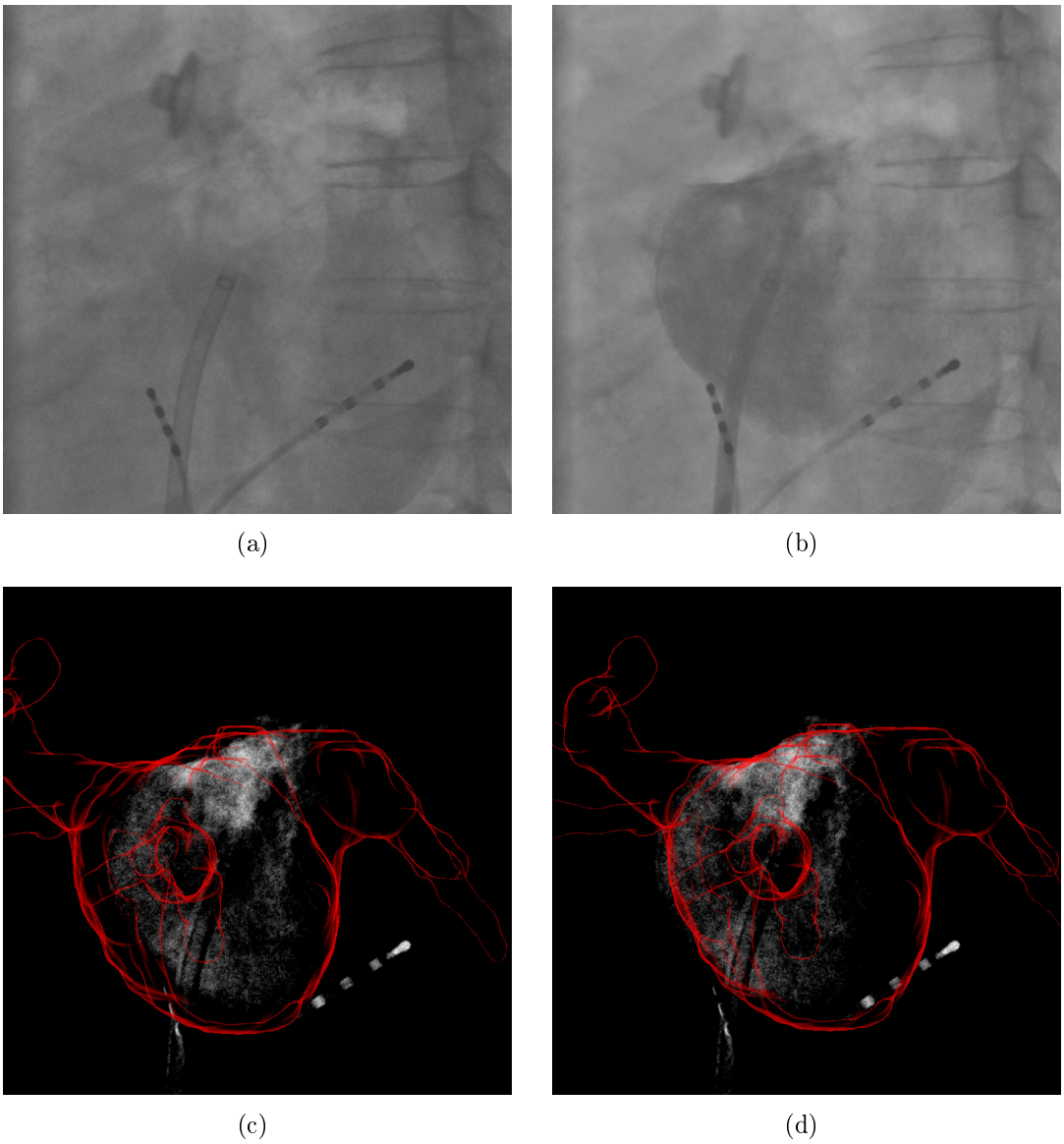

Figure 9.7: Uncontrasted (a) and contrasted (b) frame of an X-ray angiography. The registration result when using $\rho_{\text{shad}}^{\text{DSA}}$ (c) had an error of 6.7 mm. By using $\rho_{\text{CADE}}+\rho_{\text{edge}}$ (d), the left border of the LA model fits better to the left edge of the CA and the error reduced to 3.1 mm

9.4.1 Evaluation on all frames

We computed a registration for each contrasted frames and compared the result to the manual registration of the physicians. These results are clinically relevant if the physician requires a registration for a desired frame of his choice, e.g., depending on the breathing phase. As potentially every frame could be selected by the physician, the overall registration accuracy should be high. The overall accuracy is also of importance if the results are post-processed by temporal filtering.

Table 9.1: 3-D translation errors for all frames

Objective function	initial injection	subsequent injections
Thivierge-Gaulin	11.4±8.8 mm	10.4±5.4 mm
$\rho_{\text{shad}}^{\text{DSA}}$	9.3±6.9 mm	9.8±4.8 mm
$\rho_{\text{shad}}^{\text{thr}}$	9.9±7.9 mm	12.1±9.1 mm
ρ_{edge}	12.0±8.9 mm	14.6±8.7 mm
ρ_{CADE}	**8.7±6.4 mm**	**9.0±5.9 mm**
$\rho_{\text{shad}}^{\text{DSA}} + \rho_{\text{edge}}$	8.3±6.6 mm	9.6±5.4 mm
$\rho_{\text{shad}}^{\text{thr}} + \rho_{\text{edge}}$	8.3±6.7 mm	10.5±7.6 mm
$\rho_{\text{CADE}} + \rho_{\text{edge}}$	**7.9±6.3 mm**	**8.8±6.7 mm**
Clinical experts	3.3±2.7 mm	3.1±1.7 mm

The evaluation results are presented in Table 9.1. The overall inter-user-variablity observed in the manual registrations was 3.2±2.3 mm. Considering all sequences, ρ_{CADE} performed significantly better than $\rho_{\text{shad}}^{\text{thr}}$, $\rho_{\text{shad}}^{\text{DSA}}$ and the state-of-the-art method by Thivierge-Gaulin [Thiv 12]. Although ρ_{edge} gave significantly worse results than all other measures, a combination with ρ_{edge} could improve the results of $\rho_{\text{shad}}^{\text{thr}}$ and $\rho_{\text{shad}}^{\text{DSA}}$ significantly. For subsequent injections, $\rho_{\text{CADE}} + \rho_{\text{edge}}$ performed significantly better than $\rho_{\text{shad}}^{\text{thr}}$, $\rho_{\text{shad}}^{\text{DSA}}$, their respective combinations with ρ_{edge} and the method by Thivierge-Gaulin *et al.* [Thiv 12].

For $\rho_{\text{shad}}^{\text{thr}} + \rho_{\text{edge}}$ and $\rho_{\text{CADE}} + \rho_{\text{edge}}$, the error distribution for each sequence is shown in Figure 9.8, first for all initial injections and then for subsequent injections. In Figure 9.9, the error distribution is given for each frame number as counted after the CA injection. An example for a result is shown in Figure 9.7.

9.4.2 Evaluation on a single frame

Figure 9.8 indicates that many sequences have at least one frame with a registration error of less than 5 mm. In fact, there exists such a frame for over 75 % of all sequences when using $\rho_{\text{shad}}^{\text{DSA}}$ or $\rho_{\text{shad}}^{\text{thr}}$ and for over 85 % of the sequences when using ρ_{CADE}, $\rho_{\text{shad}}^{\text{DSA}} + \rho_{\text{edge}}$, $\rho_{\text{shad}}^{\text{thr}} + \rho_{\text{edge}}$ or $\rho_{\text{CADE}} + \rho_{\text{edge}}$. Zhao *et al.* [Zhao 13] proposed to automatically find a good frame in each sequence and consider only these single good frames for evaluation. In other words, from all frames of a sequence, a single frame was automatically chosen for registration. From a clinical point of view, this would, however, only make sense if the physician accepted an automatically selected frame for registration or if further motion compensation steps for the other frames were done, e.g. using device tracking [Bros 10b].

Zhao *et al.* suggested to select this single frame as follows: For each frame $i \in [1, m]$ out of the m contrasted frames, the transform T_i that maximizes the similarity measure ρ for this frame is computed. In a second step, going through all frames of a sequence, the frame with the highest overall similarity measure is picked. The associated transform is denoted $\hat{T}_i$. For the rigid translations $\boldsymbol{t} \in \mathbb{R}^3$ that we use for

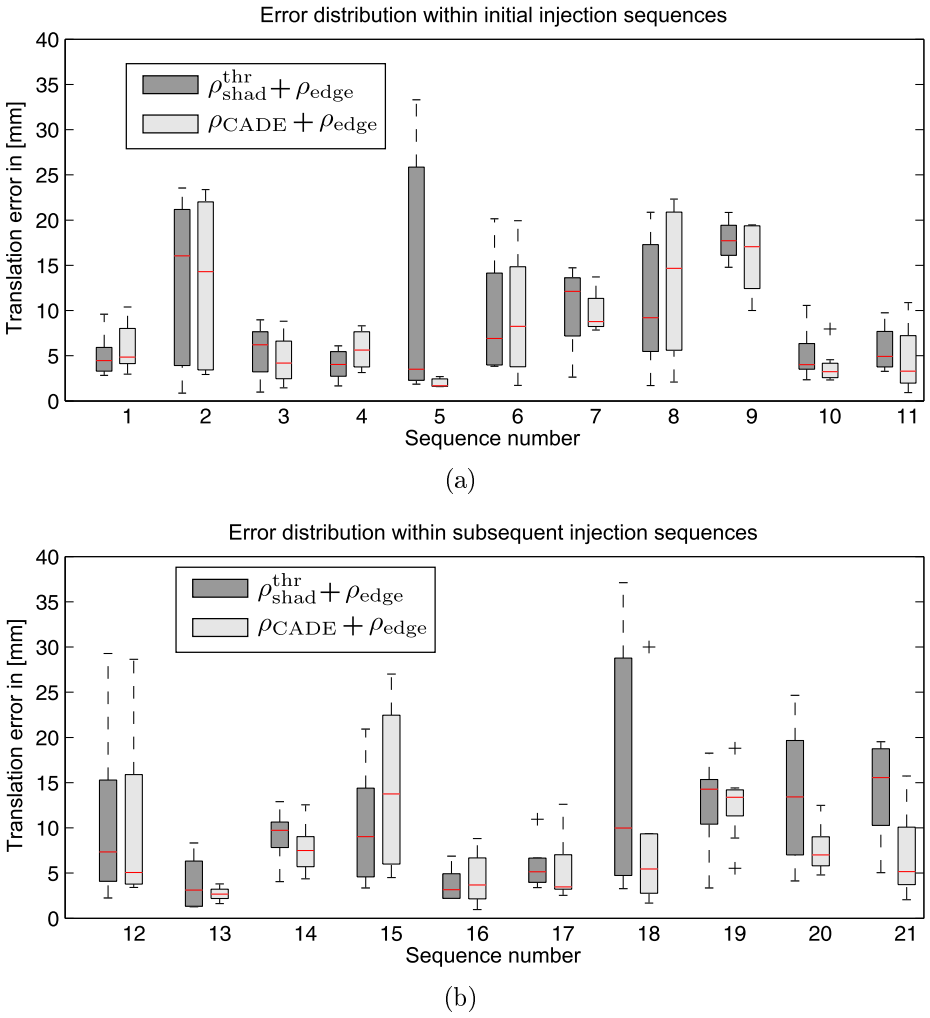

Figure 9.8: Distribution of the errors within each sequence. While there is no significant difference for initial injections (a), $\rho_{\text{CADE}} + \rho_{\text{edge}}$ performs significantly better than $\rho^{\text{thr}}_{\text{shad}} + \rho_{\text{edge}}$ for subsequent injections (b). Subsequent contrast injections are characterized by a smaller amount of contrast and the presence of more catheters making registration more difficult. Example images of sequence 1 are shown in Figure 9.2 and Figure 9.3, example images of sequence 2 are shown in Figure 9.1(a). Here, CA is very faint, and in some frames contrasted is already ejected into the left ventricle. Sequence 5 is shown in Figure 9.1(d). In this case, $\rho^{\text{thr}}_{\text{shad}} + \rho_{\text{edge}}$ got confused by edges caused by motion artefacts.

evaluation, the error to the average manual registration result $\boldsymbol{t}^*_i$ is then computed as

$$||\hat{\boldsymbol{t}}_i - \boldsymbol{t}^*_i||_2 \quad \text{with} \quad \hat{\boldsymbol{t}}_i = \arg\max_i \rho(\boldsymbol{I}^{\text{A},i}, \boldsymbol{I}^{\text{B},i}, \boldsymbol{t}_i) \quad \text{and} \quad \boldsymbol{t}_i = \arg\max_{\boldsymbol{t}} \rho(\boldsymbol{I}^{\text{A},i}, \boldsymbol{I}^{\text{B},i}, \boldsymbol{t}) \tag{9.10}$$

The evaluation results are presented in Table 9.2. Recalling subsection 9.4.1, where we found that the CADE method yielded good results for all frames, the CADE performance for a single frame was, however, not that good. This is why we

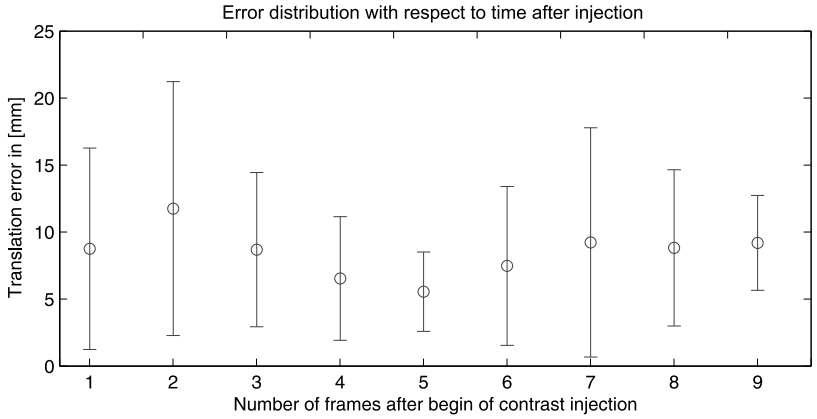

Figure 9.9: Average registration errors of $\rho_{\text{CADE}} + \rho_{\text{edge}}$ depending on the position of the frame after start of the CA injection calculated over all sequences. Frame 1 denotes the first frame which contained CA. The average error at the second frame after the CA injection was 11.8 mm ± 9.5 mm, the average error at the fifth frame was 5.5 mm ± 3.0 mm. The frame rate of all sequences was 7.5 fps. Assuming a heart rate of 60 bpm, one heart cycle takes approximately 7 frames. So, a first portion of CA is ejected into the ventricle not later than at the 7th frame. Note that the number of sequences used for calculation was not constant for each frame number as several sequences had fewer than nine contrasted frames.

investigated if a different single frame selection strategy would lead to better results. Instead of using ρ_{CADE} both for translation estimation and best frame selection, we used ρ_{CADE} only for estimating the translation $\boldsymbol{t}_i$ for each frame i. Among the obtained translations $\boldsymbol{t}_i$, we selected the frame i with the corresponding translation $\hat{\boldsymbol{t}}_i$ such that $\rho^{\text{thr}}_{\text{shad}}$ was maximized. So, Equation 9.10 was modified to

$$\begin{aligned} ||\hat{\boldsymbol{t}}_i - \boldsymbol{t}_i^*||_2 \quad \text{with} \quad \hat{\boldsymbol{t}}_i &= \arg\max_i \rho^{\text{thr}}_{\text{shad}}(\boldsymbol{I}^{\text{A},i}_{\text{thr}}, \boldsymbol{I}^{\text{B},i}_{\text{thr}}, \boldsymbol{t}_i) \\ \text{and} \quad \boldsymbol{t}_i &= \arg\max_{\boldsymbol{t}} \rho_{\text{CADE}}(\boldsymbol{I}^{\text{A},i}_{\text{thr}}, \boldsymbol{I}^{\text{B},i}_{\text{thr}}, \boldsymbol{t}) \end{aligned} \tag{9.11}$$

The results of this frame selection method are denoted by $\rho_{\text{CADE}} \triangleright \rho^{\text{thr}}_{\text{shad}}$. We did the same also for the combination with ρ_{edge}. Although only 10 sequences were available for initial contrast injections, $\rho^{\text{DSA}}_{\text{shad}}$, $\rho^{\text{thr}}_{\text{shad}} + \rho_{\text{edge}}$, and $(\rho_{\text{CADE}} + \rho_{\text{edge}}) \triangleright (\rho^{\text{thr}}_{\text{shad}} + \rho_{\text{edge}})$ gave significant better results when compared to $\rho^{\text{thr}}_{\text{shad}}$. Also the performance of ρ_{edge} was significantly less. For subsequent injections, our proposed method $\rho_{\text{CADE}} \triangleright \rho^{\text{thr}}_{\text{shad}}$ and the corresponding combination with ρ_{edge} outperformed the method by Thivierge-Gaulin *et al.*.

9.4.3 Runtime performance

The image preprocessing took 0.5 s on an Intel Xeon E3 with 3.4 GHz and 16 GB RAM. The evaluations of the similarity measures were performed completely on the GPU. On an NVIDIA GeForce GTX 660 the evaluation of $\rho^{\text{DSA}}_{\text{shad}}$, $\rho^{\text{thr}}_{\text{shad}}$ or ρ_{edge} took 1.8 ms for a given translation and 13.4±3.7 ms for ρ_{CADE}. The whole registration for a single frame took 2.9 s for $\rho^{\text{DSA}}_{\text{shad}}$ or $\rho^{\text{thr}}_{\text{shad}}$ and 21.5±5.9 s for ρ_{CADE}. For a combination

Table 9.2: 3-D translation errors for single automatically chosen frame as described in Eqs. 9.10 and 9.11

Objective function	initial injection	subsequent injections
Thivierge-Gaulin	8.3±8.2 mm	10.6±4.4 mm
$\rho_{\text{shad}}^{\text{DSA}}$	5.1±3.8 mm	9.6±5.1 mm
$\rho_{\text{shad}}^{\text{thr}}$	7.1±4.3 mm	8.1±6.6 mm
ρ_{edge}	14.1±10.0 mm	12.1±9.1 mm
ρ_{CADE}	6.0±5.0 mm	**7.0±3.8 mm**
$\rho_{\text{CADE}} \triangleright \rho_{\text{shad}}^{\text{thr}}$	***5.0 ± 5.0 mm***	*7.7 ± 4.9 mm*
$\rho_{\text{shad}}^{\text{DSA}} + \rho_{\text{edge}}$	5.1±4.2 mm	8.5±4.7 mm
$\rho_{\text{shad}}^{\text{thr}} + \rho_{\text{edge}}$	4.8±4.6 mm	7.8±5.7 mm
$\rho_{\text{CADE}} + \rho_{\text{edge}}$	6.1±5.8 mm	7.6±5.5 mm
$(\rho_{\text{CADE}} + \rho_{\text{edge}}) \triangleright (\rho_{\text{shad}}^{\text{thr}} + \rho_{\text{edge}})$	***4.6 ± 4.0 mm***	***7.3 ± 5.2 mm***

with ρ_{edge} it took 5.8 s and 27.1±5.9 s, respectively. Please note that the code for ρ_{CADE} has not been optimized for runtime performance, yet.

9.5 Discussion and Conclusions

Similarity Measures. Our novel CADE based method outperformed the shadow based similarity measures $\rho_{\text{shad}}^{\text{DSA}}$ and $\rho_{\text{shad}}^{\text{thr}}$, especially for re-registration sequences where only a small amount of CA was used. The problem with non-distinct optima for shadow based similarity measures which was already sketched in Figure 9.2 becomes also apparent in the sections of the optimization function in Figure 9.10 for $\rho_{\text{shad}}^{\text{thr}}$: for a small amount of CA like in Figure 9.10 (a), the optimum is not at the position of the ground truth, but about 15 mm off. Also for secondary injections into small structures such as the pulmonary veins, the objective function for $\rho_{\text{shad}}^{\text{thr}}$ in Figure 9.10 (c) has a large plateau. In both cases, ρ_{CADE} is more distinct, although clear extrema as for bones [Livy 03] are not obtained. Especially for secondary injections where CA was often injected into pulmonary veins, registration errors leading to inconsistent results could be avoided by ρ_{CADE}. For well contrasted sequences, the improvement by ρ_{CADE} was less as inconsistencies played only a minor role and the shape of the contrasted region in the image was more similar to the projected shadow of the left atrium. This becomes also apparent in Figure 9.10 (b) where the shapes of the objective function of $\rho_{\text{shad}}^{\text{thr}}$ and ρ_{CADE} look very similar.

We found that the similarity measure using explicit apparent edges, ρ_{edge}, yielded poor results when used on its own. A possible reason is that the objective function of ρ_{edge} has several local optima and also the global optimum does not necessarily correspond to the ground truth position. However, ρ_{edge} can improve results significantly when combined with other similarity measures. It often has a more distinct local optimum at the position of the ground truth that facilitates fine registration. This is important as the other similarity measures define a rather plateau-shaped optimal region.

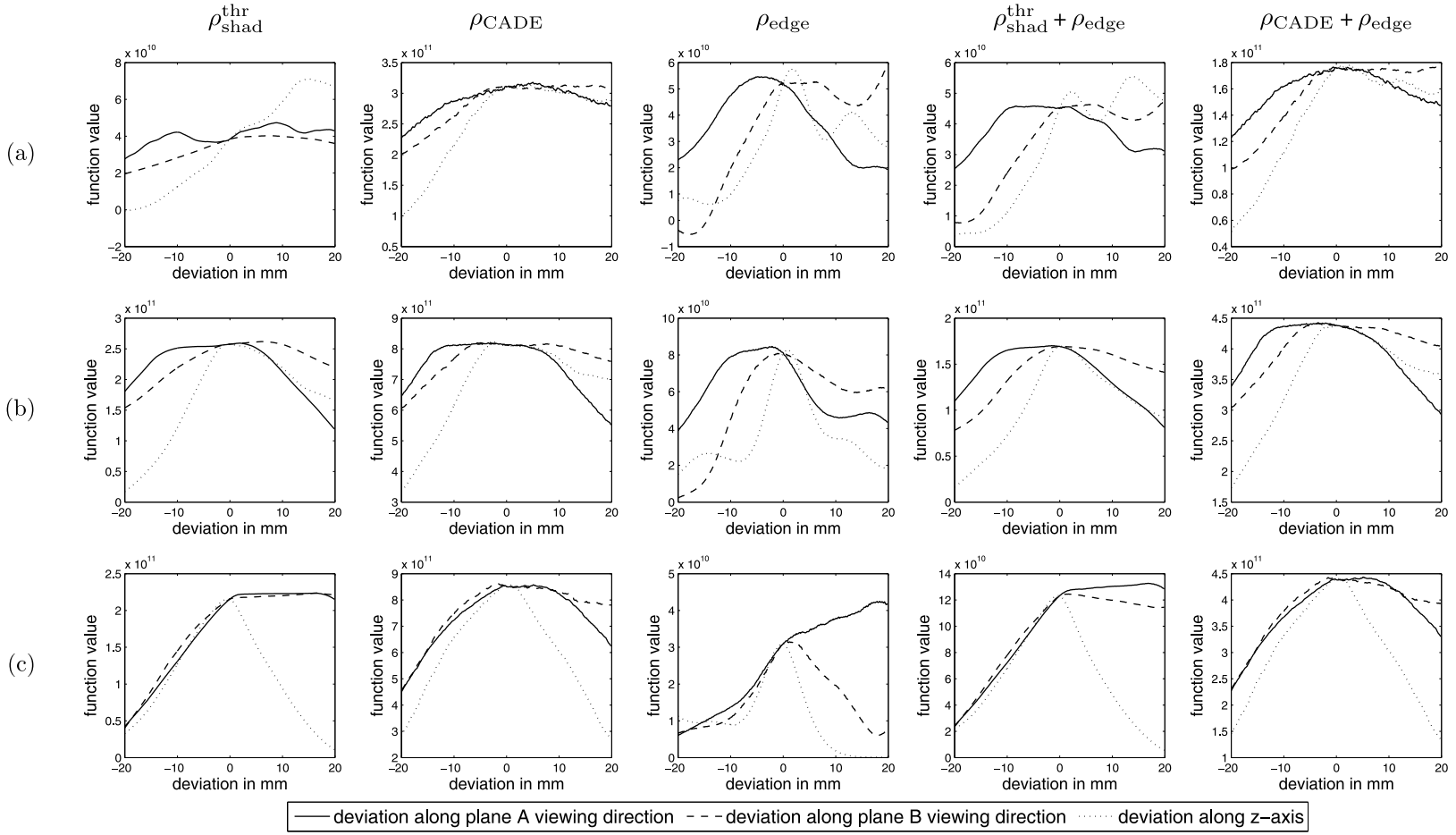

Figure 9.10: Optimization function values along sections through the ground truth position. The sections were done along the viewing direction of the detector in plane A, the corresponding orthogonal direction in the transverse plane and the z-axis of the patient coordinate system which corresponds to the cranial-caudal axis. The intersections are shown for three different frames: (a) one of the first frames of an initial injection, see Figure 9.3, (b) a frame of the same injection but with large parts of the left atrium contrasted, and (c) a secondary injection into a pulmonary vein, see Figure 9.1(g). The plots for $\rho_{\text{shad}}^{\text{DSA}}$ were left out as they look very similar as for $\rho_{\text{shad}}^{\text{thr}}$.

Time-Dependency. Figure 9.9 shows that the accuracy of the registration depends on when the frame was recorded after CA injection. The best results were achieved at the 5th frame. This was in many cases the frame before the ejection into the ventricle, i.e. it contains most CA. Especially for the first frames, where only little CA was present, registration accuracy was lower. The first frame is an exception, as it has a lower mean error than the second frame. This is probably because the previous frame, i.e. the last uncontrasted frame, is used as mask frame for DSA computation which leads to low motion artefacts and a better extraction of the contrasted region.

Best Frame Selection. We found that for our registration to work best, a well opacified frame should be selected from the sequence. This strategy was evaluated in the context of the single-frame-evaluation by selecting the frame which had the best objective function value. For methods like $\rho_{\text{shad}}^{\text{DSA}}$ and $\rho_{\text{shad}}^{\text{thr}}$, which are based on the projection shadow, the best frame usually corresponded to the most contrasted frame. The measure ρ_{CADE}, however, is not related to the amount of CA, but it depends on consistency. When relying on ρ_{CADE} for best frame selection, we get the frame yielding the most consistent registration. This is, however, not necessarily the frame with the most CA. And it is usually the frame with the most CA which provides most information for registration. We believe that this is the reason why the errors in Table 9.2 for ρ_{CADE} are higher. If, however, from the translations estimated by $\rho_{\text{CADE}}+\rho_{\text{edge}}$, the single frame was selected based on $\rho_{\text{shad}}^{\text{thr}}+\rho_{\text{edge}}$, better results were achieved as now again the frames with most CA were selected.

Sometimes, the automatic best frame selection does not provide a frame with a satisfactory result. Still, 85 % of all sequences contain at least one frame that is below a clinical relevant threshold of 5 mm [King 09, Hous 13]. To benefit from the fact that at least one frame with a good registration result is likely to be found, the frame selection could be performed manually by stepping through the frames and the associated registration results. The user can then quickly select the frame with the best registration result. Although this implementation still involves user input, the required user interaction is less than for fully manual registration.

For the remaining 15 % of the cases, or if higher accuracy level, e.g., 3 mm [Bour 14] is required, small manual adjustment may be necessary in these cases.

Runtime Performance. It is notable that the run-time for ρ_{CADE} was considerably higher compared to, e.g., $\rho_{\text{shad}}^{\text{thr}}$. This is because the CA distribution needs to be updated in each iteration before projecting it. Moreover, this part of the implementation has not yet been optimized. Although the fast run-time of e.g. $\rho_{\text{shad}}^{\text{thr}}$ will remain out of reach, we are confident that the run-time for ρ_{CADE} could be reduced to a clinically acceptable level.

Impact of Clinical Issues. In general, the performance for initial registration was better, as the amount of CA was higher and fewer catheter artefacts were present. We found by visual inspection that also the amount of breathing motion had an impact on the registration accuracy as it caused motion artefacts in the DSA computation. As a consequence, if the patient was not anesthetized, an acquisition of the CA injection should be performed under breath-hold or shallow breathing. For cases with

intubation, also jet ventilation [Good 06] or a small period of apnea could be applied to reduce breathing motion. Since our data was not acquired using a dedicated DSA program, the different brightness levels within a sequence changed. This interfered with the subtraction image computation. Although intuitively appealing, our data did not allow us to make a statement if the registration accuracy depends on the part of the LA in which CA was injected.

For initial contrast injections, an average accuracy of 4.6 ± 4.0 mm and a median error of 3.7 mm could be achieved using $\rho_{\text{CADE}} + \rho_{\text{edge}}$ together with the best-frame selection approach. This error is in the range of the inter-user-variability of 3.2 ± 2.3 mm. The faster registration method using $\rho_{\text{shad}}^{\text{thr}} + \rho_{\text{edge}}$ reached an accuracy of 4.8 ± 4.6 mm. These numbers are also similar to the accuracy reported when performing manual registration based on segmentations of the CS, the whole heart, and the spine [Bour 16] or a segmentation of the CS when 3-D and 2-D data are in the same breathing and cardiac phase [Hoff 16g] which was achieved by ventilation and rapid pacing of anesthetized patients. However, our method does not require other structures than the LA to be segmented and requires no anesthesia. Compared to a registration based on the CS alone [Bour 10], the error was reduced by over 50 %.

Though our results for $\rho_{\text{CADE}} + \rho_{\text{edge}}$ are close to the 5 mm threshold [King 09, Hous 13], it remains open if this is sufficient for a clinical application, but we believe that these results should at least provide users with an acceptable initial estimate for further manual adjustments.

Conclusions. Compared to the approach by Zhao *et al.* [Zhao 13], the use of special weights for different heart regions is not needed for any of the proposed approaches. In addition, for $\rho_{\text{shad}}^{\text{thr}} + \rho_{\text{edge}}$, a time consuming DRR generation can be avoided. As a result, a registration approach based on a combination of shadow and edge features can be computed fast. If sufficient computational power was available, the novel CADE-based measure, which takes consistency into account, should be used as it improves results significantly, especially when very small amounts of CA are injected.

CHAPTER 10

Motion-Constrained Registration to all Frames of a Contrasted Fluoroscopic Sequence

In this chapter, we propose two methods for improving the registration results obtained by the contrast based registration presented in chapter 9. The first method performs a retrospective smoothing based on a Markov chain framework, the second method incorporates a regularizer to constrain cardiac motion. Both methods were published at ISBI [Hoff 16a] and parts of this chapter are also published in the International Journal of Biomedical Imaging [Hoff 16d].

10.1 Motivation

The contrast based registration method presented in chapter 9 estimates a registration for a single frame, independently of other frames within an angiography sequence. During manual registration, however, the physician includes also information from other frames. For example, the physician performs a registration based on a single frame and watches then the angiography sequence frame by frame. The mesh may be aligned during this process to structures that are only visible in a different frame than the frame used before. This, however, is only possible as the heart moves only little for high frame rates.

The evaluation results for single frame registration in section 9.4 have shown that there are single frames with poor registration results next to frames with an accurate registration. In this chapter, we describe two methods to improve poor registration

results based on accurate registration results in the previous and following frames, respectively.

10.2 Related Work

Motion constraints for registration of 3-D models to 2-D X-ray images were applied by Berger *et al.* [Berg 15]. Here, the goal was to perform a 3-D reconstruction from projection images of moving bones. As the motion is smooth, a regularization term to minimize the difference between estimated 3-D position and the low-pass filtered 3-D position was added to the similarity measure. Also the method by Rivest *et al.* [Rive 12] uses a regularizer to restrict the difference in the transformation from one frame to the other.

Esteghamatian *et al.* used an stochastic approach to incorporate breathing motion into real-time 3-D registration. Based on the position and motion from previous frames, he guessed an initalization for registration using an extended Kalman filter [Este 08]. In our work, the goal is not to predict the new registration based on observations from the past, but to retrospectively filter our results based on all observations.

Another statistical approach for registration [Ambr 15] was proposed by Ambrosini *et al.*. Here, a 3-D vessel tree is registered to a 2-D catheter in fluoroscopic images which is placed within the vessel tree. Tracking of the catheter was performed with the help of a Hidden Markov Model. The states correspond to positions of the catheter tip within the vessel tree and the observation of each state is related to the similarity value of the associated registration result. This method is similar to ours, however, we managed to model our framework more simple using a Markov chain by assigning each state a single observation.

10.3 Markov Chain Motion Filtering

To exploit dependencies between successive frames of a sequence, we model the position of the LA model in 3-D as a time-dependent continuous Markov chain of first order. The states are transformations T which are not restricted to a certain transformation type, as long as a distance measure between two transformations can be computed[1]. The parameter τ_i denotes the actual transformation of the LA in the i-th contrasted frame, T_i refers to the estimate of the transformation for the i-th frame and $P(\tau_i = T_i)$ is the probability that for frame i the transformation T_i is observed. For convenience, we define $P(T_i) = P(\tau_i = T_i)$. The transition probability from one state into another is independent of the frame number i. It is is denoted as

[1] We discussed in chapter 9 that rotation plays only a minor role for contrast-based registration. Therefore, we restrict the transformation later to translation only. To apply the method to rotations, a distance between two rotations needs to be computed, e.g., as the difference of rotation component values with respect to the patient's body axes or by using the absolute value of the angle between both rotations.

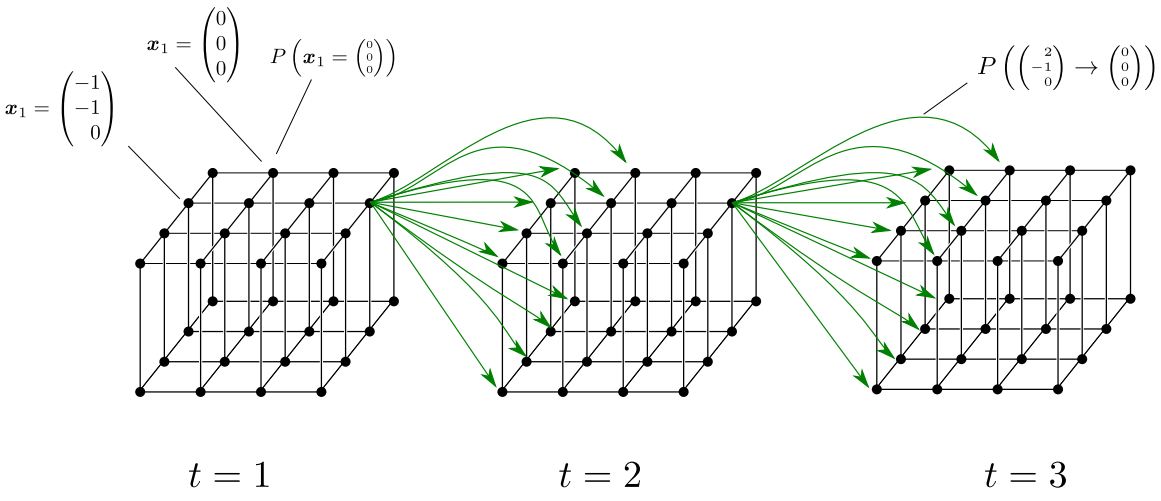

Figure 10.1: Visualization of the graph belonging to the Markov chain. In this figure, the states are discretized for sake of visualization. The graph comprises a set of states for each point in time t. Each state represents a translation of the 3-D model. Each state within a group belonging to time t has directed edges to all states belonging to group $t+1$. For sake of visualization, most of these edges are not drawn in this figure. The transition probabilities are split into an independent state probability and a transition probability that depends on the previous state. The state probability which describes how likely a translation is the correct registration for a point in time t. The transition probability describes the likeliness of the respective motion of the LA.

$P(T_i \rightarrow T_{i+1})$. Finally, a sequence of transformation $T_1, \ldots, T_n$ is to be determined such that the term

$$P(T_1, \ldots, T_n) = P(T_1) \cdot \prod_{t=2}^{n} (P(T_{t-1} \rightarrow T_t) \cdot P(T_t)) \tag{10.1}$$

is maximized.

Transition probabilities and state probabilities control the filtering differently: Due to the transition probabilities, small motions of the LA from a frame to its next frame are preferred. This results in an averaging of the LA transformation over time. The state probability determines the impact of the averaging, i.e. how much the registration result is changed by the filtering. We will model the state probability based on a confidence measure such that frames with a high-confidence registration results are less subject to temporal filtering. If the confidence value is low, i.e., the estimated error of the registration result is higher, we want to rely more on the results of the previous and next frame. Thus, high temporal averaging is performed for frames with a low confidence value. The state probabilities and the transition probability are determined as follows.

State Probability

The contrast agent visible in frame i determines the probability of the LA for being transfromed by T_i in this frame. If the dependency on other frames is ignored, the

most probable transformation T_i' is the transformation obtained by optimizing the similarity measures ρ defined in Eqs. (9.3), (9.4), (9.6) and (9.8) or a combination of them. The higher the distance between a transformation T_i and T_i' is, the lower is the state probability $P(T_i)$

The similarity measure $\rho(\boldsymbol{I}^{\mathrm{A},i}, \boldsymbol{I}^{\mathrm{B},i}, T_i')$ depends on the contents of the images $\boldsymbol{I}^{\mathrm{A},i}, \boldsymbol{I}^{\mathrm{B},i}$. Zhao *et al.* suggested to use the value $\rho(\boldsymbol{I}^{\mathrm{A},i}, \boldsymbol{I}^{\mathrm{B},i}, T_i')$ as a confidence measure: From all n registration results, the frame i where $\rho(\boldsymbol{I}^{\mathrm{A},i}, \boldsymbol{I}^{\mathrm{B},i}, T_i')$ is maximum should be selected as registration result for the complete sequence.

We confirmed a correlation of ρ and the registration error when using translations $\boldsymbol{t} \in \mathbb{R}^3$ as transformations T. The value of ρ can therefore be used as a confidence measure. By linear regression, a function $e(\rho(\boldsymbol{I}^{\mathrm{A},i}, \boldsymbol{I}^{\mathrm{B},i}, \boldsymbol{t}_i'))$ can be determined to estimate the error based on the value of ρ. With the translation $\boldsymbol{t}_i'$ of the LA found during optimization for frame i, the probability $P(\boldsymbol{t}_i)$ can be modelled as normal distribution

$$P(\boldsymbol{t}_i) = \mathcal{N}\left(\boldsymbol{t}_i; \boldsymbol{t}_i', \boldsymbol{\Sigma}_i\right). \tag{10.2}$$

So, the distance measure between the two translations is the Mahalanobis-distance that incorporates the confidence measure by setting the covariance matrix $\boldsymbol{\Sigma}_i$ to $\boldsymbol{1} \cdot e(\rho(\boldsymbol{I}^{\mathrm{A},i}, \boldsymbol{I}^{\mathrm{B},i}, \boldsymbol{t}_i'))$.

Transition Probability

The transition probability $P(T_{t-1} \to T_t)$ states how likely a movement of the LA is from frame $t-1$ to t. Over multiple breathing cycles, the LA moves about a mean position. So, the mean transformation is the identity. The likelihood of a transformation change depends on the magnitude of the change. The larger the change in translation and rotation is, the less likely is the transformation transition. To account for common motion patterns, like longitudinal motion due to breathing, motion components can be weighted differently.

When using translations $\boldsymbol{t}$ as transformations, we scale the distance between two successive translations by the translational velocity $\boldsymbol{v} \in \mathbb{R}^3$. In a training step, velocity vectors are computed for annotated data. The covariance matrix $\boldsymbol{\Sigma}_{\boldsymbol{v}}$ of the velocities gives an estimate for how likely a transition from one translation to the next is. We model the probability of a transition $\boldsymbol{t}_{t-1} \to \boldsymbol{t}_t$ as a normal distribution

$$P(\boldsymbol{t}_{t-1} \to \boldsymbol{t}_t) = \mathcal{N}\left((\boldsymbol{t}_t - \boldsymbol{t}_{t-1}) \cdot r; \boldsymbol{0}, \boldsymbol{\Sigma}_{\boldsymbol{v}}\right). \tag{10.3}$$

Besides the frame rate r, the transition probability depends also on the current breathing phase. Compared to breathing motion, cardiac motion can be neglected for translations as it rather deforms the LA. If information on the breathing phase can be estimated [Fisc 14], superior motion should be, e.g., more likely during the inhale phase. During exhale phase, inferior motion should have a higher probability. To account for breathing motion, e.g., the mean value and the covariance matrix could be estimated separately for each stage of the breathing cycle.

Most Probable State Sequence

The most likely state sequence,

$$\hat{\boldsymbol{t}}_1, \ldots, \hat{\boldsymbol{t}}_n = \underset{\boldsymbol{t}_1,\ldots,\boldsymbol{t}_n}{\arg\max}\, P(\boldsymbol{t}_1, \ldots, \boldsymbol{t}_n). \tag{10.4}$$

can be found using a log-likelihood method: By applying the logarithm to Equation 10.2 and Equation 10.3, we get

$$\begin{aligned}\hat{\boldsymbol{t}}_1, \ldots, \hat{\boldsymbol{t}}_n = \underset{\boldsymbol{t}_1 \ldots \boldsymbol{t}_n}{\arg\max} -\frac{1}{2} \Bigg(& (\boldsymbol{t}_1 - \boldsymbol{t}'_1)^\intercal \boldsymbol{\Sigma}_1^{-1} (\boldsymbol{t}_1 - \boldsymbol{t}'_1) \\ & + \sum_{i=2}^{n} \Big((\boldsymbol{t}_i - \boldsymbol{t}'_i)^\intercal \boldsymbol{\Sigma}_i^{-1} (\boldsymbol{t}_i - \boldsymbol{t}'_i) + \\ & r \cdot (\boldsymbol{t}_i - \boldsymbol{t}_{i-1})^\intercal \boldsymbol{\Sigma}_{\boldsymbol{v}}^{-1} (\boldsymbol{t}_i - \boldsymbol{t}_{i-1}) \cdot r \Big) \Bigg). \end{aligned} \tag{10.5}$$

We solved this convex optimization problem using the BFGS method [Gold 70].

Runtime Complexity

The dominant part of the runtime is the computation of the similarity measure for registration. Thus, it is sufficient to analyze the number of similarity measure evaluations. The coarse-to-fine optimization for single frame registration uses $\mathcal{O}(\nu_\mathrm{s}\nu_\mathrm{r})$ evaluations where ν_s denotes the number of scales of the coarse-to-fine scheme and ν_r denotes the number of positions that are retained to be evaluated in the next scale. For all n frames of a whole sequence, $\mathcal{O}(\nu_\mathrm{s}\nu_\mathrm{r}n)$ evaluations are required. Once the registration of each frame is computed, no further similarity measures are required as the optimization of the Markov chain is not performed in image space.

10.4 Motion Regularization

The Markov filtering approach uses explicit information of uncertainty which is estimated afterwards in Equation 10.2. In this equation, the covariance matrix $\boldsymbol{\Sigma}_i$ defines the confidence for the solution of frame i.

Yet, this confidence does not reflect the inherent ambiguities in the registration problem which are revealed by the function shape of the similarity measure. For example, the LA roof appears often as straight line and if contrast is injected against the roof, a dominant line appears in the edge image used for registration. If the projected 3-D top edge of the LA model is registered to this edge highlighted by contrast agent, one degree of freedom, namely the translation along the line, remains, see Figure 10.2.

For other frames, however, the shape of the function might look differently. If the ambiguities in function space of the first frame are orthogonal to the ambiguities for the other frame, a joint optimization for all frames would result in a translation which is best for all frames.

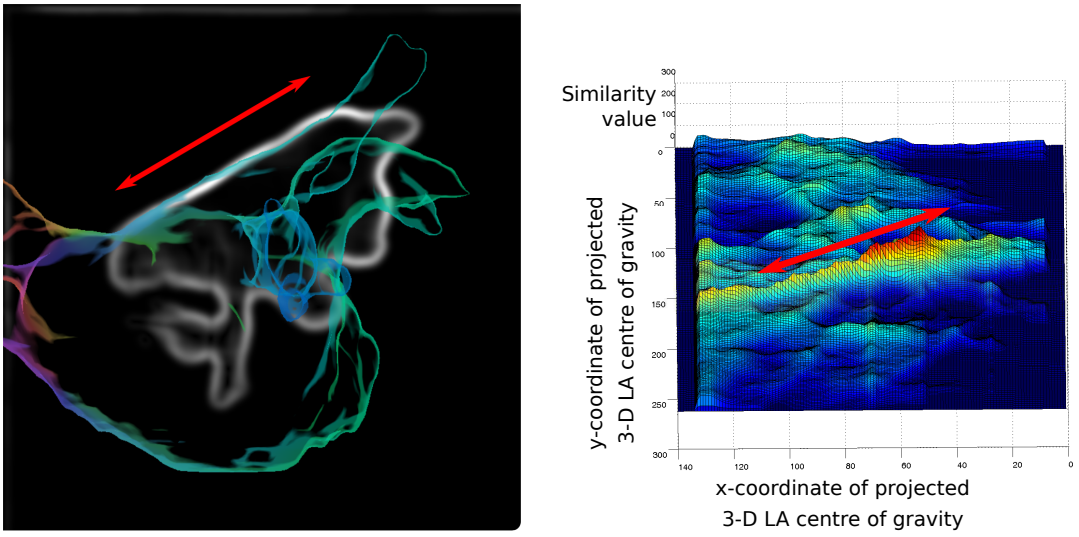

(a) (b)

Figure 10.2: (a) LA edges highlighted by contrast agent with projected 3-D edges. (b) Corresponding function value of the similarity measure. The x- and y-axes correspond to the pixel location of the projected 3-D LA centre of gravity. A translation of the overlay in (a) according to the arrows corresponds to the ridge in (b).

However, we cannot assume a fixed position for all frames. To account for small motion due to respiration or the beating heart, we propose to add a regularizer to the optimization. So, instead of optimizing the objective function ρ for each frame independently, a joint optimization

$$\hat{\boldsymbol{t}}_1, \ldots, \hat{\boldsymbol{t}}_n = \underset{\boldsymbol{t}_1 \ldots \boldsymbol{t}_n}{\arg\max} \sum_{i=1}^{n} \rho(\boldsymbol{t}_i) - \gamma \sum_{i=1}^{n-1} ||\boldsymbol{t}_{i+1} - \boldsymbol{t}_i||. \tag{10.6}$$

for all frames is performed.

This leads to an $3 \cdot n$-dimensional objective space which will contain several local optima and thus requires a good initial solution. Therefore, we initialize the T_i with the result of an independent registration performed for each frame i. We optimize Equation 10.6 using a BFGS optimizer [Gold 70] using approximated gradients.

The runtime complexity with respect to the similiarity measure evaluation is in this case higher compared to the Markov chain filtering. For initialization, $\mathcal{O}(\nu_\mathrm{s}\nu_\mathrm{r}n)$ evaluations are required, like for the Markov chain filtering, see section 10.3. However, different to the Markov chain filtering, the motion constrained filtering happens in image space. So, every iteration of the BFGS optimization requires further similarity measure evaluations. Let $\nu_\mathrm{BFGS}(3n)$ denote the number of iterations for the BFGS optimization within the $3n$-dimensional objective space. During gradient approximation, only a single component of the $3n$-dimensional vector is changed and the similarity measure is computed again for all frames. To avoid a recomputation, the last evaluated translation for each frame and the associated result were stored. This reduces the number of similarity measure evaluations per iteration from $\mathcal{O}(n^2)$ to $\mathcal{O}(n)$. The resulting complexity is in $\mathcal{O}(\nu_\mathrm{s}\nu_\mathrm{r}n + \nu_\mathrm{BFGS}(3n)n)$

Table 10.1: Translation errors

All frames			
Objective function	No motion constraint	Markov filtering	Motion regularizer
$\rho_{\text{shad}}^{\text{DSA}} + \rho_{\text{edge}}$	8.9±6.1 mm	6.9±3.9 mm	7.6±4.6 mm
$\rho_{\text{shad}}^{\text{thr}} + \rho_{\text{edge}}$	9.3±7.2 mm	7.0±4.2 mm	8.4±5.0 mm
$\rho_{\text{CADE}} + \rho_{\text{edge}}$	8.3±6.4 mm	6.2±4.3 mm	7.8±5.7 mm
Initial injections			
Objective function	No motion constraint	Markov filtering	Motion regularizer
$\rho_{\text{shad}}^{\text{DSA}} + \rho_{\text{edge}}$	8.3±6.6 mm	6.5±4.3 mm	7.5±5.1 mm
$\rho_{\text{shad}}^{\text{thr}} + \rho_{\text{edge}}$	8.3±6.7 mm	6.1±4.4 mm	7.3±4.6 mm
$\rho_{\text{CADE}} + \rho_{\text{edge}}$	7.9±6.3 mm	5.7±4.6 mm	6.3±4.8 mm
Clinical experts	3.3±2.7 mm		

10.5 Experiments and Results

We evaluated the method on the same data set as used for evaluation of the single frame registration in section 9.4. The error estimate function $e(\rho(\cdot))$ and the transition probability covariance matrix $\Sigma_{\boldsymbol{v}}$ as well as a suited regularizer weight γ was determined in a in a leave-one-patient-out cross-validation. We first performed a registration for each frame independently and used the obtained results for the proposed motion constraint registrations. The results for the temporal filtered frames are given in Table 10.1. For a combination of the CADE and edge similarity measure, Markov filtering reduced the mean error to 6.2±4.3 mm for all sequences and 5.7±4.6 mm when only initial injections were considered. The respective median errors were 4.7 mm and 4.0 mm. The results obtained by the Markov filtering were in all cases significantly better than the results without filtering and the results obtained from the regularizer-based approach. Significance was determined using a Wilcoxon signed rank test [Wilc 45] ($p < 0.1$).

The computation time for registration using a whole sequence comprises the time for initial registration which takes between 13 and 27 seconds per frame, see section 9.4 and the subsequent motion filtering operation. We ran our experiments on a PC with an Intel i7, 2.6 GHz CPU and a NVidia K1000M GPU. We achieved a runtime of 173±124 ms per sequence for Markov filtering. The optimization of the joint optimization problem using the regularizer-based approach took 6.8±5.6 minutes if $\rho_{\text{CADE}} + \rho_{\text{edge}}$ is used as objective function and 1.3±1.0 minutes for the other objective functions combined with ρ_{edge}. Please note that the runtime of a similarity measure evaluation took about three times longer in this experiments compared to the experiments for single frame registration as a different machine was used.

10.6 Discussion and Conclusions

The Markov filtering reached a higher accuracy than the approach based on the motion regularizer. This shows that the optimum of the similarity measure found for

each frame can serve as measure for uncertainty. As for single frame registration, see section 9.4, the CADE measure provided the highest accuracy. The resulting mean error was close to a clinical relevant threshold of 5.0 mm [King 09], the median error was even below this threshold.

The regularizer based approach was not only outperformed with respect to accuracy but also regarding the runtime. The high differences in runtime can be explained by the number of similarity measure evaluations for each of the methods. As the motion regularization happens in image space, the number of similarity measure evaluations is considerably higher. On the other hand, the problem is very well parallelizable and the progress in computation power of GPUs directly leads to a lower runtime.

Another drawback of the regularizer-based method is its sensitivity to the value of γ. An analysis showed that the values for γ found by the cross-validation differed considerably from the value that would have led to the best accuracy for a fixed sequence. If γ would have been chosen optimally for each single sequence, the results were almost as good as for the Markov approach. So, a fixed value does not suit all sequences and a deeper investigation would be required to find a method which chooses a good γ-value. Yet, the accuracy which can be achieved in theory if the value of γ is selected optimally is also reached using the Markov approach with less runtime. So there is virtually no need to find a good heuristic for γ.

In this current approach, the Markov filtering uses a fixed transition probability. It is only adapted to the frame rate r but actually, it depends also on the breathing phase: For example, during inhale phase, a superior motion, i.e. a motion towards the head, is more likely, while in an exhale phase, the LA likely moves down. Information regarding the breathing phase can be obtained, e.g. from external devices [Wasz 16], by tracking of the diaphragm [Cao 12, Boge 14] or from data driven methods such as manifold learning [Fisc 14] or dimensionality reduction using Laplacian Eigenmaps [Sand 16]. If information about the breathing phase was available, the transition probability could be trained for each breathing phase, e.g., by estimating the mean value and the covariance matrix separately for different stages of the breathing cycle.

To conclude, both filtering methods improved the results significantly compared to a registration performed on each frame independently. This shows that motion filtering is important to obtain accurate registration results. Although the accuracy is less compared to the selection of a single frame as proposed by Zhao *et al.* [Zhao 13], our method has the advantage that good results are obtained for all frames of a sequence. Thus, the physician can choose a frame that fits best to the required breathing phase or heart phase.

CHAPTER 11

Outlook

The methods and findings presented in this thesis can be further improved and extended. In this chapter, we sketch potential directions for future research.

11.1 Directions for Device Detection and Reconstruction

Automatic Catheter Shaft Detection. The approach for catheter shaft detection in chapter 3 is semi-automatic as a seed point needs to be specified by the user. In future work, an automatic tip detection by template matching [Schm 05], SIFT-features [Wu 13], blob detection [Ma 13] or patch-based methods [Mill 13, Mill 14] could be performed to replace the manual tip selection.

As most of these approaches do not only detect the tip region but fit a tip model to the image content, the direction of the tip is also given. This direction can be added as an additional feature for the catheter shaft search. By doing so, challenging situations, where a catheter tip is close to another catheter, can be resolved. Moreover, the detection will probably be more robust as the difficult low contrast parts of the catheter around the electrodes would be handled by the tip detection.

Joint Detection of Multiple Catheters. Another approach to make the catheter shaft detection more robust would be a joint detection of all catheters in the image. Starting from a set of seed points, all associated shafts could be searched simultaneously. A penalty term could be introduced that makes overlapping catheters less favourable. So, catheter crossings could be resolved better by forcing the catheter shaft search to choose partially different paths for each catheter.

Smoothed Catheter Reconstruction. The reconstructed catheter is in some cases not smooth but contains kinks. This problem is especially apparent if the catheter is tangent to the epipolar line. In this case, the reprojection of the catheter is still on the 2-D annotation of plane A and B, respectively. However, if the 2-D

model is viewed from a different, third, perspective, the reconstruction errors become visible.

To achieve a more accurate registration, the computation of the correspondence function can be improved. To this end, the determination of possibly corresponding points can be performed symmetrically, i.e., first points from the annotation in plane A are sampled and for each point, possible correspondences in plane B are computed. Then, points from plane B are sampled and their correspondences in plane A are determined. Moreover, a smoothing of the correspondence function can be performed.

Smoothing can also be performed after reconstruction, e.g., by fitting a spline curve with a low number of control points to the reconstructed points. This should be followed by a biplane-snake algorithm [Cane 00, Cane 02, Sche 10] to compensate for errors introduced by curve fitting. Moreover, as the snake tries to minimize its curvature, bents in 3-D that are not visible in the corresponding 2-D projections, e.g. along parts that are tangent to the epipolar line, might be reduced as well.

Joint Optimization for Cryoballoon Boundary Detection. It could be investigated how several optimization steps needed for cryoballoon boundary detection can be merged into a single joint optimization step. In this context, a L_1-data term could be used during snake fitting to reduce the effect of spurious edges. Moreover, the internal energy could be increased with each iteration of the snake algorithm to avoid being stuck in a local minimum in early stages while enforcing ellipse properties in later stages.

Combined Appearance- and Model-based Cryoballoon Reconstruction. In future work, both methods could be combined to obtain a more robust cryoballoon reconstruction method. The boundary detection could, e.g., be improved by introducing constraints for the distance between X-ray marker and balloon centre. On the other hand, the results obtained by the model-based approach could be verified using the boundary detection to find, e.g., errors in the catheter detection step.

Detection and Reconstruction of the CoolLoop Catheter. Recently, a novel cryo catheter was developed that comprises a spiral tip that curls around a guide wire. The spiral tip that can be cooled to freeze the tissue for a *wide area circular ablation* approach. As the loop-shaped tip does not encircle the complete ostium, it is important to annotate the created lesions accurately on the 3-D LA model. Our catheter detection method could be adapted to this catheter type. However, the shape of the CoolLoop catheter is more complex than for the CM catheter and it is not clear if an accurate detection in 2-D is feasible.

Therefore, the catheter guide wire could be detected and reconstructed in a first step. Afterwards, either a statistical shape model [Coot 95, Zhon 15, Zhon 16] of the loop part or a biplane-snake algorithm [Cane 00, Cane 02, Sche 10] could be used to determine the tip.

11.2 Directions for Device-based Registration

Basket Catheter Registration. The basket catheter is a diagnostic catheter that is placed into the right and the left atrium. It is spherically shaped and consists of eight wires that form a ball. All wires are supposed to touch the heart wall. Recently, a method for detection and reconstruction of this catheter was developed [Zhon 15, Zhon 16].

Once the catheter is placed inside an atrium, it can be reconstructed and used for registration. A possible approach would be to first perform a coarse registration by moving the atrium such that its centre of gravity coincides with the centre of the basket catheter. In a fine registration step, the distance from the basket catheter electrodes to the atrium wall could be minimized.

Registration using Multiple Catheters with Wall Contact. The registration idea for the basket catheter can be transferred to the CM catheter. For example the physician could place the CM catheter subsequently in each pulmonary vein. Then, an energy term that considers the distance of the CM catheter tip reconstructed at each PV could be minimized. This approach can also be combined with the cryoballoon registration presented in chapter 7 or applied when the CryoLoop catheter is used for ablation.

This approach would need to solve following problems: First, it is difficult to ensure that the electrodes of the CM catheter touch the heart wall. Even if the electrodes record cardiac signals, the electrodes do not necessarily touch the heart wall as also the blood can transmit the signals to a certain extent. A distance function would therefore need to distinguish between catheter parts inside and parts outside the LA. The second problem is that the catheters tend to deform the LA or the PVs. So even if a catheter is for a certain registration outside the LA, the overall registration is not necessarily wrong but the restriction to a rigid registration is no longer valid. Third, a respiratory motion compensation needs to be ensured. A suitable method using the CS catheter has been presented recently [Kapp 12].

11.3 Directions for Contrast-based Registration

Improved Contrast Extraction. Currently, pixels below an intensity of 0 in the DSA image are considered to be not contrasted. In theory this is a valid assumption, however, due to the AEC, the contrasted frame is brighter than the uncontrasted frame. Therefore, also parts of the contrasted pixels will have a negative intensity in the DSA image. So, the actual threshold should be below the 0-intensity.

A suitable threshold will result in a single large blot while the number of small blots is low. If the threshold, however, is too low, motion artefacts of soft tissue will increase resulting in a large number of small blots. If the threshold is too high, the segmentation will result in a smaller largest blot or in several mid-size blots.

For a set of test images, a good threshold could be determined visually. Based on a connected component analysis and a histogram of the blot sizes, the acceptable number of small blots can be determined empirically. For unseen images, a

good threshold could then be decreased until an acceptable number of small blots is reached.

Combined Device-based and Contrast-based Registration. In a future work, the device-based registration and the contrast based registration could be combined. The objective function to be optimized would then not only contain the normalized cross correlation for the contrast-based registration but would also comprise the distance of the segmented 3-D anatomy to the 3-D devices reconstructed from the 2-D images.

If a monoplane system had to be used for fluoroscopic guidance, contrast-based and device-based registration could be performed sequentially. To this end, the physician would record an angiographic sequence in A, e.g. at a 30° LAO position. Based on this sequence, a 2-D contrast-based registration could be performed. Then the physician rotates the C-arm to a, e.g. 60° RAO position and acquires a single image as a virtual B-plane. From the first sequence and the virtual B-plane image, the 3-D shape of the CS-catheter can be reconstructed. This reconstruction will be affected by cardiac motion and breathing motion. We have seen in chapter 6 that a registration based on the CS alone is not accurate enough. Yet only the depth information is missing from the contrast based registration of the first image sequence. It could be investigated, if a reconstruction of the CS obtained this way is sufficient to estimate the missing depth information.

Registration of the Right Atrium and Ventricles. By now, the registration method was evaluated only for left atria. In a next step, the performance of this approach to contrast based registration of the right atrium can be evaluated. A registration based on the right atrium would also provide a registration for the left atrium which is available for transseptal punction. Additionally, the contrast-based registration approach could be evaluated on ventricles. Due to the lack of pulmonary veins and arteries, the ventricles have a more simple anatomical structure, but subject to stronger cardiac motion. It is open how strong this affects the registration accuracy.

Breathing Motion Integration for Motion-constrained Registration. Currently, the Markov chain for motion-constraint registration incorporates no information on the breathing phase. Instead, a zero-mean normal distribution of the motion is assumed. In future work, the breathing phase could be determined, e.g., using a breathing belt or an image based approach [Fisc 14]. Then, the mean value of the normal distribution could be adapted to favour a motion of the lung corresponding to the current breathing phase. Moreover, it could be investigated how the presented methods could be applied to the device based registration proposed in chapter 6.

CHAPTER 12

Summary

The overlay of a preoperatively acquired 3-D model of the patients LA with X-ray images holds great potential to support guidance during cardiac ablation procedures. To this end, the coordinate system of the 3-D model needs to be registered with the coordinate system of the fluoroscopic images to achieve a correct overlay. In this thesis, we investigated methods that facilitate this registration process.

In chapter 2 we presented the medical background of atrial fibrillation and its treatment. We outlined current manual registration techniques, amongst others strategies that involve catheters visible in both the 3-D data set and the 2-D X-ray images and methods that are based on contrast agent which is injected into the LA to highlight its structure. Moreover we presented a novel overlay that focusses on edges in the anatomy. The overlay is colour-coded to provide the user with a better 3-D impression of the LA model. This way, corresponding structures in both views of a biplane image pair can be better identified. An evaluation on six data sets showed that this overlay helps to reduce the registration error significantly.

Device Detection and Reconstruction. If the registration strategy is based on devices visible both in the 3-D and 2-D data, they often need to be segmented in the X-ray images and their 3-D shape needs to be reconstructed. In Part I we presented automatic and semi-automatic methods for device detection and reconstruction. To supersede current manual catheter annotation, we introduced in chapter 3 a semi-automatic method for catheter detection. Based on a seed point placed by the user, a graph-representation of catheter-like structures in the image is generated by computing a shortest-path-tree. Starting from the seed point, a path in the graph that resembles a catheter shaft best is searched. For CM catheters a second path is found for its elliptical tip. The paths found for shaft and tip are rated based on features such as curvature and length which are weighted differently depending on the catheter type. The detection method achieved a success rate of 83.4 % with an error of 1.7 mm±1.2 mm for successful detections.

For device-based registration, a 3-D shape of each device needs to be computed from the devices visible in the 2-D X-ray images from two different views. To automatize this step, we developed a reconstruction method which we presented in chapter 4. This method samples points from the annotation in one view and computes for each sample possible correspondence points in the other view by means of epipolar geometry. By enforcing a monotony criterion we derived a recursive computation scheme for a maximum set of point correspondences that satisfy the monotony criterion. An evaluation using phantom data resulted in mean errors between 0.7 mm±0.2 mm and 1.0 mm±0.2 mm depending on the catheter type. A combination of semi-automatic

catheter detection and the catheter reconstruction method was also evaluated and yielded an error of 1.8 mm±1.1 mm.

Using an automatic detection of the cryo balloon X-ray marker, catheter detection and reconstruction were combined in chapter 5 to an automatic 3-D reconstruction of cryo balloons. We proposed two approaches, a model-based reconstruction approach and an appearance-based reconstruction approach. In the first approach, a model of the 3-D cryo catheter is applied to the reconstructed shaft where the detected and reconstructed X-ray marker serves as anchor point. The shaft of the model was aligned to the reconstructed catheter shaft to map the 3-D cryo balloon centre to a position on the reconstructed shaft. The 3-D centre of the cryo balloon could be reconstructed with an accuracy of 2.5 mm±1.7 mm. The second approach is based on a 2-D detection of the balloon boundary. Here, the known dimensions of the catheter are employed to restrict the set of edges that represent the balloon boundary by means of hough transform and the snake algorithm. The found balloon boundary was then used to reconstruct a 3-D-sphere representing the balloon. An evaluation of this approach led to a 3-D error of 3.6 mm±4.8 mm.

Device-based Registration. We presented in Part II of this thesis two types of registration approaches based on medical devices inside the patients body.

The first approach, presented in chapter 6 uses anatomical structures outside the left atrium that can be segmented from 3-D data and are also visible in 2-D due to catheters placed inside these structures. We investigated the accuracy of a registration based on the CS and the esophagus. Using our catheter detection and reconstruction method, a 3-D reconstruction of the CS catheter and an esophageal temperature probe was computed. The 3-D reconstruction was then registered to the respective segmentations from the 3-D volume using an ICP algorithm. Our method extends a previous approach for CS based registration to a combined registration using the CS and the esophagus. An evaluation on clinical data yielded an accuracy of 3.2 mm±1.4 mm. It turned out that a registration based on the CS and the esophagus was significantly more accurate than a registration on the CS only.

The second approach, presented in chapter 7 relies on the anatomy of the LA and a cryoballoon catheter inside the LA. Using a skeletonization of the LA mesh, a tree structure of the PVs was generated. Along this tree, the diameters at the PVs and the corresponding ostia were computed. We used this information to find the place where a cryoballoon of a given size will stick if it is pushed into a PV. This position was then registered to the 3-D cryoballoon centre reconstructed from the 2-D intraoperative images. Our evaluation showed that a registration based on the cryoballoon leads to anatomically meaningful results. In this context we developed a method for automatic ostium annotation. From the skeletonization of the LA and the tree representing the anatomic structure of the LA, features like PV diameter and diameter increase were computed. These features were used to train an SVM classifier for the detection of ostium candidates that were later clustered. The ostia of the LA were then assigned to these clusters. In an evaluation on clinical data, 86 % of all ostia could be detected with a mean error of 4.3 mm±2.6 mm.

Contrast-based Registration. In Part III we presented a pipeline for fully automatic contrast-based registration using biplane image pairs. The first part of this pipeline was a detection of contrasted frames that uses features derived from subtraction images that are used by an SVM classifier. Our method shown in chapter 8 agglomerates histogram based features of both image planes of a biplane system and features of the previous and next frame to preserve temporal information. In a comprehensive evaluation on 571 frames of 34 biplane sequences we showed that our approach outperforms two other methods that rely on a single threshold. The first contrasted frames could be detected in 85.3 % of all sequences and 81.2 % of all frames were classified correctly.

As next step of the pipeline we presented a method for automatic selection of reference images of subtraction angiography such that motion artefacts are reduced. This approach selects a reference image such that the L_1-norm of the subtraction image is minimal. In this case, moving structures like catheters cancel out as much as possible. The subtraction images were then used to derive images of the contrasted area and edges visible due to the contrast agent. These images were compared to rendered images of the LA projection shadow or projected LA edges using normalized cross correlation. To make the registration consistent with not only each of the two 2-D fluoroscopic images but also with the 3-D information implicitly available in the biplane image pair, we developed a novel similarity measure. For a given registration, this measure estimates a 3-D contrast distribution and computes how consistent the projection of the estimated contrast agent is with respect to the contrast agent visible in the 2-D images. An evaluation on 21 clinical biplane data sets from 10 different patients showed that best results are achieved by a joint optimization of an edge-based similarity measure and the novel consistency-based measure. The error in this case was 7.9 mm±6.3 mm for well contrasted sequences and 8.8 mm±6.7 mm if less contrast agent was used. If only an arbitrary single frame of each sequence is required, the error reduced to 4.6 mm±4.0 mm for well contrasted sequences. Moreover, we discussed that a similarity measure based on only the contrasted area will suffer from ambiguities which was shown by a qualitative analysis of the function space and supported by the evaluation results.

As last part of the contrast-based registration pipeline, we proposed in chapter 10 two methods for the integration of context information from previous and following frames into the registration result. The first method augments the similarity measure by a regularization term which penalizes large motion between successive frames. The other method considers the registration results for each individual frame as observations of the LA position in 3-D space. The dependency between true LA positions and observed LA positions as well as the amount of the LA motion was modelled as a Markov chain. Based on the similarity measure of each registration result, a confidence for each observation was established. The resulting registration for the whole image sequence was then calculated by computing a sequence of registrations that best explains the observations. We evaluated both approaches on the same data as for the registration of a single frame. The error for the well contrasted frames reduced from 7.9 mm±6.3 mm to 6.4 mm±4.8 mm for the regularizer-based approach and to 5.7 mm±4.6 mm when using the Markov chain-based approach.

In chapter 11 we sketched several ways to improve the methods further, e.g. by a more sophisticated contrast agent extraction or smoothing during the catheter reconstruction. Moreover we presented ideas how to transfer these methods to other devices like the CoolLoop catheter or the basket catheter and how to combine device- and contrast-based registration to provide a registration for different clinical settings, e.g. if only a monoplane system is available.

To sum up the whole thesis, we presented a comprehensive framework for automatic registration for EP applications that provides modules to automatize mostly all steps required for a contrast-based registration or a device-based registration. The contributions are the development of detection and reconstruction methods for the complete catheter, the investigation of device based registration methods beyond the CS catheter, a novel similarity measure that enforces 3-D consistency for partially contrasted objects and a motion integration as a stochastic framework.

List of Symbols

a_{a}	End angle feature for catheter detection
a_{c}	Curvature feature for catheter detection
a_{d}	Direction feature for catheter detection
b_{a}	Difference angle between start of catheter tip section and start of catheter shaft
b_{c}	Feature for catheter tip section detection stating the fraction of an ellipse covered by a tip section candidate
b_{d}	Feature representing the deviation from an ellipse for catheter tip section detection
b_{fe}	Medialness filter feature for catheter tip section detection
b_{l}	Ellipse circumference used for catheter tip section detection
b_{M}	Length of the major axis of $\mathcal{G}$
b_{m}	Length of the minor axis of $\mathcal{G}$
c_{ϵ}	Skeleton pixel cost
c_{r}	cost imposed on a pixel to reduce the search space for catheter detection
c_{t}	cost imposed on a pixel to compute the shortest path tree for catheter detection
d	3-D Distance between cryoballoon centre and X-ray marker
e	Size of the border around the shutters
f_c	Correspondence function to map points from a catheter in view A to points of the same catheter in view B
l_{g}	Length of a gap in the skeleton during transformation of the skeleton in a graph for catheter detection
l_{c}	Length of a circle in the skeleton for catheter detection
o	Fraction of point pairs that are omitted for ICP registration
p	Value at a given percentile of the cumulative histogram
r	Cryoballoon radius
r_{PV}	Radius of a pulmonary vein
s	Pixel spacing
v	2-D vertical image coordinate
w	Radiographic magnification factor
C	Contrast agent distribution estimate
E_M	Set of triangle mesh edges
$E_{\boldsymbol{I}}$	Set of edges connecting vertices in Ωthat represent neighbouring pixels
E_C	Edges associated with the curve skeleton M_C
$G_{\boldsymbol{I}}$	Graph imposed on image pixels
M	Triangle mesh
M_C	Curve Skeleton used for ostium-based registration and ostium detection
S	Curve representing the centreline of a catheter

T	Arbitrary transformation used for registration
V_M	Set of triangle mesh vertices
V_C	Vertices associated with the curve skeleton M_C
$\boldsymbol{c}$	Position of the cryo balloon centre
$\boldsymbol{e}$	2-D points on the ellipse $\mathcal{E}$ fitted to $\mathcal{G}$ for catheter detection
$\boldsymbol{m}$	Position of the detected X-ray marker
$\boldsymbol{o}$	optical centre of a C-arm
$\boldsymbol{p}$	a 2-D pixel
$\boldsymbol{p}^{\mathrm{2D}}$	Point in 2-D
$\boldsymbol{p}^{\mathrm{A}}$	2-D Point in image plane A
$\boldsymbol{q}$	a 2-D pixel
$\boldsymbol{r}$	Root of the shortest path tree $\mathcal{T}$
$\boldsymbol{s}$	2-D seed point marked by the user in the image for catheter detection
$\boldsymbol{t}$	Translation used as transformation for registration
$\boldsymbol{v}$	A 3-D voxel coordinate
$\boldsymbol{w}$	Point in 3-D world coordinate system
$\boldsymbol{C}$	Projected voxels found to be contrasted in the CADE C
$\boldsymbol{E}$	Image containing the projected edges rendered from a 3-D LA model
$\boldsymbol{F}$	Fundamental matrix
$\boldsymbol{I}_{\mathrm{b}}$	Binarized medialness filtered image for catheter detection
$\boldsymbol{I}_{\mathrm{c}}$	Image frame containing contrast agent used for DSA
$\boldsymbol{I}_{\mathrm{DOG}}$	Image containing edges of contrast agent extracted from an X-ray angiography
$\boldsymbol{I}_{\mathrm{DSA}}$	Image showing the contrast agent obtained by means of DSA
$\boldsymbol{I}_{\mathrm{DT}}$	Distance transform of skeleton image $\boldsymbol{I}_{\mathrm{s}}$
$\boldsymbol{I}_{\mathrm{eq}}$	X-ray image of a cryoballoon after histogram equalization
$\boldsymbol{I}_{\mathrm{f}}$	Medialness filtered image for catheter detection
$\boldsymbol{I}_{\mathrm{m}}$	Median filtered image showing extracted contrast agent
$\boldsymbol{I}_{\mathrm{s}}$	Thinned binary image for catheter detection
$\boldsymbol{I}_{\mathrm{sig}}$	Sigmoid filtered image used for contrast-based registration
$\boldsymbol{I}_{\mathrm{thr}}$	Binarized image of contrast agent
$\boldsymbol{I}_{\mathrm{u}}$	Uncontrasted image frame used for DSA
$\boldsymbol{I}_{\mathrm{x}}$	Image gradients in x-direction of a cryoballoon image
$\boldsymbol{I}_{\mathrm{y}}$	Image gradients in y-direction of a cryoballoon image
$\boldsymbol{K}$	2-D Gaussian kernel
$\boldsymbol{P}$	Projection matrix
$\boldsymbol{S}$	Image containing the projected shadow rendered from a 3-D LA model
$\mathcal{A}$	Sequence of points describing the esophagus centreline or the esophageal temperature probe
$\mathcal{B}$	Initial set of cryoballoon boundary pixels
$\mathcal{C}$	Sequence of points describing the CS centreline or the CS catheter
$\mathcal{E}$	Ellipse fitted to $\mathcal{G}$ for catheter detection

$\mathcal{F}$	Sequence of pixels resembling a candidate for the catheter shaft during catheter detection
$\mathcal{G}$	Catheter tip candidate consisting of a sequence of 2-D points
$\mathcal{M}$	Set of points classified as ostium centre points
$\mathcal{S}$	Optimal set of possibly corresponding points for reconstruction
$\mathcal{T}$	Shortest path tree representing the LA skeleton
$\mathcal{V}$	Cubic spline curve representing a line in the LA skeleton
$\alpha_{\max}$	Maximum angular difference between the direction to the X-ray marker and the cryoballoon centre at a point on the balloon boundary
γ	Regularizer weight for constraining the motion of the LA during registration
θ_∇	Threshold for edge extraction during cryoballoon detection
θ_α	Angular threshold for boundary extraction during cryoballoon detection
θ_r	Distance threshold for boundary extraction during cryoballoon detection
$\kappa_\mathcal{F}$	Curvature of a pixel sequence at a certain position
λ	Circular tip inclusion weight for computation of search space Ω_r
ϱ	Weight factor steering the smoothness of branches in the catheter search graph
ρ	Normalized cross correlation function
$\phi_\mathcal{F}$	Direction of a pixel sequence at a certain position
χ	Indicator function stating whether a voxel $\boldsymbol{v}$ is within the LA or not
Ω	Set of all pixels in an image
Ω_r	Reduced search space for catheter detection

List of Abbreviations

AEC	automatic exposure control
AFib	atrial fibrillation
CA	contrast agent
CADE	Contrast agent distribution estimate
CM	circular mapping (catheter)
CS	coronary sinus
CT	computed tomography
DSA	digital subtraction angiography
EAMS	electro-anatomical mapping system
EP	electrophysiology
FIRM	focal impulse and rotor mapping
LA	left atrium
LAA	left atrial appendage
LAO	left anterior oblique
LSPV	left superior pulmonary vein
MRA	MRI angiography
MRI	magnetic resonance imaging
PV	pulmonary vein
RA	right atrium
RAO	right anterior oblique
RF	radio frequency
SSD	sum of squared differences
SVM	Support Vector Machine

List of Figures

List of Tables

Bibliography

[Ambr 15] P. Ambrosini, I. Smal, D. Ruijters, W. J. Niessen, A. Moelker, and T. Walsum. "3D Catheter Tip Tracking in 2D X-ray Image Sequences Using a Hidden Markov Model and 3D Rotational Angiography". In: A. C. Linte, Z. Yaniv, and P. Fallavollita, Eds., *Augmented Environments for Computer-Assisted Interventions: 10th International Workshop, AE-CAI 2015, Held in Conjunction with MICCAI 2015, Munich, Germany, October 9, 2015. Proceedings*, (Munich, Germany, October 2015), pp. 38–49, Springer International Publishing, Cham, 2015.

[Andr 11] J. G. Andrade, P. Khairy, P. G. Guerra, M. W. Deyell, L. Rivard, L. Macle, B. Thibault, M. Talajic, D. Roy, and M. Dubuc. "Efficacy and safety of cryoballoon ablation for atrial fibrillation: A systematic review of published studies". *Heart Rhythm*, Vol. 8, No. 9, pp. 1444 – 1451, September 2011.

[Attw 92] S. Attwood, A. Hill, P. Murphy, J. Thornton, and R. Stephens. "A prospective randomized trial of laparoscopic versus open appendectomy". *Surgery*, Vol. 112, No. 3, pp. 497–501, September 1992.

[Back 97] T. Bäck, U. Hammel, and H. Schwefel. "Evolutionary computation: Comments on the history and current state". *IEEE Transactions on Evolutionary Computation*, Vol. 1, No. 1, pp. 3–17, April 1997.

[Baer 03] S. A. M. Baert, E. B. van de Kraats, T. van Walsum, M. A. Viergever, and W. J. Niessen. "Three-Dimensional Guide-Wire Reconstruction From Biplane Image Sequences for Integrated Display in 3-D Vasculature". *IEEE Transactions on Medical Imaging*, Vol. 22, No. 10, pp. 1252–1258, October 2003.

[Barb 07] A. Barbu, V. Athitsos, B. Georgescu, S. Böhm, P. Durlak, and D. Comaniciu. "Hierarchical Learning of Curves Application to Guidewire Localization in Fluoroscopy". In: *2007 IEEE Conference on Computer Vision and Pattern Recognition*, (Minneapolis, MN, USA, June 2007), pp. 1–8, 2007.

[Bend 99] H.-J. Bender, R. Männer, C. Poliwoda, S. Roth, and M. Walz. "Reconstruction of 3D Catheter Paths from 2D X-ray Projections". In: C. Taylor and A. Colchester, Eds., *Medical Image Computing and Computer-Assisted Intervention–MICCAI'99*, (Cambridge, UK, September 1999), pp. 981–989, Springer Berlin Heidelberg, 1999.

[Bens 13] T. Benseghir, G. Malandain, and R. Vaillant. "Iterative Closest Curve: a Framework for Curvilinear Structure Registration Application to 2D/3D Coronary Arteries Registration". In: K. Mori, I. Sakuma, Y. Sato, C. Barillot, and N. Navab, Eds., *Medical Image Computing and Computer-Assisted Intervention–MICCAI 2013*, (Nagoya, Japan, September 2013), pp. 179–186, Springer, 2013.

[Berg 08] M. de Berg, O. Cheong, M. van Kreveld, and M. Overmars. *Computational Geometry*. Springer-Verlag Berlin Heidelberg, 3 Ed., 2008.

[Berg 15] M. Berger, K. Müller, J.-H. Choi, A. Aichert, A. Maier, and R. Fahrig. "2D/3D Registration for Motion Compensated Reconstruction in Cone-Beam CT of Knees Under Weight-Bearing Condition". In: D. A. Jaffray, Ed., *World Congress on Medical Physics and Biomedical Engineering, June 7-12, 2015, Toronto, Canada*, (Toronto, Canada, June 2015), pp. 54–57, Springer International Publishing, Cham, 2015.

[Besl 92] P. J. Besl and N. D. McKay. "A Method for registration of 3-D shapes". *IEEE Transactions on Pattern Analysis and Machine Intelligence - special issue on interpretation of 3-D scenes - part II*, Vol. 14, No. 2, pp. 239–256, February 1992.

[Bism 12] V. Bismuth, R. Vaillant, H. Talbot, and L. Najman. "Curvilinear Structure Enhancement with the Polygonal Path Image - Application to Guide-Wire Segmentation in X-Ray Fluoroscopy". In: N. Ayache, H. Delingette, P. Golland, and K. Mori, Eds., *Medical Image Computing and Computer-Assisted Intervention - MICCAI 2012, Part II*, (Nice, France, October 2012), pp. 9–16, Springer Berlin Heidelberg, 2012.

[Boge 14] M. Bögel, C. Riess, A. Maier, J. Hornegger, and R. Fahrig. "Respiratory Motion Estimation using a 3D Diaphragm Model". In: T. M. Deserno, H. Handels, H.-P. Meinzer, and T. Tolxdorff, Eds., *Bildverarbeitung in der Medizin 2014*, (Aachen, 2014), pp. 240–245, Springer, Berlin Heidelberg, 2014.

[Bour 10] F. Bourier, A. Brost, L. Yatziv, J. Hornegger, N. Strobel, and K. Kurzidim. "Coronary Sinus Extraction for Multimodality Registration to guide Transseptal Puncture". In: T. Kahn, F. A. Jolesz, and J. S. Lewin, Eds., *8th Interventional MRI Symposium - Book of Abstracts*, (Leipzig, Germany, 2010), pp. 311–313, 2010.

[Bour 12] F. Bourier, A. Brost, A. Kleinoeder, T. Kurzendorfer, M. Koch, A. Kiraly, H.-J. Schneider, J. Hornegger, N. Strobel, and K. Kurzidim. "Navigation for Fluoroscopy-Guided Cryo-Balloon Ablation Procedures of Atrial Fibrillation". In: D. Holmes and K. Wong, Eds., *Medical Imaging 2010: Visualization, Image-Guided Proceudres, and Modeling*, (San Diego, CA, USA, February 2012), pp. 831627–1–8, 2012.

[Bour 13] F. Bourier, D. Vukajlovic, A. Brost, J. Hornegger, N. Strobel, and K. Kurzidim. "Pulmonary Vein Isolation Supported by MRI-Derived 3D-Augmented Biplane Fluoroscopy: A Feasibility Study and a Quantitative Analysis of the Accuracy of the Technique". *Journal of Cardiovascular Electrophysiology*, Vol. 24, No. 2, pp. 113–120, February 2013.

[Bour 14] F. Bourier, R. Fahrig, P. Wang, P. Santangeli, K. Kurzidim, N. Strobel, T. Moore, C. Hinkel, and A. Al-Ahmad. "Accuracy Assessment of Catheter Guidance Technology in Electrophysiology Procedures". *Journal of Cardiovascular Electrophysiology*, Vol. 25, No. 1, pp. 74–83, January 2014.

[Bour 16] F. Bourier, T. Reents, S. Ammar-Busch, V. Semmler, M. Telishevska, M. Kottmaier, C. Lennerz, C. Grebmer, C. Kolb, I. Deisenhofer, and G. Hessling. "Transseptal Puncture Guided by CT-Derived 3D-Augmented Fluoroscopy". *Journal of Cardiovascular Electrophysiology*, Vol. 27, No. 3, pp. 369–372, March 2016.

[Brod 82] W. R. Brody. "Digital subtraction angiography". *IEEE Transactions on Nuclear Science*, Vol. 29, No. 3, pp. 1176–1180, June 1982.

[Bros 09a] A. Brost. *Model-Based catheter tracking in bi-plane fluoroscopic sequences.* Master's thesis, Friedrich-Alexander-Universität Erlangen-Nürnberg, Germany, 2009.

[Bros 09b] A. Brost, R. Liao, J. Hornegger, and N. Strobel. "3-D Respiratory Motion Compensation during EP Procedures by Image-Based 3-D Lasso Catheter Model Generation and Tracking". In: G.-Z. Yang, D. Hawkes, D. Rueckert, A. Noble, and C. Taylor, Eds., *Medical Image Computing and Computer-Assisted Intervention–MICCAI 2009, Part I*, (London, UK, September 2009), pp. 394–401, Springer Berlin Heidelberg, 2009.

[Bros 09c] A. Brost, N. Strobel, L. Yatziv, W. Gilson, B. Meyer, J. Hornegger, J. Lewin, and F. Wacker. "Geometric Accuracy of 3-D X-Ray Image-Based Localization from Two C-Arm Views". In: G.-Z. Yang, D. Hawkes, D. Rueckert, A. Noble, and C. Taylor, Eds., *Workshop on Geometric Accuracy In Image Guided Interventions-Medical Image Computing and Computer Assisted Interventions, MICCAI*, (London, UK, September 2009), pp. 12–19, Springer, 2009.

[Bros 09d] A. Brost, N. Strobel, L. Yatziv, W. Gilson, B. Meyer, J. Hornegger, J. Lewin, and F. Wacker. "Accuracy of X-Ray Image-Based 3D Localization from Two C-Arm Views: A Comparison Between an Ideal System and a Real Device". In: M. Miga and K. Wong, Eds., *Medical Imaging 2009: Visualization, Image-Guided Proceudres, and Modeling*, (Lake Buena Vista, FL, USA, February 2009), pp. 72611Z–1 – 72611Z–10, 2009.

[Bros 10a] A. Brost, R. Liao, J. Hornegger, and N. Strobel. "3-D Model-Based Catheter Tracking for Motion Compensation in EP Procedures". In: K. Wong and M. Miga, Eds., *Medical Imaging 2010: Visualization, Image-Guided Proceudres, and Modeling*, (San Diego, CA, USA, February 2010), pp. 762507–1 – 762507–12, 2010.

[Bros 10b] A. Brost, R. Liao, N. Strobel, and J. Hornegger. "Respiratory motion compensation by model-based catheter tracking during EP procedures". *Medical Image Analysis*, Vol. 14, No. 5, pp. 695–706, October 2010. Special Issue on the 12th International Conference on Medical Image Computing and Computer-Assisted Intervention (MICCAI) 2009.

[Bros 11a] A. Brost, F. Bourier, A. Kleinöder, J. Raab, M. Koch, M. Stamminger, J. Hornegger, N. Strobel, and K. Kurzidim. "AFiT - Atrial Fibrillation Ablation Planning Tool.". In: P. Eisert, J. Hornegger, and K. Polthier, Eds., *Proceedings of the Vision, Modeling, and Visualization Workshop*, (Berlin, Germany, October 2011), pp. 223–230, Eurographics Association, 2011.

[Bros 11b] A. Brost, F. Bourier, L. Yatziv, M. Koch, J. Hornegger, N. Strobel, and K. Kurzidim. "First steps towards initial registration for electrophysiology procedures". In: K. H. Wong and D. R. Holmes III, Eds., *Medical Imaging 2011: Visualization, Image-Guided Procedures, and Modeling*, (Lake Buena Vista, FL, USA, February 2011), pp. 79641P–1–8, SPIE, 2011.

[Bros 12] A. Brost, A. Wimmer, R. Liao, F. Bourier, M. Koch, N. Strobel, K. Kurzidim, and J. Hornegger. "Constrained Registration for Motion Compensation in Atrial Fibrillation Ablation Procedures". *IEEE Transactions on Medical Imaging*, Vol. 31, No. 4, pp. 870–881, April 2012.

[Buda 13] A. Budai, R. Bock, A. Maier, J. Hornegger, and G. Michelson. "Robust Vessel Segmentation in Fundus Images". *International Journal of Biomedical Imaging*, Vol. 2013, No. 154860, pp. 1–11, September 2013.

[Burs 08] B. Burstein and S. Nattel. "Atrial fibrosis: mechanisms and clinical relevance in atrial fibrillation". *Journal of the American College of Cardiology*, Vol. 51, No. 8, pp. 802–809, February 2008.

[Calk 07] H. Calkins, J. Brugada, D. Packer, R. Cappato, S. Chen, H. Crijns, R. Damiano, D. Davies, D. Haines, M. Haïssaguerre, *et al.* "HRS/EHRA/ECAS Expert Consensus Statement on Catheter and Surgical Ablation of Atrial Fibrillation: Recommendations for Personnel, Policy, Procedures and Follow-Up". *Europace*, Vol. 9, No. 6, pp. 335 – 379, June 2007.

[Cane 00] C. Cañero, P. Radeva, R. Toledo, J. J. Villanueva, and J. Mauri. "3D curve reconstruction by biplane snakes". In: A. Sanfeliu, J. Villanueva, M. Vanrell, R. Alqukzar, J. Crowley, and Y. Shirai, Eds., *Proc. 15th Int Pattern Recognition Conf*, (Barcelona, Spain, September 2000), pp. 563–566, IEEE, 2000.

[Cane 02] C. Cañero, F. Vilarino, J. Mauri, and P. Radeva. "Predictive (Un)distortion Model and 3-D Reconstruction by Biplane Snakes". *IEEE Transactions on Medical Imaging*, Vol. 21, No. 9, pp. 1188–1201, September 2002.

[Cao 12] Y. Cao and P. Wang. "An Adaptive Method of Tracking Anatomical Curves in X-Ray Sequences". In: N. Ayache, H. Delingette, P. Golland, and K. Mori, Eds., *Medical Image Computing and Computer-Assisted Intervention - MICCAI 2012, Part I*, (Nice, France, October 2012), pp. 173–180, Springer, 2012.

[Caza 13] M. Cazalas, V. Bismuth, and R. Vaillant. "An Image-Based Catheter Segmentation Algorithm for Optimized Electrophysiology Procedure Workflow". In: S. Ourselin, D. Rueckert, and N. Smith, Eds., *Functional Imaging and Modeling of the Heart*, (London, UK, June 2013), pp. 182–190, Springer Berlin Heidelberg, 2013.

[Chie 12] G.-B. Chierchia, C. de Asmundis, M. Namdar, S. Westra, M. Kuniss, A. Sarkozy, F. Bayrak, D. Ricciardi, R. Casado-Arroyo, M. Rodriguez Manero, J. Y. Rao, J. Smeets, and P. Brugada. "Pulmonary vein isolation during cryoballoon ablation using the novel Achieve inner lumen mapping catheter: a feasibility study". *Europace*, Vol. 14, No. 7, pp. 962–967, July 2012.

[Cond 04] A. Condurache, T. Aach, K. Eck, and J. Bredno. "Fast detection and processing of arbitrary contrast agent injections in coronary angiography and fluoroscopy". In: T. Tolxdorff, J. Braun, H. Handels, A. Horsch, and H.-P. Meinzer, Eds., *Bildverarbeitung für die Medizin 2004*, (Berlin, March 2004), pp. 5–9, 2004.

[Coot 95] T. Cootes, C. Taylor, D. Cooper, and J. Graham. "Active Shape Models-Their Training and Application". *Computer Vision and Image Understanding*, Vol. 61, No. 1, pp. 38 – 59, January 1995.

[Corm 90] T. Cormen, C. Leiserson, and R. Rivest. *Introduction to algorithms*. MIT Press, 1990.

[Cych 94] J. M. Cychosz. *Graphics Gems IV*, Chap. Efficient Binary Image Thinning Using Neighborhood Maps, pp. 465–473. Morgan Kaufmann, 1994.

[Davi 97] M. H. Davis, A. Khotanzad, D. P. Flamig, and S. E. Harms. "A physics-based coordinate transformation for 3-D image matching". *IEEE Transactions on Medical Imaging*, Vol. 16, No. 3, pp. 317–328, June 1997.

[De B 05] S. De Buck, F. Maes, J. Ector, J. Bogaert, S. Dymarkowski, H. Heidbuchel, and P. Suetens. "An Augmented Reality System for Patient-Specific Guidance of Cardiac Catheter Ablation Procedures". *IEEE Transactions on Medical Imaging*, Vol. 24, No. 11, pp. 1512 –1524, November 2005.

[Delg 12] R. Delgado-Gonzalo, P. Thevenaz, C. S. Seelamantula, and M. Unser. "Snakes with an ellipse-reproducing property". *IEEE Transactions on Image Processing*, Vol. 21, No. 3, pp. 1258–1271, March 2012.

[Dezi 93] D. J. Deziel, K. W. Millikan, S. G. Economou, A. Doolas, S.-T. Ko, and M. C. Airan. "Complications of laparoscopic cholecystectomy: a national survey of 4,292 hospitals and an analysis of 77,604 cases". *The American journal of surgery*, Vol. 165, No. 1, pp. 9–14, January 1993.

[Dick 06] T. Dickfeld, R. Kato, M. Zviman, S. Lai, G. Meininger, A. C. Lardo, A. Roguin, D. Blumke, R. Berger, H. Calkins, and H. Halperin. "Characterization of Radiofrequency Ablation Lesions With Gadolinium-Enhanced Cardiovascular Magnetic Resonance Imaging". *Journal of the American College of Cardiology*, Vol. 47, No. 2, pp. 370 – 378, January 2006.

[Doug 92] E. Dougherty. *Mathematical morphology in image processing*. CRC press, 1992.

[Duda 72] R. Duda and P. Hart. "Use of the Hough transformation to detect lines and curves in pictures". *Communications of the ACM*, Vol. 15, No. 1, pp. 11–15, January 1972.

[Ecab 08] O. Ecabert, J. Peters, H. Schramm, C. Lorenz, J. von Berg, M. Walker, M. Vembar, M. Olszewski, K. Subramanyan, G. Lavi, and J. Weese. "Automatic Model-Based Segmentation of the Heart in CT Images". *IEEE Transactions on Medical Imaging*, Vol. 27, No. 9, pp. 1189–1201, September 2008.

[Ecto 08] J. Ector, S. D. Buck, W. Huybrechts, D. Nuyens, S. Dymarkowski, J. Bogaert, F. Maes, and H. Heidbüchel. "Biplane three-dimensional augmented fluoroscopy as single navigation tool for ablation of atrial fibrillation: Accuracy and clinical value". *Heart Rhythm*, Vol. 5, No. 7, pp. 957 – 964, July 2008.

[Eite 94] T. Eiter and H. Mannila. "Computing Discrete Fréchet Distance". Tech. Rep., Technische Universität Wien, 1994.

[Este 08] M. Esteghamatian, Z. Azimifar, P. Radau, and G. Wright. "Real-Time 2D-3D MR Cardiac Image Registration During Respiration Using Extended Kalman Filter Predictors". In: *2008 9th International Conference on Signal Processing*, (Beijing, China, October 2008), pp. 1325–1328, IEEE, 2008.

[Estn 06] H. L. Estner, I. Deisenhofer, A. Luik, G. Ndrepepa, C. von Bary, B. Zrenner, and C. Schmitt. "Electrical isolation of pulmonary veins in patients with atrial fibrillation: reduction of fluoroscopy exposure and procedure

duration by the use of a non-fluoroscopic navigation system (NavX®)". *Europace*, Vol. 8, No. 8, pp. 583–587, August 2006.

[Estn 15] H. L. Estner, M. Grazia Bongiorni, J. Chen, N. Dagres, A. Hernandez-Madrid, and C. Blomström-Lundqvist. "Use of fluoroscopy in clinical electrophysiology in Europe: results of the European Heart Rhythm Association Survey". *Europace*, Vol. 17, No. 7, pp. 1149–1152, July 2015.

[Fein 95] W. Feinberg, J. Blackshear, A. Laupacis, R. Kronmal, and R. Hart. "Prevalence, age distribution, and gender of patients with atrial fibrillation: analysis and implications". *Archives of internal medicine*, Vol. 155, No. 5, p. 469, March 1995.

[Feld 07] T. Feldman and W. G. Fisher. *Problem Oriented Approaches in Interventional Cardiology*, Chap. Transseptal puncture, pp. 203–218. CRC Press, 2007.

[Felz 04] P. Felzenszwalb and D. Huttenlocher. "Distance Transforms of Sampled Functions". Tech. Rep., Cornell University, 2004.

[Fies 08] A. Fieselmann, S. Lautenschläger, F. Deinzer, M. John, and B. Poppe. "Automated 3D Segmentation of the Esophagus For Planning of Atrial Ablation Therapy". In: DGMP (Deutsche Gesellschaft für Medizinische Physik), Ed., *Medizinische Physik 2008*, (Oldenburg, 2008), 2008.

[Fisc 14] P. Fischer, T. Pohl, and J. Hornegger. "Real-Time Respiratory Signal Extraction from X-Ray Sequences using Incremental Manifold Learning". In: G. Wang and B. He, Eds., *2014 IEEE 11th International Symposium on Biomedical Imaging (ISBI)*, (Beijing, China, April 2014), pp. 915–918, 2014.

[Fran 06] E. Franken, P. Rongen, M. van Almsick, and B. ter Haar Romeny. "Detection of Electrophysiology Catheters in Noisy Fluoroscopy Images". In: R. Larsen, M. Nielsen, and J. Sporring, Eds., *Medical Image Computing and Computer-Assisted Intervention – MICCAI 2006*, (Copenhagen, Denmark, October 2006), pp. 25–32, Springer Berlin Heidelberg, 2006.

[Fran 98] A. Frangi, W. Niessen, K. Vincken, and M. Viergever. "Multiscale vessel enhancement filtering". In: W. Wells, A. Colchester, and S. Delp, Eds., *Medical Image Computing and Computer-Assisted Interventation–MICCAI'98*, (Cambridge, MA, USA, October 1998), pp. 130–137, Springer Berlin / Heidelberg, 1998.

[Furn 11] A. Fürnkranz and F. Ouyang. "Non-invasive imaging prior to cryoballoon ablation of atrial fibrillation: what can we learn?". *Europace*, Vol. 13, No. 2, pp. 153–154, 2011.

[Furn 14] A. Fürnkranz, S. Bordignon, D. Dugo, L. Perotta, M. Gunawardene, B. Schulte-Hahn, B. Nowak, B. Schmidt, and J. K. Chun. "Improved 1-Year Clinical Success Rate of Pulmonary Vein Isolation with the Second-Generation Cryoballoon in Patients with Paroxysmal Atrial Fibrillation". *Journal of Cardiovascular Electrophysiology*, Vol. 25, No. 8, pp. 840–844, August 2014.

[Fust 06] V. Fuster, L. Rydén, D. Cannom, H. Crijns, A. Curtis, K. Ellenbogen, J. Halperin, J. Le Heuzey, G. Kay, J. Lowe, *et al.* "ACC/AHA/ESC 2006 Guidelines for the Management of Patients With Atrial Fibrillation - Executive Summary". *Journal of the American College of Cardiology*, Vol. 48, No. 4, p. 854, August 2006.

[Geps 97] L. Gepstein, G. Hayam, and S. A. Ben-Haim. "A Novel Method for Non-fluoroscopic Catheter-Based Electroanatomical Mapping of the Heart: In Vitro and In Vivo Accuracy Results". *Circulation*, Vol. 95, No. 6, pp. 1611–1622, March 1997.

[Gold 70] D. Goldfarb. "A family of variable-metric methods derived by variational means". *Mathematics of computation*, Vol. 24, No. 109, pp. 23–26, January 1970.

[Gonz 08] R. C. Gonzalez and R. E. Woods. *Digital Image Processing*. Prentice Hall, 3. Ed., 2008.

[Good 05] E. Good, H. Oral, K. Lemola, J. Han, K. Tamirisa, P. Igic, D. Elmouchi, D. Tschopp, S. Reich, A. Chugh, F. Bogun, F. Pelosi, and F. Morady. "Movement of the Esophagus During Left Atrial Catheter Ablation for Atrial Fibrillation". *Journal of the American College of Cardiology*, Vol. 46, No. 11, pp. 2107–2110, December 2005.

[Good 06] J. S. Goode, R. L. Taylor, C. W. Buffington, M. M. Klain, and D. Schwartzman. "High-frequency jet ventilation: Utility in posterior left atrial catheter ablation". *Heart Rhythm*, Vol. 3, No. 1, pp. 13 – 19, January 2006.

[Guez 98] A. Guéziec, P. Kazanzides, B. Williamson, and R. Taylor. "Anatomy-Based Registration of CT-Scan and Intraoperative X-Ray Images for Guiding a Surgical Robot". *IEEE Transactions on Medical Imaging*, Vol. 17, No. 5, pp. 715 –728, October 1998.

[Guls 08] M. Gülsün and H. Tek. "Robust Vessel Tree Modeling". In: D. Metaxas, A. L., G. Fichtinger, and G. Szekely, Eds., *Medical Image Computing and Computer-Assisted Intervention–MICCAI 2008, Part 1*, (New York, NY, USA, September 2008), pp. 602–611, Springer Berlin Heidelberg, 2008.

[Hali 98] R. Halir and J. Flusser. "Numerically stable direct least squares fitting of ellipses". In: N. M. Thalmann and V. Skala, Eds., *Proc. 6th International Conference in Central Europe on Computer Graphics and Visualization. WSCG*, (Plzen - Bory, Czech Republic, February 1998), pp. 125–132, Citeseer, 1998.

[Hama 98] A. Hamadeh, S. Lavallee, and P. Cinquin. "Automated 3-Dimensional Computed Tomographic and Fluoroscopic Image Registration". *Computer Aided Surgery*, Vol. 3, No. 1, pp. 11–19, December 1998.

[Hart 03] R. Hartley and A. Zissermann. *Multiple view geometry in computer vision*. Cambridge Univ Press, 2 Ed., 2003.

[Haus 08] T. H. Hauser, D. C. Peters, J. V. Wylie, and W. J. Manning. "Evaluating the left atrium by magnetic resonance imaging". *Europace*, Vol. 10, No. suppl 3, pp. iii22–iii27, November 2008.

[Hoff 12a] M. Hoffmann. *3-D Catheter Reconstruction from Two Views for Electrophysiology Procedures*. Diploma thesis, Friedrich-Alexander-Universität Erlangen-Nürnberg, Germany, 2012.

[Hoff 12b] M. Hoffmann, A. Brost, C. Jakob, F. Bourier, M. Koch, K. Kurzidim, J. Hornegger, and N. Strobel. "Semi-Automatic Catheter Reconstruction from Two Views". In: N. Ayache, H. Delingette, P. Golland, and K. Mori, Eds., *Medical Image Computing and Computer-Assisted Intervention – MICCAI 2012, Part II*, (Nice, France, October 2012), pp. 584–591, Springer Berlin Heidelberg, 2012.

[Hoff13a] M. Hoffmann, F. Bourier, N. Strobel, and J. Hornegger. "Structure-Enhancing Visualization for Manual Registration in Fluoroscopy". In: H.-P. Meinzer, T. M. Deserno, H. Handels, and T. Tolxdorff, Eds., *Bildverarbeitung für die Medizin 2013*, (Heidelberg, March 2013), pp. 241–246, Berlin Heidelberg, 2013.

[Hoff13b] M. Hoffmann, A. Brost, C. Jakob, M. Koch, F. Bourier, K. Kurzidim, J. Hornegger, and N. Strobel. "Reconstruction method for curvilinear structures from two views". In: D. R. Holmes and Z. R. Yaniv, Eds., *Medical Imaging 2013: Image-Guided Procedures, Robotic Interventions, and Modeling*, (Lake Buena Vista, FL, USA, February 2013), pp. 86712F–1 – 86712F–8, 2013.

[Hoff15] M. Hoffmann, S. Müller, K. Kurzidim, N. Strobel, and J. Hornegger. "Robust Identification of Contrasted Frames in Fluoroscopic Images". In: H. Handels, T. M. Deserno, H.-P. Meinzer, and T. Tolxdorff, Eds., *Bildverarbeitung für die Medizin 2015*, (Lübeck, March 2015), pp. 23–28, Springer Berlin Heidelberg, 2015.

[Hoff16a] M. Hoffmann, N. Strobel, J. Hornegger, and A. Maier. "Contrast-Based Registration Of Left Atria To Fluoroscopic Image Sequences By Temporal Markow Filtering And Motion Regularization". In: IEEE, Ed., *2016 IEEE 13th International Symposium on Biomedical Imaging*, (Prague, April 2016), pp. 621–624, 2016.

[Hoff16b] M. Hoffmann, A. Brost, M. Koch, F. Bourier, A. Maier, K. Kurzidim, N. Strobel, and J. Hornegger. "Electrophysiology Catheter Detection and Reconstruction from Two Views in Fluoroscopic Images". *IEEE Transactions on Medical Imaging*, Vol. 35, No. 2, pp. 567–579, February 2016.

[Hoff16c] M. Hoffmann, M. Koch, N. Strobel, and A. Maier. "Automatic Detection of Ostia in the Left Atrium". In: T. Tolxdorff, T. M. Deserno, H. Handels, and H.-P. Meinzer, Eds., *Bildverarbeitung für die Medizin 2016*, (Berlin, March 2016), pp. 224–229, Berlin Heidelberg, 2016.

[Hoff16d] M. Hoffmann, C. Kowalewski, A. Maier, K. Kurzidim, N. Strobel, and J. Hornegger. "Contrast-based 3-D/2-D Registration of the Left Atrium: Fast vs. Consistent". *International Journal of Biomedical Imaging*, Vol. 2016, No. 7690391, pp. 1–15, February 2016.

[Hoff16e] M. Hoffmann, C. Kowalewski, A. Maier, K. Kurzidim, N. Strobel, and J. Hornegger. "3-D/2-D Registration of Cardiac Structures by 3-D Contrast Agent Distribution Estimation". 2016. arXiv:1601.06062 [cs.CV].

[Hoff16f] M. Hoffmann and N. Strobel. "Verfahren zur automatischen Erkennung von anatomischen Landmarken und Vorrichtung". Patent DE201610204225. 2016.

[Hoff16g] M. Hoffmann, N. Strobel, and A. Maier. "Registration of Atrium Models to C-arm X-ray Images Based on Devices Inside the Coronary Sinus and the Esophagus". In: H. Handels, T. M. Deserno, H.-P. Meinzer, and T. Tolxdorff, Eds., *Bildverarbeitung für die Medizin 2016*, (Berlin, March 2016), pp. 86–91, 2016.

[Hous13] R. J. Housden, M. Basra, Y. Ma, A. P. King, R. Bullens, N. Child, J. Gill, C. A. Rinaldi, V. Parish, and K. S. Rhode. "Three-modality registration for guidance of minimally invasive cardiac interventions". In: S. Ourselin, D. Rueckert, and N. Smith, Eds., *Functional Imaging and Modeling of the Heart*, (London, June 2013), pp. 158–165, Springer, 2013.

[Irib 11] A. Iribarne, R. Easterwood, E. Y. Chan, J. Yang, L. Soni, M. J. Russo, C. R. Smith, and M. Argenziano. "The golden age of minimally invasive cardiothoracic surgery: current and future perspectives". *Future cardiology*, Vol. 7, No. 3, pp. 333–346, May 2011.

[Jaco 91] M. Jacobs, J. Verdeja, and H. Goldstein. "Minimally invasive colon resection (laparoscopic colectomy).". *Surgical Laparoscopy Endoscopy & Percutaneous Techniques*, Vol. 1, No. 3, pp. 144–150, September 1991.

[Kapp 12] S. Käppler, A. Brost, M. Koch, W. Wu, F. Bourier, T. Chen, K. Kurzidim, J. Hornegger, and N. Strobel. "Motion Estimation Model for Cardiac and Respiratory Motion Compensation". In: Purang and J. Abolmaesumi, Eds., *Information Processing in Computer-Assisted Interventions*, (Pisa, Italy, June 2012), pp. 94–103, Berlin Heidelberg, 2012.

[Kapp 13] S. Käppler, W. Wu, T. Chen, M. Koch, A. Kiraly, N. Strobel, and J. Hornegger. "Semi-automatic catheter model generation using biplane x-ray images". In: B. Parvi and M. Viergever, Eds., *10th IEEE International Symposium on Biomedical Imaging*, (San Francisco, CA, USA, April 2013), pp. 1416 – 1419, IEEE, 2013.

[Kapt 03] B. Kaptein, E. Valstar, B. Stoel, P. Rozing, and J. Reiber. "A new model-based RSA method validated using CAD models and models from reversed engineering". *Journal of Biomechanics*, Vol. 36, No. 6, pp. 873 – 882, June 2003.

[Kari 09a] R. Karim, R. Mohiaddin, and D. Rueckert. "Left atrium pulmonary veins: segmentation and quantification for planning atrial fibrillation ablation". In: M. Miga and K. Wong, Eds., *Medical Imaging 2009: Visualization, Image-Guided Proceudres, and Modeling*, (Lake Buena Vista, FL, USA, February 2009), pp. 72611T–1–11, International Society for Optics and Photonics, 2009.

[Kari 09b] R. Karim. *Segmentation of the Left Atrium and Pulmonary Veins from Contrast-Enhanced MR Images*. PhD thesis, Imperial College London, 2009.

[Kass 88] M. Kass, A. Witkin, and D. Terzopoulos. "Snakes: Active contour models". *International Journal of Computer Vision*, Vol. 1, No. 4, pp. 321–331, January 1988.

[Khos 13] M. Khoshnam and R. Patel. "A pseudo-rigid-body 3R model for a steerable ablation catheter". In: R. Dillmann and R. Siegwart, Eds., *2013 IEEE International Conference on Robotics and Automation (ICRA)*, (Karlsruhe, Germany, May 2013), pp. 4427–4432, IEEE, 2013.

[King 09] A. King, R. Boubertakh, K. Rhode, Y. Ma, P. Chinchapatnam, G. Gao, T. Tangcharoen, M. Ginks, M. Cooklin, J. Gill, D. Hawkes, R. Razavi, and T. Schaeffter. "A subject-specific technique for respiratory motion correction in image-guided cardiac catheterisation procedures". *Medical Image Analysis*, Vol. 13, No. 3, pp. 419 – 431, June 2009.

[Klei 10] A. Kleinöder. *Catheter Reconstruction from Two X-Ray Projections*. Master's thesis, Friedrich-Alexander-Universität Erlangen-Nürnberg, 2010.

[Klei 11] A. Kleinoeder, A. Brost, F. Bourier, M. Koch, K. Kurzidim, J. Hornegger, and N. Strobel. "Cryo-Balloon Reconstruction from Two Views". In: B. Macq and P. Schelkens, Eds., *Proceedings of IEEE International*

Conference on Image Processing, (Brussels, Belgium, September 2011), pp. 989–992, 2011.

[Klei 12] A. Kleinoeder, A. Brost, F. Bourier, M. Koch, K. Kurzidim, J. Hornegger, and N. Strobel. "Cryo-balloon catheter position planning using AFiT". In: D. R. H. III and K. H. Wong, Eds., *Medical Imaging 2012: Image-Guided Procedures, Robotic Interventions, and Modeling*, (San Diego, CA, USA, February 2012), 2012.

[Klem 07] H. U. Klemm, D. Steven, C. Johnsen, R. Ventura, T. Rostock, B. Lutomsky, T. Risius, T. Meinertz, and S. Willems. "Catheter motion during atrial ablation due to the beating heart and respiration: Impact on accuracy and spatial referencing in three-dimensional mapping". *Heart Rhythm*, Vol. 4, No. 5, pp. 587 – 592, May 2007.

[Knec 08] S. Knecht, H. Skali, M. D. O'Neill, M. Wright, S. Matsuo, G. M. Chaudhry, C. I. Haffajee, I. Nault, G. H. Gijsbers, F. Sacher, F. Laurent, M. Montaudon, O. Corneloup, M. Hocini, M. Haïssaguerre, M. V. Orlov, and P. Jaïs. "Computed tomography - fluoroscopy overlay evaluation during catheter ablation of left atrial arrhythmia". *Europace*, Vol. 10, No. 8, pp. 931–938, August 2008.

[Knec 13] S. Knecht, M. Kuehne, D. Altmann, P. Ammann, B. Schaer, S. Osswald, and C. Sticherling. "Anatomical Predictors for Acute and Mid-Term Success of Cryoballoon Ablation of Atrial Fibrillation Using the 28 mm Balloon". *Journal of Cardiovascular Electrophysiology*, Vol. 24, No. 2, pp. 132–138, February 2013.

[Koch 14] M. Koch, A. Brost, F. Bourier, J. Hornegger, and N. Strobel. "Automatic planning of atrial fibrillation ablation lines using landmark-constrained nonrigid registration". *Journal of Medical Imaging*, Vol. 1, No. 1, pp. 015002–1–8, May 2014.

[Koch 15] M. Koch, M. Hoffmann, M. Pfister, J. Hornegger, and N. Strobel. "Optimized viewing angles for cardiac electrophysiology ablation procedures". *International Journal of Computer Assisted Radiology and Surgery*, Vol. 10, No. 5, pp. 651–664, August 2015.

[Kojo 10] P. Kojodjojo, M. D. O'Neill, P. B. Lim, L. Malcolm-Lawes, Z. I. Whinnett, T. V. Salukhe, N. W. Linton, D. Lefroy, A. Mason, I. Wright, N. S. Peters, P. Kanagaratnam, and D. W. Davies. "Pulmonary venous isolation by antral ablation with a large cryoballoon for treatment of paroxysmal and persistent atrial fibrillation: medium-term outcomes and non-randomised comparison with pulmonary venous isolation by radiofrequency ablation". *Heart*, Vol. 96, No. 17, pp. 1379–1384, September 2010.

[Kurz 12] T. Kurzendorfer, A. Brost, F. Bourier, M. Koch, K. Kurzidim, J. Hornegger, and N. Strobel. "Cryo-Balloon Catheter Tracking in Atrial Fibrillation Ablation Procedures". In: T. Tolxdorff, T. M. Deserno, H. Handels, and H.-P. Meinzer, Eds., *Bildverarbeitung für die Medizin 2012*, (Berlin, March 2012), pp. 386–391, Springer Berlin Heidelberg, 2012.

[Kurz 13] T. Kurzendorfer, A. Brost, C. Jakob, P. W. Mewes, F. Bourier, M. Koch, K. Kurzidim, J. Hornegger, and N. Strobel. "Cryo-Balloon Catheter Localization in Fluoroscopic Images". In: D. R. Holmes and Z. R. Yaniv, Eds., *Medical Imaging 2013: Image-Guided Procedures, Robotic Interventions, and Modeling*, (Lake Buena Vista, FL, USA, February 2013), pp. 86710C–1 – 86710C–8, 2013.

[Kurz 16] T. Kurzendorfer, P. Mewes, A. Maier, N. Strobel, and A. Brost. "Cryo-Balloon Catheter Localization Based on a Support-Vector-Machine Approach". *IEEE Transactions on Medical Imaging*, Vol. 35, No. 8, pp. 1892–1902, August 2016.

[Li 09] J. H. Li, M. Haim, B. Movassaghi, J. B. Mendel, G. M. Chaudhry, C. I. Haffajee, and M. V. Orlov. "Segmentation and registration of three-dimensional rotational angiogram on live fluoroscopy to guide atrial fibrillation ablation: A new online imaging tool". *Heart Rhythm*, Vol. 6, No. 2, pp. 231 – 237, February 2009.

[Liao 13] R. Liao, W. You, Y. Liu, M. Yan, M. John, and S. Shea. "Integrated spatiotemporal analysis for automatic contrast agent inflow detection on angiography and fluoroscopy during transcatheter aortic valve implantation". *Medical Physics*, Vol. 40, No. 4, p. 041914, April 2013.

[Livy 03] H. Livyatan, Z. Yaniv, and L. Joskowicz. "Gradient-based 2-D/3-D rigid registration of fluoroscopic X-ray to CT". *IEEE Transactions on Medical Imaging*, Vol. 22, No. 11, pp. 1395–1406, November 2003.

[Ma 10] Y. Ma, A. King, N. Gogin, C. Rinaldi, J. Gill, R. Razavi, and K. Rhode. "Real-Time Respiratory Motion Correction for Cardiac Electrophysiology Procedures Using Image-Based Coronary Sinus Catheter Tracking". In: T. Jiang, N. Navab, J. Pluim, and M. Viergever, Eds., *Medical Image Computing and Computer-Assisted Intervention - MICCAI 2010 Part I*, (Bejing, China, September 2010), pp. 391–399, Springer Berlin / Heidelberg, 2010.

[Ma 13] Y. Ma, N. Gogin, P. Cathier, R. J. Housden, G. Gijsbers, M. Cooklin, M. O'Neill, J. Gill, C. A. Rinaldi, R. Razavi, and K. S. Rhode. "Real-time x-ray fluoroscopy-based catheter detection and tracking for cardiac electrophysiology interventions". *Medical Physics*, Vol. 40, No. 7, pp. 071902–1 – 071902–13, July 2013.

[Mark 12] P. Markelj, D. Tomaževič, B. Likar, and F. Pernuš. "A review of 3D/2D registration methods for image-guided interventions". *Medical Image Analysis*, Vol. 16, No. 3, pp. 642 – 661, April 2012.

[Meye 99] S. A. Meyer and P. D. Wolf. "Registration of three-dimensional cardiac catheter models to single-plane fluoroscopic images". *IEEE Transactions on Biomedical Engineering*, Vol. 46, No. 12, pp. 1471–1479, December 1999.

[Mill 13] F. Milletari, N. Navab, and P. Fallavollita. "Automatic Detection of Multiple and Overlapping EP Catheters in Fluoroscopic Sequences". In: K. Mori, I. Sakuma, Y. Sato, C. Barillot, and N. Navab, Eds., *Medical Image Computing and Computer-Assisted Intervention – MICCAI 2013, Part III*, (Nagoya, Japan, September 2013), pp. 371–379, Springer Berlin Heidelberg, 2013.

[Mill 14] F. Milletari, V. Belagiannis, N. Navab, and P. Fallavollita. "Fully Automatic Catheter Localization in C-Arm Images Using l1-Sparse Coding". In: P. Golland, N. Hata, C. Barillot, J. Hornegger, and R. Howe, Eds., *Medical Image Computing and Computer-Assisted Intervention – MICCAI 2014 Part II*, (Boston, MA, USA, September 2014), pp. 570–577, Springer International Publishing, 2014.

[Misc 00] M. Mischke and N. Navab. "Recovering projection geometry: How a cheap camera can outperform an expensive stereo system". In: *IEEE Conference on Computer Vision and Pattern Recognition, 2000. Proceedings. Volume 2*, (Hilton Head Island, SC, USA, June 2000), pp. 193–200, IEEE, 2000.

[Moli 98] M. C. Molina, G. P. M. Prause, P. Radeva, and M. Sonka. "3D catheter path reconstruction from biplane angiograms". In: K. M. Hanson, Ed., *Medical Imaging 1998: Image Processing*, (San Diego, CA, USA, February 1998), pp. 504–512, 1998.

[Mull 13] K. Müller, C. Schwemmer, J. Hornegger, Y. Zheng, Y. Wang, G. Lauritsch, C. Rohkohl, A. K. Maier, C. Schultz, and R. Fahrig. "Evaluation of interpolation methods for surface-based motion compensated tomographic reconstruction for cardiac angiographic C-arm data". *Medical Physics*, Vol. 40, No. 3, 2013.

[Mull 16] K. Müller, M. Ahmad, M. Spahn, J.-H. Choi, S. Reitz, N. Köster, Y. Lu, R. Fahrig, and A. Maier. "Towards Material Decomposition on Large Field-of-View Flat Panel Photon-Counting Detectors - First in-vivo Results". In: M. Kachelriess, Ed., *Proceedings of the fourth international conference on image formation in x-ray computed tomography*, (Bamberg, Germany, July 2016), pp. 479–482, 2016.

[Nara 12] S. M. Narayan, D. E. Krummen, K. Shivkumar, P. Clopton, W.-J. Rappel, and J. M. Miller. "Treatment of Atrial Fibrillation by the Ablation of Localized Sources: CONFIRM (Conventional Ablation for Atrial Fibrillation With or Without Focal Impulse and Rotor Modulation) Trial". *Journal of the American College of Cardiology*, Vol. 60, No. 7, pp. 628 – 636, August 2012.

[Pete 89] P. Petersen, J. Godtfredsen, G. Boysen, E. Andersen, and B. Andersen. "Placebo-controlled, randomised trial of warfarin and aspirin for prevention of thromboembolic complications in chronic atrial fibrillation. The Copenhagen AFASAK Study". *The Lancet*, Vol. 1, No. 8631, pp. 175 – 179, January 1989.

[Poly 12] M. Polyanskaya, C. Schwemmer, A. Linarth, G. Lauritsch, and J. Hornegger. "Robust lumen segmentation of coronary arteries in 2-D angiographic images". In: D. R. Haynor and S. Ourselin, Eds., *Medical Imaging 2012: Image-Guided Procedures, Robotic Interventions, and Modeling*, (San Diego, CA, USA, February 2012), p. 83142N, SPIE, 2012.

[Prat 91] W. K. Pratt. *Digital Image Processing*. John Wiley & Sons, 1991.

[Redd 12] V. Y. Reddy, D. Shah, J. Kautzner, B. Schmidt, N. Saoudi, C. Herrera, P. Jaïs, G. Hindricks, P. Peichl, A. Yulzari, H. Lambert, P. Neuzil, A. Natale, and K.-H. Kuck. "The relationship between contact force and clinical outcome during radiofrequency catheter ablation of atrial fibrillation in the TOCCATA study". *Heart Rhythm*, Vol. 9, No. 11, pp. 1789 – 1795, November 2012.

[Reim 15] S. Reiml, M. Pfister, D. Toth, A. Maier, M. Hoffmann, M. Kowarschik, and J. Hornegger. "Automatic Detection of Stent Graft Markers in 2-D Fluoroscopy Images". In: S. Balocco, M. A. Zuluaga, G. Zahnd, and S.-L. Lee, Eds., *Joint MICCAI workshop on Computing and Visualisation for Intravascular Imaging and Computer-Assisted Stenting*, (München, September 2015), pp. 34–41, 2015.

[Rett 09] M. E. Rettmann, D. R. Holmes III, D. L. Packer, and R. A. Robb. "Identification of left pulmonary vein ostia using centerline tracking". In: M. Miga and K. Wong, Eds., *Medical Imaging 2009: Visualization, Image-Guided Proceudres, and Modeling*, (Lake Buena Vista, FL, USA, February 2009), pp. 726228–726228–7, 2009.

[Rive 12] D. Rivest-Henault, H. Sundar, and M. Cheriet. "Nonrigid 2D/3D registration of coronary artery models with live fluoroscopy for guidance of cardiac interventions". *IEEE Transactions on Medical Imaging*, Vol. 31, No. 8, pp. 1557–1572, August 2012.

[Roug 93] A. Rougée, C. Picard, C. Ponchut, and Y. Trousset. "Geometrical calibration of X-ray imaging chains for three-dimensional reconstruction". *Computerized Medical Imaging and Graphics*, Vol. 17, No. 4, pp. 295–300, October 1993.

[Sand 16] J. Sanders, P. Ritt, T. Kuwert, A. H. Vija, and A. Maier. "Fully Automated Data-Driven Respiratory Signal Extraction from SPECT Images Using Laplacian Eigenmaps". *IEEE Transactions on Medical Imaging*, Vol. 35, No. 11, pp. 2425–2435, November 2016.

[Sche 10] M. Schenderlein, S. Stierlin, R. Manzke, V. Rasche, and K. Dietmayer. "Catheter Tracking in Asynchronous Biplane Fluoroscopy Images by 3D B-Snakes". In: K. Wong and M. Miga, Eds., *Medical Imaging 2010: Visualization, Image-Guided Proceudres, and Modeling*, (San Diego, CA, USA, February 2010), pp. 76251U–1 – 76251U–9, 2010.

[Schm 05] F. Schmidt. *Catheter localization in coronary biplane x-ray imaging*. Master's thesis, Friedrich-Alexander-Universität Erlangen-Nürnberg, Germany, 2005.

[Schm 13] M. Schmidt, U. Dorwarth, F. Straube, M. Daccarett, J. Rieber, M. Wankerl, J. Krieg, A. W. Leber, U. Ebersberger, A. Huber, E. Rummeny, and E. Hoffmann. "Cryoballoon in AF ablation: Impact of PV ovality on AF recurrence". *International Journal of Cardiology*, Vol. 167, No. 1, pp. 114 – 120, July 2013.

[Siev 02] H. Sievert, M. D. Lesh, T. Trepels, H. Omran, A. Bartorelli, P. Della Bella, T. Nakai, M. Reisman, C. DiMario, P. Block, P. Kramer, D. Fleschenberg, U. Krumsdorf, and D. Scherer. "Percutaneous Left Atrial Appendage Transcatheter Occlusion to Prevent Stroke in High-Risk Patients With Atrial Fibrillation: Early Clinical Experience". *Circulation*, Vol. 105, No. 16, pp. 1887–1889, April 2002.

[Sing 06] S. N. Singh, X. C. Tang, B. N. Singh, P. Dorian, D. J. Reda, C. L. Harris, R. D. Fletcher, S. C. Sharma, J. E. Atwood, A. K. Jacobson, H. D. Lewis, Jr, B. Lopez, D. W. Raisch, and M. D. Ezekowitz. "Quality of Life and Exercise Performance in Patients in Sinus Rhythm Versus Persistent Atrial FibrillationA Veterans Affairs Cooperative Studies Program Substudy". *Journal of the American College of Cardiology*, Vol. 48, No. 4, pp. 721–730, August 2006.

[Spie 09] M. Spiegel, M. Pfister, D. Hahn, V. Daum, J. Hornegger, T. Struffert, and A. Dörfler. "Towards Real-time Guidewire Detection and Tracking in the Field of Neuroradiology". In: M. Miga and K. Wong, Eds., *Medical Imaging 2009: Visualization, Image-Guided Proceudres, and Modeling*, (Lake Buena Vista, FL, USA, February 2009), pp. 726105–1 – 726105–8, 2009.

[Spor 04] S. C. Sporton, M. J. Earley, A. W. Nathan, and R. J. Schilling. "Electroanatomic Versus Fluoroscopic Mapping for Catheter Ablation Procedures:". *Journal of Cardiovascular Electrophysiology*, Vol. 15, No. 3, pp. 310–315, March 2004.

[Sra 05] J. Sra, D. Krum, A. Malloy, M. Vass, B. Belanger, E. Soubelet, R. Vaillant, and M. Akhtar. "Registration of Three-Dimensional Left Atrial Computed Tomographic Images With Projection Images Obtained Using Fluoroscopy". *Circulation*, Vol. 112, No. 24, pp. 3763–3768, December 2005.

[Sra 07] J. Sra, G. Narayan, D. Krum, A. Malloy, R. Cooley, A. Bhatia, A. Dhala, Z. Blanck, V. Nangia, and M. Akhtar. "Computed Tomography-Fluoroscopy Image Integration-Guided Catheter Ablation of Atrial Fibrillation". *Journal of cardiovascular electrophysiology*, Vol. 18, No. 4, pp. 409–414, April 2007.

[Stat 16] Statistisches Bundesamt, Ed. *Gesundheit - Ausgaben*, 2016. Fachserie 12 Reihe 7.1.2.

[Stev 10] J. Stevenhagen, P. Voort, L. Dekker, R. W M Bullens, H. Van Den Bosch, and A. Meijer. "Three-Dimensional CT Overlay in Comparison to CartoMerge for Pulmonary Vein Antrum Isolation". *Journal of Cardiovascular Electrophysiology*, Vol. 21, No. 6, pp. 634–639, June 2010.

[Tang 09] M. Tang, C. Kriatselis, G. Ye, S. Nedios, M. Roser, N. Solowjowa, E. Fleck, and J.-H. Gerds-Li. "Reconstructing and Registering Three-Dimensional Rotational Angiogram of Left Atrium during Ablation of Atrial Fibrillation". *Pacing and Clinical Electrophysiology*, Vol. 32, No. 11, pp. 1407–1416, 2009.

[Tele 12] A. Telea and A. C. Jalba. "Computing Curve Skeletons from Medial Surfaces of 3D Shapes". In: H. Carr and S. Czanner, Eds., *Theory and Practice of Computer Graphics*, (Rutherford, UK, September 2012), The Eurographics Association, 2012.

[Thiv 12] D. Thivierge-Gaulin, C. Chou, A. Kiraly, C. Chefd'Hotel, N. Strobel, and F. Cheriet. "3D-2D registration based on mesh-derived image bisection". In: B. M. Dawant, G. E. Christensen, J. M. Fitzpatrick, and D. Rueckert, Eds., *Biomedical Image Registration*, (Nashville, TN, USA, July 2012), pp. 70–78, Springer Berlin Heidelberg, 2012.

[Toma 05] E. H. Tomas Akenine-Möller. *Real-time rendering*. A. K. Peters, Ltd., Natick, MA, USA, 2nd Ed., 2005.

[Toth 15] D. Toth, M. Pfister, A. Maier, M. Kowarschik, and J. Hornegger. "Adaption of 3D Models to 2D X-Ray Images during Endovascular Abdominal Aneurysm Repair". In: N. Navab, J. Hornegger, W. M. Wells, and A. Frangi, Eds., *Medical Image Computing and Computer-Assisted Intervention – MICCAI 2015, Part I*, (Munich, October 2015), pp. 339–346, Springer International Publishing, Cham, 2015.

[Unbe 16] M. Unberath, A. Aichert, S. Achenbach, and A. Maier. "Virtual Single-frame Subtraction Imaging". In: M. Kachelriess, Ed., *Proceedings of the Fourth International Conference on Image Formation in X-ray Computed Tomography*, (Bamberg, July 2016), pp. 89 – 92, 2016.

[Van 12] P. Van Der Voort, J. Stevenhagen, L. Dekker, R. Bullens, and A. Meijer. "Three-dimensional computed tomography overlay for pulmonary vein antrum isolation: Follow-up and clinical outcomes". *Netherlands Heart Journal*, Vol. 20, No. 7-8, pp. 302–306, June 2012.

[Vapn 13] V. Vapnik. *The nature of statistical learning theory*. Springer Science & Business Media, 2013.

[Vogt 13] J. Vogt, J. Heintze, K. J. Gutleben, B. Muntean, D. Horstkotte, and G. Nölker. "Long-Term Outcomes After Cryoballoon Pulmonary Vein IsolationResults From a Prospective Study in 605 Patients". *Journal of the American College of Cardiology*, Vol. 61, No. 16, pp. 1707–1712, April 2013.

[Wang 09] P. Wang, T. Chen, Y. Zhu, W. Zhang, S. K. Zhou, and D. Comaniciu. "Robust guidewire tracking in fluoroscopy". In: *2009 IEEE Conference on Computer Vision and Pattern Recognition (CVPR 2009)*, (Maimi, FL, USA, June 2009), pp. 691–698, IEEE, 2009.

[Wang 10] P. Wang, W.-S. Liao, T. Chen, S. K. Zhou, and D. Comaniciu. "Graph Based Interactive Detection of Curve Structures in 2D Fluoroscopy". In: T. Jiang, N. Navab, J. Pluim, and M. A. Viergever, Eds., *Medical Image Computing and Computer-Assisted Intervention – MICCAI 2010 Part III*, (Bejing, China, September 2010), pp. 269–277, Springer Berlin Heidelberg, 2010.

[Wasz 16] J. Wasza, P. Fischer, H. Leutheuser, T. Oefner, C. Bert, A. Maier, and J. Hornegger. "Real-Time Respiratory Motion Analysis Using 4-D Shape Priors". *IEEE Transactions on Biomedical Engineering*, Vol. 63, No. 3, pp. 485–495, March 2016.

[Wije 06] S. N. Wijewickrema, A. P. Paplinski, and C. E. Esson. "Reconstruction of spheres using occluding contours from stereo images". In: Y. Y. Tang, P. Wang, and G. Lorette, Eds., *18th International Conference on Pattern Recognition, 2006. ICPR 2006.*, (Hongkong, China, August 2006), pp. 151–154, IEEE, 2006.

[Wilc 45] F. Wilcoxon. "Individual comparisons by ranking methods". *Biometrics bulletin*, Vol. 1, No. 6, pp. 80–83, December 1945.

[Witt 03] F. H. Wittkampf, E.-J. Vonken, R. Derksen, P. Loh, B. Velthuis, E. F. Wever, L. V. Boersma, B. J. Rensing, and M.-J. Cramer. "Pulmonary Vein Ostium Geometry: Analysis by Magnetic Resonance Angiography". *Circulation*, Vol. 107, No. 1, pp. 21–23, 2003.

[Wolf 91] P. Wolf, R. Abbott, and W. Kannel. "Atrial fibrillation as an independent risk factor for stroke: the Framingham Study". *Stroke*, Vol. 22, No. 8, pp. 983–988, August 1991.

[Wu 11] W. Wu, T. Chen, A. Barbu, P. Wang, N. Strobel, S. K. Zhou, and D. Comaniciu. "Learning-based Hypothesis Fusion for Robust Catheter Tracking in 2D X-ray Fluoroscopy". In: *2011 IEEE Conference on Computer Vision and Pattern Recognition*, (Provicence, RI, USA, June 2011), pp. 1097–1104, IEEE, 2011.

[Wu 13] X. Wu, J. Housden, Y. Ma, D. Rueckert, and K. Rhode. "Real-Time Catheter Extraction from 2D X-Ray Fluoroscopic and 3D Echocardiographic Images for Cardiac Interventions". In: O. Camara, T. Mansi, M. Pop,

K. Rhode, M. Sermesant, and A. Young, Eds., *Statistical Atlases and Computational Models of the Heart. Imaging and Modelling Challenges*, (Nagoya, Japan, September 2013), pp. 198–206, Springer Berlin Heidelberg, 2013.

[Yatz 12] L. Yatziv, M. Chartouni, S. Datta, and G. Sapiro. "Toward Multiple Catheters Detection in Fluoroscopic Image Guided Interventions". *IEEE Transactions on Information Technology in Biomedicine*, Vol. 16, No. 4, pp. 770 –781, July 2012.

[Zhao 13] X. Zhao, S. Miao, L. Du, and R. Liao. "Robust 2-D/3-D Registration of CT Volumes with Contrast-Enhanced X-ray Sequences in Electro-physiology Based on a Weighted Similarity Measure and Sequential Subspace Optimization". In: *2013 IEEE International Conference on Acoustics, Speech and Signal Processing (ICASSP),*, (Vancouver, Canada, May 2013), pp. 934–938, 2013.

[Zhen 11] Y. Zheng, T. Wang, M. John, S. K. Zhou, J. Boese, and D. Comaniciu. "Multi-part Left Atrium Modeling and Segmentation in C-arm CT Volumes for Atrial Fibrillation Ablation". In: G. Fichtinger and A. M. T. Peters, Eds., *Medical Image Computing and Computer-Assisted Intervention–MICCAI 2011 Part III*, (Toronto, Canada, September 2011), pp. 487–495, Springer, 2011.

[Zhen 12] Y. Zheng, M. John, J. Boese, and D. Comaniciu. "Precise segmentation of the left atrium in C-arm CT volumes with applications to atrial fibrillation ablation". In: *9th IEEE International Symposium on Biomedical Imaging (ISBI), 2012*, (Barcelona, Spain, May 2012), pp. 1421–1424, IEEE, 2012.

[Zhon 15] X. Zhong, M. Hoffmann, N. Strobel, and A. Maier. "Semi-Automatic Basket Catheter Reconstruction from Two X-Ray Views". In: J. Gall, P. Gehler, and B. Leibe, Eds., *Pattern Recognition*, (Aachen, Germany, October 2015), pp. 379–389, Springer International Publishing, 2015.

[Zhon 16] X. Zhong, M. Hoffmann, N. Strobel, and A. Maier. "Improved Semi-Automatic Basket Catheter Reconstruction from two X-Ray Views". In: T. Tolxdorff, T. M. Deserno, H. Handels, and H.-P. Meinzer, Eds., *Bildverarbeitung für die Medizin 2016*, (Charité - Universitätsmedizin Berlin, March 2016), pp. 26–31, 2016.

Picture Credits

[goog] CardioNetworks ECGpedia user googletrans. "De-WPW" https://commons.wikimedia.org/wiki/File:De-WPW_%28CardioNetworks_ECGpedia%29.png (last checked: 28-04-2016). Released by the author under the CC-BY-SA 3.0 license. The license can be found at https://creativecommons.org/licenses/by-sa/3.0/

[Ozha] Ozhank. "Planes of the human body". http://openclipart.org/detail/125287/planes-of-the-body-by-ozhank-125287 (last checked: 29-01-2012). Released by the author to public domain.

All clinical images are courtesy of Klinikum Barmherzige Brüder Regensburg.